

© 2007 by Zhengyu Zhang. All rights reserved.

EXTRINSIC COHESIVE MODELING OF DYNAMIC
FRACTURE AND MICROBRANCHING INSTABILITY
USING A TOPOLOGICAL DATA STRUCTURE

BY

ZHENGYU ZHANG

B.E., Tong Ji University, 1995

M.S., University of Illinois at Urbana-Champaign, 2003

DISSERTATION

Submitted in partial fulfillment of the requirements
for the degree of Doctor of Philosophy in Civil Engineering
in the Graduate College of the
University of Illinois at Urbana-Champaign, 2007

Urbana, Illinois

Doctoral Committee:

Professor Glaucio H. Paulino, Chair
Professor Robert H. Dodds Jr.
Professor Keith D. Hjelmstad
Professor B.F. Spencer Jr.
Professor Yonggang Huang, Northwestern University

Abstract

Realistic numerical analysis of dynamic failure process has long been a challenge in the field of computational mechanics. The challenge consists of two aspects: a realistic representation of fracture criteria, and its efficient incorporation into a viable numerical scheme. This study investigates the dynamic failure process in a variety of materials by incorporating a Cohesive Zone Model (CZM) into the finite element scheme. The CZM failure criterion uses both a finite cohesive strength and work to fracture in the material description. Based on crack initiation criteria, CZMs can be categorized into two groups, i.e., intrinsic and extrinsic. This study focuses on *extrinsic* CZMs, which eliminates many of the inherent drawbacks present in the *intrinsic* CZMs. The extrinsic CZM approach allows spontaneous and adaptive insertion of arbitrary cracks in space and time, i.e., where needed and when needed. To that effect, a novel topology-based data structure is employed in the study, which provides both versatility and robustness, and allows adaptive insertion of cohesive elements as required by simulation. Both two-dimensional and three-dimensional problems are analyzed. A series of dynamic fracture phenomena, including spontaneous crack initiation, dynamic crack micro-branching and crack competition, are successfully captured by the CZM simulations. To better analyze mesh size dependence of the numerical scheme, an investigation of cohesive zone size is also presented, which indicates limitations of conventional cohesive zone size estimates in dynamic and rate-dependent problems.

To my loving family

Acknowledgments

I take this opportunity to express my profound gratitude towards my advisor Professor Glaucio H. Paulino. This work would have been impossible without his constant guidance, invaluable suggestions and warm encouragement. His rich knowledge and experience, with his enthusiasm and dedication to research, have been a source of motivation and constant inspiration during my study. Moreover, I deeply appreciate the time and effort Prof. Paulino spent on reading and correcting my paper and thesis. His comments and suggestions constitute an indispensable ingredient of this thesis.

I am also thankful to Professor Robert H. Dodds, Jr. and Professor Yonggang Huang for their kind advice and help at various stages of my study. I am indebted to Professor Waldemar Celes for many constructive discussions and hands-on help.

I would also like to thank many of my friends at the U of I for their warm friendship and support. I benefited tremendously from the vibrant and friendly discussions with my group members – Youn-Sha Chan, Matthew Carl Walters, Alok Sutradhar, Jeong-Ho Kim, Seong-Hyeok Song, Zhaoxu Dong, Kyoungsoo Park, Huiming Yin, Bin Shen, Eshan Dave, Tam Hong Nguyen and Cameron Talischi. Thanks to their company, my study and life at the U of I are more enjoyable and fulfilling. I would also like to thank my friends, Rui Zhao and Mu Gao, for their constant care and help.

I am grateful to my family, for their abiding love and care. Every step I make in my life witnesses their support. I would also like to thank my husband, Chijie Lin. He is most supportive of my study, and patiently takes care of Anna and Benjamin when I am busy with research.

Table of Contents

List of Tables	viii
List of Figures	ix
Chapter 1 Introduction	1
1.1 Background	1
1.2 Cohesive Zone Model (CZM)	2
1.2.1 Historical Aspects	3
1.2.2 Xu and Needleman’s Model	5
1.2.3 Camacho and Ortiz’s Model	7
1.2.4 Unified Potential-based PPR Model	10
1.2.5 Virtual Internal Bond Model	11
1.3 Scope of Current Work and Thesis Organization	15
Chapter 2 Finite Element Formulation – Volumetric and Intrinsic Cohesive	17
2.1 Explicit Dynamic Analysis	17
2.2 Fracture of Functionally Graded Materials (FGMs)	21
2.3 Bilinear Cohesive Fracture Model	22
2.4 A Cohesive Fracture Model for FGMs	23
2.5 One-Dimensional Wave Propagation	24
2.5.1 Problem Description	25
2.5.2 Mesh Size Control	26
2.5.3 Results and Discussions	26
2.6 Mixed-mode Crack Propagation Using Intrinsic CZM	32
2.6.1 Kalthoff-Winkler Experiments	32
2.6.2 Bilinear Cohesive Model and Initial Stiffness Considerations	34
2.6.3 Results	35
2.6.4 Influence of Material Variation	42
Chapter 3 Topology-based Data Structure Representation	49
3.1 Introduction	49
3.2 Intrinsic and Extrinsic Cohesive Models	51
3.3 On Topological Data Structures	52
3.4 Adjacency-based Topological Data Structure (TopS)	54

3.4.1	Topological Entities	54
3.4.2	Adjacency Relationships	56
3.5	Finite Elements for Fragmentation Simulation	58
3.5.1	Adjacency Relationships	58
3.6	Topological Classification of Facets	60
3.6.1	Previous Proposals	60
3.6.2	Systematic Topological Classification	61
3.6.3	Adjacency Relationships	62
3.6.4	Application to 3D Meshes	64
3.6.5	Application to 2D Meshes	67
3.6.6	Avoiding Non-manifold Configurations	67
3.7	Computational Experiments	70
3.8	Mixed-mode Dynamic Crack Growth Fracture Simulation	73
3.9	Remarks	81
Chapter 4 Cohesive Zone Size: Static, Dynamic and Rate Effects		83
4.1	Static Cohesive Zone Size	83
4.1.1	Surrogate Problem Description	84
4.1.2	Solution Method	85
4.1.3	Verification	88
4.1.4	Effect of the Cohesive Parameters	95
4.2	Dynamic Cohesive Zone Size	102
4.2.1	Solution Method and Verification	102
4.2.2	Effect of Loading Rates	105
4.3	Rate Effects	111
4.3.1	Phenomenological Rate-dependent Models	112
4.3.2	Numerical Implementation Issues	115
4.3.3	Constant Cohesive Rate-toughening	116
4.3.4	Pseudo-analytical Cohesive Rate-toughening	120
4.3.5	Discussion	128
Chapter 5 Dynamic Fracture and Microbranching Instability in Brittle Materials		130
5.1	Introduction	130
5.2	Related Work	132
5.3	Simulation of Sharon and Fineberg's Experiment	134
5.3.1	Problem Description	134
5.3.2	Reduced Dimension Model	136
5.3.3	Mesh Convergence	137
5.3.4	Influence of Applied Load on Microbranch Patterns	142
5.3.5	Influence of Applied Load on Crack Velocity	145
5.3.6	Influence of Check-Time Intervals for Cohesive Element Insertion	147
5.3.7	Energy Evolution	149

Chapter 6	Three-Dimensional Crack Initiation and Propagation . .	152
6.1	Problem Description	152
6.2	Structured vs. Unstructured Mesh	154
6.2.1	3D Structured Mesh Generation	154
6.2.2	Fully Structured Mesh	155
6.2.3	Unstructured In-plane and Structured Through-thickness Mesh	158
6.2.4	Structured In-plane and Unstructured Through-thickness Mesh	162
6.2.5	Fully Unstructured Mesh	163
6.3	Cohesive Damage Zone Development	163
6.4	Energy Evolution	167
6.5	Load History	169
Chapter 7	Conclusions and Future Work	172
7.1	Concluding Remarks	172
7.2	Suggestions for Future Work	174
References	177
Curriculum Vitae	187

List of Tables

2.1	Steel and Alumina material properties	25
2.2	Material properties of 18Ni(300) steel and cohesive model parameters used in simulating Kalthoff-Winkler Experiments [13].	35
2.3	Crack initiation time for different meshes	36
2.4	Crack turning time for different meshes (see Figure 2.15 (b)).	41
2.5	Material property for pre-notched plate with graded fracture toughness, which is subjected to mixed-mode dynamic loading. The bulk material is homogeneous.	44
2.6	Material property for pre-notched plate with graded modulus, fracture toughness and cohesive strength, which is subjected to mixed-mode dynamic loading.	46
3.1	Elapsed times (in seconds) for inserting cohesive elements at all the facets of the models. Each time reported is the average of 5 simulations for each specific model, inserting the elements in different random order.	75
3.2	Material properties of 18Ni(300) steel and cohesive model parameters.	80
4.1	Properties of weakly bonded Aluminum DCB [56].	85
4.2	Cohesive zone size for various T_{\max} values.	96
4.3	Cohesive zone size for various G_{Ic} values.	101
4.4	Average crack velocity from rate-independent analysis and corresponding rate-toughening fracture energy	117
5.1	Properties of PMMA [108] strip subjected to initial stretch.	136
5.2	Mesh discretization and time step control associated with Figure 5.4.	138
5.3	Crack initiation time and average crack speed for loading case $\varepsilon = 0.015$ using different mesh discretizations.	140
5.4	Comparison of crack initiation time and average crack speed for different loading cases as shown in Figure 5.9.	145
6.1	Material properties of concrete beam specimen [49].	154
6.2	Crack initiation time and crack velocity for $\gamma = 0.5, 0.6, 0.7, 0.8$	165
6.3	Crack initiation time and load capacity $\gamma = 0.5, 0.6, 0.7, 0.8$	171

List of Figures

1.1	Schematic representation of crack tip zones with different material response characteristics.	2
1.2	Cohesive zone concept; (a) voids and micro-cracks form in the regions close to the crack tip; (b) CZM considers material softening and separation using distributed cohesive tractions along a cohesive surface at the crack tip vicinity. Circled numbers ① and ② denote the corresponding positions on the cohesive zone and cohesive law curves where material begins to soften (①) and where material completely loses fracture resistance capacity (②).	3
1.3	The <i>intrinsic</i> potential-based exponential cohesive model in (a) pure tension and (b) pure shear.	6
1.4	The extrinsic initial-rigid cohesive model in (a) pure tension and (b) pure shear.	9
1.5	Unified mixed-mode potential (PPR) and its gradients for the intrinsic cohesive zone model with $\phi_n = 100$ N/m, $\phi_t = 200$ N/m, $\sigma_{\max} = 40$ MPa, $\tau_{\max} = 30$ MPa, $\alpha = 5$, $\beta = 1.3$, $\lambda_n = 0.1$, and $\lambda_t = 0.2$	12
1.6	A general cohesive force law for an isotropic VIB derived considering equibiaxial stretching.	14
2.1	Schematic representation of <i>bulk</i> elements and <i>cohesive</i> elements in the finite element formulation. The notations are as follows: T denotes traction, Δ denotes separation; σ denotes stress, and ε denotes strain.	18
2.2	Bilinear cohesive model; (a) pure normal traction-separation; (b) pure tangential traction-separation.	23
2.3	Geometry and applied force for a fixed-free thin bar; (a) geometry; (b) applied load history.	25
2.4	Bar cross section material property: (a) homogeneous bar, (b) bi-material bar, (c) tri-layered bar, and (d) graded bar.	26
2.5	Stress history for homogeneous bar (2D simulation) subjected to transient loading and its comparison with 1D analytical solution; numerical results obtained at points $x = L$ (thick solid line), $x = 0.5L$ (dashed line) and $x = 0$ (dash-dot line); 1D analytical results (thin solid line) obtained for the same three points.	27

2.6	Comparison of 2D numerical results (solid line) with 1D analytical results (dashed line) for the same three points in Figure 2.5 when Poisson ratio $\nu = 0$	28
2.7	Stress history of six points (indicated by solid dots in the insert) on a bi-material bar subjected to transient loading. Solid, dashed and dash-dot lines indicate points at $x = L, 0.5L, 0$, respectively. Thin and thick lines indicate points at Alumina and Steel side, respectively.	29
2.8	Stress history of nine points (indicated by solid dots in the insert) on a tri-layer bar subjected to transient loading. Solid, dashed and dash-dot lines indicate points at $x = L, 0.5L, 0$, respectively. Thin, intermediate-thick and thick lines indicate Alumina-rich side, mid-plane and Steel-rich side of the graded interface, respectively.	30
2.9	Stress history of nine points (indicated by solid dots in the insert) on a graded beam subjected to transient loading. Solid, dashed and dash-dot lines indicate points at $x = L, 0.5L, 0$, respectively. Thin, intermediate-thick and thick lines indicate Alumina-rich side, mid-plane and Steel-rich side, respectively.	30
2.10	Comparison of stress contours (Pa) of the four bars: (a) homogeneous, (b) bi-material, (c) tri-layer, and (d) smoothly graded.	31
2.11	(a) Geometry and loading of the Kalthoff-Winkler experiments [50]; (b) 2-D plane-strain FEM simulation model.	33
2.12	Fracture path for different mesh designs considering $G_{IIc} = G_{Ic}$. The blue elements denote the region with cohesive elements, and all simulations use cohesive strength $T_n^{max} = E/110$ except for (c), which uses $T_n^{max} = E/30$; (a) 80×80 grid; (b) 100×64 grid; (c) 80×80 grid; (d) 64×100 grid.	37
2.13	Influence of mesh discretization on dynamic fracture behavior; (a) final crack paths for the first set of mesh discretization with total number of 25,600 T6 elements, and different mesh orientations; (b) final crack paths for square shape grids with element sizes $h = 1.25, 1, 0.8$ mm.	38
2.14	Comparison of fracture path for different meshes; (a) crack length growth history; (b) smoothed crack velocity history.	38
2.15	Stress field σ_x and crack evolution in a 120×120 grid mesh; (a) crack pattern at $t = 30\mu s$ after crack propagation starts; (b) close-up of stress field at crack tip at $t = 30\mu s$; (c) crack pattern at $t = 40\mu s$; (d) crack pattern at $t = 60\mu s$	39
2.16	Crack path for fracture toughness $G_{IIc} = 3G_{Ic}$. The blue elements denote the region with cohesive elements and simulations are performed using 80×80 grid meshes; (a) $T_t^{max} = T_n^{max}$; (b) $T_t^{max} = 3T_n^{max}$	42
2.17	Influence of different mode II and mode I fracture toughness ratios: $G_{IIc} = G_{Ic}$ and $G_{IIc} = 3G_{Ic}$; (a) final crack paths; (b) smoothed crack velocity history.	42

2.18	Comparison of fracture path for different cohesive toughness and strength gradation profiles. Results obtained using 80 by 80 grid mesh; (a) final crack paths; (b) two cohesive strength gradation profiles. cohesive strength varies between $E/110$ to $E/55$ within the cohesive region; case 1: fracture toughness and cohesive strength are lower at LHS; case 2: fracture toughness and cohesive strength are lower at RHS; (c) crack length versus time; (d) crack tip speed versus time.	45
2.19	Comparison of fracture paths for graded stiffness and graded fracture toughness along the Cartesian x direction. Results obtained using 80 by 80 grid mesh; (a) final crack paths; (b) material gradation profiles for E and cohesive strength. Case 1: material is softer and has lower fracture toughness at LHS; case 2: material is softer and has lower fracture toughness at RHS; average E and T_n^{max} are kept the same as the homogeneous case; (c) crack length versus time; (d) crack tip speed versus time.	47
3.1	Schematic representation of topological entities in the data structure (TopS). Solid boxes represent explicit entities and dashed boxes represent implicit entities. Solid arrows represent explicitly stored adjacency and dashed arrows represent implicitly stored adjacency, which are extracted based on the element templates.	55
3.2	The twenty-five topological adjacency relationships defined among the data structure topological data. Three of them are of special interest for fragmentation simulations: the two elements adjacent to a given facet, the set of elements adjacent to a given edge, and the set of elements adjacent to a given vertex.	57
3.3	Illustration of element types (both volumetric and cohesive) for fragmentation simulation.	59
3.4	Cases of facet classification identified by Pandolfi and Ortiz [15,16] in an illustrative tetrahedral model (for simplicity, the diagonal edges on the mesh boundary are not represented). Fractured facets are dashed and segments on the boundary are in bold.	60
3.5	Proposed procedures to classify the fractured facet: (a) two original adjacent tetrahedral elements; (b) the new cohesive element is inserted; (c) retrieval of elements around each edge starting at the first element, trying to reach the second one; (d) retrieval of elements around each vertex starting at the first element, trying to reach the second one. . .	63
3.6	Illustrative tetrahedral mesh (for simplicity, the diagonal edges on the mesh boundary are not represented). After the facet (f) is fractured, it remains possible to rotate around an internal edge (e) to reach the second element (E2) from the first one (E1).	64

3.7	Illustrative tetrahedral mesh (for simplicity, the diagonal edges on the mesh boundary are not represented). After the facet (f) is fractured, it is not possible to rotate around a boundary edge (e) to reach the second element (E2) from the first one (E1). As a result, the edge is duplicated (e') and the eventual mid-side nodes (N) are duplicated (N'). In this case, the connectivity of elements is updated.	65
3.8	Illustrative tetrahedral mesh (for simplicity, the diagonal edges on the mesh boundary are not represented). After the facet (f) is fractured, it is not possible to rotate around a boundary vertex (v) to reach the second element (E2) from the first one (E1), if the vertex is shared by two edges of the facet also on the boundary. As a result, the associated node (N) is duplicated (N') and the connectivity of elements is updated.	66
3.9	Illustrative tetrahedral mesh (for simplicity, the diagonal edges on the mesh boundary are not represented). After the facet (f) is fractured, it remains possible to rotate around a vertex (v1) to reach the second element (E2) from the first one (E1), even if the vertex is on the boundary (v2), but not shared by two edges of the facet also on the boundary.	66
3.10	Different configuration of fractured facet in 2D with their corresponding topological changes in an illustrative triangular mesh. Eventual mid-side nodes are not illustrated, but they would be duplicated whenever their associated edges are duplicated.	67
3.11	Non-manifold configurations in 3D and 2D models. The left configuration represents a singularity at a non-manifold edge; the other two represent a singularity at a non-manifold vertex.	68
3.12	A non-manifold configuration that may arise during the course of a fragmentation simulation. A new cohesive element is inserted along an internal facet of a model: (a) illustrative tetrahedral model with one of its internal faces highlighted in gray; (b) same model displaying the internal facet in isolation: one edge of the facet lies on one boundary of the model and the opposite vertex lies on another side of the mesh boundary; (c) model configuration after the insertion of a CZ element along the internal facet: the edge on the boundary is duplicated but the opposite vertex is not, thus a non-manifold configuration is characterized at this location. The mesh representation using TopS remains valid under this configuration.	69
3.13	Cylindrical model used in the computational experiments.	70
3.14	Illustrative triangular mesh (for both T3 and T6) displaying a discretization of 5×30	71
3.15	Illustrative quadrilateral mesh (for both Q4 and Q8) displaying a discretization of 5×30	71
3.16	General tetrahedral mesh (for both Tetra4 and Tetra10) displaying a discretization of $5 \times 30 \times 5$	72

3.17	General hexahedral mesh (for both Hexa8 and Hexa20) displaying a discretization of $5 \times 30 \times 5$	72
3.18	Illustrative hexahedral configuration after inserting cohesive elements (in blue) at 20% of the facets, exemplifying the resulting (arbitrary) crack patterns. In (b), we impose a separation in between each bulk element interface in order to better illustrate the mesh with the inserted cohesive elements.	74
3.19	Time vs. number of inserted CZ elements for linear and quadratic triangular meshes.	76
3.20	Time vs. number of inserted CZ elements for linear and quadratic quadrilateral meshes.	77
3.21	Time vs. number of inserted CZ elements for linear and quadratic tetrahedral meshes.	77
3.22	Time vs. number of inserted CZ elements for linear and quadratic hexahedral meshes.	78
3.23	Stress contour and crack propagation plots of the Kalthoff-Winkler experiment at different time instants: (a) $20\mu s$; (b) $30\mu s$; (c) $50\mu s$; (d) $60\mu s$	79
3.24	(a) Main crack path extracted from completely debonded cohesive surfaces in Figure 3.23; (b) crack speed derived from crack length growth versus time increment. Rayleigh wave speed is 2799m/s	81
4.1	Schematic representation of double cantilever problem. Separation a advances under statically imposed displacement u_{load} along a weak interface joining the double cantilever beams.	84
4.2	Definition of degrees of freedom for a 2-node Euler beam element.	86
4.3	Cohesive element stiffness k_c varies with separation Δ	87
4.4	Analytical solution for reaction force P at the loading point versus imposed displacement u_{load}	89
4.5	Comparison of DCB ($P-u$) response for different meshes with analytical solution.	90
4.6	Definition of leading point and trailing point.	90
4.7	Crack growth vs. applied loading; crack tip is defined at the <i>trailing point</i> of the cohesive zone.	91
4.8	Crack growth vs. applied loading; crack tip is defined at the <i>leading point</i> of the cohesive zone.	92
4.9	Normalized cohesive zone size versus imposed displacement loading for various meshes.	93
4.10	Schematic representation of cohesive zone size evaluation where the leading and trailing points are located at nodes; (a) the leading point (LP) advances while the trailing point (TP) remains stationary; (b) the leading point remains stationary while the trailing point advances to the next node; (c) both the leading and trailing points advance.	94

4.11	Comparison of DCB ($P-u$) response for two different T_{\max} choice and different loading step.	94
4.12	Comparison of DCB ($a-u$) response for two different T_{\max} choice and different loading steps. The crack tip is defined as the leading point of cohesive zone.	95
4.13	Comparison of DCB ($P-u$) response for various T_{\max} values.	97
4.14	Comparison of DCB $a-u$ response for various T_{\max} values. Crack tip is defined as the <i>trailing point</i> of cohesive zone.	97
4.15	Comparison of DCB <i>leading point</i> position versus imposed loading for various T_{\max} values.	98
4.16	Comparison of DCB cohesive zone size versus crack length for various T_{\max} values.	98
4.17	Comparison of DCB $P-u$ response for various G_{Ic} values.	99
4.18	Comparison of DCB $a-u$ response for various G_{Ic} values.	100
4.19	Comparison of DCB <i>leading point</i> position versus applied displacement loading for various G_{Ic} values.	100
4.20	Comparison of DCB cohesive zone size versus crack length for various G_{Ic} values.	101
4.21	Crack tip location vs. applied displacement at free tip for the dynamic DCB problem and loading rate $V_{\text{load}} = 0.2m/s$	104
4.22	Crack tip velocity history for dynamic DCB problem at loading rate $V_{\text{load}} = 0.2m/s$. Pseudo analytical result indicates corresponding quasi-static case result derived from $a-u_{\text{load}}$ curve shown in Figure 4.21.	104
4.23	Numerical result for reaction force P at the loading point versus applied displacement u_{load} for $V_{\text{load}} = 0.2m/s$ case compared to analytical solution for the quasi-static problem.	106
4.24	Crack length history for loading cases $V_{\text{load}} = 0.2$ m/s, 1m/s, 5m/s, 10m/s; (a) normalized crack length vs. normalized imposed displacement. Solid line for $V_{\text{load}} = 0.2m/s$ and dotted line for $V_{\text{load}} = 1m/s$ are virtually indistinguishable; (b) normalized crack length vs. time.	107
4.25	Crack tip velocity history for dynamic DCB problem at loading rate $V_{\text{load}} = 1m/s$	108
4.26	Crack tip velocity history for dynamic DCB problem at loading rate $V_{\text{load}} = 10m/s$	108
4.27	Comparison of crack velocity history for loading cases $V_{\text{load}} = 0.2$ m/s, 1m/s, 5m/s, 10m/s. Velocity profile is scaled by the applied loading rate of each case.	109
4.28	Schematic representation of cohesive zone size evaluation where the leading and trailing points are interpolated between nodes.	110
4.29	Cohesive zone size for loading cases $V_{\text{load}} = 0.2, 1$ 5 and $10m/s$	110

4.30	Rate-dependent fracture behavior in dynamic crack propagation in PMMA [97]. (a) the energy flux into the crack tip (G) as a function of steady-state crack velocity (Fig. 3 in [97]); (b) the relative surface area (A) created by a crack as a function of the energy flux G into the crack tip. The linear dependence above v_c indicates that nearly all of the energy goes into creating new surface, while the energy cost per unit surface area is unchanged. A linear fit (line) to the data yields $A = 1.0 + 1.05 \times 10^{-6}G$ (Fig. 4 in [97]).	112
4.31	Phenomenological rate-dependent cohesive model.	114
4.32	Rate-dependent intrinsic bilinear cohesive zone with constant cohesive strength and varying fracture energy.	115
4.33	Crack evolution vs. applied displacement for $V_{\text{load}} = 1, 5$ and $10m/s$. Rate toughening effect is considered by assuming a constant velocity throughout each simulation.	117
4.34	Crack velocity history for $V_{\text{load}} = 1m/s$. Fracture energy for all cohesive elements ($59N/m$) is based on assumed velocity ($29m/s$) obtained from rate-independent study.	118
4.35	Crack velocity history for $V_{\text{load}} = 5m/s$. Fracture energy for all cohesive elements ($96N/m$) is based on assumed velocity ($150m/s$) obtained from rate-independent study.	118
4.36	Crack velocity history for $V_{\text{load}} = 10m/s$. Fracture energy for all cohesive elements ($145N/m$) is based on assumed velocity ($250m/s$) obtained from rate-independent study.	119
4.37	Cohesive zone size for different loading cases $V_{\text{load}} = 1, 5$ and $10m/s$. Rate-toughened fracture energy for each case is $59, 96$ and $145N/m$	120
4.38	Ratio of the two terms in Equation (4.32) for varying crack acceleration rate \dot{v}_{crack}	122
4.39	Pseudo-velocity by solving Equation (4.36) and considering the rate-toughening effect on velocity reduction using different method. Method 1: no reduction; Method 2: linear decreasing from 1 to 0.9 as crack location from a_0 to L ; Method 3: use half of the velocity predicted using rate-independent G_c value.	124
4.40	Method 2 corrects for underestimated u in Equation (4.35); (a) fracture resistance G variation along crack path a based on Method 1 solution; (b) comparison of $u - a$ relationship obtained using Equation (4.35) approximation and more accurate numerical integration process.	124
4.41	Crack velocity history for $V_{\text{load}} = 10m/s$. Fracture energy $G_c(v)$ is based on assumed velocity obtained from <i>Method 1</i>	127
4.42	Crack velocity history for $V_{\text{load}} = 10m/s$. Fracture energy $G_c(v)$ is based on assumed velocity obtained from <i>Method 2</i>	127
4.43	Crack velocity history for $V_{\text{load}} = 10m/s$. Fracture energy $G_c(v)$ is based on assumed velocity obtained from <i>Method 3</i>	128
4.44	Cohesive zone size for different loading cases $V_{\text{load}} = 1, 5$ and $10m/s$ considering the rate toughening effect.	129

5.1	Experimental observation of branching instability as crack propagates in PMMA. Figure reproduced from Figure 4 of Sharon and Fineberg [96]. The critical crack speed at which microbranch appears is denoted as V_c . (a) the velocity of the crack is a smooth function of time for $V=300 \text{ m/s} < V_c$ (left), at $V=400 \text{ m/s} \approx V_c$ the crack velocity starts to oscillate (center), the oscillation amplitudes increase at higher velocity (right); (b) for $V=300 \text{ m/s} < V_c$ the fracture surface is smooth (left), at $V \approx 400 \text{ m/s}$ small regions of different texture are distributed along the surface (center), at $V \approx 600 \text{ m/s}$ these regions coalesce, forming a periodic pattern with wavelength on the order of 1 mm (right); (c) A single crack is observed (left) for $V < V_c$. Microbranches appear at $V \approx V_c$ (center), and increase in length at higher velocities (right).	131
5.2	Model of the experimental setting by Sharon and Fineberg [96]; the length to height ratio (L:H) is maintained between 2 to 4, in order to represent steady-state crack propagation condition.	135
5.3	Schematic representation of the geometry and boundary condition for the 2-D steady-state crack propagation problem, using reduced dimension based on Sharon and Fineberg [96]; the length to height ratio (L:H) is 4.	135
5.4	Mesh discretization with T6 elements for pre-cracked PMMA strip subjected to initial stretch; (a) mesh pattern and characteristic length h , which is defined as grid spacing; (b) mesh with grid 16×64 , $h=250\mu\text{m}$. Other meshes with grid 32×128 ($h=125\mu\text{m}$), grid 48×192 ($h=83\mu\text{m}$) and grid 64×256 ($h=62.5\mu\text{m}$) use the same mesh pattern with different levels of refinement	138
5.5	Mesh size influence on fracture pattern for applied stretch $\varepsilon = 0.015$; (a) 16×64 grid, simulation time $t=24\mu\text{s}$; (b) 32×128 grid, simulation time $t=22\mu\text{s}$; (c) 48×192 grid, simulation time $t=21\mu\text{s}$. Notice that the crack branches arrest, as in the experiments by Sharon and Fineberg [96] – this is due to extrinsic CZM framework using TopS.	140
5.6	Crack velocity versus time considering initial stretch $\varepsilon = 0.015$ and various levels of mesh refinement; (a) grid 16×64 ; (b) grid 32×128 ; (c) grid 48×192	141
5.7	Mesh size influence on fracture pattern for applied stretch $\varepsilon = 0.012$; (a) 16×64 grid, simulation time $t=32\mu\text{s}$; (b) 32×128 grid, simulation time $t=24\mu\text{s}$; (c) 48×192 grid, simulation time $t=24\mu\text{s}$; (d) 64×256 grid, simulation time $t=23.4\mu\text{s}$	143
5.8	Mesh size influence on fracture pattern for applied stretch $\varepsilon = 0.01$; (a) crack arrests for coarse mesh (16×64 grid); (b) crack pattern for refined mesh (48×192 grid); (c) associated crack velocity history for refined mesh (48×192 grid).	144

5.9	Comparison of branch patterns for various loading cases considering different applied strains (ε) and using an initial mesh discretization consisting of a 48×192 grid. (a) $\varepsilon = 0.0085$; (b) $\varepsilon = 0.009$; (c) $\varepsilon = 0.010$; (d) $\varepsilon = 0.012$; (e) $\varepsilon = 0.015$	146
5.10	Comparison of branch patterns at $t = 19.8\mu s$ for applied initial stretch $\varepsilon = 0.0085$ using different cohesive element insertion checking intervals. (a) cohesive element insertion checked at every 10 time steps; (b) cohesive element insertion checked at every time step.	147
5.11	Comparison of branch patterns at $t = 25.4\mu s$ for applied initial stretch and $\varepsilon = 0.008$ using different cohesive element insertion checking intervals. (a) cohesive element insertion checked at every 10 time steps; (b) cohesive element insertion checked at every time step.	148
5.12	Energy components evolution with time for crack propagation problem with initial stretch $\varepsilon = 0.008$. Mesh used is 64×256 grids, cohesive element insertion is checked at every 10 time steps.	150
5.13	Components of the cohesive energy.	151
6.1	Geometry and loading condition of three-point-bending beam experiment [49]. Initial notch position is described by parameter γ which measures relative notch position from midspan to the left support. . .	153
6.2	Possible crack propagation location and effect of pre-notch position on final failure; (a) crack grows from pre-notch tip for $\gamma < \gamma_t$ cases; (b) crack initiates from midspan and continues to grow until specimen failure for $\gamma > \gamma_t$ cases.	153
6.3	Illustration of structured and unstructured 2D mesh; (a) structured mesh consisting of grid mesh divided into triangles; grid can have different aspect ratios; (b) unstructured mesh.	154
6.4	Creation of structured mesh through thickness direction.	155
6.5	Sample fully structured 3D mesh, $\gamma = 0.5$, mesh grid size is $2\text{mm} \times 2\text{mm}$ within central zone where fracture may occur. Largest in-plane grid size outside central zone is $5\text{mm} \times 5\text{mm}$	156
6.6	Results comparison for fully structured mesh; (a) mesh grid $3\text{mm} \times 3\text{mm}$, 110,540 Tet4 elements and 26,015 nodes; (b) mesh grid $2.5\text{mm} \times 3.3\text{mm}$, 100,600 Tet4 elements and 23,713 nodes; (c) mesh grid $2\text{mm} \times 2\text{mm}$, 293,658 Tet4 elements and 66,443 nodes.	157
6.7	Unstructured in-plane and structured through-thickness meshes and results, mesh size inside crack propagation region is 2mm except for case (a), which uses 3mm; (a) $\gamma = 0.5$, 101,684 Tet4 elements and 20,220 nodes; (b) $\gamma = 0.5$, 209,418 Tet4 elements and 40,638 nodes; (c) $\gamma = 0.6$, 300,495 Tet4 elements and 57,914 nodes; (d) $\gamma = 0.7$, 305,184 Tet4 elements and 58,691 nodes.	160

6.8	Results comparison for structured in-plane and unstructured through-thickness meshes; (a) In-plane mesh grid $1.7\text{mm} \times 2.3\text{mm}$, 161,593 Tet4 elements and 32,189 nodes; (b) In-plane mesh grid $2.3\text{mm} \times 1.7\text{mm}$, 171,061 Tet4 elements and 33,876 nodes; (c) In-plane mesh grid $2\text{mm} \times 2\text{mm}$, 180,297 Tet4 elements and 35,308 nodes.	161
6.9	Time history of crack tip height for $\gamma = 0.5$ with S-U meshes of different in-plane mesh aspect ratios. Result for Fully Unstructured (U-U) mesh is plotted using dotted line for comparison purpose.	162
6.10	Crack patterns for fully unstructured meshes; (a) $\gamma = 0.5$, 98,123 Tet4 elements and 19,915 nodes; (b) $\gamma = 0.6$, 107,113 Tet4 elements and 21,599 nodes; (c) $\gamma = 0.7$, 96,003 Tet4 elements and 19,363 nodes; (d) $\gamma = 0.8$, 105,289 Tet4 elements and 21,169 nodes;	164
6.11	Time history of crack tip height for $\gamma = 0.5, 0.6, 0.7, 0.8$. Fully unstructured mesh.	165
6.12	Comparison of (a) crack surfaces representing full decohesion and (b) all inserted cohesive surfaces during simulation.	166
6.13	Cohesive damage zone of $\gamma = 0.5$ case using fully unstructured mesh; (a) gray scale representation of damage development in all cohesive elements; (b) damage zone contour in beam.	167
6.14	Damage zone plots for (a) $\gamma = 0.5$; (b) $\gamma = 0.6$, (c) $\gamma = 0.7$, (d) $\gamma = 0.8$.	168
6.15	Energy components evolution with time for $\gamma = 0.5$, fully unstructured mesh.	169
6.16	Reaction force at loading point evolution with time for $\gamma = 0.5$, fully unstructured mesh.	170
6.17	Comparison of reaction force at loading point evolution with time for $\gamma = 0.5, 0.6, 0.7, 0.8$, fully unstructured mesh.	171

Chapter 1

Introduction

Among the various numerical schemes addressing static and dynamic fracture problems, cohesive Zone Models (CZMs) are of growing interest for fracture modeling and are currently widely used in simulations of both crack growth along predefined path and arbitrary paths. The CZM approach is able to simulate fracture processes where cracking occurs spontaneously. The fracture path and speed become natural outputs of the simulation rather than specified as *ad hoc* or *a priori*. In a recent review paper, Cox et al. [24] contended that CZM simulation is particularly promising in investigating certain fracture phenomena including dynamic crack branching.

Various models have been proposed, and their advantages, disadvantages and limitations have been debated. This Chapter introduces and motivates the topic of CZMs by providing a brief review of the history of these models. Emphasis is placed on two representative models in each category of the “*intrinsic*” and “*extrinsic*” CZMs, along with a critical evaluation of the two classes of cohesive models. Potential-based CZMs of interest are also briefly discussed. Finally, the scope of the current work and the thesis organization are presented at the end of the Chapter.

1.1 Background

A realistic fracture model that is physics-based and is adaptable simultaneously to experimental calibration and numerical implementation remains elusive. A schematic drawing is shown in Figure 1.1 to describe three regions at the crack tip where different classes of material responses are dominant. The outer-ring represents the so-called *K-field* and relies on the classical approach based on linear elastic fracture mechanics (LEFM), where the material behavior is linear and stress and strain fields can be determined with a single parameter, typically the stress intensity factor (SIF) or energy release rate. The intermediate ring is dominated by inelastic effects, e.g., the *Hutchinson-Rice-Rosengren (HRR) field* [45, 92], where the inelastic response is incorporated. For the inner ring, which is very close to the crack tip, the microstructure

of material, e.g., distribution of microcracks and voids, will significantly influence the material response due to effects such as void nucleation. In continuum mechanics, the Gurson model [43] successfully incorporates these effects into the constitutive model for ductile materials, however, the large number of parameters that must be calibrated pose a strong challenge for using the model widely.

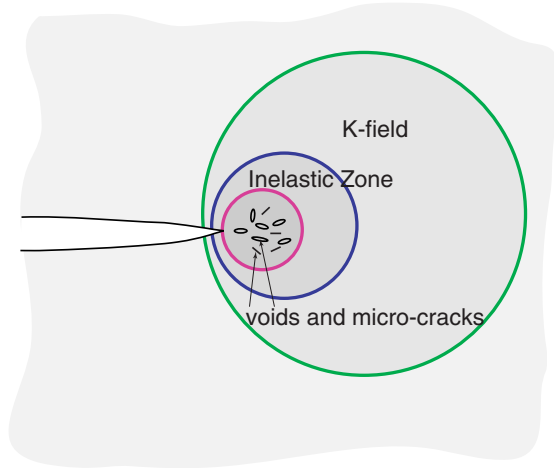


Figure 1.1: Schematic representation of crack tip zones with different material response characteristics.

There are a few shortcomings with the above-referenced approaches. First, whether only LEFM model is used to describe a crack tip field or more complicated phenomena incorporated, an external criterion is required for the crack to propagate, and the crack propagation direction is also imposed. Second, phenomena such as fracture instability (which is not yet thoroughly understood), cannot be simulated with a purely phenomenological model. Third, crack branching and fragmentation that usually occur in impact loading events cannot be properly simulated. Finally, the classical approaches require preexisting, crack-like flaws. The nucleation of voids can be treated in Gurson model; however, as explained above, the wide usage of this model remains problematic.

1.2 Cohesive Zone Model (CZM)

An alternative way to describe the near-tip behavior and to propagate the crack is by means of the CZM, which incorporates a cohesive strength and finite work to fracture in the description of material behavior. The concept of “cohesive failure”

is illustrated in Figure 1.2 for the tensile (mode I) case. At the immediate vicinity of the crack tip, the material cannot sustain infinitely high stress, and the material softens, resulting, for example, from void growth and microcrack formation. This status is simulated with the traction-separation relationship law inside the *cohesive zone*, which is along the plane of the potential crack propagation. Within the extent of the cohesive zone, the material points that were identical when the material was intact, separate to a distance Δ due to the influence of the stress state at the crack tip vicinity. The cohesive zone surface sustains a distribution of tractions T which are function of the displacement jump across the surface Δ , and the relationship between the traction T and separation Δ is defined as the constitutive law for the cohesive zone surface. As an example, in the intrinsic model by Xu and Needleman [108], the constitutive law indicates that with increasing interfacial separation Δ , the traction T across the cohesive interface first increases smoothly, reaches a maximum value at critical separation, then decreases, and finally becomes asymptotically close to zero at a characteristic separation value, where decohesion occurs. The extrinsic model, on the other hand, assumes a monotonically decreasing curve for a traction-separation relationship [16].

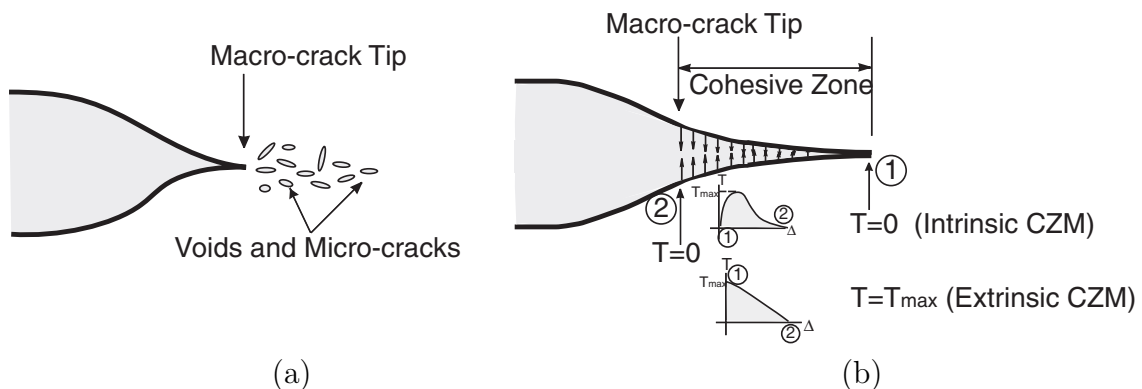


Figure 1.2: Cohesive zone concept; (a) voids and micro-cracks form in the regions close to the crack tip; (b) CZM considers material softening and separation using distributed cohesive tractions along a cohesive surface at the crack tip vicinity. Circled numbers ① and ② denote the corresponding positions on the cohesive zone and cohesive law curves where material begins to soften (①) and where material completely loses fracture resistance capacity (②).

1.2.1 Historical Aspects

Barenblatt [5, 6] and Dugdale [27] first proposed the cohesive zone concept for brittle materials and perfectly plastic materials, respectively. It is postulated that a process

zone exists at the crack tip region, along which a constant cohesive traction (equal to yield strength) closes the material separation. Afterwards, models considering materials with softening behavior (thus the traction-separation is a decreasing function) were also developed – see [9] and [10]. With the development of modern numerical simulation techniques, e.g., FEM, and the availability of large-scale computation, the CZM has been adapted into numerical simulation schemes, and various models have been proposed, e.g., intrinsic CZM with exponential form [108] and bilinear form [41, 113], and extrinsic CZM with monotonically decreasing cohesive strength [76]. These CZMs incorporate a cohesive strength and finite work to fracture in the description of material behavior, and allow simulation of near-tip behavior and crack propagation. However, the onset of crack initiation criteria are different from *intrinsic* and *extrinsic* CZMs. The advantages, disadvantages, and limitations of these models were discussed in a few papers – see [76, 108, 41, 113]. In general, intrinsic CZMs have been successful in reproducing fracture phenomena when the crack path is predefined. For instance, Needleman [69] considered the inclusion debonding case using a potential-based cohesive traction-separation relationship. Tvergaard [104] investigated the fiber debonding problem considering both normal and tangential separations using a CZM without the potential form. The model by Xu and Needleman [108], which incorporates both normal and tangential traction-separation relationships, was widely used later on due to its simplicity and potential form. All of the intrinsic CZMs incorporate an initial slope in the traction-separation curve that leads to the artificial reduction of stiffness. The other CZM category belongs to the class of extrinsic models, e.g., [16], which eliminates the artificial compliance typical of the intrinsic models mentioned above. Ortiz and coworkers developed models for three-dimensional (3-D) fracture growth and fragmentation simulation [71]. However, depending on implementation, the extrinsic model may lead to time-discontinuous numerical results [77]. There have been discussions and debates regarding the pros and cons of each model (see Falk et al. [33]). During recent years, the CZM has become an active research field and many models have been proposed that consider increasing physical complexity, e.g., the rate-dependent behavior, damage, and viscoelasticity [58, 112, 23, 60]. In the following, the discussion will focus on the basic characteristics of a few representative CZMs: the potential-based model by Xu and Needleman [108], the initial-rigid model by Camacho and Ortiz [16], the generalized potential-based model by Park et al. [78], and the Virtual Internal Bond model by Klein, Gao and coworkers [55, 56, 57]. The cohesive zone model for Functionally Graded Materials (FGMs) will be discussed in Chapter 2.

1.2.2 Xu and Needleman's Model

The model proposed by Xu and Needleman [108] assumes a scalar decohesion potential ϕ in the form

$$\phi(\mathbf{\Delta}) = \phi_n + \phi_n \exp\left(-\frac{\Delta_n}{\delta_n}\right) \left\{ \left[1 - r + \frac{\Delta_n}{\delta_n}\right] \frac{(1-q)}{(r-1)} - \left[q + \frac{(r-q)\Delta_n}{(r-1)\delta_n}\right] \exp(-\Delta_t^2) \right\} \quad (1.1)$$

from which the cohesive traction force can be obtained as

$$\mathbf{T} = -\frac{\partial\phi}{\partial\mathbf{\Delta}} \quad (1.2)$$

where $\mathbf{T} = [T_n, T_t]$ is the traction force vector — in the two dimensional case it comprises traction in normal and tangential directions. The displacement jump vector $\mathbf{\Delta} = [\Delta_n, \Delta_t]$ denotes the displacement discontinuity across the cohesive surface in the normal and tangential directions. The parameters ϕ_n and ϕ_t are the energies required for pure normal and tangential separation, respectively. The parameters δ_n and δ_t are the critical opening and sliding displacements for normal and tangential separation, respectively, which are related to the cohesive normal strength σ_{\max} and the tangential strength τ_{\max} as

$$\phi_n = e\sigma_{\max}\delta_n, \quad \phi_t = \sqrt{e/2}\tau_{\max}\delta_t. \quad (1.3)$$

Moreover,

$$q = \phi_t/\phi_n \quad (1.4)$$

is the energy ratio and r is defined as the value of Δ_n/δ_n after complete shear separation with $T_n = 0$. The resulting normal and shear traction components are derived from (1.2):

$$\begin{aligned} T_n &= -\frac{\phi_n}{\phi_t} \exp\left(-\frac{\Delta_n}{\delta_n}\right) \left\{ \frac{\Delta_n}{\delta_n} \exp\left(-\frac{\Delta_t^2}{\delta_t^2}\right) + \frac{(1-q)}{(r-1)} \left[1 - \exp\left(-\frac{\Delta_t^2}{\delta_t^2}\right)\right] \left[r - \frac{\Delta_n}{\delta_n}\right] \right\} \\ T_t &= -\frac{\phi_n}{\phi_t} \left(2\frac{\delta_n}{\delta_t}\right) \frac{\Delta_t}{\delta_t} \left\{ q + \frac{(r-q)\Delta_n}{(r-1)\delta_n} \right\} \exp\left(-\frac{\Delta_n}{\delta_n}\right) \exp\left(-\frac{\Delta_t^2}{\delta_t^2}\right) \end{aligned} \quad (1.6)$$

Figure 1.3 (a) shows the normal traction across the surface, T_n , as a function of Δ_n with $\Delta_t = 0$. The maximum value of T_n is σ_n and occurs when $\Delta_n = \delta_n$. The variation of T_t with Δ_t is shown in Figure 1.3 (b). The maximum value of $|T_t| = \tau_{max}$ is attained when $\Delta_t = \sqrt{2}\delta_t/2$.

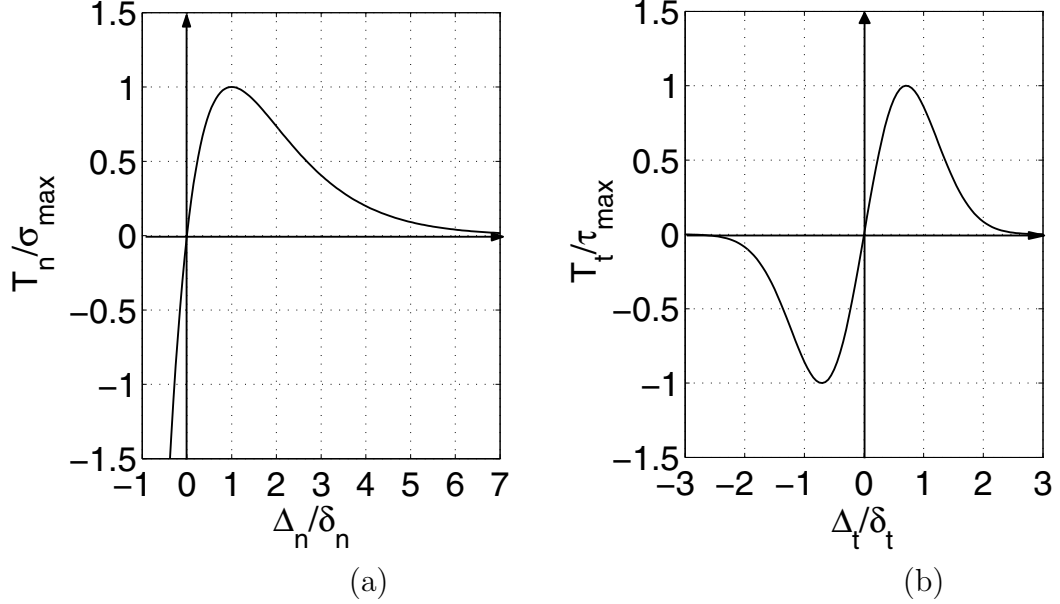


Figure 1.3: The *intrinsic* potential-based exponential cohesive model in (a) pure tension and (b) pure shear.

With the model described above, Xu and Needleman [108] investigated dynamic behavior of fast crack growth in brittle solids and demonstrated that the model is capable of simulating many dynamic fracture phenomena such as crack branching, dependence of crack speed on impact velocity, and abrupt crack arrest.

The above intrinsic model, sometimes referred to as “cohesive surface network” [56], requires the existence of cohesive elements in the structure before the simulation begins. This renders certain simplicity to the numerical implementation; however this approach adds fictitious compliance to the structure (see a detailed discussion in [115] Chapter 3), and hence affects adversely the accuracy of numerical simulation. To mitigate the influence of this artifact, a large initial stiffness i.e., steep initial slope of T_n versus Δ_n and T_t versus Δ_t curves in Figure 1.3 is desired. Since neither cohesive energy nor cohesive strength had been experimentally determined with a high degree of certainty [56], some latitude is permitted for the choice of cohesive strength. Orowan [70] estimated $E/\sigma_{max} = 30$, and in the work by Xu and Needleman [108], $\sigma_{max} = E/10$ is generally used. However, a consequent drawback with a higher initial stiffness is that smaller elements and smaller time step are required to produce stable results.

The distinct features of Xu and Needleman’s model [108] are summarized as follows:

- It is an *intrinsic* model, in the sense that the cohesive surface elements are embedded in the structure, so the mesh is unchanged during the entire computation time. No extrinsic criterion is needed for crack nucleation or propagation.
- The normal and tangential traction-separation relationships are derived from one cohesive energy potential expression, in which four parameters need to be determined, i.e., ϕ_n , ϕ_t , σ_{max} , τ_{max} . Usually it is assumed that $\phi_n = \phi_t$, and $r = \Delta_n/\delta_n = 0$, which means that under pure shear deformation, the normal displacement jump remains zero after complete separation.
- The formulation generates a healing effect so that the closing fracture surfaces do not take permanent damage into account.
- The elastic response of the cohesive elements prior to crack propagation introduces artificial compliance to the computation model and reduces accuracy.

1.2.3 Camacho and Ortiz's Model

This model minimizes the artificial softening effect due to the elastic deformation of cohesive interface present in Xu and Needleman's model [108]. Ideally, the initial interface stiffness should be infinity, i.e., prior to crack propagation, the cohesive interface should not generate any deformation. Figure 1.4 illustrates the model by Camacho and Ortiz [16] which possesses this characteristic. In the implementation stage, the cohesive elements are adaptively inserted into the mesh, i.e., the initial topology of the mesh does not have any cohesive elements. When a certain fracture criterion is met, a cohesive element is inserted into the proper location of the mesh which allows the crack to propagate. Since this model requires a failure criterion that is external to the cohesive law, this kind of CZMs is referred to as *extrinsic*. The failure criterion may be chosen in terms of a critical fracture stress σ_{fr} determined from the critical mode I stress intensity factors K_{Ic} and the initial flaw size a_0 of the material

$$\sigma_{fr} = \frac{K_{Ic}}{\sqrt{\pi a_0}} \quad (1.7)$$

This model is based on *effective quantities*. The *effective stress* σ_{eff} is defined as

$$\sigma_{\text{eff}} = \sqrt{T_n^2 + \beta_\tau T_t^2} \quad \text{for } T_n \geq 0 \quad (1.8a)$$

$$\sigma_{\text{eff}} = \sqrt{\beta_\tau (|T_t| - \mu|T_n|)} \quad \text{for } T_n < 0 \quad (1.8b)$$

where T_n and T_t are the cohesive tractions along normal and tangential directions, respectively; β_τ is the shear stress factor that represents the mode mixity effect, and μ is the friction coefficient. When the fracture condition $\sigma_{\text{eff}} \geq \sigma_{\text{fr}}$ is met, a new surface is introduced into the mesh by doubling nodes and creating the cohesive zone elements. The cohesive force that resists the opening and sliding of the new surface is assumed to weaken irreversibly with increasing crack opening. Permanence of damage is retained by keeping track of the maximum displacement in the simulation history and using it as the indicator for loading or unloading, as shown in Figure 1.4. The cohesive traction and separation relationship is described as follows:

- $T_n \geq 0$, **tensile case.** Under loading condition, when the current displacement is larger than that in history, the cohesive traction ramps down linearly as the displacement jump increases and reduces to zero as the opening reaches critical opening displacement $\Delta_n = \delta_n$. The decohesion is complete at this point, and the cohesive force vanishes thereafter.

$$\begin{aligned}
 T_n &= \sigma_{\text{max}} \left(1 - \frac{\Delta_n}{\delta_n} \right) \\
 T_t &= \tau_{\text{max}} \left(\frac{\Delta_n}{\delta_n} \right) \text{sgn}(\Delta_t)
 \end{aligned}
 \quad \text{for } \Delta_n \geq \Delta_{n(\text{max})} \quad (1.9)$$

where $\Delta_{n(\text{max})}$ is the maximum normal opening displacement recorded in history, and $\text{sgn}(x) = x/|x|$ is the signum function. If unloading occurs, the crack begins to close, and the traction obeys the linear unloading relation

$$\begin{aligned}
 T_n &= \sigma_{\text{max}} \left(1 - \frac{\Delta_{n(\text{max})}}{\delta_n} \right) \frac{\Delta_n}{\Delta_{n(\text{max})}} \\
 T_t &= \tau_{\text{max}} \left(1 - \frac{\Delta_{n(\text{max})}}{\delta_n} \right) \frac{\Delta_n}{\Delta_{n(\text{max})}} \text{sgn}(\Delta_t)
 \end{aligned}
 \quad \text{for } \Delta_n < \Delta_{n(\text{max})} \quad (1.10)$$

as shown in Figure 1.4(a). If the crack reopens, the reloading path follows the unloading path along the reverse direction until $\Delta_{n(\text{max})}$ and then follows the original ramp-down relation (1.9).

- $T_n < 0$, **compression case.** In Ortiz and Camacho's study [16], when normal compression occurs, a contact algorithm is employed to treat the normal dis-

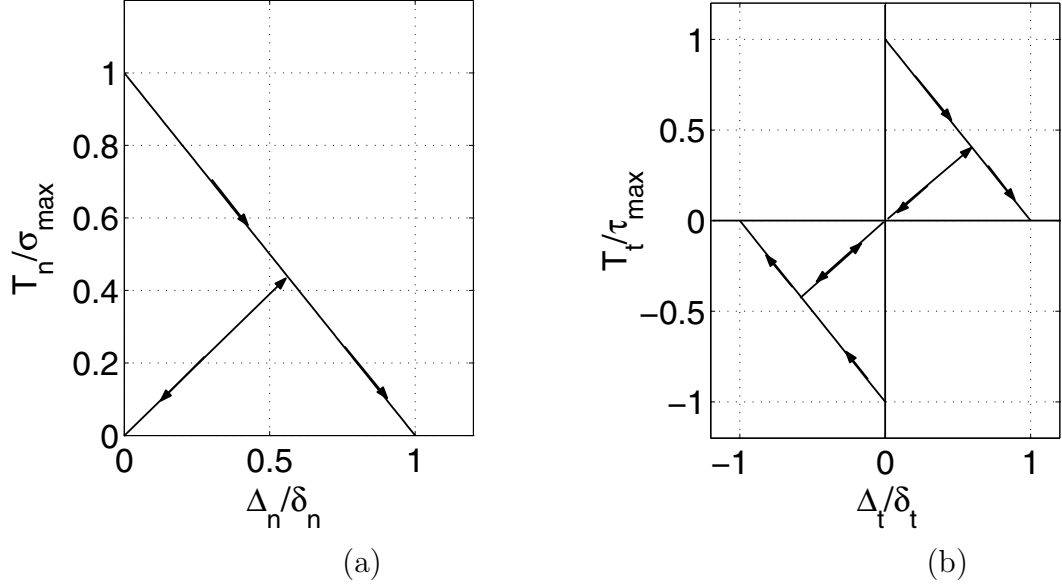


Figure 1.4: The extrinsic initial-rigid cohesive model in (a) pure tension and (b) pure shear.

placement penetration, while the tangential traction-separation relations follow

$$T_t = \tau_{\max} \left(1 - \frac{\Delta_{t(\max)}}{\delta_t} \right) \text{sgn}(\Delta_t) \quad \text{for } \Delta_t \geq \Delta_{t(\max)} \quad (1.11)$$

$$T_t = \tau_{\max} \left(1 - \frac{\Delta_{t(\max)}}{\delta_t} \right) \frac{\Delta_t}{\Delta_{t(\max)}} \quad \text{for } \Delta_t < \Delta_{t(\max)} \quad (1.12)$$

for loading and unloading cases, respectively, where $\Delta_{t(\max)}$ is the maximum tangential opening displacement in the simulation history.

With the model above, Camacho and Ortiz [16] investigated impact damage in brittle materials. Simulation of severe fragmentation under high velocity impact loading was carried out, in which thermal effects and rate dependence were also considered.

The features of Camacho and Ortiz's model [16] are summarized as follows:

- It is an *extrinsic* model, in that the cohesive elements are adaptively inserted into the mesh. It avoids the artificial softening effect present in *intrinsic* models; however, at the price of extra work consisting of adaptively updating the mesh by renumbering nodes and elements. Moreover, an extrinsic failure criterion is required.
- The critical fracture stress is determined by the linear elastic fracture mechanics

formula, and is much lower than that used in Xu and Needleman's [108] model. In their work, Camacho and Ortiz [16] used a value around $E/\sigma_{max} = 600$.

- Permanent damage is considered.
- It is based on *effective quantities*, which can be considered a drawback of the model.
- Explicit contact/friction algorithm is employed to treat normal displacement penetration case.
- The relations between normal and tangential components of the traction and displacement jump are not coupled. The effect of mode mixity is represented by the arbitrary parameter β_τ , the value of which can vary within a large range due to lack of experimental evidence.

1.2.4 Unified Potential-based PPR Model

Recently, Park et al. [78] proposed a generalized potential-based CZM, which was largely motivated by the fact that the existing potential-based CZMs, e.g., Xu and Needleman's model [108], do not successfully handle mixed-mode fracture with different Mode-I and Mode-II fracture energies. For example, the application of Xu and Needleman's model [108] usually assumes identical Mode-I and Mode-II fracture energies ($\phi_n = \phi_t$). Different energy values may lead to counter-intuitive cohesive traction-separation behavior, e.g., negative normal cohesive traction (repulsive) at positive separation. Besides, CZMs such as Xu and Needleman's model [108] are unable to adjust initial stiffness slope, which is critical in controlling artificial compliance.

The generalized potential for mixed-mode fracture, called the PPR (Park-Paulino-Roesler) potential, is expressed as follows:

$$\Psi(\Delta_n, \Delta_t) = \min(\phi_n, \phi_t) + \left[\Gamma_n \left(1 - \frac{\Delta_n}{\delta_n} \right)^\alpha \left(\frac{m}{\alpha} + \frac{\Delta_n}{\delta_n} \right)^m + \langle \phi_n - \phi_t \rangle \right] \left[\Gamma_t \left(1 - \frac{\Delta_t}{\delta_t} \right)^\beta \left(\frac{n}{\beta} + \frac{\Delta_t}{\delta_t} \right)^n + \langle \phi_t - \phi_n \rangle \right] \quad (1.13)$$

where parameters m and n are nondimensional constants, α , β are shape parameters that control the initial traction-separation slope for both normal and tangential

directions, δ_n , δ_t are material length scale parameters, Γ_n , Γ_t are energy constants, and ϕ_n , ϕ_t are fracture energies in Mode-I and Mode-II.

Figure 1.5 illustrates an example case with Mode-II fracture energy being twice as much as Mode-I fracture energy. The gradients of the potential, i.e., the constitutive relationship of traction-separations in normal and tangential separation directions are also plotted. With the chosen parameters, in the normal separation case, the softening curve is similar to the exponential form in Xu and Needleman’s model, while for tangential separation, an extended traction plateau is present, which may represent ductile material behavior. This versatile model is capable of characterizing different fracture energies, considering different cohesive strengths, and describing various material softening behaviors in order to represent a wide range of material failure responses. The challenge, however, is how to calibrate the model parameters from experiments.

1.2.5 Virtual Internal Bond Model

The Virtual Internal Bond (VIB) model is different from the above-referenced three models in that it does not differentiate the *bulk material* and *cohesive surface*, but rather incorporates the cohesive surface effect into the continuum constitutive relationship. In essence, it is an elasticity model. In the previous models described above, the bulk response is accounted for by means of bulk elements, for which the constitutive relationship is described with the continuum Hooke’s Law, while the fracture behavior is captured by explicit cohesive elements, which follows a cohesive traction-separation relationship. In contrast, there is no “cohesive element” in the VIB model, and the behavior of the bulk material depends on the local strain status. The increasing strain localization softens the material, and when a certain “fracture” criterion is satisfied, the crack is initiated or propagated.

The VIB model assumes cohesive interactions between material particles from an atomistic view, and the network of cohesive bonds is statistically incorporated into the constitutive law of the material via the Cauchy-Born rule, i.e., by equating the strain energy density on the continuum level to the potential energy stored in the cohesive bonds due to an imposed deformation. With this approach, fracture is directly introduced into the continuum constitutive behavior.

For a homogeneous, hyperelastic solid, internal cohesive bonds are assumed to exist between material particles at the microstructure level. Each bond is described by a potential energy function $U(\ell)$ where ℓ denotes the deformed bond length, which

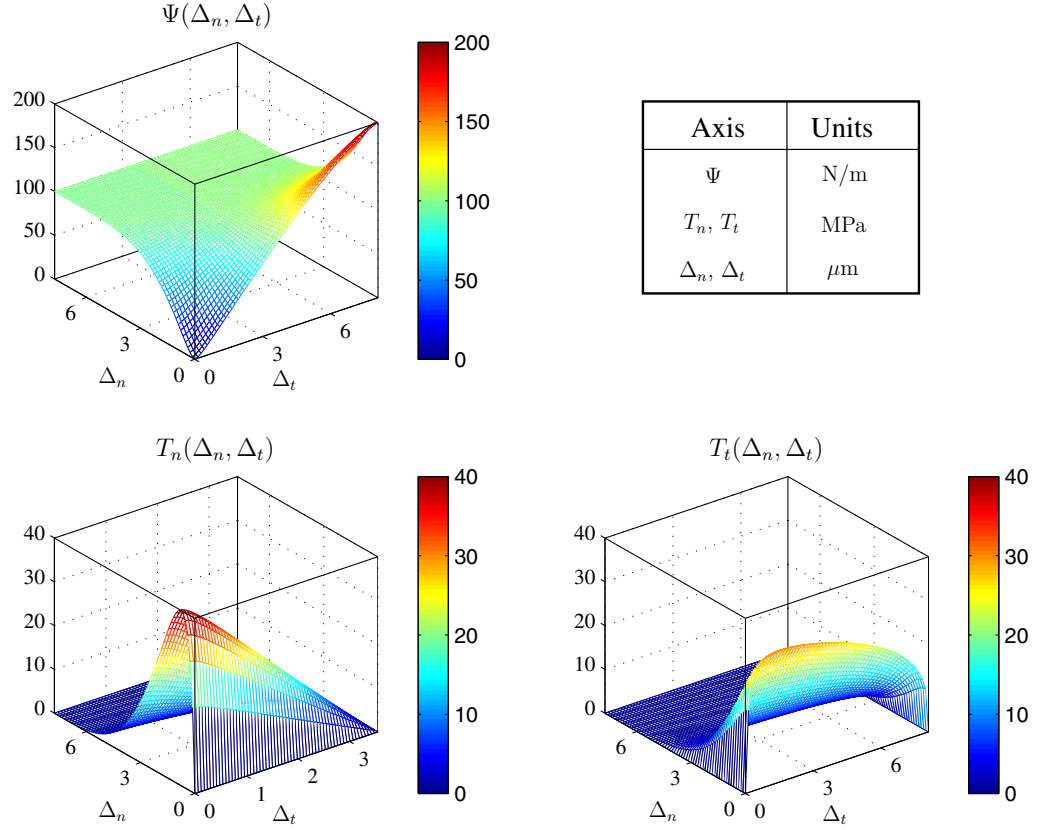


Figure 1.5: Unified mixed-mode potential (PPR) and its gradients for the intrinsic cohesive zone model with $\phi_n = 100$ N/m, $\phi_t = 200$ N/m, $\sigma_{\max} = 40$ MPa, $\tau_{\max} = 30$ MPa, $\alpha = 5$, $\beta = 1.3$, $\lambda_n = 0.1$, and $\lambda_t = 0.2$.

can be expressed in terms of right Cauchy-Green tensor as

$$\ell = \ell_0 \sqrt{\xi_I C_{IJ} \xi_J}, \quad (1.14)$$

where ξ_I denotes the bond orientation in the Lagrangian configuration, ℓ_0 denotes the length of the unstretched bond, and (C_{IJ}) is the IJ component of the Cauchy-Green tensor \mathbf{C} . The important idea in this model is to link the discrete microstructure cohesive description and the macroscopic continuum model by the Cauchy-Born rule as

$$\Phi(C_{IJ}) = \langle U(\ell) \rangle = \left\langle \ell_0 \sqrt{\xi_I C_{IJ} \xi_J} \right\rangle \quad (1.15)$$

where Φ denotes the strain energy density. The position of each bond is characterized by a spherical coordinate system (ℓ_0, θ, ϕ) , and the notation $\langle \dots \rangle$ is defined as the volumetric average

$$\langle \dots \rangle \equiv \int \int \int (\dots) D(\ell_0, \theta, \phi) \sin \theta d\ell_0 d\theta d\phi \quad (1.16)$$

where $D(\ell_0, \theta, \phi)$ is the bond density function, which characterizes the spatial distribution of internal bonds.

By employing a finite deformation formulation, the symmetric second Piola-Kirchhoff stress tensor \mathbf{S} and material tangent moduli tensor \mathbf{C} can be represented in component form as

$$S_{IJ} = 2 \frac{\partial \Phi}{\partial C_{IJ}} = \left\langle \frac{\ell_0 U'(\ell)}{\ell} \xi_I \xi_J \right\rangle \quad (1.17)$$

$$C_{IJKL} = 4 \frac{\partial^2 \Phi}{\partial C_{IJ} \partial C_{KL}} = \left\langle \ell_0^4 \left(\frac{U'(\ell)}{\ell^2} - \frac{U''(\ell)}{\ell^3} \right) \xi_I \xi_J \xi_K \xi_L \right\rangle \quad (1.18)$$

Notice that now the ‘‘material parameters’’ in \mathbf{C} are no longer *constant*; rather, they become function of the cohesive bond distribution $D(\ell_0, \theta, \phi)$, bond cohesive potential $U(\ell)$, as well as local deformation $\ell(C_{IJ})$.

Several special bond cases are proposed [55], e.g., for plane stress, isotropic solid,

$$D(\ell_0, \theta, \phi) = D_0 \delta_D(\ell_0 - \ell_0^*) \delta_D(\theta - \pi/2) \quad (1.19)$$

where δ_D denotes the Dirac delta function, and ℓ_0^* is the characteristic bond length.

By Taylor expansion of strain energy density expression (1.15) within small strain

case, the linear elasticity case is produced, and the elastic modulus takes the form

$$c_{ijkl} = \mu(\delta_{ij}\delta_{kl} + \delta_{ik}\delta_{jl} + \delta_{il}\delta_{kj}) \quad (1.20)$$

where μ is defined as the shear modulus

$$\mu = \frac{\pi}{4} \langle \ell_0^2 U''(\ell_0) \rangle \quad (1.21)$$

with other parameters taking the following forms

$$\lambda = \mu, \quad \nu = 1/3, \quad E = \frac{2\pi}{3} \langle \ell_0^2 U''(\ell_0) \rangle \quad (1.22)$$

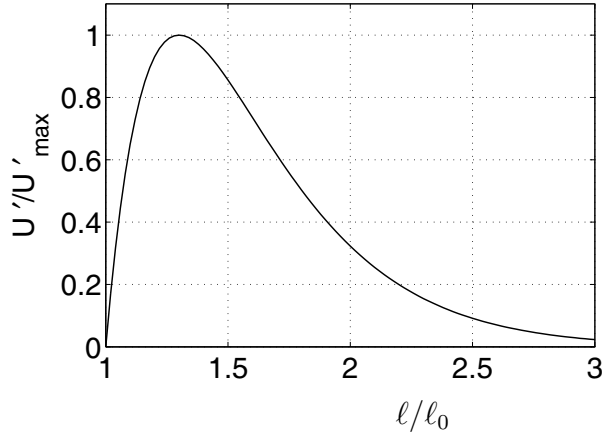


Figure 1.6: A general cohesive force law for an isotropic VIB derived considering equibiaxial stretching.

With the above form, once the potential $U(\ell)$ is defined, the constitutive model is set. A phenomenological cohesive force law is introduced (Figure 1.6)

$$U'(\ell) = A(\ell - \ell_0) \exp\left(-\frac{\ell - \ell_0}{B}\right) \quad (1.23)$$

in which the parameters A and B need to be calibrated from experiments. The constant A represents the material “stiffness” at the unstretched state $U''(\ell_0) = A$, and B denotes a characteristic length. With the D_0 distribution for isotropic plane stress case (Eq. (1.19)), the cohesive strength under equibiaxial stretching is given by

$$\sigma_c = \frac{D_0 \ell_0^4}{\Omega_0} \frac{AB\pi}{e(\ell_0 + B)} \quad (1.24)$$

where Ω_0 denotes representative volume. In the work by Klein et al. [55, 56, 57], the VIB model has been used to simulate failure detection, crack propagation, and fracture toughening. Zhang et al. [114] employed the method to study crack nucleation, propagation, kinking and subsequent propagation of a Mode-II crack, as well as the buckling-driven delamination of a thin film from a substrate.

The features of VIB model are summarized as follows:

- It links the cohesive traction between material particles at the microstructural level and the material constitutive law at the macroscopic level, by equating the strain energy density and the average value of cohesive bond potential. No cohesive surface is explicitly generated in the numerical simulation.
- The elastic parameters, e.g., Young’s modulus E and Poisson’s ratio ν , are no longer constant, but depend on the cohesive bond behavior, which in turn depends on local deformation. With accumulated strain localization, material becomes weaker.

1.3 Scope of Current Work and Thesis Organization

The general objective of this thesis is to address the computational modeling and simulation of dynamic fracture with arbitrary crack paths using CZMs. The author’s master thesis mainly addressed *intrinsic* CZM, while for most of the study in the current Ph.D. thesis, *extrinsic* CZM is employed. In order to successfully incorporate an extrinsic CZM into the numerical scheme, a robust and efficient data structure is mandatory. A novel data structure is thus discussed in detail in the present work. With the convenience of the topological data structure, a variety of dynamic fracture behavior including spontaneous crack nucleation, crack propagation and branching/microbranching, as well as crack competition, are investigated successfully.

The contents of the remaining Chapters of this thesis are outlined as follows. The numerical scheme incorporating cohesive zone elements is presented in Chapter 2. The explicit dynamic scheme for the FEM is employed, and to verify the numerical procedure, first a wave propagation problem in functionally graded materials (FGMs) is studied, which illustrates the explicit updating scheme without cohesive elements involved. This chapter then conceptually introduces the intrinsic cohesive elements in the numerical scheme and provides simulations for a mixed-mode crack propagation

problems (which employs an intrinsic CZM). Chapter 3 addresses the critical issue of a novel topology-based data structure. This data structure balances performance with computer memory demands, which are most important for large-scale simulations involving fracture/fragmentation. It also provides a transparent interface to the user, and explicit support for adaptive cohesive interface insertion. After that, Chapter 4 investigates cohesive zone size in both static and dynamic cases. This study suggests that in some cases the conventional estimate of cohesive zone size is not accurate enough to provide a useful guideline for mesh discretization, which has been a pitfall for CZM analysis in the literature. Chapter 5 presents microbranching simulation in PMMA material which employs 2D extrinsic cohesive fracture modeling. Results agree well with experimental observations, and clearly surpasses previous investigations using intrinsic CZM. Chapter 6 focuses on a 3D example, which studies the influence of loading position on crack initiation/propagation profile for a 3-point-bending concrete specimen. Mesh quality is carefully studied in detail, which also illustrates the importance of an efficient data structure. Finally, a summary of the current work is presented in Chapter 7.

Chapter 2

Finite Element Formulation – Volumetric and Intrinsic Cohesive

This Chapter first outlines the explicit dynamic analysis scheme incorporating cohesive zone elements, followed by two examples. Both homogeneous and heterogeneous material systems are considered. The first example examines wave propagation patterns for a fixed-free slender bar considering homogeneous, bi-material, tri-layered and smoothly graded materials (Steel/Alumina), which also provide verification of the numerical procedures. Comparison of stress histories in these samples indicates that the smooth transition of material gradation alleviates considerably the stress discontinuity in the bi-material system (with sharp interface). The second example investigates dynamic mixed-mode crack propagation in pre-cracked steel and graded plates using a novel intrinsic CZM for graded materials.

2.1 Explicit Dynamic Analysis

To incorporate a cohesive zone model into the numerical approach of dynamic fracture investigation, the *cohesive element* is developed and implemented as part of the finite element scheme, which follows the cohesive *traction-separation* relationship, e.g., the models discussed above. In contrast, the conventional finite element, which is now called “*bulk element*” or “*volumetric element*”, follows the conventional *stress-strain* relationship.

Figure 2.1 illustrates the concept of the two classes of elements. The bulk behavior of the material is counted for by the conventional volumetric elements, whose constitutive relationship is usually defined by Hooke’s Law. To model fracture initiation and propagation, cohesive elements are positioned along the possible path of crack propagation, attached to the volumetric elements, and are capable of performing decohesion, depending on whether the decohesion force the element experiences has exceeded the cohesive strength. The constitutive law of cohesive elements is inherently embedded in the finite element model, so that the presence of cohesive elements allows spontaneous crack propagation, and thus is promising in the investigation of

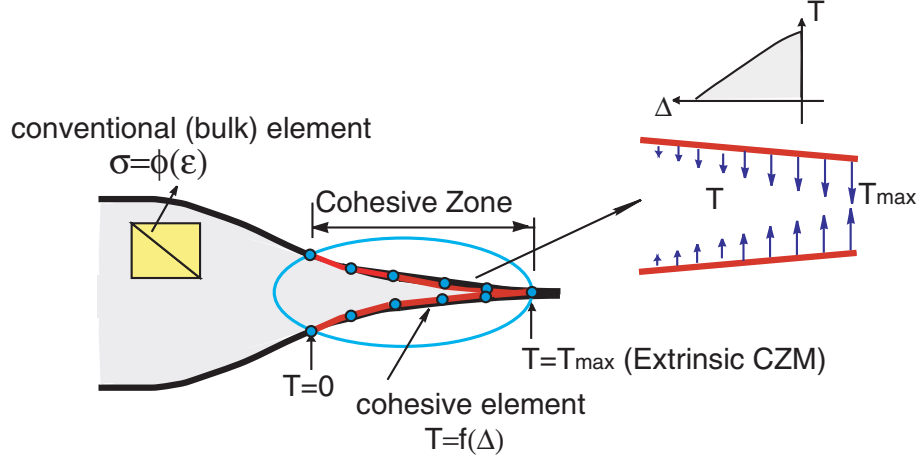


Figure 2.1: Schematic representation of *bulk* elements and *cohesive* elements in the finite element formulation. The notations are as follows: T denotes traction, Δ denotes separation; σ denotes stress, and ϵ denotes strain.

bifurcation and/or impact dynamic loading problems, where multiple crack paths are possible.

The FEM formulation with cohesive elements can be derived from the principle of virtual work, as described in the following. The principle of virtual work of the 2D dynamic finite element formulation can be expressed as ([108]):

$$\int_{\Omega} (\text{div} \boldsymbol{\sigma} - \rho \ddot{\mathbf{u}}) \delta \mathbf{u} d\Omega - \int_{\Gamma} (\mathbf{T} - \boldsymbol{\sigma} \mathbf{n}) \delta \mathbf{u} d\Gamma = 0 \quad (2.1)$$

where Ω represents domain area, Γ denotes boundary line with normal vector \mathbf{n} , \mathbf{u} is the displacement vector, \mathbf{T} is the traction at boundary, and $\boldsymbol{\sigma}$ is the Cauchy stress tensor. The superposed dot in $\ddot{\mathbf{u}}$ denotes differentiation with respect to time, and ρ is the material density. If cohesive surface is *not* considered, by applying the divergence theorem and integration by parts to the general expression in (2.1), the following conventional expression can be obtained:

$$\int_{\Omega} (\boldsymbol{\sigma} : \delta \mathbf{E} + \rho \ddot{\mathbf{u}} \cdot \delta \mathbf{u}) d\Omega - \int_{\Gamma_{ext}} \mathbf{T}_{ext} \cdot \delta \mathbf{u} d\Gamma_{ext} = 0 \quad (2.2)$$

where Γ_{ext} represents the boundary line on which external traction \mathbf{T}_{ext} is applied, and \mathbf{E} is the Green strain tensor. When the cohesive surface is considered, the contribution of cohesive traction-separation work emerges when the integral by parts

technique is applied to (2.1), and one more term appears in the resultant expression:

$$\int_{\Omega} (\boldsymbol{\sigma} : \delta \mathbf{E} + \rho \ddot{\mathbf{u}} \cdot \delta \mathbf{u}) d\Omega - \int_{\Gamma_{ext}} \mathbf{T}_{ext} \cdot \delta \mathbf{u} d\Gamma_{ext} - \int_{\Gamma_{coh}} \mathbf{T}_{coh} \cdot \delta \Delta \mathbf{u} d\Gamma_{coh} = 0 \quad (2.3)$$

where Γ_{coh} represents the internal cohesive surfaces Γ_{coh} on which the cohesive tractions \mathbf{T}_{coh} and displacement jumps $\Delta \mathbf{u}$ are present. Notice that in FGMs the mass density is no longer constant, but depends on position.

The integrals in Eqs. (2.1-2.3) are carried out in the deformed configuration. If infinitesimal deformation is assumed, the undeformed configuration can be used instead. However, when using finite deformation formulation, it is preferable to convert the integral from deformed configuration to original configuration, and work conjugates other than $\boldsymbol{\sigma}$ and \mathbf{E} are used instead. The large deformation formulation scheme is briefly described in the following.

In the finite deformation domain, the displacement vector \mathbf{u} is defined as:

$$\mathbf{u} = \mathbf{x} - \mathbf{X} \quad (2.4)$$

where \mathbf{x} and \mathbf{X} denote the location of the material point in the undeformed and deformed configurations, respectively. The deformation gradient tensor \mathbf{F} and the Lagrangian strain tensor \mathbf{E} are defined as

$$\mathbf{F} = \frac{\partial \mathbf{x}}{\partial \mathbf{X}}, \quad (2.5)$$

$$\mathbf{E} = \frac{1}{2}(\mathbf{F}^T \mathbf{F} - \mathbf{I}), \quad (2.6)$$

respectively, where \mathbf{I} is a fourth-order identity tensor.

The principle of virtual work (2.1), with all quantities referred to undeformed configuration, can be re-written as

$$\int_{\Omega} (\text{div} \mathbf{P} - \rho \ddot{\mathbf{u}}) \delta \mathbf{u} d\Omega - \int_{\Gamma} (\mathbf{T} - \mathbf{P} \mathbf{n}) \delta \mathbf{u} d\Gamma = 0 \quad (2.7)$$

where Ω represents the domain area (or volume), Γ denotes the boundary line (or surface) with normal vector \mathbf{n} and \mathbf{T} is the traction at boundary. The first Piola-Kirchhoff stress tensor \mathbf{P} is related to the Cauchy stress tensor $\boldsymbol{\sigma}$ as

$$\mathbf{P} = J \boldsymbol{\sigma} \mathbf{F}^{-T}, \quad \text{where } J = \det \mathbf{F} \quad (2.8)$$

At the boundary, the following relationship holds: $\mathbf{T} = \mathbf{P}\mathbf{n}$. By applying the divergence theorem and integral by parts to the general expression in (2.7), if cohesive surface is *not* considered, the following conventional expression can be obtained (in the absence of cohesive surface):

$$\int_{\Omega} (\mathbf{P} : \delta\mathbf{F} + \rho\ddot{\mathbf{u}} \cdot \delta\mathbf{u}) d\Omega - \int_{\Gamma_{ext}} \mathbf{T}_{ext} \cdot \delta\mathbf{u} d\Gamma_{ext} = 0 \quad (2.9)$$

When the cohesive surface is considered, one more term appears in the resultant expression:

$$\int_{\Omega} (\mathbf{P} : \delta\mathbf{F} + \rho\ddot{\mathbf{u}} \cdot \delta\mathbf{u}) d\Omega - \int_{\Gamma_{ext}} \mathbf{T}_{ext} \cdot \delta\mathbf{u} d\Gamma_{ext} - \int_{\Gamma_{coh}} \mathbf{T}_{coh} \cdot \delta\Delta\mathbf{u} d\Gamma_{coh} = 0 \quad (2.10)$$

By means of the following relationship for the second Piola-Kirchhoff stress tensor \mathbf{S}

$$\mathbf{S} = \mathbf{F}^{-1}\mathbf{P} = J\mathbf{F}^{-1}\boldsymbol{\sigma}\mathbf{F}^{-T} \quad (2.11)$$

the alternative expression of Eqn. (2.10) becomes

$$\int_{\Omega} (\mathbf{S} : \delta\mathbf{E} + \rho\ddot{\mathbf{u}} \cdot \delta\mathbf{u}) d\Omega - \int_{\Gamma_{ext}} \mathbf{T}_{ext} \cdot \delta\mathbf{u} d\Gamma_{ext} - \int_{\Gamma_{coh}} \mathbf{T}_{coh} \cdot \delta\Delta\mathbf{u} d\Gamma_{coh} = 0 \quad (2.12)$$

In the present work the explicit central difference time stepping scheme [14] is used, and the updating scheme for nodal displacements, accelerations and velocities from time step n to $n + 1$ is:

$$\mathbf{u}_{n+1} = \mathbf{u}_n + \Delta t\dot{\mathbf{u}}_n + \frac{1}{2}(\Delta t)^2\ddot{\mathbf{u}}_n \quad (2.13)$$

$$\ddot{\mathbf{u}}_{n+1} = \mathbf{M}^{-1}(\mathbf{F} - \mathbf{R}_{int_{n+1}} + \mathbf{R}_{coh_{n+1}}) \quad (2.14)$$

$$\dot{\mathbf{u}}_{n+1} = \dot{\mathbf{u}}_n + \frac{\Delta t}{2}(\ddot{\mathbf{u}}_n + \ddot{\mathbf{u}}_{n+1}) \quad (2.15)$$

where Δt denotes the time step, \mathbf{M} is the mass matrix, \mathbf{F} is the external force vector, \mathbf{R}_{int} and \mathbf{R}_{coh} are the global internal and cohesive force vectors, which are obtained from the contribution of *bulk* and *cohesive* elements, respectively.

The formulation described above applies to both homogeneous and non-homogeneous problems. By introducing the generalized isoparametric element formulation in the numerical scheme, the material gradient is treated appropriately at the element level. A detailed description can be found in the author's master's thesis [115].

2.2 Fracture of Functionally Graded Materials (FGMs)

Functionally graded materials or FGMs are a new generation of engineered composites characterized by spatially varied microstructures accomplished through nonuniform distribution of the reinforcement phase with different properties, sizes and shapes, as well as by interchanging the roles of reinforcement and matrix (base) materials in a continuous manner. This new concept of engineering the material microstructure and recent advances in material processing science allows one to fully integrate material and structural design considerations [68, 80].

The initial emphasis for FGMs focused on the synthesis of thermal barrier coatings for aerospace applications, however, subsequent investigations have addressed a wide variety of applications [101]. Many of these applications involve dynamic events such as blast protection for critical structures and armors for ballistic protection. For example, a functionally graded armor composite with a tailored ceramic to metal through-thickness gradient combines the beneficial effects of ceramics (e.g. hardness) and metals (e.g. toughness) in the same material system while suppressing adverse strength reduction that would occur with discrete interfaces [21] – also see [42] for an investigation of functionally graded TiB/Ti armors. Other applications of FGMs include bone and dental implants, piezoelectric and thermoelectric devices, and optical materials with graded refractive indices [80, 101]. Parallel to advancements in FGM manufacturing and experimentation, methodologies to evaluate and predict FGM properties and behaviors have been developed. For example, homogenization technique and higher-order theory have been adopted to evaluate effective material properties and responses [1, 2].

Fracture mechanics of FGMs has been an active area of research during recent years [15, 30, 79, 82]. Eischen investigated mixed-mode cracks in non-homogeneous materials and proposed a path-independent J_2 formulation by incorporating strain energy along the crack surfaces [28, 29]. Dolbow and Gosz [26] presented an interaction energy integral method for accurate evaluation of mixed-mode stress intensity factors at FGM crack tips. Kim and Paulino [51, 52, 81, 53, 54] provided techniques for evaluating mixed-mode stress intensity factors, J-integrals, interaction integrals, T-stress, and crack initiation angles under static and quasi-static conditions for both isotropic and orthotropic materials. To fully exploit their multi-functionality and high performance, further understanding of the dynamic fracture behavior of FGMs

is desired, especially when these materials are exposed to hostile environments and subject to impact loading.

2.3 Bilinear Cohesive Fracture Model

As discussed in the literature, e.g., [11, 56, 115], insertion of cohesive elements introduces fictitious compliance to the structure. This effect is inherent to the intrinsic CZM approach. However, if carefully treated, this unwelcome effect can be restricted to certain limits within which extent the numerical analysis can still reliably simulate the problem. The magnitude of artificial compliance introduced is primarily related to the initial slope of the traction-separation law. A stiffer slope represents more rigid initial bonds between bulk elements, resulting in less fictitious compliance. To minimize mesh size dependence, the compliance introduced to the system should ideally be the same for various mesh discretizations. This requirement is difficult to satisfy for the Xu and Needleman [108] model, for which the traction-separation law has a defined shape, and thus a defined initial slope.

A bilinear cohesive model is thus adopted in favor of its adjustable slope attribute. Zavattieri and Espinosa [113] presented a bilinear cohesive zone model, for which the material fails when the parameter λ (which is a function of the normal and tangential separations) reaches the unity. Here, we specialize the expression for λ as follows

$$\lambda = \sqrt{\left(\frac{\Delta_n}{\delta_n}\right)^2 + \left(\frac{\Delta_t}{\delta_t}\right)^2} \quad (2.16)$$

The parameters Δ_n , Δ_t are the current normal and tangential cohesive interface separations, while δ_n , δ_t are the critical separation values at which the interface is considered to have failed in the two modes, respectively. Similarly to the model by [41], the choice of a “critical separation” λ_{cr} allows the users to specify the initial slope of the cohesive law. Apparently, the value of λ_{cr} ought to be close to zero to ensure initially stiff cohesive bonds. The cohesive law is stated as

$$T_n = T_n^{max} \frac{\Delta_n}{\delta_n} \frac{1 - \lambda^*}{\lambda^*(1 - \lambda_{cr})} \quad (2.17)$$

$$T_t = T_t^{max} \frac{\Delta_t}{\delta_t} \frac{1 - \lambda^*}{\lambda^*(1 - \lambda_{cr})} \quad (2.18)$$

where λ^* is defined as

$$\lambda^* = \begin{cases} \lambda_{cr} & \text{if } \lambda \leq \lambda_{cr} \\ \lambda & \text{if } \lambda > \lambda_{cr} \end{cases}$$

The traction-separation relationships for pure mode I and pure mode II cases are plotted in Figure 2.2. In Figure 2.2 (a), the traction-separation relationship in the compression region has the same slope as in the tension region. To maintain irreversibility of interface weakening, the parameter λ is set to retain its maximum value throughout the loading history.

$$\lambda = \max(\lambda_{current}, \lambda_{previous})$$

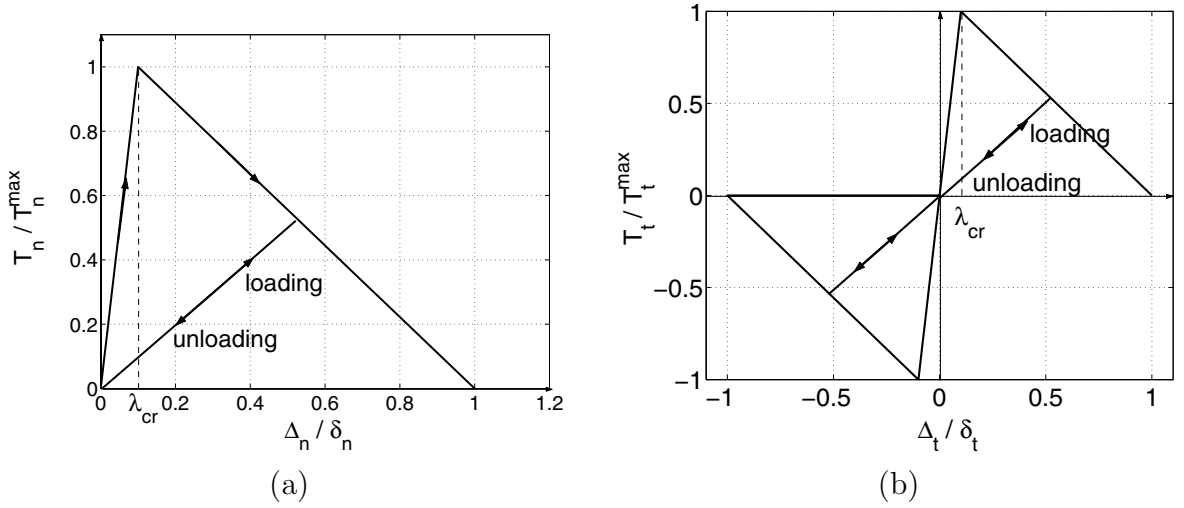


Figure 2.2: Bilinear cohesive model; (a) pure normal traction-separation; (b) pure tangential traction-separation.

2.4 A Cohesive Fracture Model for FGMs

In order to simulate crack propagation in FGM, we extended the bilinear model of Figure 2.2 to incorporate material gradation using material dependent parameters. A volume fraction based phenomenological cohesive zone model for FGM that introduces two material specific parameters to account for the interaction between different material phases was presented by [48]. We adopt similar consideration but use bilinear cohesive model. Let

$$\mathbf{T}_{FGM} = [T_n^{FGM}, T_t^{FGM}]$$

denote the traction force vector across the cohesive surfaces of a two-phase FGM, which comprises normal and tangential traction force components. The cohesive traction \mathbf{T}_{FGM} is approximated by the following volume-fraction-based formula

$$\mathbf{T}_{\text{FGM}}(\mathbf{x}) = \frac{V_1(\mathbf{x})}{V_1(\mathbf{x}) + \beta_1[1 - V_1(\mathbf{x})]} \mathbf{T}_1 + \frac{1 - V_1(\mathbf{x})}{1 - V_1(\mathbf{x}) + \beta_2 V_1(\mathbf{x})} \mathbf{T}_2 \quad (2.19)$$

where the subscripts 1 and 2 denote the two material phases, parameter $V_1(\mathbf{x})$ denotes the volume fraction of the material phase 1, while β_1 and β_2 are the two cohesive gradation parameters that describe the transition of failure mechanisms from pure material phase 1 to pure material phase 2. The traction forces associated with each material phase (\mathbf{T}_1 and \mathbf{T}_2) are determined from Eqs. (2.17-2.18), while the separation parameter λ (Eq. (2.16)) is evaluated for each material phase. The following expressions thus follow:

$$\begin{aligned} T_n^{\text{FGM}}(\mathbf{x}) &= \frac{V_1(\mathbf{x})}{V_1(\mathbf{x}) + \beta_1[1 - V_1(\mathbf{x})]} T_{n1}^{\text{max}} \frac{\Delta_n}{\delta_{n1}} \frac{1 - \lambda_1^*}{\lambda_1^*(1 - \lambda_{cr1})} \\ &+ \frac{1 - V_1(\mathbf{x})}{1 - V_1(\mathbf{x}) + \beta_2 V_1(\mathbf{x})} T_{n2}^{\text{max}} \frac{\Delta_n}{\delta_{n2}} \frac{1 - \lambda_2^*}{\lambda_2^*(1 - \lambda_{cr2})} \end{aligned} \quad (2.20)$$

$$\begin{aligned} T_t^{\text{FGM}}(\mathbf{x}) &= \frac{V_1(\mathbf{x})}{V_1(\mathbf{x}) + \beta_1[1 - V_1(\mathbf{x})]} T_{t1}^{\text{max}} \frac{\Delta_t}{\delta_{t1}} \frac{1 - \lambda_1^*}{\lambda_1^*(1 - \lambda_{cr1})} \\ &+ \frac{1 - V_1(\mathbf{x})}{1 - V_1(\mathbf{x}) + \beta_2 V_1(\mathbf{x})} T_{t2}^{\text{max}} \frac{\Delta_t}{\delta_{t2}} \frac{1 - \lambda_2^*}{\lambda_2^*(1 - \lambda_{cr2})} \end{aligned} \quad (2.21)$$

With the above formulation, the cohesive traction reduces to that of the material 1 when $V_1 = 1$ and to that of the material 2 when $V_1 = 0$, as expected. The two additional parameters, β_1 and β_2 , which are material dependent, should be calibrated by experiments.

2.5 One-Dimensional Wave Propagation

Transient wave propagation along a fixed-free bar is investigated considering homogeneous, bi-material, and graded material properties along the height direction. The objective of this example is to investigate the influence of material gradation on the wave propagation pattern.

2.5.1 Problem Description

Consider the fixed-free slender bar illustrated in Figure 2.3(a). The bar is of length $L = 1m$, and height $H = 0.05m$. A transient axial loading with high frequency (Figure 2.3(b)) is applied across the right free surface of the bar, which consists of a sine pulse of duration $50\mu s$. The fundamental period is $T = 0.0174s$. Four material gradation cases along the beam height are considered: homogeneous, bi-material, tri-layered, and smoothly graded, as shown in Figure 2.4 (a), (b), (c) and (d), respectively. The material system under consideration is taken as: Steel for homogeneous bar, Steel/Alumina for both bi-material and graded bars. The material properties for Steel and Alumina are provided in Table 2.1. For bi-material bar, the cross section is made of Steel in the upper half and Alumina in the lower half, with a sharp interface in the middle. For the tri-layered bar, the cross section is made of Steel in the upper layer, Alumina in the lower layer, and smooth transition layer in between. For graded regions, material property varies linearly from pure Steel at upper surface to pure Alumina at lower surface.

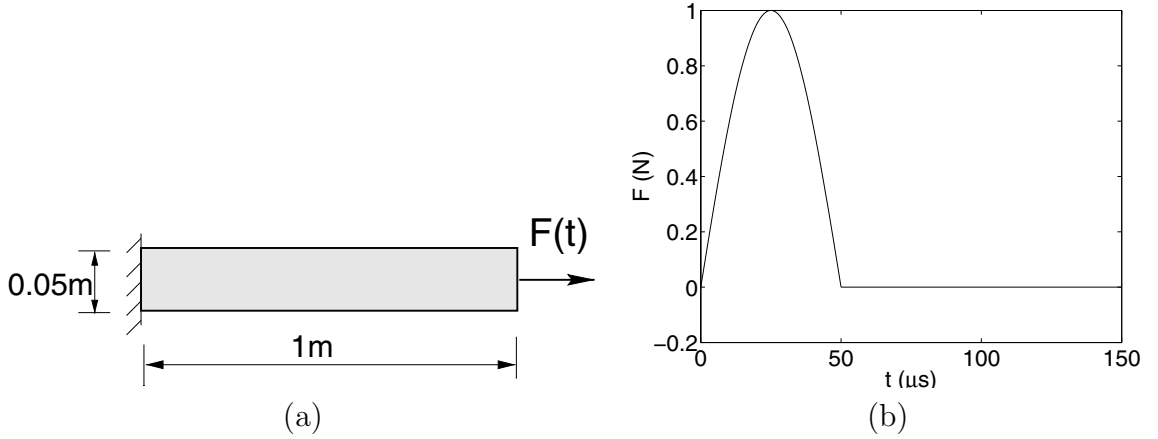


Figure 2.3: Geometry and applied force for a fixed-free thin bar; (a) geometry; (b) applied load history.

Table 2.1: Steel and Alumina material properties

Material	E GPa	ν	ρ (kg/m ³)	C_d (m/s)
Steel	210	0.31	7800	6109
Alumina	390	0.22	3950	10617

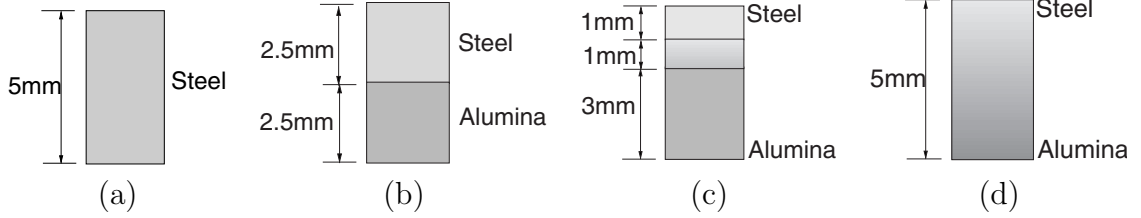


Figure 2.4: Bar cross section material property: (a) homogeneous bar, (b) bi-material bar, (c) tri-layered bar, and (d) graded bar.

2.5.2 Mesh Size Control

High-order modes participate in the bar response of Figure 2.3, which in turn requires refined element size [20]. To capture the transient response, the time step must be small enough in order to track the change of the applied load, and adequate element size can be estimated according to the Courant condition. For example, when the applied force period is discretized into 100 time steps, the corresponding element size is

$$h = C_d \times \Delta t = 6109 \times \frac{50 \times 10^{-6}}{100} = 3.06 \times 10^{-3} m = 3.06 mm \quad (2.22)$$

Considering material gradation along the height direction, the bar of Figure 2.3(a) is discretized into 300×15 quads, each divided into four T6 elements. This leads to a mesh with 36,631 nodes and 18,000 T6 elements, which is used for the wave propagation problem.

2.5.3 Results and Discussions

The analytical solution for a 1D stress wave propagation is given by Meirovitch [66]

$$\sigma(x, t) = \sigma^0 f\left(t + \frac{x}{C_d}\right) + \hat{\sigma}^0 f\left(t - \frac{x}{C_d}\right) \quad (2.23)$$

where the first and second term on the right hand side indicate the left-traveling-wave and the right-traveling-wave, respectively. The parameters σ^0 and $\hat{\sigma}^0$ are the magnitude of the impact stress $f(t)$, while the sign depends on the boundary condition where the wave impacts. When the stress wave reaches a fixed end, the stress magnitude doubles while the velocity changes sign; when the stress wave reaches a free end, the stress vanishes while the velocity doubles.

The numerical simulations employ 2D finite elements. Thus the current numerical model is not 1D in nature, however it reasonably resembles a 1D case as the bar

is slender. Therefore, we set the analytical solution of the homogeneous bar as a reference result to which the numerical results are compared. Because the bars under consideration possess different material properties, the results reported are normalized in order to provide meaningful comparison. Therefore, stress is reported as σ/σ^0 and time as $t \times C_d/L$.

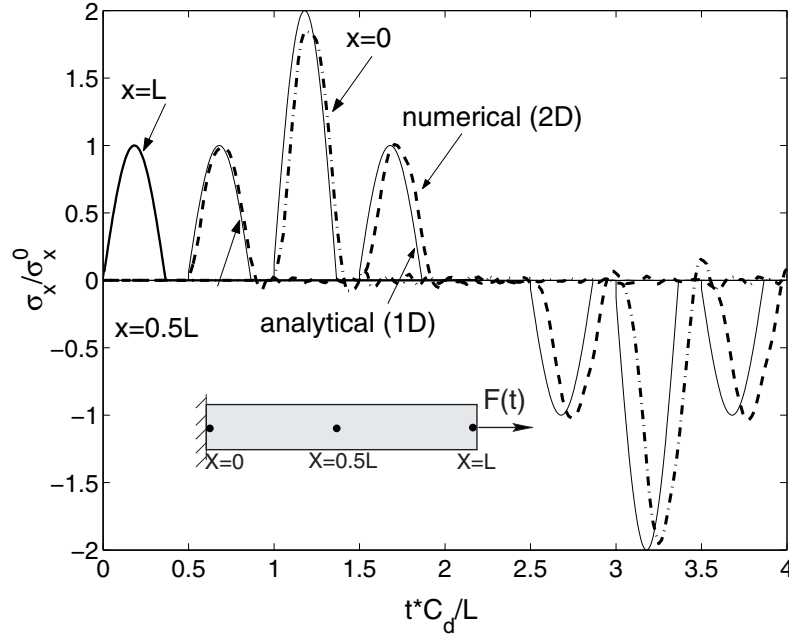


Figure 2.5: Stress history for homogeneous bar (2D simulation) subjected to transient loading and its comparison with 1D analytical solution; numerical results obtained at points $x = L$ (thick solid line), $x = 0.5L$ (dashed line) and $x = 0$ (dash-dot line); 1D analytical results (thin solid line) obtained for the same three points.

Homogeneous bar. In the 1D homogeneous case, the stress wave propagates at a constant speed and retains its initial shape. This is shown in Figure 2.5. Three locations along the beam are chosen to represent the stress wave behavior. The free end ($x = L$) experiences the stress wave which retains its shape, and afterwards this boundary becomes stress-free, as shown in Figure 2.5 with the solid ($x = L$) curve. The stress wave travels across point $x = 0.5L$ (dash curve) at normalized time $t' = t \times C_d/L = 0.5$, and impacts the fixed end point $x = 0$ (dash-dot curve) at $t' = 1$, where its magnitude is doubled. The wave reflects back, passes the $x = 0.5L$ position, and reaches the free end at $t' = 2$. Between the next cycle (normalized time $t' = 2$ to 4), the wave becomes compressive, travels towards the fixed end, and reflects back following a similar pattern as described between normalized time

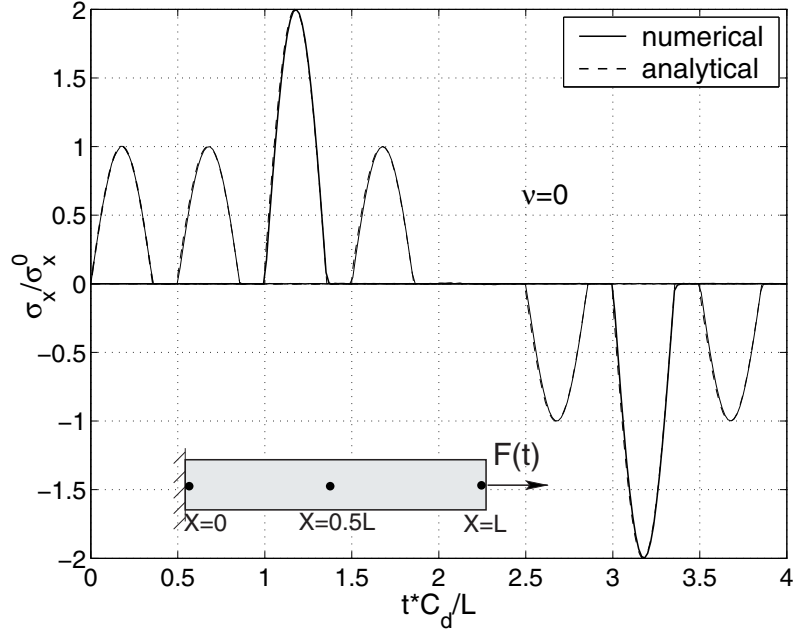


Figure 2.6: Comparison of 2D numerical results (solid line) with 1D analytical results (dashed line) for the same three points in Figure 2.5 when Poisson ratio $\nu = 0$.

$t' = 0$ to 2. The numerical result is also compared with the 1D analytical solution in Figure 2.5. It is clearly shown that the shape and magnitude of numerical results follow closely with the analytical solution. However, there are small fluctuations in the 2D simulation which are absent from the 1D analytical solution. When Poisson ratio $\nu = 0$, the problem becomes 1D and the upper and lower boundaries do not move. In the 2D simulation, as stress front propagates, the Poisson ratio effect results in constant vertical fluctuation of the upper and lower boundaries, which in turn induces fluctuation in stress wave. The difference in period is due to the negligence of the Poisson ratio effect in the 1D analytical solution. To verify the above statement, another simulation using Poisson ratio $\nu = 0$ is carried out. The amplitude and period of the numerical result matches the analytical solution, as shown in Figure 2.6.

Bi-material bar. For the bi-material system, a stress jump is present at the interface between two material phases. The results plotted in Figure 2.7 compare the stress history of three pairs of nodes residing across the material interface, at locations $x = 0$, $0.5L$, and L , respectively. Apparently, stress travels at the same speed along the x direction inside the two phases, as it reaches peaks at the same time intervals for each pair of nodes. The magnitudes differ, as expected, because the stiffer side sustains higher stress. Compared to the homogeneous case, the stress

magnitude is lower at the Steel side, and higher at the Alumina side. Fluctuations are more noticeable than the homogeneous case due to the reflected wave at the material interface that compounds the wave pattern. Although the wave speed is different for the two material phases, the faster one “*drags*” the slower one and the wave propagates at the wave speed of Alumina.

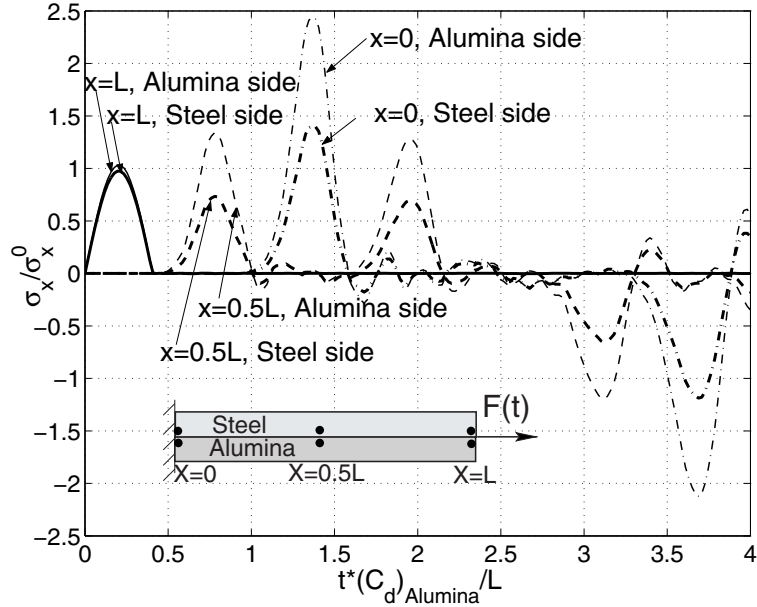


Figure 2.7: Stress history of six points (indicated by solid dots in the insert) on a bi-material bar subjected to transient loading. Solid, dashed and dash-dot lines indicate points at $x = L$, $0.5L$, 0 , respectively. Thin and thick lines indicate points at Alumina and Steel side, respectively.

Tri-layer bar with Thin Graded interface. For the tri-layer bar, the graded middle layer ($y = 3$ to 4mm) provides a smooth transition for material variation from the top layer (Steel, $y = 4$ to 5mm) to the bottom layer (Alumina, $y = 0$ to 3mm). Because there are no distinctive interfaces between these layers, stress jump is alleviated compared to the bi-material case. The results plotted in Figure 2.8 compare the stress history of three groups of nodes residing at the upper ($y = 4\text{mm}$), middle ($y = 3.5\text{mm}$) and lower ($y = 3\text{mm}$) positions of the graded layer, at locations $x=0$, $0.5L$, and L , respectively. Apparently, stress travels at the same speed along the x direction, and the stiffer side sustains higher stress.

Graded bar. Due to the gradual variation of material gradation, stress jump does not occur, but varies smoothly along the height direction. The results plotted in

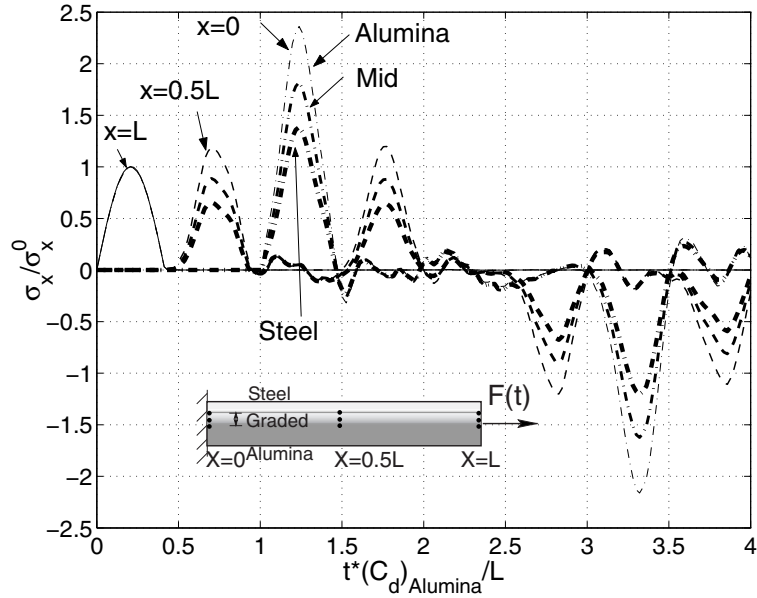


Figure 2.8: Stress history of nine points (indicated by solid dots in the insert) on a tri-layer bar subjected to transient loading. Solid, dashed and dash-dot lines indicate points at $x = L, 0.5L, 0$, respectively. Thin, intermediate-thick and thick lines indicate Alumina-rich side, mid-plane and Steel-rich side of the graded interface, respectively.

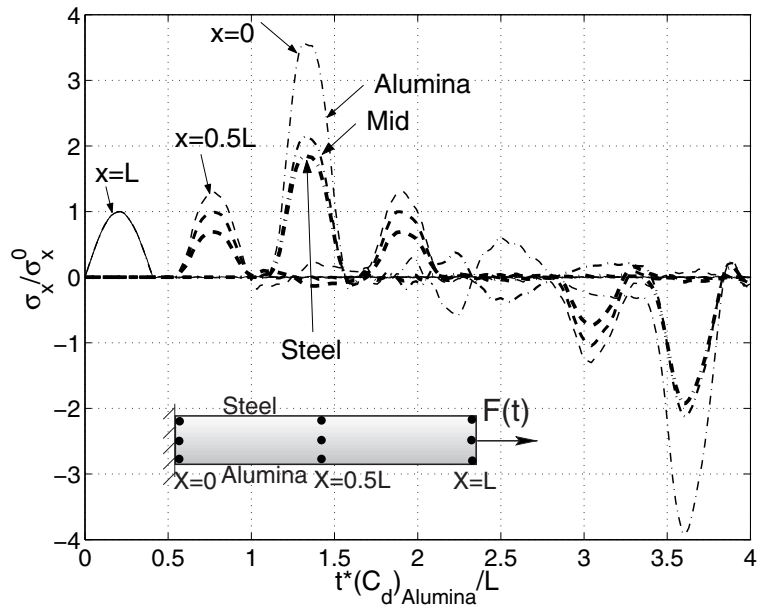


Figure 2.9: Stress history of nine points (indicated by solid dots in the insert) on a graded beam subjected to transient loading. Solid, dashed and dash-dot lines indicate points at $x = L, 0.5L, 0$, respectively. Thin, intermediate-thick and thick lines indicate Alumina-rich side, mid-plane and Steel-rich side, respectively.

Figure 2.9 compare the stress history of three groups of nodes residing at the upper, lower and middle surface, at locations $x=0$, $0.5L$ and L , respectively. Similarly to the bi-material case, the wave that moves fastest “*drags*” the rest to move along, so at the monitored points of the same x location, the peak values occur simultaneously. At the free end, despite the material difference, the stress surges across the entire bar height with the same magnitude (because this is the initial boundary condition prescribed). The stress magnitude differs noticeably at other places, especially at the fixed end, where the Alumina-rich side experience much higher stress than the opposite side. Also, the fluctuation is even more significant, due to the large number of wave tides that travel at different speeds.

Stress Contour. Stress contours provide a more intuitive image of the wave pattern. The stress distribution inside the bar at certain time instances is shown for the three bars discussed above in Figure 2.10. It clearly reveals a stress jump along a material interface in the bi-material bar, while a smooth distribution of stress is achieved for the graded and tri-layer bars.

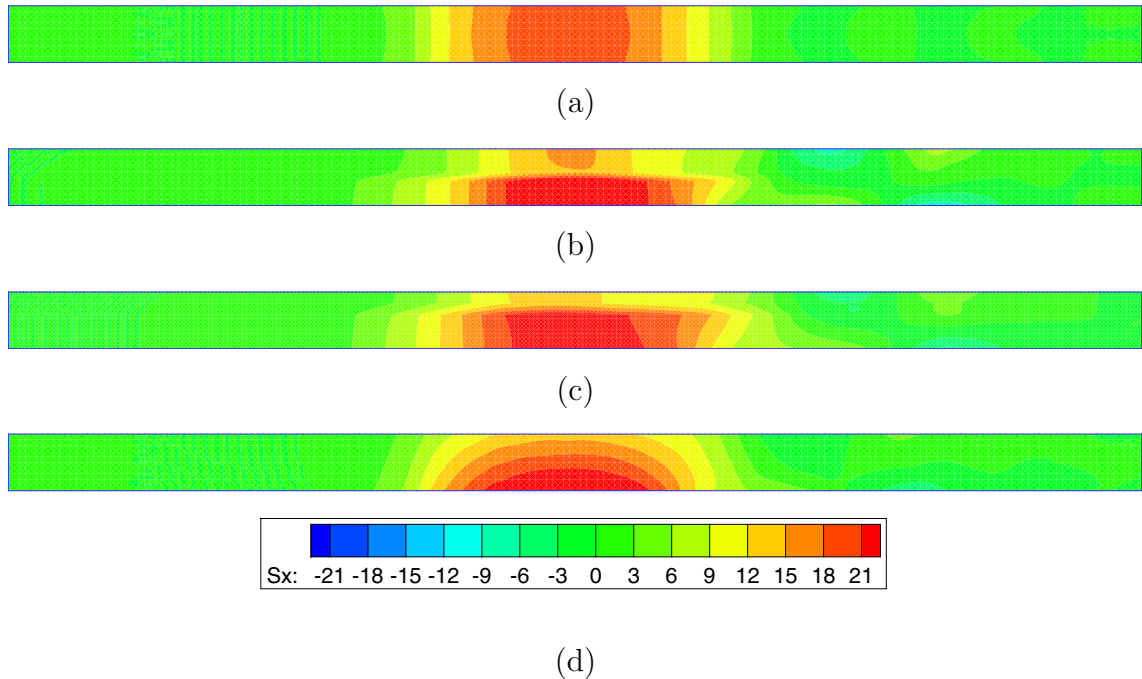


Figure 2.10: Comparison of stress contours (Pa) of the four bars: (a) homogeneous, (b) bi-material, (c) tri-layer, and (d) smoothly graded.

With the above observation, we conclude that the material variation strongly influences the wave pattern. The stress front travels at the speed of the stiffest

material, and the stress peak at the stiffer material side can be remarkably higher than the homogeneous case if linear elastic behavior is considered and there is no other source of inelasticity. For example, for the smoothly graded case, the highest stress at the Alumina side reaches about four times the applied impact traction magnitude.

2.6 Mixed-mode Crack Propagation Using Intrinsic CZM

This section is devoted to the study of mixed-mode dynamic fracture by using an intrinsic CZM. A clear understanding of physical mechanisms governing the dynamic crack propagation under mixed-mode loading remains elusive. General observation drawn primarily from quasi-static analysis indicates that under mixed-mode loading, the existing crack tends to grow according to the local mode-I condition, e.g., in the direction of maximum hoop stress at the immediate vicinity of the crack tip. Another widely adopted fracture criterion in quasi-static crack propagation analysis is based on energy consideration, in which the crack tries to find the path of least resistance and thus maximizes the energy release rate [4]. These approaches require evaluation of external fracture criterion during simulation. In this section, the cohesive zone model is employed to study a mixed-mode dynamic crack propagation problem, where the cohesive elements allow crack initiation and turning of crack paths to occur spontaneously without predefining the crack path nor prescribing a separate fracture criterion.

2.6.1 Kalthoff-Winkler Experiments

Kalthoff and Winkler [50] tested specimens, as shown in Figure 2.11 (a), where a plate with two edge notches is subjected to an impact by a projectile. The two notches extend to approximately a half-plate width. The experiments demonstrated different fracture/damage behaviors of a maraging steel material under various loading rates. Depending on the loading rate v_0 and notch tip radius r_0 , the crack tip experiences a different stress intensity factor rate. At a lower strain rate factor v_0/r_0 , brittle fracture occurs with a propagation angle of around 70° from the original crack plane. At a higher strain rate factor, failure occurs due to the shear localization originated from the shear band formation ahead of the notch. The maraging steel used in the original experiments is X2 NiCoMo 18 9 5, and the counterpart material in the ANSI

system is maraging steel 18Ni(300) (alternatively labeled as 18Ni1900 as in [13], in which 1900MPa represents the material tensile strength in metric unit system, while 300ksi is measured in English units). The material properties are listed in Table 2.2. Notice the factor of the notch tip radius in this problem: with a sharp crack, shear band damage mode can occur at even low impact loading rates. For the mesh used in this study, the notch tip is originally sharp ($r_0 = 0$), and theoretically it results in an infinite v_0/r_0 ratio. However, the presence of cohesive elements eliminates stress singularity at the crack tip and introduces a finite separation at the crack tip. Moreover, when the notch tip is subjected to the influence of an impinging stress wave, it does not retain a ($r_0 = 0$) shape.

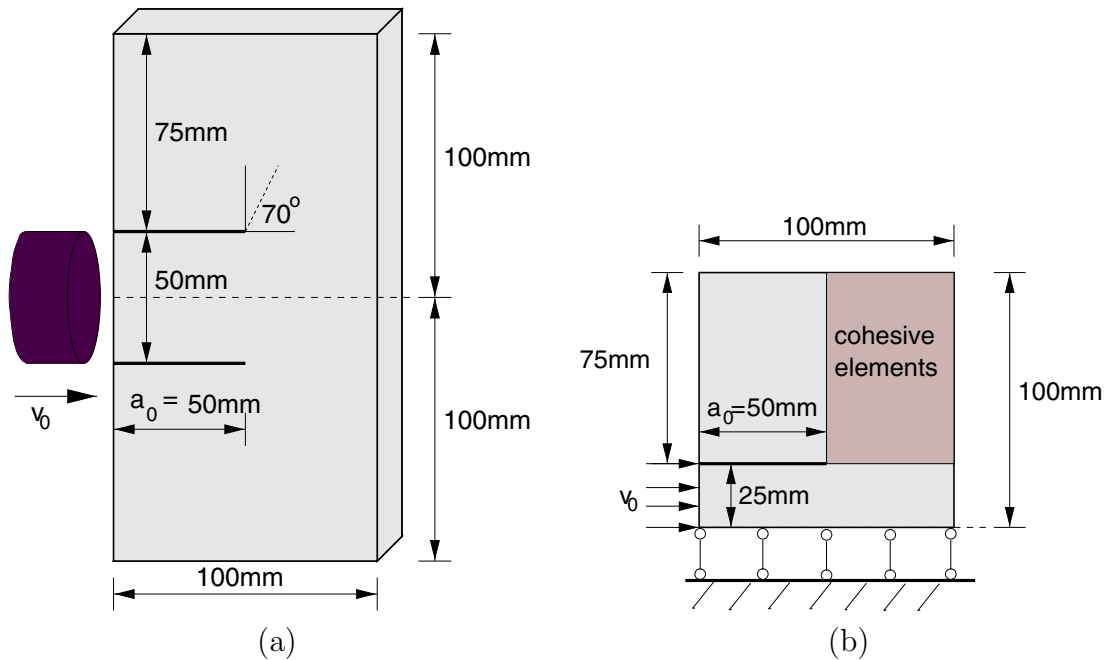


Figure 2.11: (a) Geometry and loading of the Kalthoff-Winkler experiments [50]; (b) 2-D plane-strain FEM simulation model.

Both the brittle failure and the shear band failure modes have been studied extensively (e.g., [119] for the latter case). In this study, we attempt to simulate the brittle failure mode. Belytschko et al. [13] modeled these experiments using the extended FEM (XFEM) with both loss of hyperbolicity criterion and tensile stress criterion. The overall crack propagation angle of around 58° was reported for the former, and 65° for the latter. The Virtual Internal Bond model combined with meshfree methods were employed by [56], and produced an average crack growth angle of 63° and 79° depending on the texture of integration grid. Both studies also reported simulations using Xu and Needleman's [108] cohesive model, but with

different mesh discretization and cohesive strength. In this study, we investigate the overall crack propagation angle, crack initiation time and propagation speed with a set of progressively refined element sizes. The impact loading rate is chosen as $16.5m/s$, following the work by [13]. Because the problem possesses symmetry, only half of the geometry is modeled, as shown in Figure 2.11 (b).

2.6.2 Bilinear Cohesive Model and Initial Stiffness Considerations

The crack trajectory in this problem is not known *a priori*. In order to simulate crack propagation along an arbitrary path, cohesive zone elements are inserted into a relatively large region through which the crack may potentially grow, as shown in Figure 2.11 (b). Initially, all bulk elements are bound together with cohesive force provided by the cohesive elements. Fracture occurs at high stress regions, where the local stress overcomes cohesive strength and the cohesive elements gradually lose resistance capability against separation, until complete decohesion takes place.

In the fracture problems where crack paths are predefined (see examples in the author's master's thesis [115], and later in Chapter 4), there is essentially one line of cohesive elements added to the finite element mesh, and hence mesh refinement does not affect structure stiffness, as the total area of cohesive elements remains the same for various mesh discretizations. For the mixed-mode fracture problem under study, on the other hand, mesh refinement implies that larger total area of cohesive elements are inserted, along with larger capacity to dissipate energy, and addition of artificial compliance to the system. Therefore, the bilinear model discussed in Section 2.2 is adopted in this study in favor of its adjustable initial slope.

The material property and typical cohesive model parameters used in this study are given in Table 2.2. Due to the lack of experimental information about the CZM parameters, we assume

$$G_{IIc} = G_{Ic}, \quad T_t^{\max} = T_n^{\max}, \quad \delta_t = \delta_n$$

where the fracture toughness of opening and sliding modes are related to cohesive strengths and critical openings as

$$G_{Ic} = \frac{1}{2} T_n^{\max} \delta_n, \quad G_{IIc} = \frac{1}{2} T_t^{\max} \delta_t$$

for the bilinear cohesive model. In this study, the cohesive strength adopted in the bilinear model is relatively low ($T_n^{\max} = E/110$) as compared to the usual case when the model by [108] is employed ($T_n^{\max} = E/10$). However, a stiff initial slope is chosen ($\lambda \leq 0.01$) to limit the artificial compliance introduced. For example, when a 80×80 grid mesh is used, the additional compliance introduced can be estimated as [113]

$$E_{\text{add}} = \frac{T_n^{\max}}{\lambda_{cr} \delta_n} \times h = \frac{E/110}{0.01(25.63 \times 10^{-6})} \times \frac{0.1/80}{3} = 14.8 E$$

where h is an equivalent cohesive element spacing estimated as grid spacing over the number of cohesive elements within a unit grid. For these parameters, the additional elasticity introduced E_{add} within the cohesive elements region is much larger than the material Young's modulus E as long as the interface separation experienced by the cohesive elements does not exceed $\lambda_{cr} \delta_n$. As the mesh is refined, e.g., 100×80 and 120×120 grids, the initial slope is also adjusted to maintain the same value of E_{add} .

Table 2.2: Material properties of 18Ni(300) steel and cohesive model parameters used in simulating Kalthoff-Winkler Experiments [13].

E (<i>GPa</i>)	ν	ρ (<i>kg/m</i> ³)	C_d (<i>m/s</i>)	G_{Ic} (<i>kJ/m</i> ²)	T_n^{\max} (<i>GPa</i>)	δ_n (μm)
190	0.3	8000	5654	22.2	1.733	25.63

Two sets of calculations are carried out to investigate the capabilities of the bilinear cohesive model. The first set studies the effect of mesh orientation on the fracture propagating path. With sufficiently refined mesh, the crack is assumed to find the same path for different meshes. Three rectangular unit cells with aspect ratios of $height/width = \{25/16, 1, 16/25\}$ are considered. Therefore, the plate geometry is discretized into 64×100 , 80×80 and 100×64 rectangles, each divided into four T6 elements. The second set of calculations investigates the effect of mesh size. Results obtained from 100×100 and 120×120 are compared to those from 80×80 , for instance.

2.6.3 Results

The fracture paths for three aspect ratios of the ‘‘unit mesh grid’’ are shown in Figure 2.12. These results indicate that, despite the different mesh orientation bias, the overall crack propagation paths of the three different meshes are similar. Notice that the crack path is not straight, but tends to propagate further towards the right

surface when it moves closer to the boundary (see Figure 2.12 (a)). In order to avoid this “boundary effect”, the crack angle is measured up to about first 2/3 crack length (the crack tip projection on x axis is $x = 0.08m$). The propagation angle is estimated to be around 72° to 74° , which agrees well with the experimental prediction (70°).

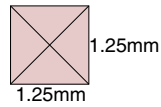
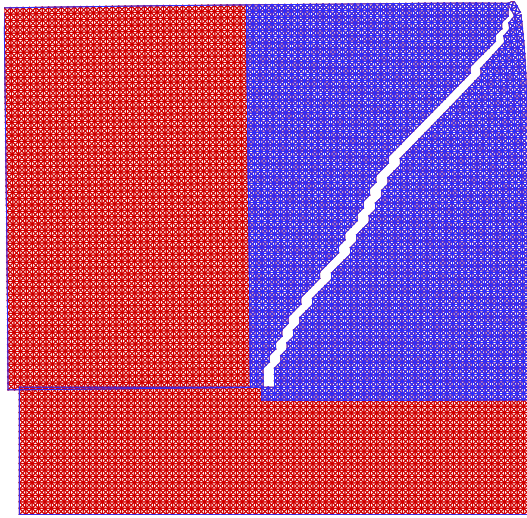
In all of the cases shown in Figure 2.12, the crack first propagates for a short distance at a right angle from the original crack path, and then zigzags through the inclined element edges and vertical edges in the meshes with a grid aspect ratio of 1 and 25/16 (Figure 2.12 (a), (c) and (d)), while it propagates primarily along the inclined element edges for the remaining case of grid aspect ratio 16/25, resulting in an apparently smoother crack path (Figure 2.12 (b)). Additional calculation for the 80×80 grid mesh is carried out using a different cohesive strength $T_n^{\max} = E/30$. The crack path is remarkably similar to the one with $T_n^{\max} = E/110$ case, especially at the beginning stage of crack propagation. A close comparison of the final fracture pattern for the three different mesh orientations is shown in Figure 2.13 (a). Clearly, the crack finds similar paths in meshes with different aspect ratio bias.

Two different sets of meshes of further refinement are tested, with 100×100 , 120×80 , 80×120 grids, and 120×120 , 150×96 , 96×148 grids, respectively. Each set of three meshes represent the three different aspect ratios discussed above. Although not all the results are reported here, the simulations demonstrate similar global crack paths for these settings, e.g., as shown in Figure 2.13 (b) for mesh with an aspect ratio of 1. The computational crack initiation times are summarized in Table 2.3.

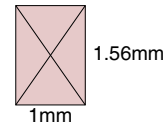
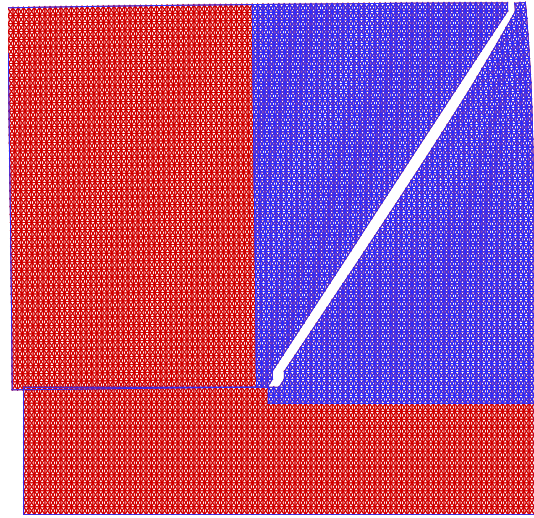
Table 2.3: Crack initiation time for different meshes

Mesh grid	Crack init. time (μs)	Mesh grid	Crack init. time (μs)	Mesh grid	Crack init. time (μs)
80×80	20.7	100×100	19.3	120×120	18.5
64×100	20.0	80×120	19.1	96×148	18.8
100×64	19.1	120×80	18.8	150×96	18.5

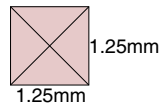
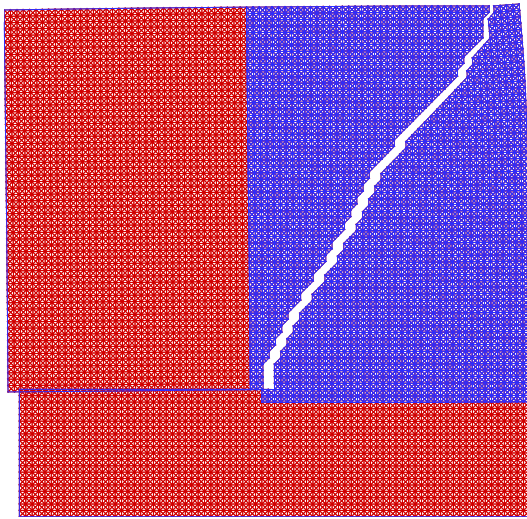
Crack length versus time is plotted in Figure 2.14 (a) for five typical meshes used in the study. Clearly, the crack evolution with time maintains a similar speed in all the cases investigated. When computing the crack speed using discrete data at each time step, local oscillation of relatively small amplitude occurs due to mesh discretization effect involved in crack propagation. In order to focus on the global crack speed variation trend instead of local oscillation, the smoothed crack tip speed is calculated by taking the derivative of a polynomial fitting curve of crack length.



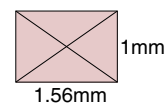
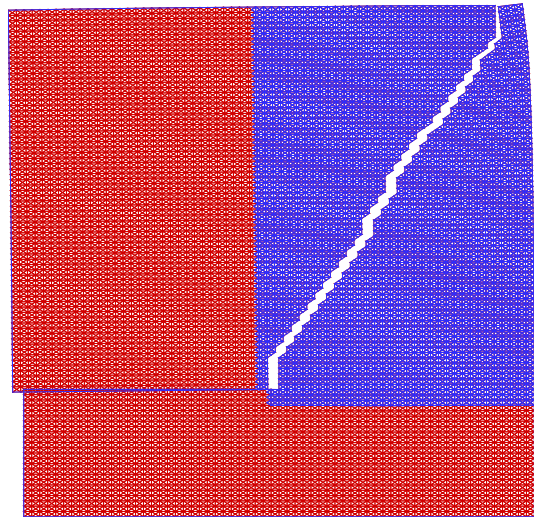
(a) 80×80 grid mesh



(b) 100×64 grid mesh



(c) 80×80 grid mesh



(d) 64×100 grid mesh

Figure 2.12: Fracture path for different mesh designs considering $G_{IIc} = G_{Ic}$. The blue elements denote the region with cohesive elements, and all simulations use cohesive strength $T_n^{\max} = E/110$ except for (c), which uses $T_n^{\max} = E/30$; (a) 80×80 grid; (b) 100×64 grid; (c) 80×80 grid; (d) 64×100 grid.

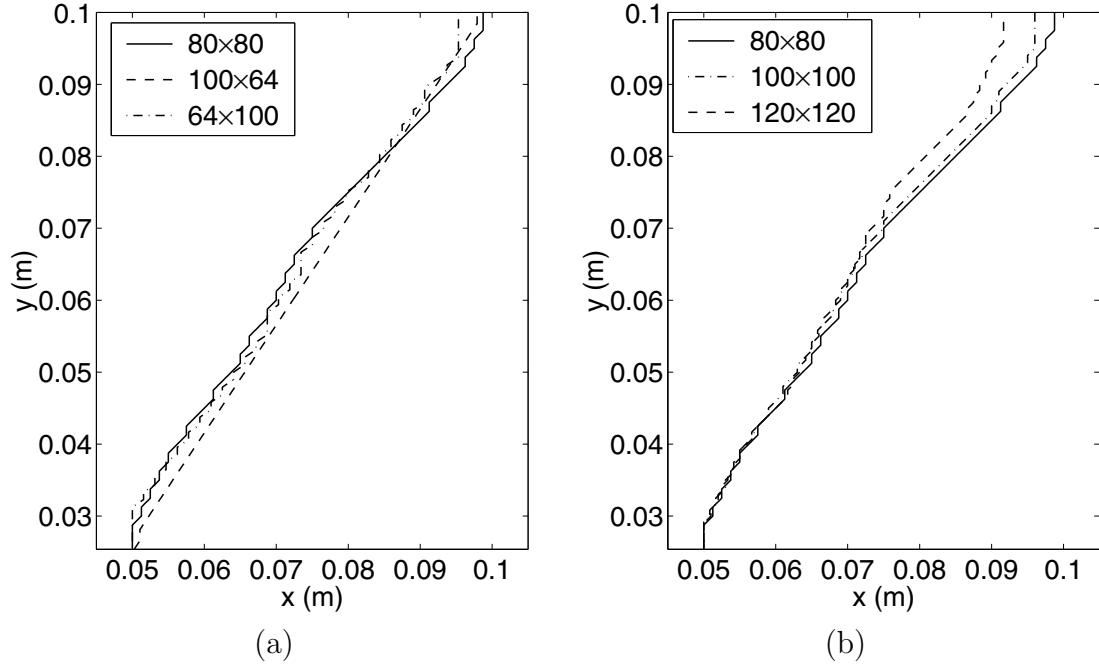


Figure 2.13: Influence of mesh discretization on dynamic fracture behavior; (a) final crack paths for the first set of mesh discretization with total number of 25,600 T6 elements, and different mesh orientations; (b) final crack paths for square shape grids with element sizes $h = 1.25, 1, 0.8\text{mm}$.

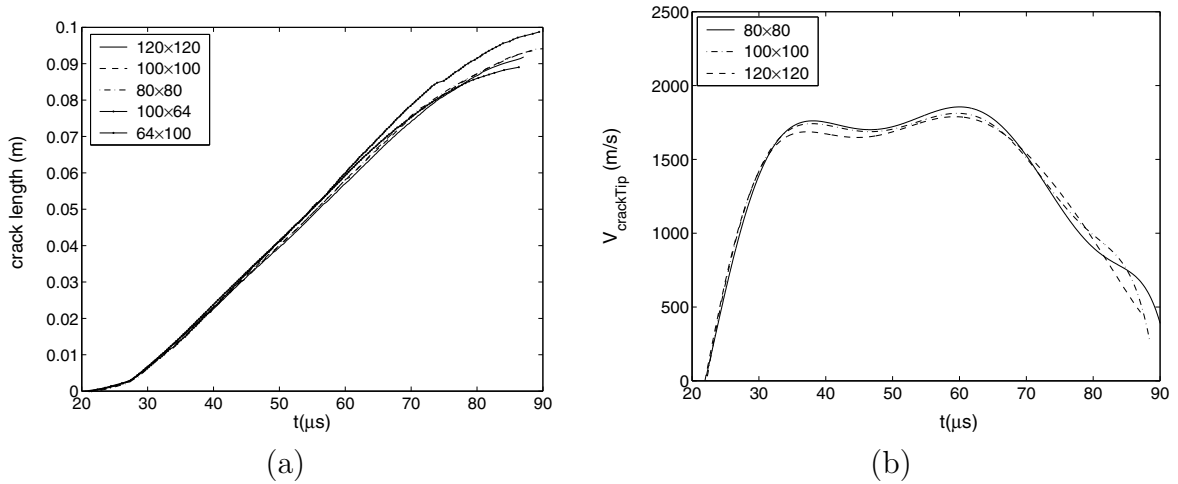


Figure 2.14: Comparison of fracture path for different meshes; (a) crack length growth history; (b) smoothed crack velocity history.

The crack tip velocity is thus plotted in Figure 2.14 (b). After crack initiation, the crack speed maintains a relatively steady speed of around 1800m/s , about 65% of the Rayleigh wave speed. This value is similar to that reported by [13].

Although the overall crack path follows a slanted direction, the initial crack

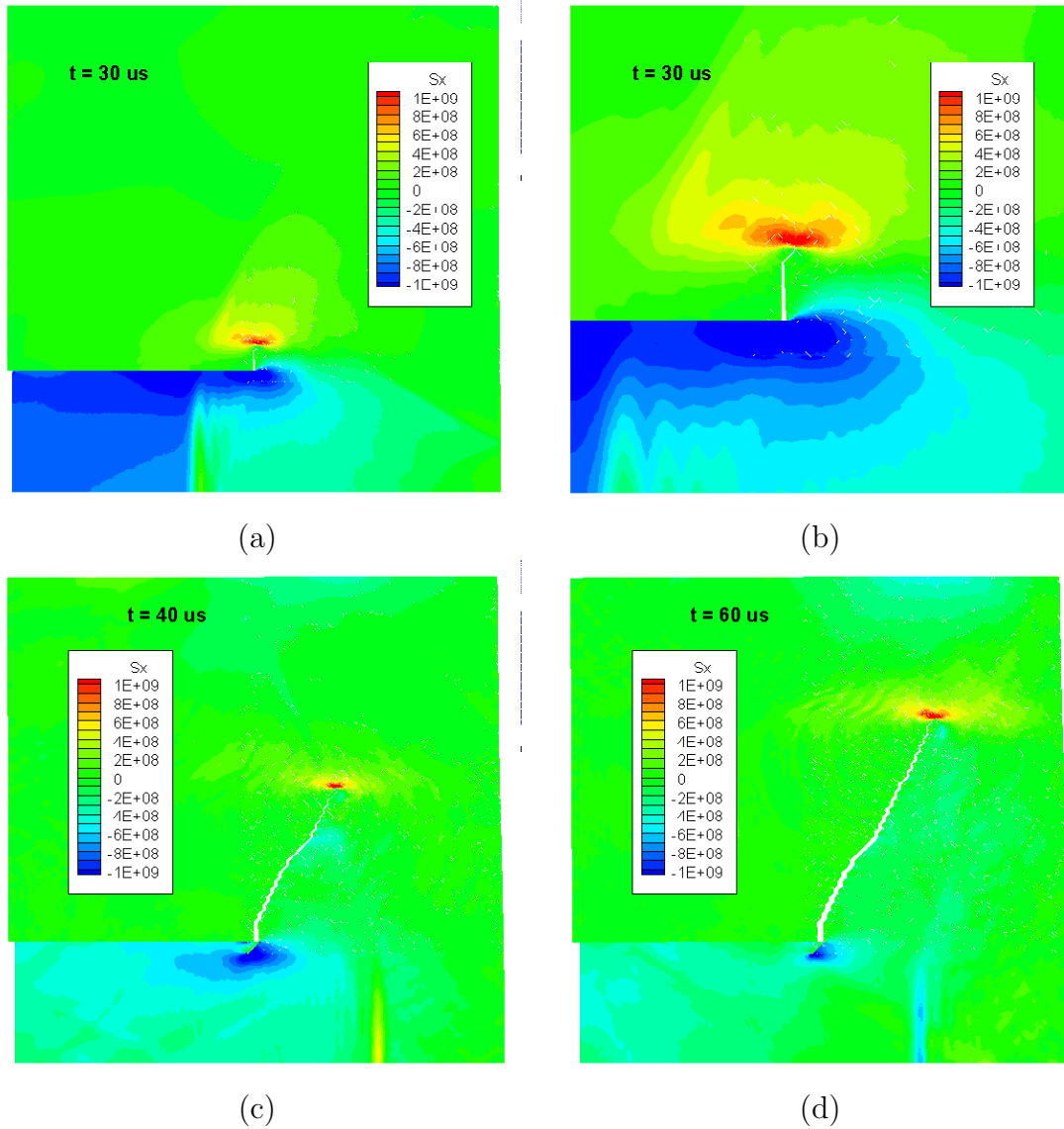


Figure 2.15: Stress field σ_x and crack evolution in a 120×120 grid mesh; (a) crack pattern at $t = 30 \mu s$ after crack propagation starts; (b) close-up of stress field at crack tip at $t = 30 \mu s$; (c) crack pattern at $t = 40 \mu s$; (d) crack pattern at $t = 60 \mu s$.

propagation always shows a short vertical segment in all of the mesh cases studied. Other researchers [56, 13] also reported similar results when using the cohesive model approach. This is not incidental, and the stress contour plots in Figure 2.15 illustrate the critical role of wave propagation and reflection on the crack propagation direction. When the load is applied along the left edge of the lower plate section (below the initial crack plane), it creates compressive waves that propagate continuously rightwards along the lower plate section. Before the first tide of stress waves reaches the initial crack tip, the stress distribution across the height direction of the lower section is fairly uniform, while the upper plate section remains stress-free. When the wave reaches the crack tip, the upper crack surface near the crack tip stays stationary, while the lower crack surface near the crack tip is under the influence of a rightward compressive wave. This creates a tearing effect at the crack tip. Afterwards, the waves continue to propagate rightwards in the lower plate section as compressive wave, and also propagate around the crack tip into the upper section (above the initial crack plane) of the plate. The stress waves along the upper crack surface are now tensile propagating towards the left edge. Therefore the upper and lower surfaces of the crack are subjected to the influence of stresses of opposite sign and direction along the Cartesian x coordinate, and a strong tearing effect is created at the crack tip. The principle tensile stress at the crack tip is thus in the x direction, and the crack tip begins to open up and propagate in vertical direction when the local stress built up is high enough to overcome the cohesive strength. This initiation time occurs around $19\mu s$ (Table 2.3). The crack maintains a vertical path until the reflective wave from the right boundary reaches the crack tip region. The additive stress wave is now tensile, and when it interferes with the initial crack tip stress field, the principle tensile stress is no longer in pure x direction, and thus results in a slanted crack path. The crack turning time for different meshes are reported in Table 2.4. Clearly, all of the cases indicate a similar time instant of around $28\mu s$, which is approximately the time needed for the first tide of the reflective waves to reach the crack tip:

$$t_{turn} \approx \frac{1.5 \times W}{C_d} = \frac{1.5 \times 0.1}{5654} = 26.5\mu s$$

where W is the width of the specimen.

Another interesting issue is the different toughness associated with Mode-I and Mode-II fracture modes. In section 2.6.2, we assumed that both the opening and sliding modes have the same fracture toughness. This assumption is not strictly true for real materials, which generally possess higher sliding toughness than opening tough-

Table 2.4: Crack turning time for different meshes (see Figure 2.15 (b)).

mesh grid	crack deviation time (μs)	mesh grid	crack deviation time (μs)	mesh grid	crack deviation time (μs)
80×80	28.4	100×100	28.2	120×120	28.3
64×100	29.9	80×120	29.7	96×148	30.1
100×64	27.8	120×80	28.1	150×96	28.4

ness. Material property manuals usually only report the mode I fracture toughness, as opening fracture is the dominant failure mode, and the experimental techniques for measuring the mode I fracture toughness are far more mature than those for the mode II toughness. To test how significant the aforementioned assumption influences the fracture behavior, we further carried out simulations using different sliding fracture toughness:

$$\begin{aligned}
 G_{IIc} &= 3G_{Ic}, & T_t^{max} &= T_n^{max} \\
 G_{IIc} &= 3G_{Ic}, & T_t^{max} &= 3T_n^{max}
 \end{aligned}$$

while the mode I fracture parameters are maintained the same as before. Figure 2.16 presents the crack trajectories in the two cases. Further comparison of these two specimens with $G_{IIc} = G_{Ic}$ specimen are summarized in Figure 2.17. Evidently, the simulated fracture paths (*cf.* Figure 2.16 (a) and (b), and Figure 2.17 (a)) using different G_{IIc} values are close, especially during the beginning stage of crack growth. It is easily understood that the overall crack velocity (Figure 2.17 (b)) is slower for simulations using higher G_{IIc} values, as increased toughness hinders crack propagation. However, the difference is minor and the overall trends of crack growths are similar. Within the limited scope of the present work, the underlying mechanism to explain the relatively minor influence of different sliding toughness is that when the crack advances, the local crack growth is controlled by the opening fracture mode, so that as long as the mode I toughness used in the simulations are the same, the fracture behaviors are similar. On the other hand, the mode toughness ratio $G_{IIc}/G_{Ic} = 3$ used in the simulation is moderate. Other mode toughness ratios are tested, and the trend of crack paths (including that shown in Figure 2.17) suggests that with higher sliding toughness and higher sliding strength, the crack growth angle, particularly the part towards the “boundary”, is closer to an overall angle of 70° , the experimental result. However, this issue certainly warrants further investigation.

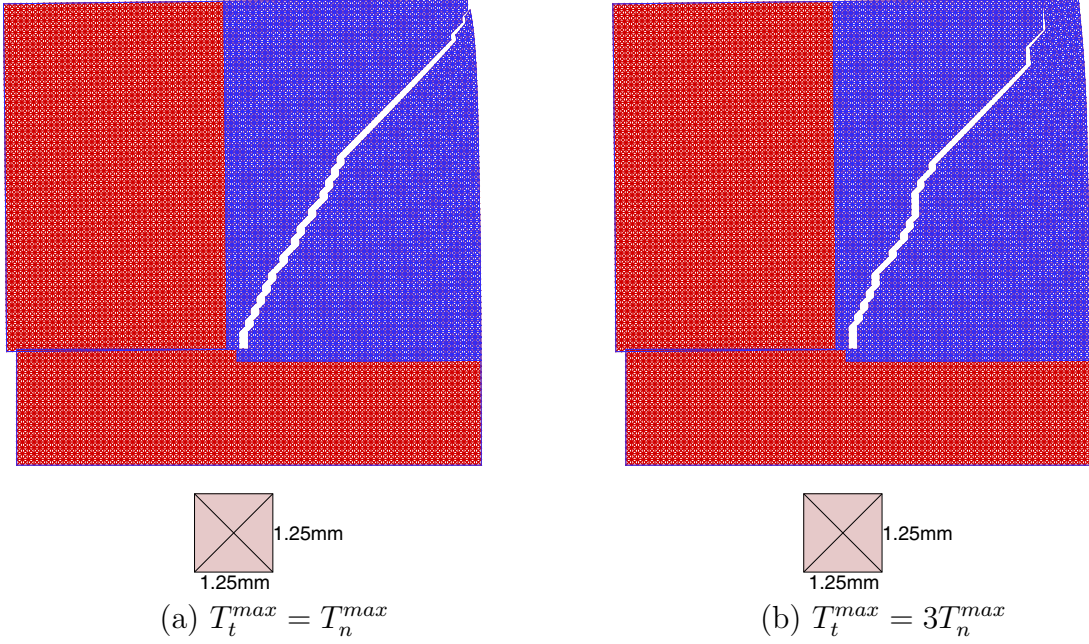


Figure 2.16: Crack path for fracture toughness $G_{IIc} = 3G_{Ic}$. The blue elements denote the region with cohesive elements and simulations are performed using 80×80 grid meshes; (a) $T_t^{max} = T_n^{max}$; (b) $T_t^{max} = 3T_n^{max}$.

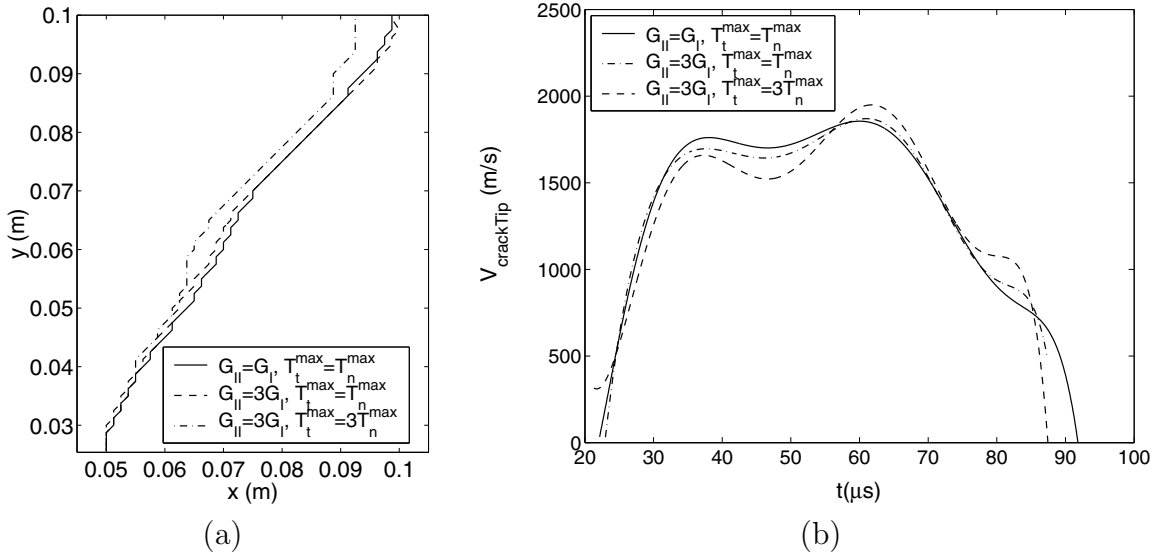


Figure 2.17: Influence of different mode II and mode I fracture toughness ratios: $G_{IIc} = G_{Ic}$ and $G_{IIc} = 3G_{Ic}$; (a) final crack paths; (b) smoothed crack velocity history.

2.6.4 Influence of Material Variation

Following the homogeneous material example, this section extends the study to simulation of the same experimental setting with graded material properties. For

the sake of comparison with the previous results, the hypothetical material properties used in this section are conceived based on the homogeneous maraging steel described in Table 2.2. Although the variation of a wide range of material property parameters will contribute to changing fracture behavior, this study focuses on two of the most important material properties in dynamic fracture problem. One is the fracture toughness, as it is directly related to the material resistance capacity; and the other is material stiffness, as it is related to wave propagation velocity and local stress level. To isolate the influence of different parameters on the fracture behavior, first the simulation is carried out with graded fracture parameters (including fracture toughness and cohesive strength), and next with both graded Young’s modulus and fracture parameters (including fracture toughness and cohesive strength).

Graded cohesive strength and fracture toughness. Consider a linear variation of fracture toughness G and cohesive strength T_n^{max} inside the cohesive region along the Cartesian x direction, i.e., $G(x)$ and $T_n^{max}(x)$. The material properties are given in Table 2.5, where subscript 1, 2 and *tip* denote the left side, right side and the initial crack tip of the specimen. The material properties for the homogeneous specimen are also included. For the graded specimens, the bulk material remains homogeneous, and the fracture toughness gradation within the cohesive element region is linear. The Mode-I and Mode-II fracture toughness and cohesive strength are assumed to be the same, i.e., $G_{Ic} = G_{IIc}, T_n^{max} = T_t^{max}$. The specimen with $G(W) = 2G(0)$ is denoted as “LHS weaker” case, while the other one with opposite material gradation profile (i.e., $G(0) = 2G(W)$) is denoted as “RHS weaker” case.

Since the bulk material is homogeneous, the wave propagation speed is constant for all three cases, and the stress carried by the wave propagation builds up at the crack tip at the same rate. The critical stage of crack initiation depends on the local material toughness, and presumably takes place earlier for the specimen weaker at the initial crack tip. The results are compared in Figure 2.18 for the graded specimens with the homogeneous case of same mesh discretization and time step control.

As expected, the specimen with lower cohesive strength at crack tip (“LHS weaker” case in Figure 2.18 (b)) experiences crack initiation earlier. For this material profile, the cohesive strength is the same as in the homogeneous case, hence the crack initiation times for the two cases are almost identical ($t_{init} = 20.7\mu s$ for both cases, see Table 2.5). The crack initiation time for “RHS weaker” specimen is around $t_{init} = 26.6\mu s$, close to the time when the reflected waves reach the crack tip, and therefore the crack starts to propagate at a slanted angle, instead of along the vertical

Table 2.5: Material property for pre-notched plate with graded fracture toughness, which is subjected to mixed-mode dynamic loading. The bulk material is homogeneous.

Property	Material Gradation		
	Homog.	FGM-LHS weaker	FGM-RHS weaker
E (GPa)	190	190	190
C_d (m/s)	5654	5654	5654
G_1 (kJ/m ²)	22.2	22.2	44.4
G_{tip} (kJ/m ²)	22.2	22.2	44.4
G_2 (kJ/m ²)	22.2	44.4	22.2
T_1^{max} (GPa)	1.733	1.733	3.466
$T_{\text{tip}}^{\text{max}}$ (GPa)	1.733	1.733	3.466
T_2^{max} (GPa)	1.733	1.733	1.733
λ_{cr}	0.01	0.01	0.01
t_{init} (μs)	20.7	20.7	26.6

direction as in the homogeneous case. One observes that as the fracture toughness is graded, the crack tends to propagate more into the weaker region (Figure 2.18 (a)), while the homogeneous case is in between of the two graded cases.

The influence of fracture toughness on dynamic crack propagation can also be observed in the crack speed evolution profile (Figure 2.18 (c) and (d)). For the homogeneous case, the average fracture toughness is lower than the graded material cases, resulting in lower resistance against crack advance, and thus the overall crack speed is highest among the three. The ‘‘LHS weaker’’ specimen possesses similar material properties compared to the homogeneous case at the region where the crack starts to propagate, therefore the initial crack speed is also similar to that of the homogeneous one. As the crack propagates into tougher regions, the crack speed becomes slower than that of the homogeneous case. On the other hand, the ‘‘RHS weaker’’ specimen exhibits the reverse behavior: the crack speed is slower in the beginning, and then accelerates as the crack advances into the region of lower fracture resistance.

Graded modulus, cohesive strength and fracture toughness. The next set of simulations consider linearly graded Young’s modulus E , fracture toughness G and cohesive strength T_n^{max} along the Cartesian x direction, i.e., $E(x)$, $G(x)$ and $T_n^{\text{max}}(x)$.

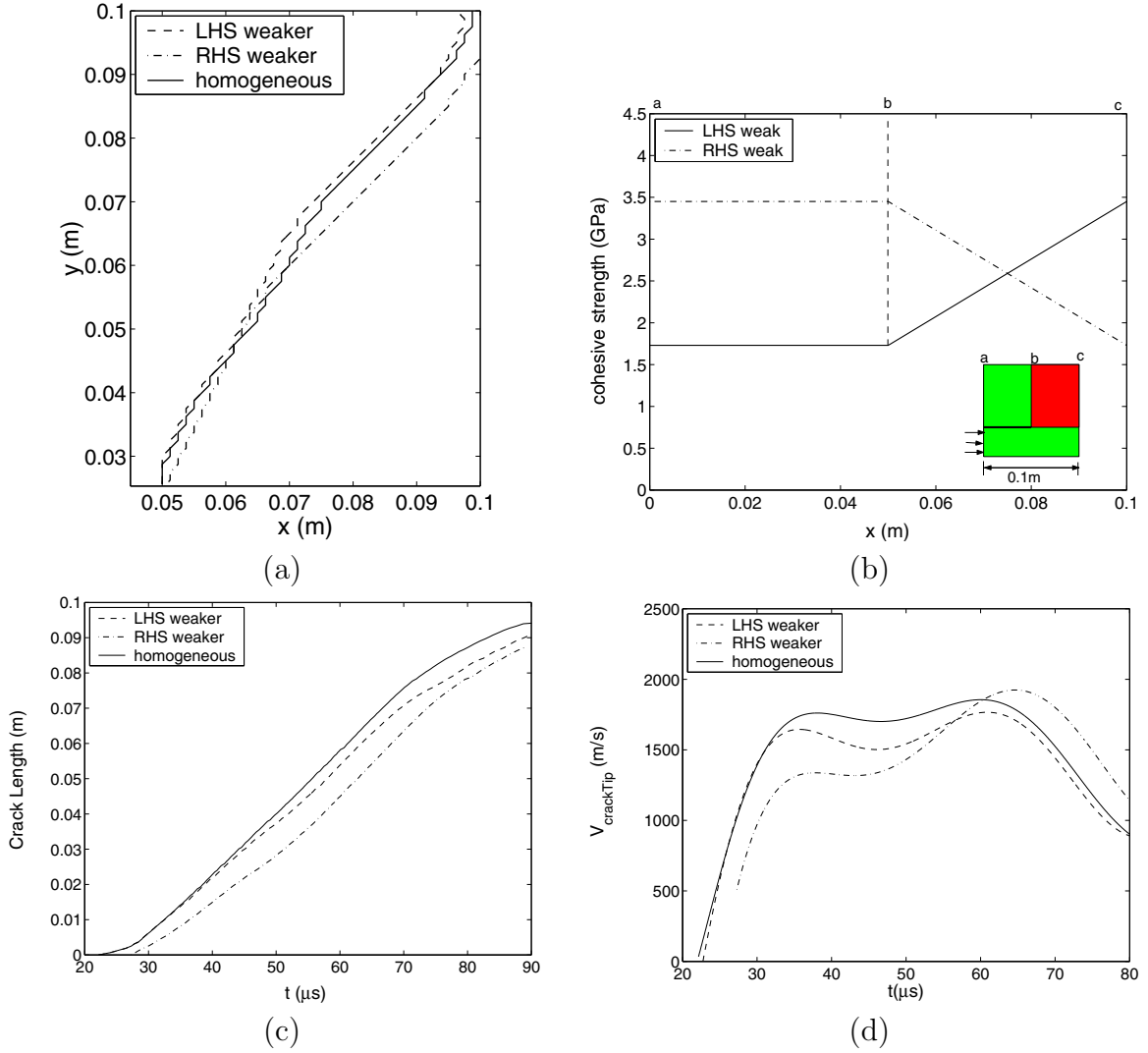


Figure 2.18: Comparison of fracture path for different cohesive toughness and strength gradation profiles. Results obtained using 80 by 80 grid mesh; (a) final crack paths; (b) two cohesive strength gradation profiles. cohesive strength varies between $E/110$ to $E/55$ within the cohesive region; case 1: fracture toughness and cohesive strength are lower at LHS; case 2: fracture toughness and cohesive strength are lower at RHS; (c) crack length versus time; (d) crack tip speed versus time.

The material properties are given in Table 2.6. The average material properties for the two graded specimens are the same as those of the homogeneous case, and the specimen which possesses E and G values at the right-hand-side twice as high as the left-hand-side is denoted as “LHS softer” case, while the other one with opposite material gradation profile is denoted as “RHS softer” case. Since the bulk material is graded, the wave propagation speed varies for the FGM case, while it is constant for the homogeneous case.

Table 2.6: Material property for pre-notched plate with graded modulus, fracture toughness and cohesive strength, which is subjected to mixed-mode dynamic loading.

Property	Material Gradation		
	Homog.	FGM-LHS softer	FGM-RHS softer
E_1 (GPa)	190	127	253
E_{tip} (GPa)	190	190	190
E_2 (GPa)	190	253	127
G_1 (kJ/m ²)	22.2	14.8	29.6
G_{tip} (kJ/m ²)	22.2	22.2	22.2
G_2 (kJ/m ²)	22.2	29.6	14.8
T_1^{max} (GPa)	1.733	1.155	2.301
$T_{\text{tip}}^{\text{max}}$ (GPa)	1.733	1.733	1.733
T_2^{max} (GPa)	1.733	2.301	1.155
t_{init} (μ s)	20.7	24.8	18.2

The crack paths and evolutions with time are plotted in Figure 2.19 for the graded specimens as well as the homogeneous case. Apparently, the crack tends to grow into the weaker region (Figure 2.19 (a)). After the velocity loading is applied to the lower left surface, the stress waves propagate rightwards and the stress concentration builds up at the crack tip. Since the material fracture toughness at the initial crack tip ($x = 0.05m$, $y = 0.0275m$) are the same for all three cases, the crack initiation time is primarily determined by the rate of stress concentration at the crack tip. Because the material stiffness varies along the x direction, the stress waves propagate at varying speeds. For the “RHS softer” specimen, the average stiffness between the left surface (where the load is applied) and the crack tip is higher than the other two cases, and consequently the average wave speed is faster. Therefore, it takes shorter time for the crack tip tensile stress to reach the critical value for this case than the opposite material gradation case, and thus the crack initiates earlier. The crack initiation time for the “RHS softer” specimen ($T_{\text{init}} = 18.2\mu\text{s}$) is $6.6\mu\text{s}$ earlier than the “LHS softer” specimen ($T_{\text{init}} = 24.8\mu\text{s}$), while the homogeneous case exhibits a crack initiation time in between ($T_{\text{init}} = 20.7\mu\text{s}$), as shown in Table 2.6 and Figure 2.19 (c). After crack initiation, two factors control crack propagation speed: the local fracture toughness represented by the cohesive properties, and the crack extension driving force, which is related to the material stiffness, since the stress level resulting from forced displacement is lower in compliant material than in stiffer

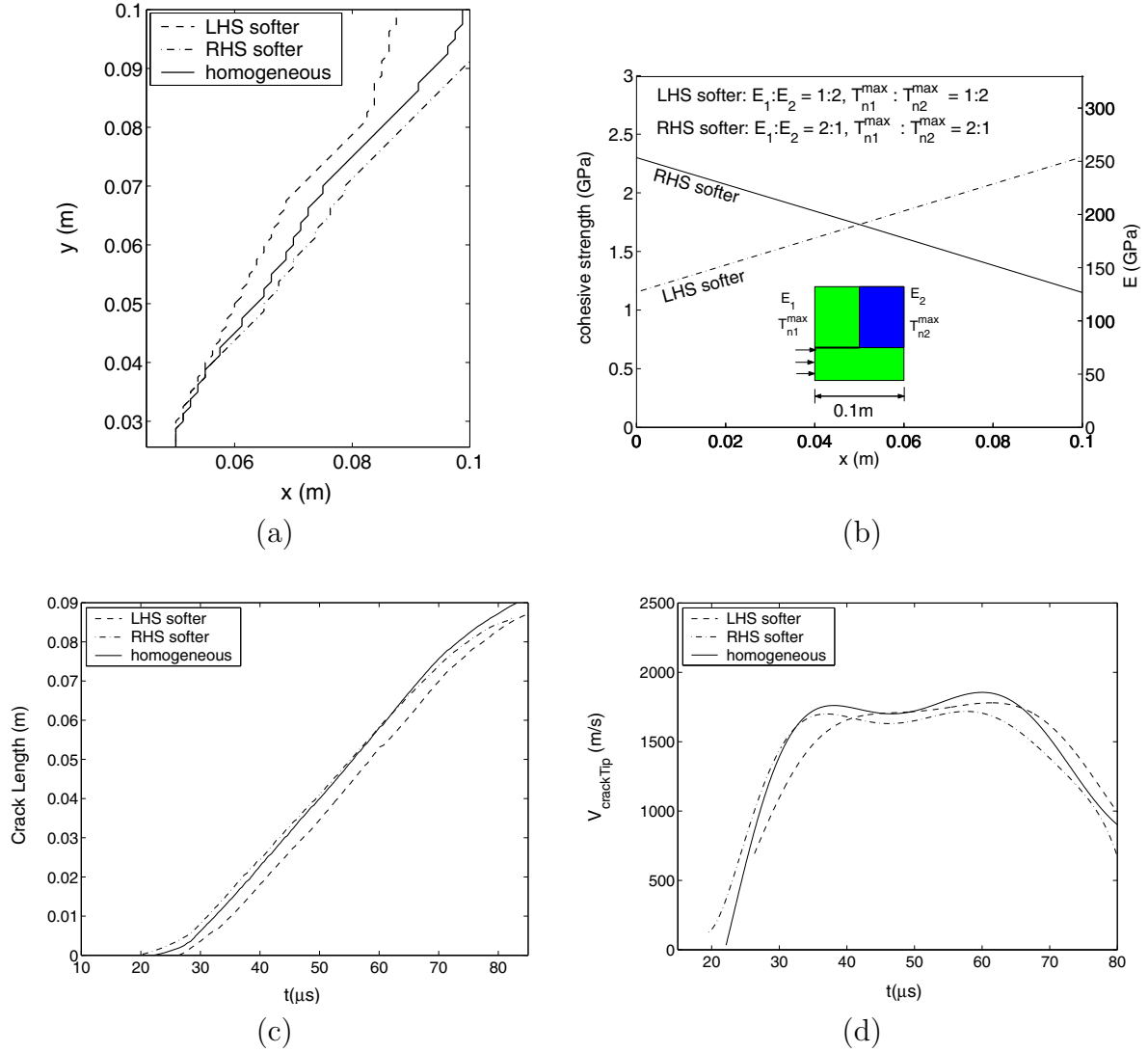


Figure 2.19: Comparison of fracture paths for graded stiffness and graded fracture toughness along the Cartesian x direction. Results obtained using 80 by 80 grid mesh; (a) final crack paths; (b) material gradation profiles for E and cohesive strength. Case 1: material is softer and has lower fracture toughness at LHS; case 2: material is softer and has lower fracture toughness at RHS; average E and T_n^{max} are kept the same as the homogeneous case; (c) crack length versus time; (d) crack tip speed versus time.

material. Therefore, when the crack in “RHS softer” specimen grows along a slanted direction into materials of gradually lower fracture toughness and lower stiffness, the lower fracture resistance tends to accelerate crack propagation, while the lower stress level accompanied by the compliant material tends to decelerate crack extension. The two effects partly counteract each other. Similar effects are in action in the reversed material gradation profile case (“LHS softer” specimen). Therefore, it is not

surprising that the difference in crack propagation velocities for the two cases and the homogeneous case is relatively small compared to the previous test with only cohesive strength graded (compare Figure 2.18 (d) and Figure 2.19 (d)).

Chapter 3

Topology-based Data Structure Representation

A common approach to insert cohesive elements in finite element meshes consists of adding discrete interfaces between bulk elements. The insertion of cohesive elements along bulk element interfaces for fragmentation simulation imposes changes in the topology of the mesh. This Chapter presents a unified topology-based framework for supporting both intrinsic and extrinsic fragmentation simulations, being able to handle two- and three-dimensional models, with any order of finite elements. We represent the finite element model using a compact and complete topological data structure, which is capable of retrieving all adjacency relationships needed for supporting the simulation. Moreover, we introduce a new systematic topological classification of fractured facets, which is composed by a set of procedures that consistently perform all the topological changes needed to update the model. The proposed topology-based framework is general and ensures that the model representation remains valid during fragmentation, even for complex crack patterns. The framework effectiveness is illustrated by arbitrary insertion of cohesive elements in different finite element meshes, including both two- and three-dimensional models.

3.1 Introduction

Fracture and fragmentation, including dynamic events [24, 16] have a broad range of engineering applications [4]. In general, such phenomena involve switching from a continuum to a discrete discontinuity, which can be investigated by means of a cohesive zone model (CZM) of fracture. The CZM can be computationally simulated either by of enrichment functions [13] or inter-element techniques [116, 117]. The latter is the approach of choice in this work, i.e., cohesive elements are inserted between bulk (or volumetric) finite elements. We distinguish two types of cohesive elements: intrinsic and extrinsic. In the former case, the cohesive elements are inserted *a-priori*, i.e., at the pre-processing stage (before the simulation starts). In the later case, the cohesive elements are inserted adaptively during the course of the

finite element analysis, i.e., the cohesive elements are inserted when needed, and where needed. The present data structure handles both types of cohesive elements, either in two-dimensional (2D) or three-dimensional (3D) models, with Lagrangian-type finite elements of any order.

During the course of extrinsic fragmentation analysis, new cohesive elements are adaptively inserted at element interfaces, thus imposing changes in the topology of the mesh. In order to efficiently treat these topology changes, access to a topological data structure is needed. In fact, several finite element applications, especially adaptive analysis, require a topological data structure that provides adjacency information among the mesh topological entities [12, 39, 89, 90, 72, 61, 17, 44]. For instance, in adaptive fragmentation simulations, element connectivity varies as new cohesive interfaces are inserted. The insertion of a cohesive element may require the duplication of nodes. Whether a node has to be duplicated depends on the topological classification of the facet along which the cohesive element has to be inserted [75, 76, 18]. Intrinsic cohesive zone models can also benefit from a topology-based framework. Although the regions where to insert the cohesive elements are chosen in advance, the support of a topological data structure allows the use of conventional mesh generators to get the initial bulk element mesh. The cohesive elements can then be automatically inserted within the selected regions (e.g. along a line or a rectangular area for 2D applications; and along a plane or a volumetric region for 3D applications).

The storage space usually required by a complete topological data structure can become a crucial problem [12, 39] for finite element mesh representation. To address this problem, we have introduced a new compact adjacency-based topological data structure for finite element mesh representation - see our previous work [18, 19]. The proposed data structure requires reduced storage space while being complete, in the sense that it preserves the ability to extract all topological adjacency relationship among the mesh entities in time proportional to the number of retrieved entities.

In this Chapter, we explore the use of the Topological data Structure (TopS) proposed in [18, 19] for supporting fracture and fragmentation simulations using cohesive zone modeling. We introduce a new topology-based algorithm that systematically classifies fractured facets (i.e., facet along which fracture has occurred), and identifies the topological modifications needed to preserve model consistency. The algorithm follows a set of procedures that consistently perform all the topological changes needed to update the model. The same set of procedures can be used for any type of finite element mesh, for both two- and three-dimensional models, including linear, quadratic, and higher order elements. One of the main advantages of this approach is

that the same topological framework is employed for consistently supporting a variety of fragmentation simulations, despite the model dimension and the element order.

This Chapter is organized as follows. Section 3.2 discusses the interface models for cohesive fracture. Section 3.3 discusses previous works on topological data structure for mesh representation and for fragmentation simulations. Section 3.4 presents the topological data structure framework adopted in this work. Section 3.5 illustrates elements that are presently available in the data structure and shows how to incorporate a new element using the concept of element template. Section 3.6 (conceptually, the main section of the Chapter) addresses topological classification of facets, which define the fracture path. Section 3.7 provides many numerical results demonstrating that the elapsed time scales linearly with respect to the number of cohesive elements inserted. In Section 3.8, applications of the proposed framework in actual dynamic fracture analysis are demonstrated through a 2D finite element simulation, which is similar to the example given in Section 2.4 but uses extrinsic CZM instead of the intrinsic one. Finally, concluding remarks and suggestions for future work are given in Section 3.9.

3.2 Intrinsic and Extrinsic Cohesive Models

A preliminary discussion on both intrinsic and extrinsic CZMs is presented in Section 1.2. In general, the so-called intrinsic models assume that all cohesive elements are embedded in the discretized structure prior to the beginning of the simulation, and thus the mesh connectivity remains unchanged during the whole simulation process [116, 99, 100, 32, 113, 109]. From the mesh representation point of view, intrinsic models allow easy implementation. However, they introduce artificial compliance, which depends on the area of cohesive element surfaces introduced and the cohesive law parameters relative to bulk element property, e.g. the ratio of cohesive strength to elastic modulus [56]. If the crack grows along a pre-defined path with relatively few number of cohesive elements, the adverse effect is relatively minor; while for simulations involving cohesive elements inserted in a large area or volume, the adverse effect can be more pronounced and lead to convergence problems in implicit simulations [99].

On the other hand, the so-called extrinsic models require adaptive insertion of cohesive elements (in space and time) in the finite element mesh [74]. This usually requires an elaborate updating scheme for the modified mesh by inserting new nodes

and interface elements [18, 19]. Therefore, the geometrical and topological (e.g. connectivities) information need to be updated as the simulation progresses. The extrinsic model avoids the artificial softening effect present in intrinsic models.

The above observations regarding intrinsic and extrinsic models are of a general nature, and both models are of interest in this work. Different types of CZMs within each group are developed based on various considerations, and one may be preferred over the other depending on the problem. The topological data structure (TopS) used in this work applies to both models. The advantage for extrinsic models is obvious. In regard to intrinsic models, the data structure can be used to generate cohesive elements within pre-specified regions of an existing mesh. For instance, in assessing cracks in materials with microstructure, the data structure can be of great help in generating intrinsic elements around particles [64] or grain boundaries [46].

3.3 On Topological Data Structures

Topological data structures define a model by means of a set of topological entities. These entities should provide an unambiguous abstraction of the underlying model [17,30-32]. For finite element mesh representation, the usually defined topological entities include region, face, edge, and vertex [12, 39, 89, 90]. Regions are three-dimensional entities bounded by a set of faces, which are two-dimensional. Edges are one-dimensional entities that delimit the faces, and vertices are zero-dimensional entities that represent the boundary of edges and are associated to the mesh nodes. For three-dimensional (3D) meshes, each region corresponds to a finite element and internal faces represent the interface between two elements. For two-dimensional (2D) meshes, each face corresponds to a finite element and internal edges represent the interface between elements.

Previous works have proposed the use of topological data structures, originally designed for solid modeling [106, 107, 62], to support fracture simulation [105, 63]. The result is a highly integrated framework where mesh entities are related to the corresponding geometric model entities, but such topological data structures impose a prohibitive cost of storage space for large finite element meshes. In order to minimize the required storage space, researchers have been engaged in the development of reduced (compact) topological data structures [12, 39]. The main idea consists of not explicitly representing all the topological entities. Representation of implicit entities are created, as required, on-the-fly. This approach tends to reduce the

storage space needed to represent the mesh but faces the challenge of appropriate management of implicit entities in order to maintain the model consistency [12]. As an alternative solution, some topological data structures have been specifically designed for attending the needs of particular mesh generation algorithms [61, 17] and analysis applications [44]. In references [89, 90], a different approach has been proposed. Instead of using a particular data structure, the authors have presented an algorithm-oriented mesh database. They are then able to dynamically extract different meshes representation according to the application needs in terms of adjacencies. In general, this is achieved by extracting and explicitly storing the adjacency relationships needed by a particular application, resulting in efficient representations for querying operations. However, this approach still faces the challenge of keeping the whole data structure consistent when modifying the mesh. Moreover, explicitly storing all the needed sets of adjacencies may demand a large amount of memory space (see Garimella [39] for a few comparisons). It might be better to efficiently extract each relationship just when required.

Previous reduced topological data structures have represented implicit faces and edges by their bounding nodes [12, 39, 89, 90], but those representations are ambiguous for fragmentation simulation. Finite element models for fragmentation simulation require the representation of cohesive elements [75, 76, 80, 47], which may have distinct edges with the same bounding nodes. Pandolfi and Ortiz [75, 76] have proposed topological data structures for supporting fragmentation simulations. Their work focused specifically on representing quadratic tetrahedral meshes. They have opted for explicitly representing all topological entities and their corresponding adjacency relationships, thus ending up with data structures that require large amounts of storage space.

Notice that the use of region, face, edge, and vertex as the defined topological entities imposes challenges for generalizing previous proposals [12, 39, 89, 90, 105, 63]. If this set of topological entities is used for designing a unique topological framework to represent both 2D and 3D meshes, one faces the problem of managing different semantics associated to faces and regions. Faces, in 2D, represent finite elements, while in 3D they represent the boundary of finite elements. Similarly, in 3D, regions represent elements but are meaningless for 2D meshes. It would be better if the semantics associated to each topological entity did not change, despite the mesh dimension. This is a major contribution of the topological data structure, TopS [18, 19], which is employed here to support the topological framework for fragmentation simulations.

3.4 Adjacency-based Topological Data Structure (TopS)

In order to support both intrinsic and extrinsic fragmentation simulations, we use a novel compact adjacency-based topological data structure (TopS) that requires small storage space while providing access to all adjacency relationships in time proportional to the number of retrieved entities. This basic data structure is presented in detail in reference [18, 19]. Here, we briefly describe its main concepts and focus on its use for supporting large scale finite element fragmentation simulations.

3.4.1 Topological Entities

TopS was designed to represent meshes with any type of elements defined by templates of ordered nodes. Therefore, it defines a new set of topological entities, which is used to describe both 2D and 3D models. It explicitly represents only two topological entities: element and node. The element is an abstract entity that represents finite elements (any type and order). The node represents finite element nodes (both corner and mid-side nodes). Each element has references to its boundary nodes and to the adjacent elements. The element is specialized for each type of finite element. For instance, a quadratic tetrahedral finite element would have ten boundary nodes and four adjacent elements. Each node, besides its position, keeps a reference to one of its incident elements.

TopS also defines and implicitly represents other topological entities. Facet represents the interface between two elements. Edge represents a one-dimensional entity and is bounded by two vertices. Vertex represents a corner node (there is no vertex associated to a mid-side node). Thus, essentially, vertex is a node, but not every node is a vertex. An important point to note is that, for being able to handle both 2D and 3D meshes, the facet always represents the interface between two elements. Thus, for 3D models, a facet corresponds to a two-dimensional entity and is defined by a cyclic set of edges. For 2D meshes, it corresponds to a one-dimensional entity and is defined by a unique edge. Facets resting on the model boundary have only one interfacing element.

In order to facilitate retrieving topological adjacency relationships, TopS also defines and implicitly represents oriented topological entities, namely facet-use, edge-use, and vertex-use, associated to the use of facets, edges, and vertices by an element, respectively. Each finite element in isolation is composed by a set of facets, edges,

and vertices. These local entities are labeled by identification numbers (id's). The topology of each element is known in advance and depends only on the element type (e.g. T3, T6, Tetra4, Tetra10). Consequently, for each type of element, we define its element template [12]. Based on an element template, we can extract all adjacency relationships relating the local entities of such an element type. The local facets, edges, and vertices of an element in isolation correspond, respectively, to the use of facets, edges, and vertices of the mesh by that element. Therefore, the element template provides access to adjacency relationships relating entity-uses within an element.

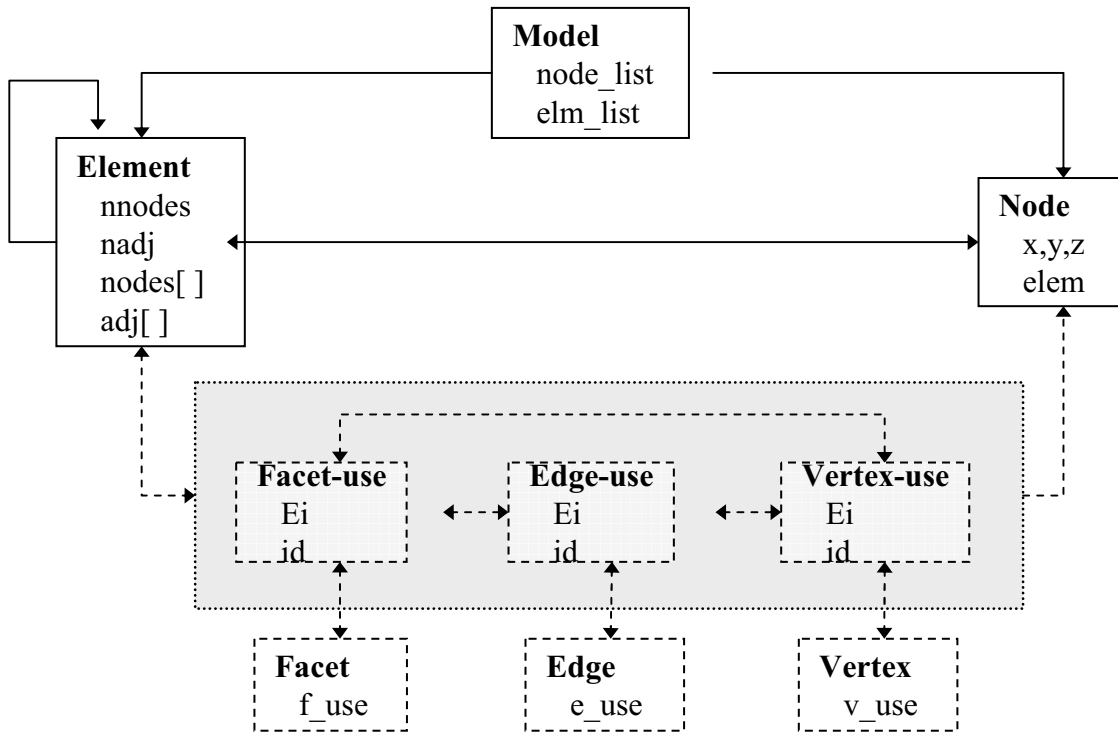


Figure 3.1: Schematic representation of topological entities in the data structure (TopS). Solid boxes represent explicit entities and dashed boxes represent implicit entities. Solid arrows represent explicitly stored adjacency and dashed arrows represent implicitly stored adjacency, which are extracted based on the element templates.

Element and node are explicitly represented by abstract types. Each element or node has to be allocated and included in the model. Facet, edge, vertex, and their associated uses, are implicitly represented and retrieved, when required, on-the-fly. To

easily handle these implicit entities, TopS represents them as concrete types, being treated as ordinary values, similarly to any other built-in type of a programming language. By using concrete types, we avoid the need of dynamic allocation while manipulating implicit entities: they are returned by value and allocated on the stack, which greatly simplifies managing entity uniqueness and lifetime. Each implicit entity is represented by integer values packed in a 32-bit word [19]. Each facet-use, edge-use, or vertex-use is represented by a reference to the element (E_i) using the entity and a local number (id) that identifies the corresponding entity within the element, (E_i, id). Each facet, edge, or vertex is simply represented by one of its use. One should note that by representing edges and facets in this way, two different edges (or facets) sharing the same bounding nodes, a quite common topological configuration in fractured models, have different representations because they are associated with different edge-uses (or facet-uses). A main drawback of previous reduced representations is to rely implicitly on the bounding nodes [12, 39, 89, 90], thus being unable to distinguish the two different edges (or facets).

The diagram in Figure 3.1 shows the entities represented by the data structure, together with the stored data and the directly retrieved topological adjacency. From the model, we have access to the set of nodes and elements that compose the mesh. From each element, we can directly access the adjacent elements and the boundary nodes. Conversely, from each node, we access an incident element. Based on the element template, from an element, we can also access its associated facet-uses, edge-uses, and vertex-uses, thus having access to facets, edges, and vertices. From each entity-use, we can also access its boundary nodes.

3.4.2 Adjacency Relationships

There are a total of twenty-five adjacency relationships among the five defined topological entities (element, node, facet, edge, and vertex), as illustrated by Figure 3.2. As shown by Celes et al. [18], the data structure is capable of retrieving any of these relationships in time proportional to the number of retrieved entities. Three of them are of particular interest for fragmentation simulations, and are marked by thicker lines in Figure 3. These are the relationships that provide access to all the adjacent elements of a given facet, edge, or vertex.

Finding the adjacent elements of a given facet, edge, or vertex corresponds to retrieving all the uses associated to the given facet, edge, or vertex, respectively. Based on the data structure representation, together with the element templates,

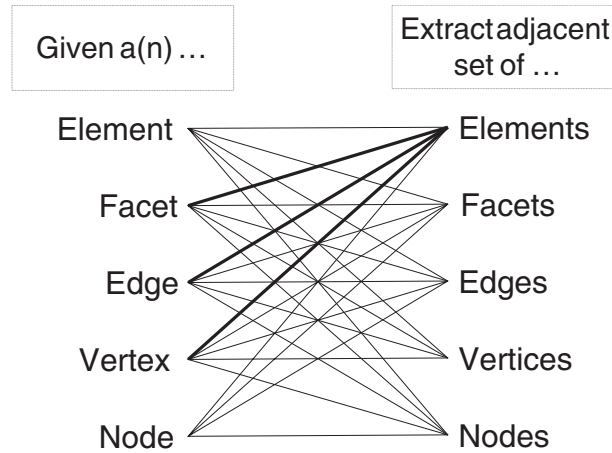


Figure 3.2: The twenty-five topological adjacency relationships defined among the data structure topological data. Three of them are of special interest for fragmentation simulations: the two elements adjacent to a given facet, the set of elements adjacent to a given edge, and the set of elements adjacent to a given vertex.

these sets of uses can be efficiently retrieved:

- *Uses of a facet:* given a facet, we first access one of its uses from its representation. Then, with the referenced element and the local facet id, we access the other use of the same facet, by using the adjacency information stored in the element representation.
- *Uses of an edge:* given an edge, we first access one of its uses from its representation. Then, based on the element template, we access the adjacent facet-uses within the element. By using the adjacency information stored in the element, we can reach each adjacent element and then access the uses of the corresponding edge. The procedure is repeated until all adjacent elements are visited.
- *Uses of a vertex:* given a vertex, we first access one of its uses from its representation. Then, based on the element template, we access the set of adjacent facet-uses within the element. By using the adjacency information stored in the element, we can reach each adjacent element and then access the uses of the corresponding vertex. The procedure is repeated until all adjacent elements are visited.

It is important to note that these sets of uses are all retrieved based on the adjacency information provided by the element representation, which provides access

to the adjacent element. Once we have the set of uses, we can have access to the adjacent elements: it suffices to access the element associated with each one of the retrieved entity-use (facet, edge, or vertex).

3.5 Finite Elements for Fragmentation Simulation

In order to handle fragmentation simulation, we have added support for different types of finite elements in the data structure. Previous proposals [75, 76] have opted for identifying cohesive elements as attributes attached to the facets of bulk elements. We have opted for explicitly representing the cohesive elements. In this way, cohesive elements are treated as any other type of element, resulting in a more flexible and concise data structure. As an example of such flexibility, cohesive elements can hold application attributes, as any other element. Moreover, with respect to their representation in the data structure, the same bulk element type can be used for analysis other than fragmentation simulation. Similarly, the interface elements (between bulk elements) can be used for any analysis regarding interfacial behavior (e.g. non-cohesive).

3.5.1 Adjacency Relationships

Figure 3.3 illustrates a few types of finite elements added for fragmentation simulation. For instance, for 2D simulation, we have added support for both linear and quadratic triangular and quadrilateral element (T3, T6, Q4, and Q8), together with the two corresponding cohesive elements: the cohesive element with linear edge (CohE2) and the cohesive element with quadratic edge (CohE3). For 3D, we have added support for both linear and quadratic tetrahedral and hexahedral elements (Tetra4, Tetra10, Hexa8, and Hexa20), and for their corresponding cohesive elements (CohT3, CohT6, CohQ4, and CohQ8, respectively). It is important to note that the cohesive elements internally represent the mesh boundary. Thus, their element templates dictate that there is only one local facet adjacent to anyone of their vertices or edges, even when opposite vertices share the same nodes. As an example, it is valid for a cohesive element of type CohE2 to have the following illustrative incidence: nodeA, nodeB, nodeC, nodeB. This indicates that two vertices of the element share the same node. However, the element template dictates that the second vertex of the element is adjacent to a local facet while the fourth vertex is adjacent to a different local facet.

The concept of element template [12, 18] is quite flexible and versatile. For

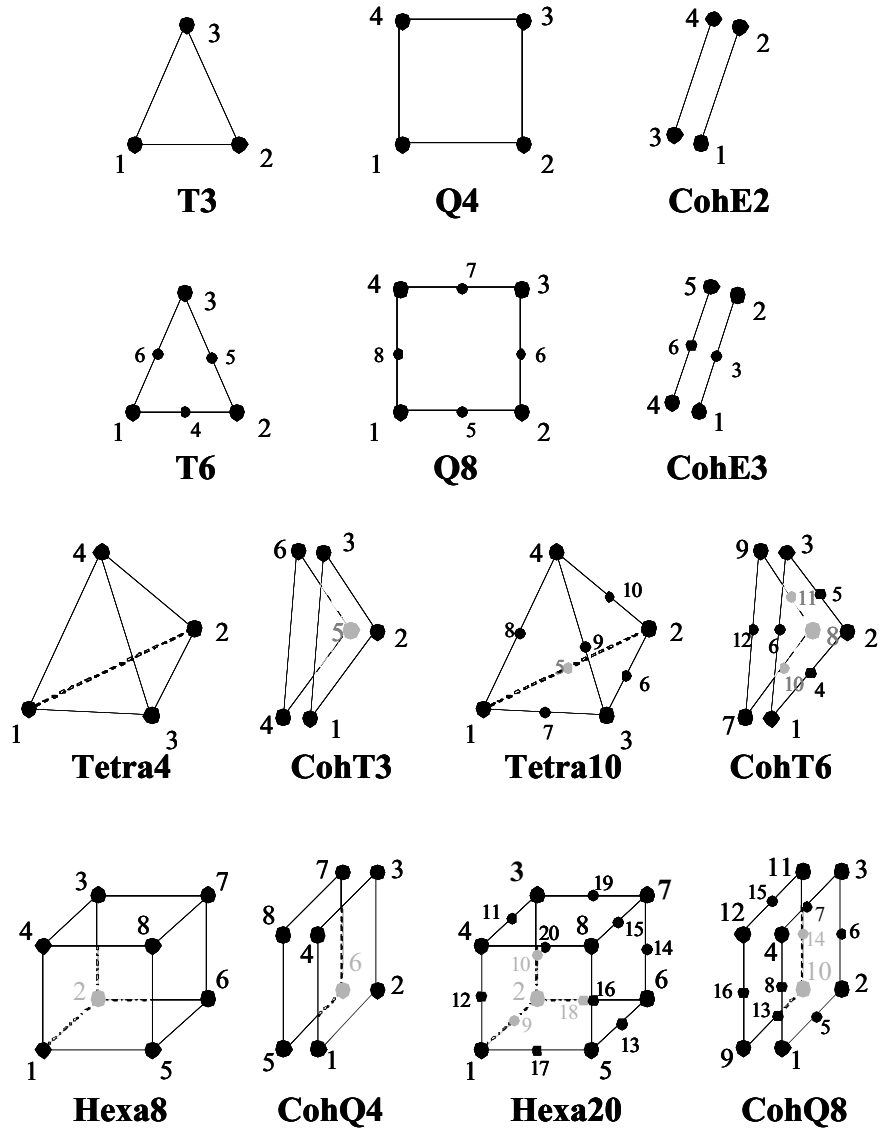


Figure 3.3: Illustration of element types (both volumetric and cohesive) for fragmentation simulation.

instance, if a new type of element is needed, it can be easily incorporated in TopS by means of its element template, which relates to the local topological entities of an element in isolation. This general concept holds for both bulk and interface elements.

3.6 Topological Classification of Facets

During the course of extrinsic fragmentation simulation, the analysis application identifies at which facets new cohesive elements are to be inserted, depending on the fracture criterion used by the simulation. The insertion of new cohesive elements imposes topological changes in the data structure. In order to identify which operations have to be done for updating the data structure, we need a criterion to topologically classify the fractured facets. In this section, we first review previous proposals restricted to quadratic tetrahedral elements and then introduce a new systematic topological classification that can be applied to any type of element.

3.6.1 Previous Proposals

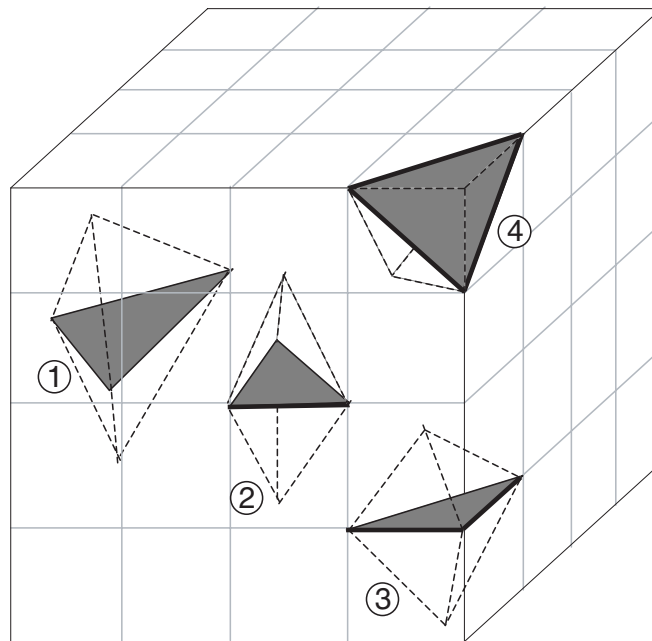


Figure 3.4: Cases of facet classification identified by Pandolfi and Ortiz [15,16] in an illustrative tetrahedral model (for simplicity, the diagonal edges on the mesh boundary are not represented). Fractured facets are dashed and segments on the boundary are in bold.

Pandolfi and Ortiz [75, 76] have proposed a set of rules to classify the fractured facet in order to perform the appropriate topological changes in the model. Their criterion is applied to quadratic tetrahedral elements and is based on the position of the facet with respect to the model boundary (external, internal, or created by cracks). More precisely, in their data structure, a facet is bounded by a set of segments (edges), and the criterion to classify a facet is based on the position of the segments of the facet with respect to the boundary. As illustrated in Figure 3.4, four different cases are identified. In all cases the facet itself is duplicated. The remaining required topological operations vary according to the case:

- Zero segments on the model boundary: no further operation is required;
- One segment on the boundary: the segment (and its mid-side node) is duplicated;
- Two segments on the boundary: the segments (and their mid-side nodes) are duplicated; the corner-node shared by both segments is a candidate to be duplicated;
- All the three segments of the facet on the boundary: the segments (and their mid-side nodes) are duplicated and all three corner-nodes are candidates to be duplicated.

The approach by Pandolfi and Ortiz [75, 76] is restricted to quadratic tetrahedral elements. Although extension for tetrahedral elements of other order is straightforward, their criterion cannot be directly applied to other element types. For instance, for hexahedral elements, several other cases should be identified.

3.6.2 Systematic Topological Classification

In order to overcome the limitations of previous proposals, we introduce a new systematic topological classification that can be applied to any type of element, including both two- and three-dimensional elements. We define a set of procedures that, carried out step-by-step, consistently classify the facets, thus identifying the topological changes needed to update the data structure.

Once the analysis application identifies the facet where to include a new cohesive element, we have access to both associated facet-uses. Without loss of generality, let us name them as first facet-use (fu1) and second facet-use (fu2). Therefore, we can

also name the interfacing elements: first element (E1) and second element (E2), as illustrated in Figure 3.5(a).

The following procedures should then be carried out:

1. Insert the new cohesive element: the new cohesive element is created and inserted in the model, sharing facets with the two interfacing elements (E1 and E2). Accordingly, the adjacency of both elements is updated to reference the new inserted element (Figure 3.5(b)). Element E1 is no longer adjacent to element E2, and vice-versa; they both now are adjacent to the new inserted cohesive element.
2. For each edge-use (eu) of the facet-use (fu1) associated to the first interfacing element (E1), do:
 - Starting at eu, try to retrieve all other uses of the same edge, based on the updated element adjacencies (Figure 6(c)). If the edge-use associated to the second element (E2) cannot be reached (due to changes in the element adjacencies), duplicate the edge, which leads to duplicating all mid-side nodes, if they exist. If the second element is reached, the edge should not be duplicated.
3. For each vertex-use (vu) of the first facet-use (fu1) associated to the first interfacing element (E1), do:
 - Starting at vu, try to retrieve all other uses of the same vertex, based on the updated element adjacencies (Figure 6(d)). If the vertex-use associated to the second element (E2) cannot be reached (due to changes in the element adjacencies), duplicate the vertex, which leads to duplicating the associated corner node. If the second element is reached, the vertex should not be duplicated.

3.6.3 Adjacency Relationships

Whenever a node is duplicated, element connectivity has to be updated. The new created node should replace the original node in all the “uses” reached by the retrieval described above. In other words, all elements associated to the visited edge-uses (or vertex-uses) must have their incidence updated, and all element(s) not reached during the retrieval will continue referencing the original node.

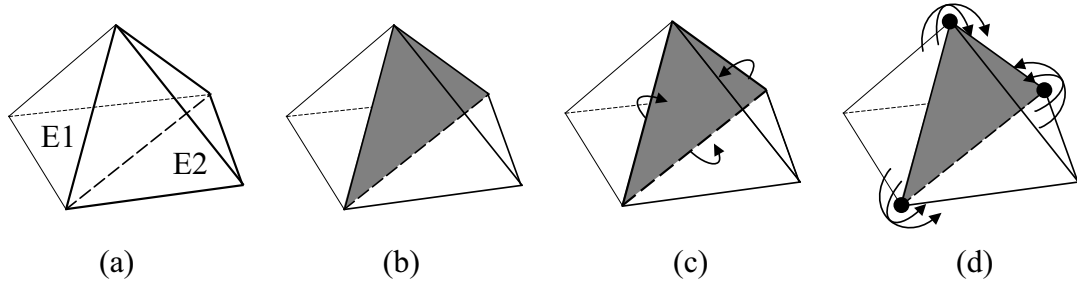


Figure 3.5: Proposed procedures to classify the fractured facet: (a) two original adjacent tetrahedral elements; (b) the new cohesive element is inserted; (c) retrieval of elements around each edge starting at the first element, trying to reach the second one; (d) retrieval of elements around each vertex starting at the first element, trying to reach the second one.

The following Pseudo-code illustrates the algorithm just described for inserting cohesive elements along fractured facet of bulk elements.

Pseudo-code: Procedures to insert a new cohesive element along a facet.

```

function InsertCohesive ( facet )

    fu1 = GetFacetUse ( facet, 1 )
    fu2 = GetFacetUse ( facet, 2 )
    E2 = GetElement ( fu2 )

    CreateCohesiveElement ( facet )

    for each edgeuse eu of fu1 do
        set = GetEdgesAdjacentToElement ( eu )
        if not IsInSet ( set, E2 ) then
            DuplicateEdge ( GetEdge ( eu ) )
        end if
    end for

    for each vertexuse vu of fu1 do
        set = GetVerticesAdjacentToElement ( vu )
        if not IsInSet ( set, E2 ) then
            DuplicateVertex ( GetVertex ( vu ) )
    
```

```

    end if
  end for

end function

```

3.6.4 Application to 3D Meshes

The proposed set of procedures suffices for classifying all the cases identified by Pandolfi and Ortiz for tetrahedral quadratic meshes [75, 76]. In fact, it is easy to see that the procedures do correctly make all the required topological changes. Thus Pandolfi and Ortiz work [75, 76] becomes a particular case of the present general criterion. Before enumerating each one of the identified cases, let us consider the general case in 3D.

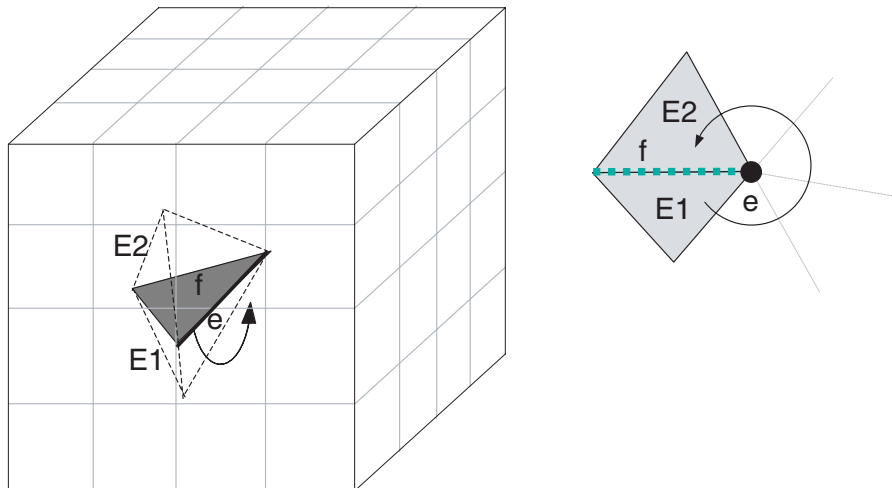


Figure 3.6: Illustrative tetrahedral mesh (for simplicity, the diagonal edges on the mesh boundary are not represented). After the facet (f) is fractured, it remains possible to rotate around an internal edge (e) to reach the second element ($E2$) from the first one ($E1$).

First, we should note that for an internal edge, after breaking the interface between the two interfacing elements, it is always possible to reach the second element from the first one, rotating around the edge, that is, following the cyclic chain of edge-uses. Conversely, if the edge is resting on the model boundary, it is not possible to access the second element from the first. Therefore, an edge on the boundary of a 3D model

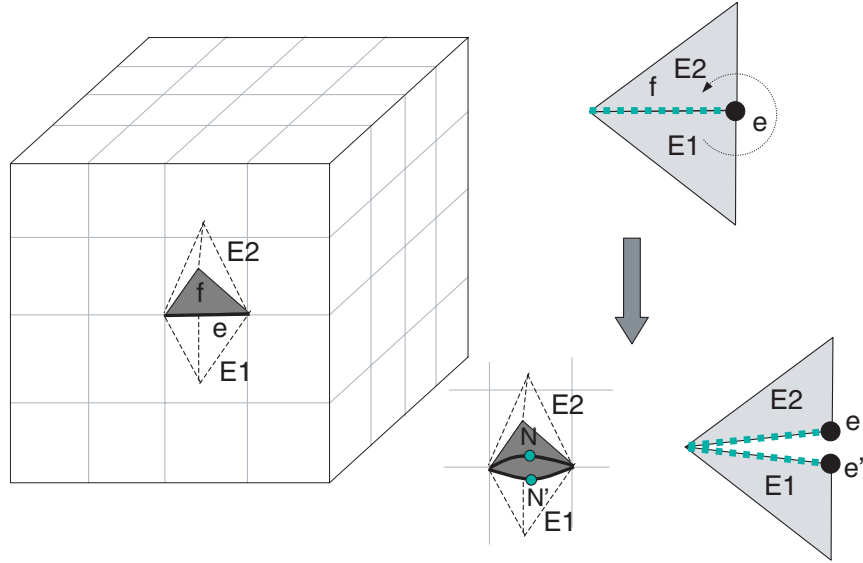


Figure 3.7: Illustrative tetrahedral mesh (for simplicity, the diagonal edges on the mesh boundary are not represented). After the facet (f) is fractured, it is not possible to rotate around a boundary edge (e) to reach the second element ($E2$) from the first one ($E1$). As a result, the edge is duplicated (e') and the eventual mid-side nodes (N) are duplicated (N'). In this case, the connectivity of elements is updated.

will always be duplicated. Figures 3.6 and 3.7 illustrate both situations together with the corresponding cross-section views.

Second, we have to investigate what happens to the surroundings of a vertex that is adjacent to a fractured facet. If the vertex is on the boundary of the model and shared by two adjacent edges of the facet that are also on the boundary, there is no way to access the second element from the first one, after the adjacency between the two elements is broken. In this case, the vertex is duplicated. This situation is illustrated in Figure 3.8 together with the effect of the topological changes. On the other hand, if the vertex is in the interior of the model or on the boundary but shared by none or only one edge of the facet, it remains possible to reach the second element. These situations are illustrated in Figure 3.9.

All the topological cases identified by Pandolfi and Ortiz [75, 76] fit well under this model. One should still note that the proposed procedures also apply for hexahedral elements, without any change, despite which edges of the facet rest on the boundary model. In fact, the extension to other elements is one of the advantages of the proposed topological classification.

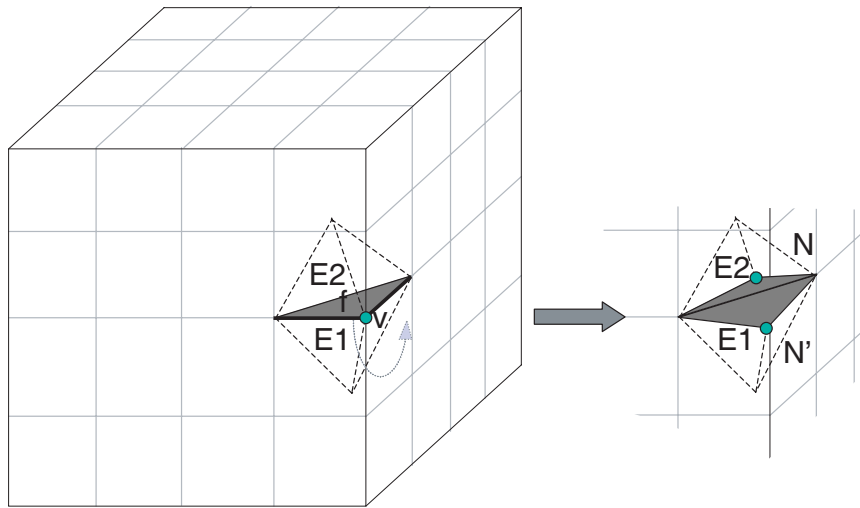


Figure 3.8: Illustrative tetrahedral mesh (for simplicity, the diagonal edges on the mesh boundary are not represented). After the facet (f) is fractured, it is not possible to rotate around a boundary vertex (v) to reach the second element ($E2$) from the first one ($E1$), if the vertex is shared by two edges of the facet also on the boundary. As a result, the associated node (N) is duplicated (N') and the connectivity of elements is updated.

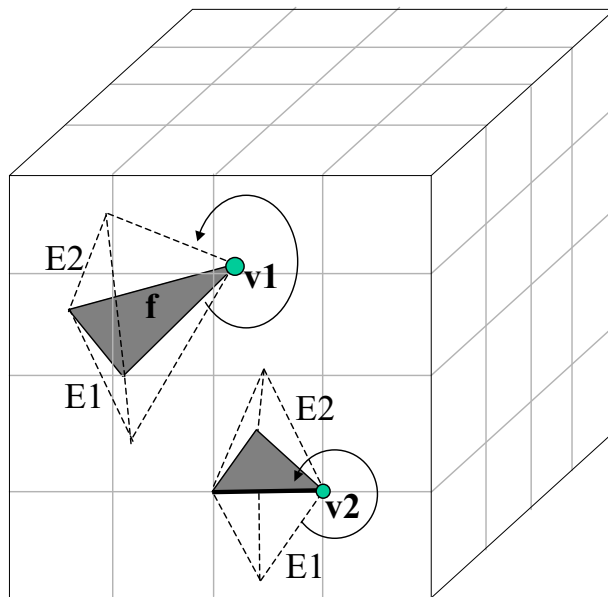


Figure 3.9: Illustrative tetrahedral mesh (for simplicity, the diagonal edges on the mesh boundary are not represented). After the facet (f) is fractured, it remains possible to rotate around a vertex ($v1$) to reach the second element ($E2$) from the first one ($E1$), even if the vertex is on the boundary ($v2$), but not shared by two edges of the facet also on the boundary.

3.6.5 Application to 2D Meshes

The same set of procedures described above also work for 2D models. It is important to note that, in 2D, each facet is defined by a unique edge. Conversely, each edge-use of an element has only one facet-use adjacent to it. Therefore, once the interface between two elements is broken, there is no way to access the second element starting at the associated edge-use of the first element. The unique facet-use is no longer adjacent to the second element. As a result, in 2D models, the edge associated to the fractured facet is always duplicated, and existing mid-side nodes, if any, are duplicated. Figure 3.10 illustrates three different configurations together with the resulting topological changes.

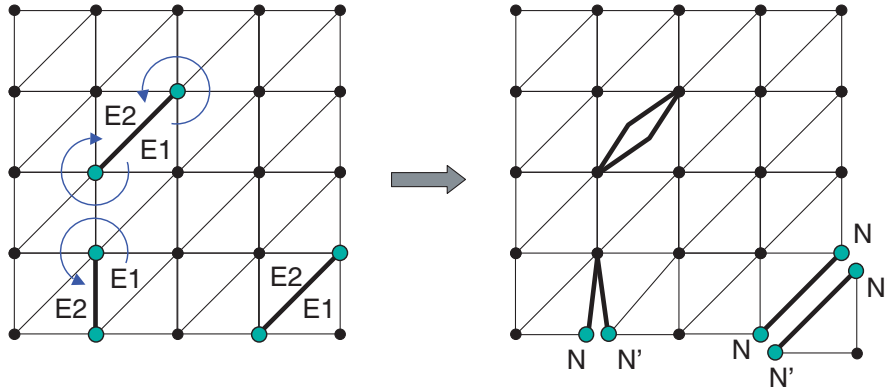


Figure 3.10: Different configuration of fractured facet in 2D with their corresponding topological changes in an illustrative triangular mesh. Eventual mid-side nodes are not illustrated, but they would be duplicated whenever their associated edges are duplicated.

The procedure related to each vertex of the fractured facet may present different results. If it is an interior vertex, it is always possible to access the second element rotating around the vertex. However, if the vertex rests on the model boundary, the second element can no longer be reached, and the vertex has to be split (Figure 3.10).

3.6.6 Avoiding Non-manifold Configurations

Pandolfi and Ortiz [75] have mentioned that, “inevitably, non-manifold situations, such as shell pinched at a point, do indeed arise during fragmentation”. We shall demonstrate that, under the topological framework proposed here (TopS), the model representation remains valid during fragmentation, even for complex crack patterns.

TopS was designed to provide support for representing meshes with manifold domains. This means that the external boundary of a 3D mesh must have 2-manifold topology; therefore, each edge on the boundary is shared by exactly two boundary faces. Accordingly, for 2D models, the external boundary must have 1-manifold topology, with each vertex on the boundary having exactly two boundary edges connected to it. Under these conditions, the data structure is complete, in the sense that it can efficiently retrieve all the adjacency relationships among the defined topological entities [18].

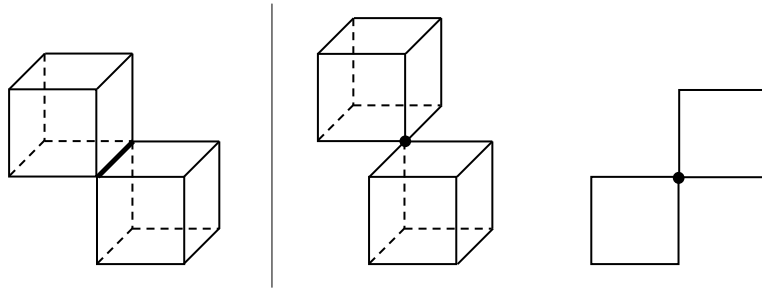


Figure 3.11: Non-manifold configurations in 3D and 2D models. The left configuration represents a singularity at a non-manifold edge; the other two represent a singularity at a non-manifold vertex.

For a model discretized by finite elements, there are two types of non-manifold configurations, illustrated in Figure 3.11, that are not presently supported by TopS. In the first configuration, two non-adjacent elements in 3D share the same edge. In the second, two non-adjacent elements, either in 3D or in 2D, share the same vertex. The former configuration represents a singularity at a non-manifold edge and the latter a singularity at a non-manifold vertex [25]. If neither of these two configurations occurs, the mesh representation is valid and complete. We should note that a set of disjoint elements represents a mesh with a manifold boundary. In fact, a fragmentation simulation may result in a set of disjoint manifold sub-meshes, each one composed by one or more connected elements. During the course of the simulation, two non-adjacent elements may have nodes with the same geometric positions, thus having the same appearance as the configurations illustrated in Figure 12. However, as long they are different nodes, the non-manifold configuration is not characterized. From a topological point of view, the two elements are disjoint.

As long as we start with a valid mesh representation, the proposed topological procedures to insert a cohesive element ensure that the adaptive model representation remains valid during the course of the simulation, even for complex crack patterns.

In other words, the singularities illustrated in Figure 3.11 do not arise while inserting cohesive element in a mesh. A “singularity” at a non-manifold edge can only occur if we have more than one connected sub-mesh sharing the same edge. The second procedure (see Section 6.2) to classify fracture facets avoids such a configuration. After breaking the interface between the two elements, we check whether the elements around the edge remains connected. Whenever the connectivity is broken, we duplicate the edge, attaching the new edge to one of the connected set of elements. The third proposed procedure works in a similar way to avoid the occurrence of singularity at non-manifold vertices. The vertex is duplicated whenever the elements around it do not remain connected.

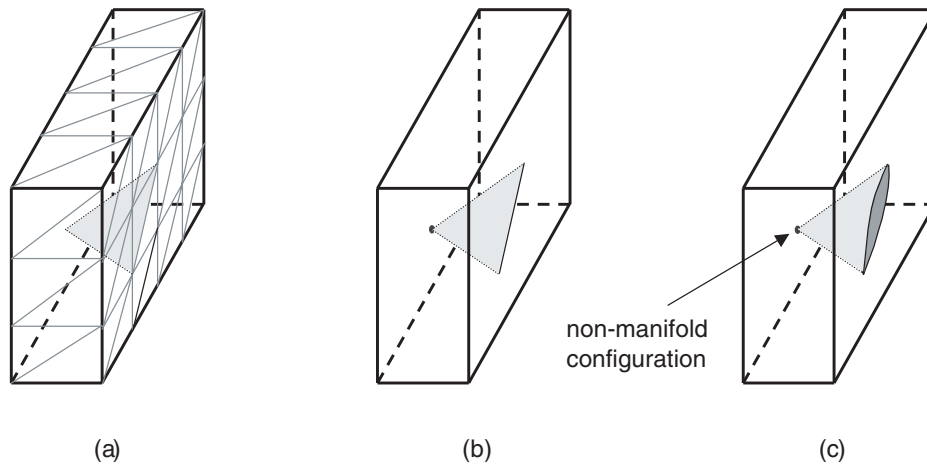


Figure 3.12: A non-manifold configuration that may arise during the course of a fragmentation simulation. A new cohesive element is inserted along an internal facet of a model: (a) illustrative tetrahedral model with one of its internal faces highlighted in gray; (b) same model displaying the internal facet in isolation: one edge of the facet lies on one boundary of the model and the opposite vertex lies on another side of the mesh boundary; (c) model configuration after the insertion of a CZ element along the internal facet: the edge on the boundary is duplicated but the opposite vertex is not, thus a non-manifold configuration is characterized at this location. The mesh representation using TopS remains valid under this configuration.

There is another non-manifold configuration that, in fact, may arise during the course of a fragmentation simulation. It occurs when a cohesive element is inserted along an internal facet whose vertices lie on different sides of the mesh boundary. Such an occurrence is illustrated in Figure 3.12, where one edge of an internal triangular facet lies on one boundary of the model and thus is duplicated; the opposite vertex lies on another side of the mesh boundary. As this vertex is not duplicated, a

non-manifold configuration is characterized at this location. Such a non-manifold configuration, however, does not invalidate the mesh representation because there is only one connected set of elements around the non-manifold vertex. Thus the data structure remains complete under this configuration. In fact, according to the proposed topological classification, the node is not duplicated because it is possible to reach, from one element adjacent to the fracture facet, the second adjacent element. This criterion avoids the emergence of more than one connected set of elements around a vertex, which is the necessary condition for the data structure to be complete.

3.7 Computational Experiments

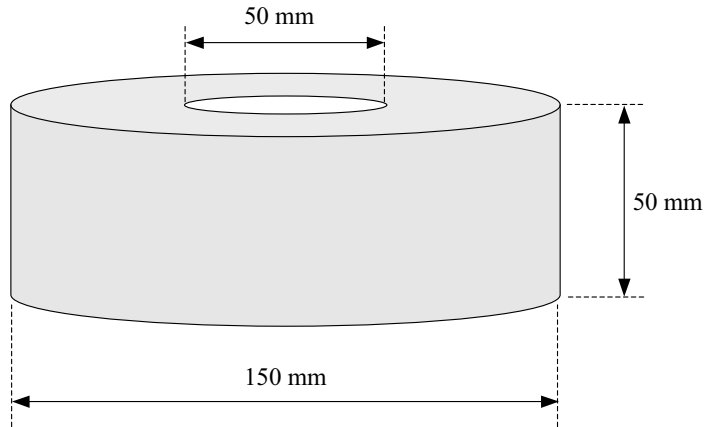


Figure 3.13: Cylindrical model used in the computational experiments.

We have run a set of computational experiments to test the scalability, efficiency, and correctness of the proposed algorithm to insert cohesive elements along the facet of bulk elements. In the experiments, we have considered a variety of models, from 2D to 3D, including both linear and quadratic meshes, thus demonstrating that the proposed approach is general and can be applied to a variety of models. The algorithm to insert cohesive elements is exactly the same, despite the model under consideration; that is, the code to implement the insertion of cohesive elements is the same, for 2D and 3D models, and for linear and quadratic meshes. This is the main advantage of using the described topological data structure: we achieve a unified topological framework for representing finite element models used on fragmentation simulations.

The basic model under consideration is a cylindrical specimen as illustrated in Figure 3.13. Different 2D and 3D finite element meshes were generated to represent

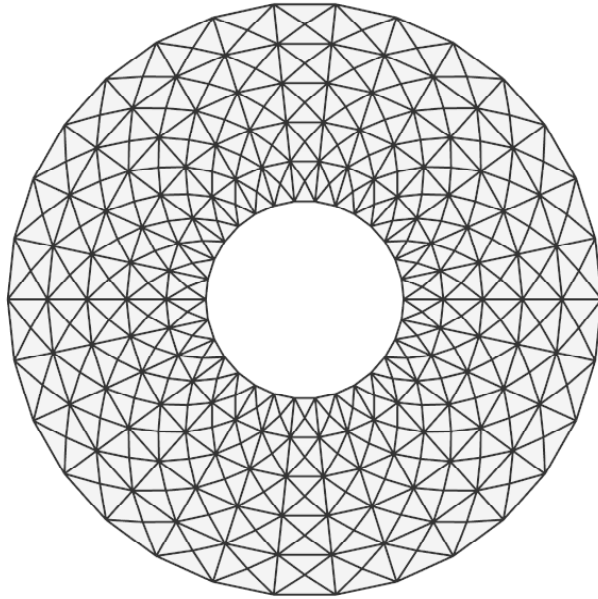


Figure 3.14: Illustrative triangular mesh (for both T3 and T6) displaying a discretization of 5×30 .

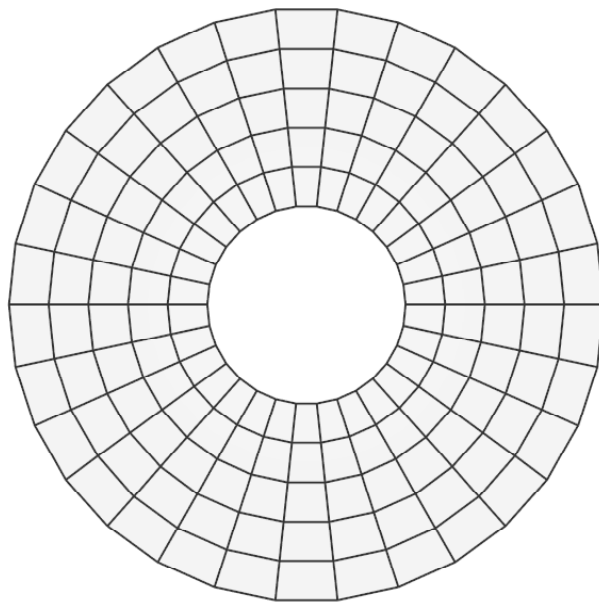


Figure 3.15: Illustrative quadrilateral mesh (for both Q4 and Q8) displaying a discretization of 5×30 .

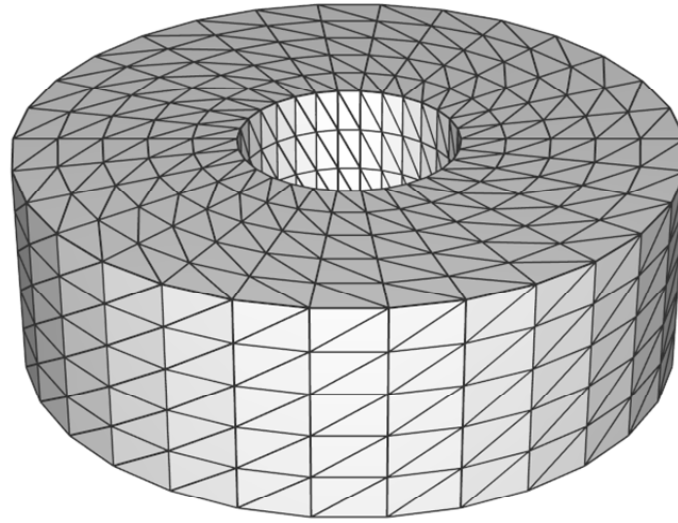


Figure 3.16: General tetrahedral mesh (for both Tetra4 and Tetra10) displaying a discretization of $5 \times 30 \times 5$.

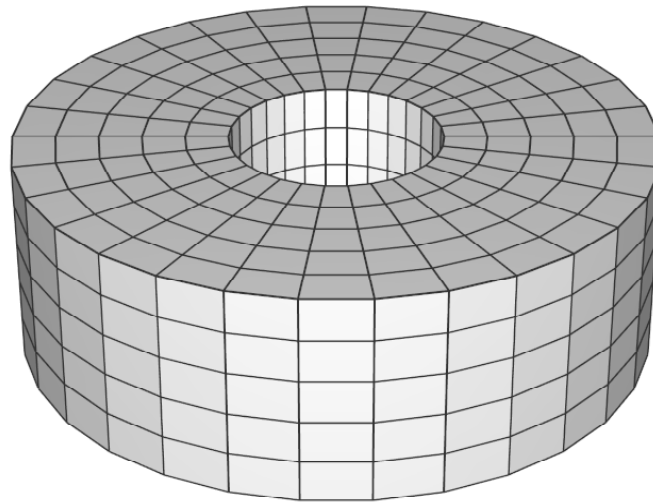


Figure 3.17: General hexahedral mesh (for both Hexa8 and Hexa20) displaying a discretization of $5 \times 30 \times 5$.

the cylindrical model, at different discretization, using both linear and quadratic elements: T3, T6, Q4, Q8, Tetra4, Tetra10, Hexa8, and Hexa20. Figures 3.14, 3.15, 3.16 and 3.17 show the resulting meshes at illustrative discretizations.

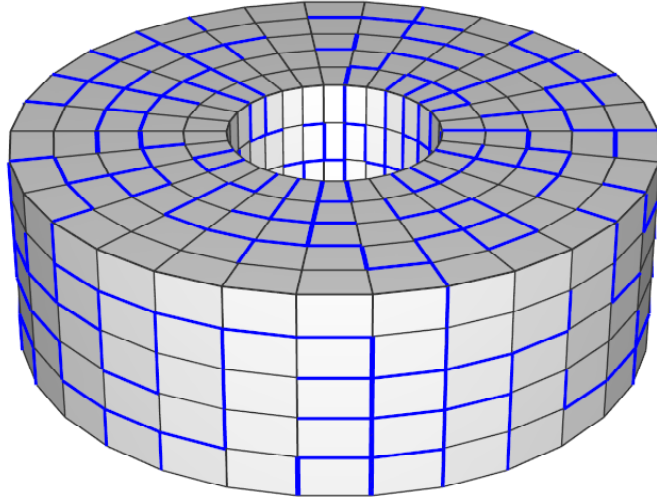
For each generated mesh, we have tested the proposed framework decoupled from any mechanics simulation (setting up experiments similar to the one described by Pandolfi and Ortiz [75]). Cohesive elements were inserted, in a random order, at all the facets of the underlying meshes. The random order in which the cohesive elements are inserted results in arbitrarily complex crack pattern during the experiment. In the end, each node of the mesh is used by only one bulk element. We then have checked if the final obtained number of topological entities (nodes, elements, facets, edges, and vertices) were the expected ones. Figure 3.18 shows the achieved configuration of an illustrative hexahedral mesh after inserting cohesive elements, in a random order, along 20% of the facets of the model, illustrating the resulted arbitrary crack patterns. In Figure 3.18(b), we impose a separation in between each bulk element interface in order to better illustrate the mesh with the inserted cohesive elements (represented in blue).

Table 3.7 presents the time needed to perform the insertion of cohesive elements at all bulk element interfaces. For each type of mesh, we run the test for different mesh discretizations. Figures 3.19, 3.20, 3.21 and 3.22 plot the elapsed time against the number of cohesive elements inserted for the triangular, quadrilateral, tetrahedral, and hexahedral meshes, respectively. As can be noted, the proposed approach scales linearly with the size of the model, despite the element type in use: the elapsed time is linearly proportional to the number of inserted cohesive elements. These results demonstrate that the insertion of a cohesive elements is based on local topological procedures, thus its performance is independent of the size of the model.

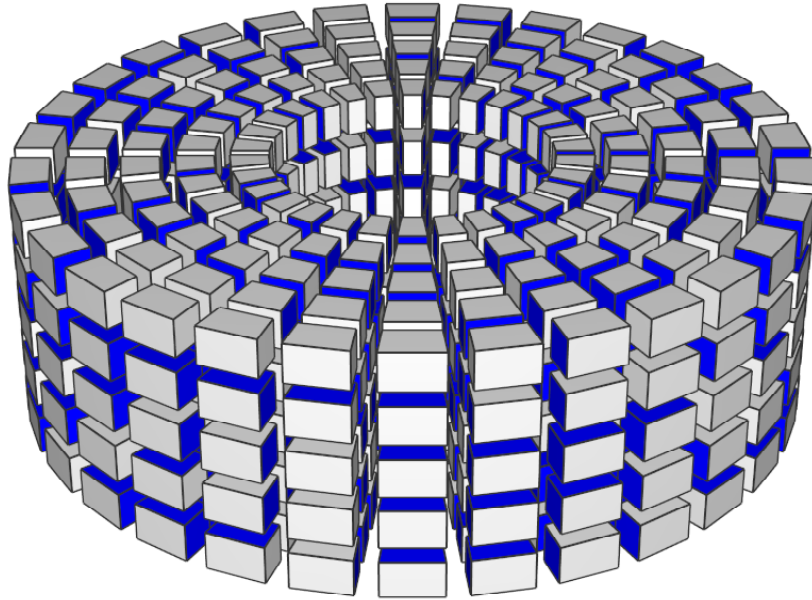
3.8 Mixed-mode Dynamic Crack Growth Fracture Simulation

In this section, we demonstrate the application of the topological data structure in dynamic fracture analysis through a 2D finite element simulation of mixed-mode dynamic crack growth in a pre-cracked steel plate subjected to impact loading.

The cohesive zone model employed in the section follows that proposed by Pandolfi and Ortiz [75], which is based on effective quantities (both tractions and displacements). The traction-separation relations for pure normal and tangential separation



(a)



(b)

Figure 3.18: Illustrative hexahedral configuration after inserting cohesive elements (in blue) at 20% of the facets, exemplifying the resulting (arbitrary) crack patterns. In (b), we impose a separation in between each bulk element interface in order to better illustrate the mesh with the inserted cohesive elements.

Table 3.1: Elapsed times (in seconds) for inserting cohesive elements at all the facets of the models. Each time reported is the average of 5 simulations for each specific model, inserting the elements in different random order.

Element type	Mesh discretization	# of bulk elems	Initial # of nodes	# of CZM elems	Final # of nodes	Time(s)
T3	100×600	240,000	120,600	359,400	720,000	7.636
	200×1200	960,000	481,200	1,438,800	2,880,000	30.172
	300×1800	2,160,000	1,081,800	3,238,200	6,480,000	67.660
	400×2400	3,840,000	1,922,400	5,757,600	11,520,000	120.054
	500×3000	6,000,000	3,003,000	8,997,000	18,000,000	184.782
T6	100×600	240,000	481,200	359,400	1,440,000	9.29
	200×1200	960,000	1,922,400	1,438,800	5,760,000	36.946
	300×1800	2,160,000	4,323,600	3,238,200	12,960,000	84.940
	400×2400	3,840,000	7,684,800	5,757,600	23,040,000	150.040
	500×3000	6,000,000	12,006,000	8,997,000	36,000,000	236.814
Q4	100×600	60,000	60,600	119,400	240,000	2.028
	200×1200	240,000	241,200	478,800	960,000	8.126
	300×1800	540,000	541,800	1,078,200	2,160,000	18.384
	400×2400	960,000	962,400	1,917,600	3,840,000	32.552
	500×3000	1,500,000	1,503,000	2,997,000	6,000,000	51.866
Q8	100×600	60,000	181,200	119,400	480,000	2.778
	200×1200	240,000	722,400	478,800	1,920,000	10.996
	300×1800	540,000	1,623,600	1,078,200	4,320,000	25.250
	400×2400	960,000	2,884,800	1,917,600	7,680,000	43.798
	500×3000	1,500,000	4,506,000	2,997,000	12,000,000	67.508
Tetra4	10×60×10	36,000	7,260	69,600	144,000	7.428
	20×120×20	288,000	52,920	566,400	1,152,000	60.972
	30×180×30	972,000	172,980	1,922,400	3,888,000	209.726
	40×240×40	2,304,000	403,440	4,569,600	9,216,000	489.204
	50×300×50	4,500,000	780,300	8,940,000	18,000,000	954.472
Tetra10	10×60×10	36,000	52,920	69,600	360,000	8.208
	20×120×20	288,000	403,440	566,400	2,880,000	65.782
	30×180×30	972,000	1,339,560	1,922,400	9,720,000	223.848
	40×240×40	2,304,000	3,149,280	4,569,600	23,040,000	545.292
	50×300×50	4,500,000	6,120,600	8,940,000	45,000,000	1067.520
Hexa8	10×60×10	6,000	7,260	16,800	48,000	1.152
	20×120×20	48,000	52,920	139,200	384,000	9.664
	30×180×30	162,000	172,980	475,200	1,296,000	33.690
	40×240×40	384,000	403,440	1,132,800	3,072,000	81.918
	50×300×50	750,000	780,300	2,220,000	6,000,000	158.350
Hexa20	10×60×10	6,000	27,720	16,800	120,000	1.444
	20×120×20	48,000	206,640	139,200	960,000	12.336
	30×180×30	162,000	680,760	475,200	3,240,000	42.656
	40×240×40	384,000	1,594,080	1,132,800	7,680,000	101.076
	50×300×50	750,000	3,090,600	2,220,000	15,000,000	198.356

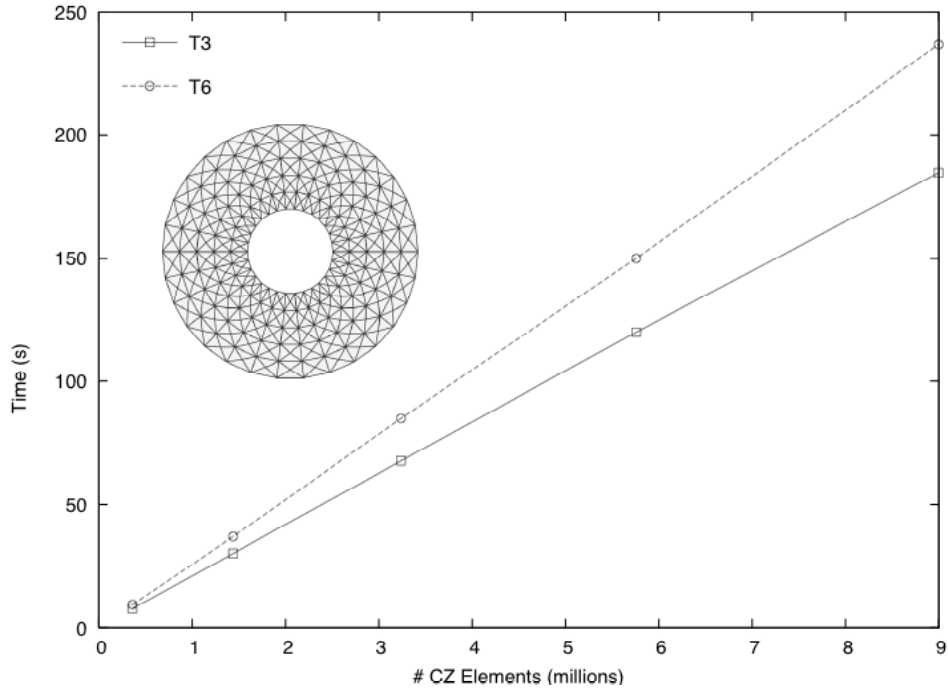


Figure 3.19: Time vs. number of inserted CZ elements for linear and quadratic triangular meshes.

can display linear softening and linear unloading/reloading. Essentially, the cohesive force that resists the opening and sliding of the new surface is assumed to weaken irreversibly with increasing interface separation. Irreversibility is retained by keeping track of the maximum displacement in the simulation history and by using it as the indicator for loading or unloading. Under loading condition, when the current effective opening displacement is larger than that in the history $\delta_{\text{eff}}^{(\text{max})}$, the cohesive traction ramps down linearly as displacement jump increases, and reduces to zero as opening reaches critical opening displacement δ_{nc} . Decohesion is complete at this point and cohesive force vanishes thereafter. If the interface reopens, the reloading path follows the unloading path in the reverse direction until the maximum effective displacement is reached, and then follows the original ramp-down relation.

Since the problem is presented for illustration purposes, we will focus on the ability of the data structure in handling the changing geometry. The results presented as well as the parameter chosen are not for validation purposes.

Consider the Kalthoff and Winkler [38] experiment, which tested a plate with two edge notches subjected to an impact by a projectile, as shown in Figure 2.11 (a). For completeness, the problem description is briefly repeated here (more details in

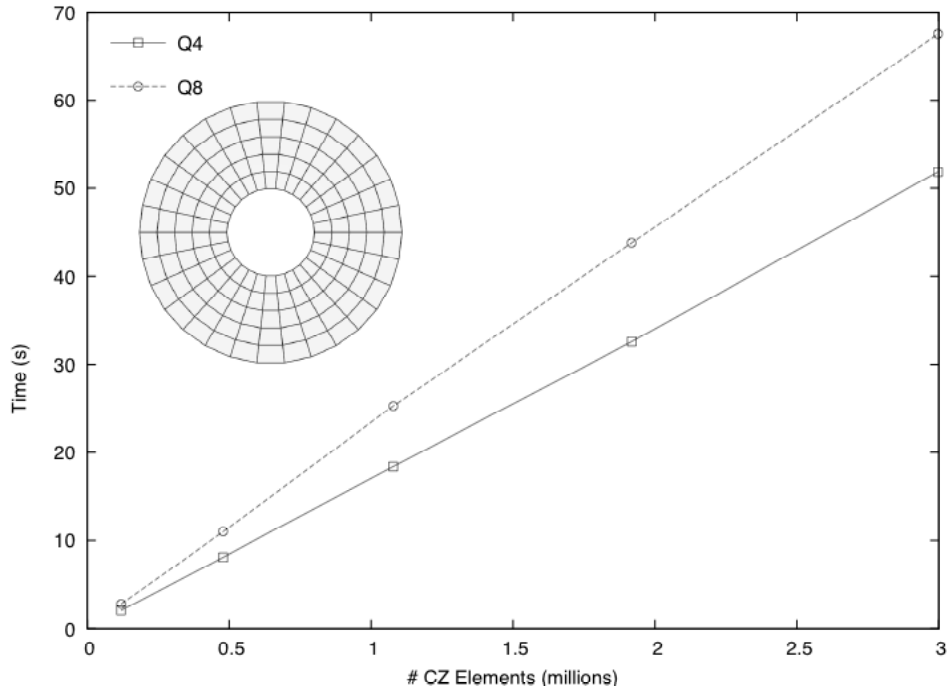


Figure 3.20: Time vs. number of inserted CZ elements for linear and quadratic quadrilateral meshes.

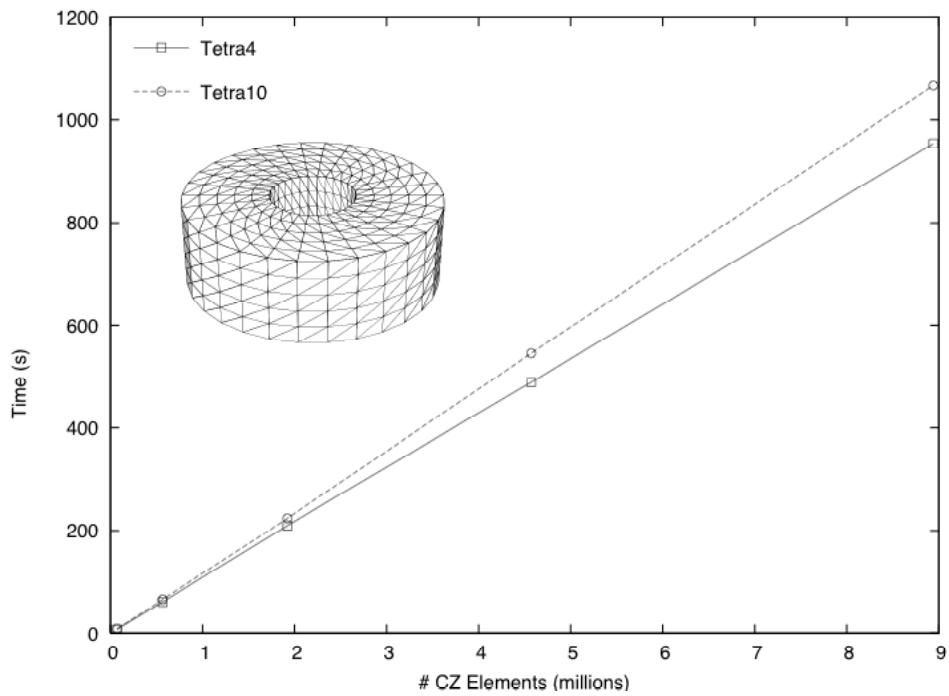


Figure 3.21: Time vs. number of inserted CZ elements for linear and quadratic tetrahedral meshes.

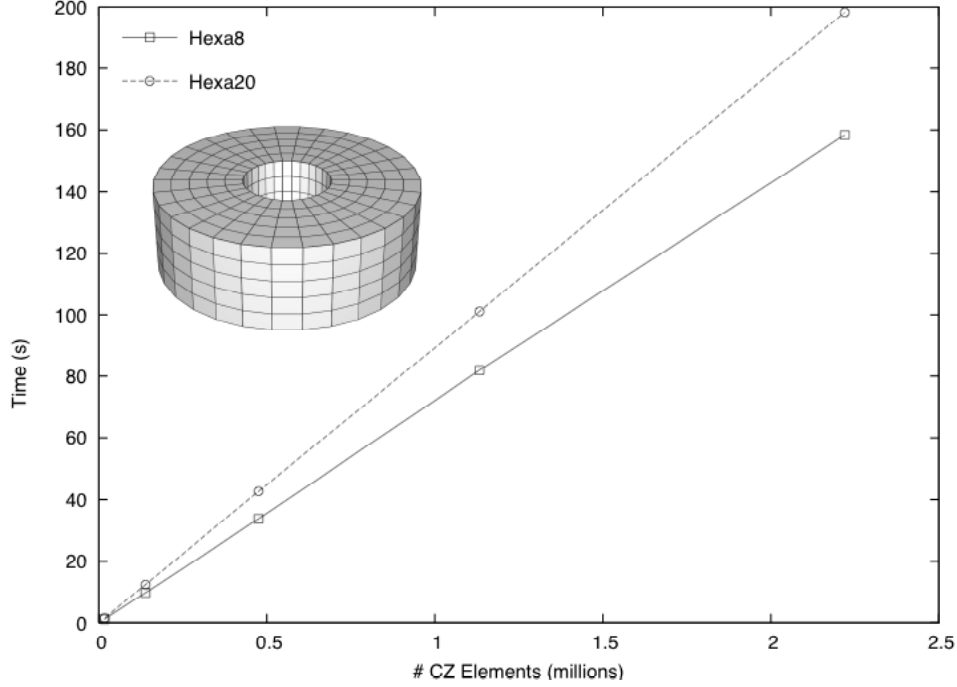


Figure 3.22: Time vs. number of inserted CZ elements for linear and quadratic hexahedral meshes.

Section 2.4).

The experiments demonstrated different fracture/damage behaviors of a maraging steel material under various loading rates. The material properties are listed in Table 3.2. The parameters are defined as following: E , μ and ρ denote Young's modulus, Poisson's ratio and mass density of the bulk material; parameters G_{IC} and G_{IIC} denote fracture energy for opening crack (mode-I fracture) and sliding crack (mode-II fracture); T_n^{max} and T_t^{max} are cohesive strength along normal and sliding directions, while Δ_n and Δ_t are the corresponding separations when material failure occurs under pure mode-I and mode-II fracture.

In this study, our objective is to simulate the brittle failure mode and investigate the overall crack propagation behavior. The impact-loading rate is chosen as 16.5m/s. Since the problem possesses symmetry, only half of the geometry (100mm×100mm) is modeled, as shown in Figure 2.11 (b).

Numerical simulation is carried out using a mesh of 80×80 squares each divided into four T6 elements. Time step is set to $\Delta t = 5 \times 10^{-3} \mu s$. Figure 3.23 shows a set of stress contour plots taken at different times. Crack initiates at around $t = 25 \mu s$.

The impact load is applied along the left boundary of the lower plate section

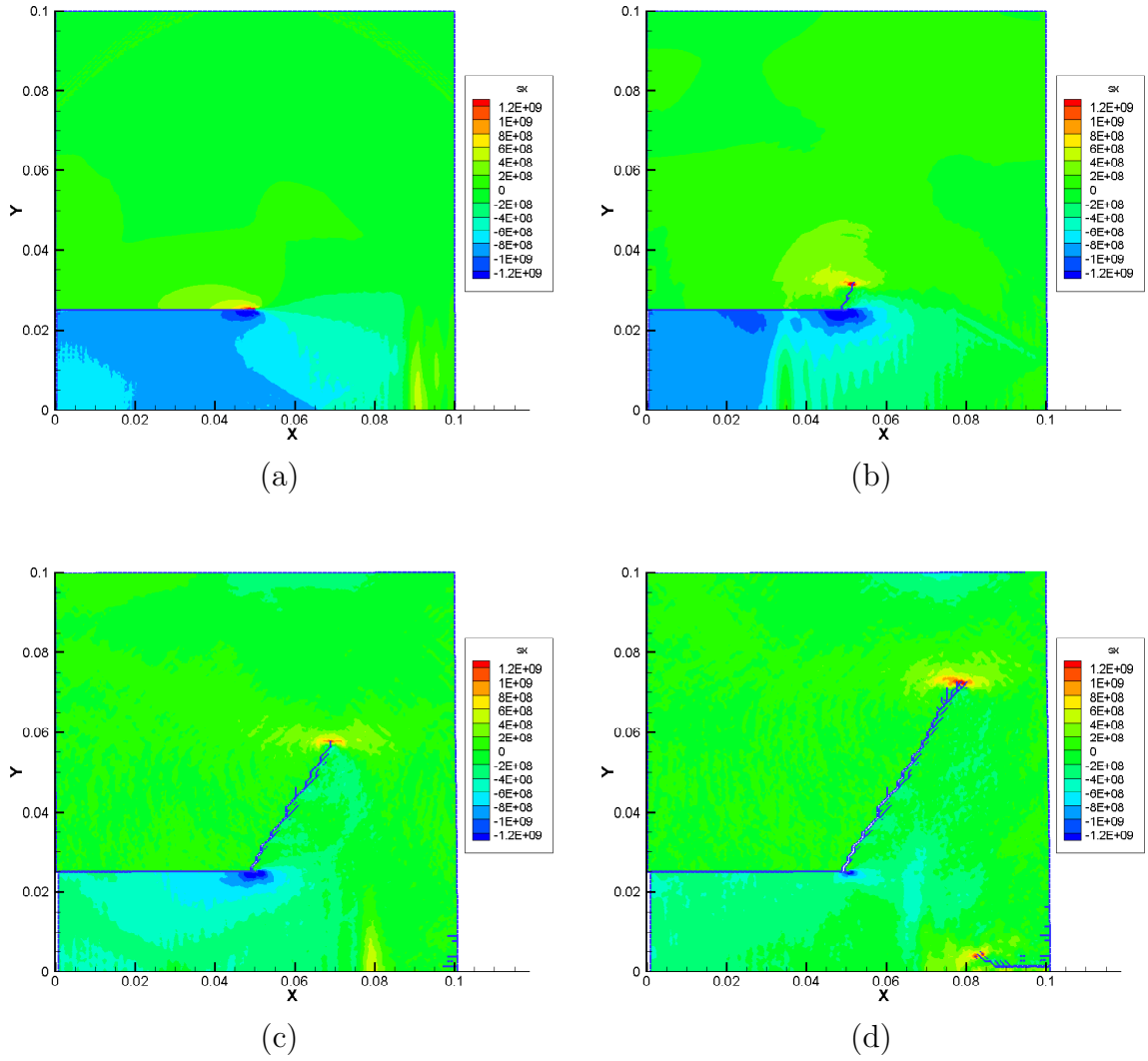


Figure 3.23: Stress contour and crack propagation plots of the Kalthoff-Winkler experiment at different time instants: (a) $20\mu s$; (b) $30\mu s$; (c) $50\mu s$; (d) $60\mu s$.

Table 3.2: Material properties of 18Ni(300) steel and cohesive model parameters.

E (GPa)	ν	ρ (kg/m ³)	$G_{Ic} = G_{IIc}$ (KJ/m ²)	$T_n^{\max} = T_t^{\max}$ (GPa)	$\delta_n = \delta_t$ (μ m)
190	0.3	8000	22.2	1.2	37.0

(below the initial crack plane). It creates compressive waves propagating towards the right surface within the lower section of the plate. Before the first tide of stress waves reaches the initial crack tip ($x = 50mm$, $y = 25mm$) at around $t = 18\mu s$, the upper plate section ($y > 25mm$) remains stress-free. When the wave reaches the crack tip, the upper crack surface, near the crack tip, stays stationary, while the lower crack surface near the crack tip is under the influence of a rightward compressive wave. This creates a tearing effect at the crack tip. Afterwards, the waves continue to propagate rightwards in the lower plate section as compressive wave, and also propagate around the crack tip into the upper section (above the initial crack plane) of the plate. The stress waves along the upper crack surface are now tensile propagating towards left boundary. Therefore the upper and lower surfaces of the crack are subjected to influence of stresses of opposite sign and direction along the Cartesian x coordinate (horizontal), and a strong tearing effect is created at the crack tip. When the local stress reaches the cohesive strength, cohesive element is inserted and crack initiates. This occurs at around $25\mu s$. Reflective wave from the right boundary also influence the crack propagation and crack finally grows along a direction of about 60° .

Due to bending effect, crack initiation also occurs at the right edge (Figure 3.23 (d)). Belytschko et al. [13] studied the same problem using extended FEM with loss of hyperbolicity criterion, and the damage zone at the bending side is also present in their analysis. We also compare the results with those obtained by Zhang and Paulino [116] using intrinsic CZMs. The overall crack behaviors are similar for the two studies, while the bending crack is not as noticeable in the intrinsic CZM study because it employs a higher cohesive strength value.

Micro-cracks emanating from the main crack are also observed in the crack growth pattern (Figure 3.23). These cracks typically arrest shortly after the main crack tip advances. We define cohesive element decohesion when all its Gauss points separation jump exceed a critical separation value. Thus by extracting only the cohesive elements that have undergone complete decohesion, we obtain a “clean” fracture pattern, as shown in Figure 3.24 (a). Clearly, the micro-cracks observed in Figure 25 do not grow beyond one element length.

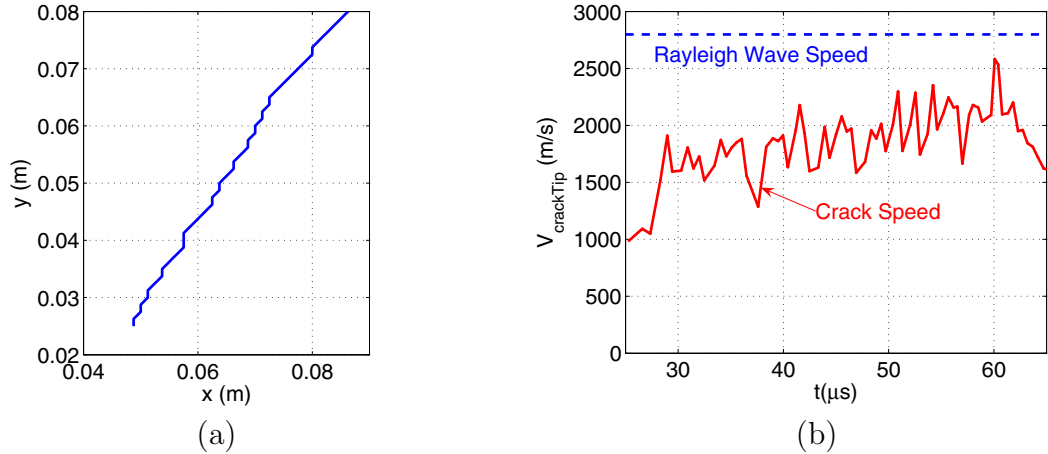


Figure 3.24: (a) Main crack path extracted from completely debonded cohesive surfaces in Figure 3.23; (b) crack speed derived from crack length growth versus time increment. Rayleigh wave speed is 2799m/s.

Crack velocity is also computed from crack length versus time increment information, as shown in Figure 3.24 (b) along with the Rayleigh wave speed (2799m/s) for comparison purpose. The average crack speed is around 1700m/s, which is slightly lower than that estimated by Belytschko et al. [13], which is 1800m/s.

3.9 Remarks

In this Chapter, we propose a topological framework for supporting both intrinsic and extrinsic fragmentation simulation. The proposed framework is general in the sense that it supports any finite element mesh with elements defined by ordered list of nodes. Based on TopS, a reduced topological data structure [18, 19], we propose a new systematic topological classification of fracture facet, thus achieving a general algorithm to insert cohesive elements along facets of bulk-elements: the same algorithm works for 2D and 3D models, including both linear and quadratic elements. The proposed approach to classify fractured facets can also be applied to other topological data structures, as long as they are complete.

We have run a set of computational experiments that demonstrate the scalability and correctness of the proposed approach. The insertion of cohesive elements is based on local topological operations. As a consequence, the time needed to insert cohesive elements at all facets of a model is linearly proportional to the number of inserted elements. Such linear scaling is demonstrated by the plots of Figures 3.19

through 3.22, including millions of CZ elements. We also have integrated TopS with actual extrinsic fragmentation simulation. Simulation results, for both 2D and 3D models, demonstrates the effective use of the proposed topological framework.

Although we have emphasized the use of the topological data structure (TopS) to provide support for fragmentation simulations with cohesive elements, it has other potential applications. For instance, TopS can be used to generate multiple arbitrary cracks (e.g. in the context of linear elastic fracture mechanics [4]) in existing crack-free meshes for complex 3D domains.

Chapter 4

Cohesive Zone Size: Static, Dynamic and Rate Effects

The crack tip zone, which exhibits nonlinear material separation behavior, is called the damage zone, fracture zone, or cohesive zone, under slightly different contexts. An essential issue of physical importance is the size of the damage zone. Numerical simulations, involving cohesive zone elements, require that the cohesive zone be sufficiently discretized in order to capture the nonlinear behavior. In this Chapter, we investigate the cohesive zone size through a simple, but insightful, 1D double-cantilever beam example. First, we evaluate the cohesive zone size in quasi-static crack propagation case, which serves as both verification of the numerical procedure, as well as a detailed parametric study for comparison with the static estimate from the literature. Second, we investigate the cohesive zone size in dynamic case with different loading rates. Third, the rate-dependent cohesive zone concept is introduced and the influence of rate-dependency is analyzed.

4.1 Static Cohesive Zone Size

A well-known static estimate of the cohesive zone size for a constant traction-separation relation [91] states the following relationship

$$\ell_{cz} \propto \frac{EG_{Ic}}{T^2} \quad (4.1)$$

However, the cohesive models commonly employed in numerical simulations in the literature involve non-constant traction-separation relationships. Therefore, cohesive strength T in the above expression (4.1) is usually taken as the average traction T_{ave} by equating the cohesive energy of a particular cohesive law to that of the constant traction-separation law. For exponential cohesive law, $T_{ave} = 0.453T_{max}$, while for bilinear cohesive law, $T_{ave} = 0.5T_{max}$.

In this section, the static double cantilever problem results reveal the influence of cohesive parameters on cohesive zone size, and also indicate that Equation (4.1)

provides only a rough estimate of the cohesive region size ℓ_{cz} .

4.1.1 Surrogate Problem Description

To numerically investigate cohesive zone size, the double-cantilever beam geometry (DCB) is chosen because an analytical solution exists. A schematic representation of the DCB geometry is illustrated in Figure 4.1.

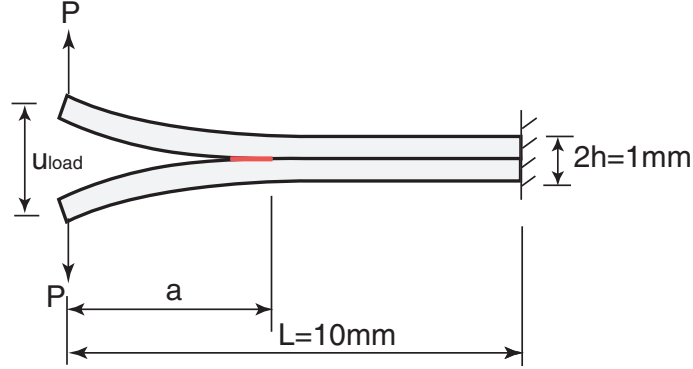


Figure 4.1: Schematic representation of double cantilever problem. Separation a advances under statically imposed displacement u_{load} along a weak interface joining the double cantilever beams.

The relationship between the deflection at the free tip u_{load} and the reaction force P can be computed using simple beam theory by assuming cantilever behavior for the free arm of the specimen a :

$$u_{load} = \frac{Pa^3}{3EI} \quad (4.2)$$

where E is Young's modulus, $I = bh^3/12$ is moment of inertia, b is the beam thickness and h is the beam height. Compliance of the system is defined as deflection over accompanying force:

$$C = \frac{2u_{load}}{P} = \frac{2a^3}{3EI} \quad (4.3)$$

while energy release rate G can be computed as

$$G = \frac{P^2}{2b} \frac{\partial C}{\partial a} = \frac{P^2}{2b} \frac{\partial}{\partial a} \left(\frac{2a^3}{3EI} \right) = \frac{P^2 a^2}{bEI} = \frac{12P^2 a^2}{b^2 h^3 E} \quad (4.4)$$

In a load control specimen, the rate of change of energy release rate at constant

applied force P is *positive*:

$$\left. \frac{dG}{da} \right|_P = \frac{24P^2a}{b^2h^3E} = \frac{2G}{a} > 0 \quad (4.5)$$

In a displacement control specimen, the rate of change of the energy release rate at constant applied displacement u_{load} is *negative*:

$$G = \frac{P^2a^2}{bEI} = \frac{9EIu_{\text{load}}^2}{a^4b} = \frac{3u_{\text{load}}^2h^3E}{4a^4} \quad (4.6)$$

$$\left. \frac{dG}{da} \right|_{u_{\text{load}}} = -\frac{3EIu_{\text{load}}^2h^3}{a^5} = -\frac{4G}{a} < 0 \quad (4.7)$$

Assume that the crack growth begins when energy release rate G reaches a critical value G_c . The crack growth *continues* in *load control* specimen without increasing load P once the condition is satisfied, as G will always be above G_c as the crack advances ($dG/da > 0$). On the other hand, for *displacement control* specimen, the crack *arrests* as G decreases with crack growth ($dG/da < 0$), and additional imposed displacement is required to resume crack growth. In view of such behavior, displacement control is used to achieve stable crack growth.

Table 4.1: Properties of weakly bonded Aluminum DCB [56].

E (GPa)	ν	ρ (kg/m ³)	G_{Ic} (J/m ²)	T_n^{max} (MPa)	δ_n (μm)
69	0.3	2700	52.5	138	0.76

For the sake of discussion, the material selected is Aluminum, with properties shown in Table 4.1. For this study, fracture energy G_{Ic} is assumed to be 52.5 J/m^2 and cohesive strength is taken to be $T_n^{\text{max}} = E/500 = 138 \text{ MPa}$. These values correspond to a weakly bonded interface. For the parametric study conducted in Section 4.1.4, these values vary between $G = 1G_0$ and $10G_0$ where $G_0 = 52.5 \text{ J/m}^2$, and T_n^{max} varies between $E/5000$ and $E/200$.

4.1.2 Solution Method

For the static loading problem, the “explicit” updating scheme outlined in Chapter 2 is not applicable. Hence static analysis is briefly described here. The bulk behavior is simulated by 2-node Euler-Bernoulli beam elements illustrated in Figure 4.2. The associated shape functions for the DOFs are listed in Eqn. (4.8).

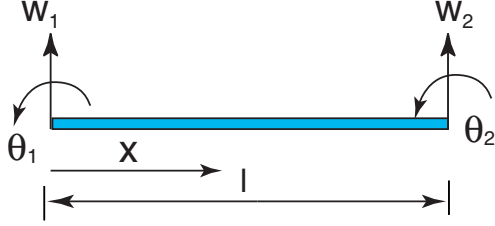


Figure 4.2: Definition of degrees of freedom for a 2-node Euler beam element.

$$\begin{aligned}
 N_1^w(x) &= 1 - 3(x/\ell)^2 + 2(x/\ell)^3 & (4.8) \\
 N_1^\theta(x) &= x - 2x^2/\ell + x^3/\ell^2 \\
 N_2^w(x) &= 3(x/\ell)^2 - 2(x/\ell)^3 \\
 N_2^\theta(x) &= -x^2/\ell + x^3/\ell^2
 \end{aligned}$$

This approach neglects shear deformation in the arms, and assumes that the cantilever arm is fixed at the crack tip. This is a good approximation for a slender beam.

Bulk Element Stiffness Matrix. For the bulk element, stiffness matrix is assembled from element stiffness matrix as

$$[\mathbf{K}]_{\text{bulk}} = \sum_{i=1}^{n_{\text{elem}}} [\mathbf{k}]_{\text{bulk}}^e \quad (4.9)$$

$$[\mathbf{k}]_{\text{bulk}}^e = \int_0^\ell EI \{ \mathbf{N}''(x) \}^T [\mathbf{N}''(x)] dx \quad (4.10)$$

Cohesive Element Stiffness Matrix. Unlike bulk stiffness matrix $[\mathbf{K}]_{\text{bulk}}$ which is constant at any loading step, cohesive stiffness matrix depends on the current separation stage of each cohesive element. In the following formulation,

$$[\mathbf{K}]_{\text{coh}} = \sum_{i=1}^{n_{\text{cohel}}} [\mathbf{k}]_{\text{coh}}^e \quad (4.11)$$

$$[\mathbf{k}]_{\text{coh}}^e = \int_0^\ell k_c(u) \{ \mathbf{N}(x) \}^T [\mathbf{N}(x)] dx \quad (4.12)$$

and the instantaneous cohesive stiffness parameter k_c depends on the current separation, as shown in Figure 4.3. In the numerical integration, three Gauss points are used for calculating $[\mathbf{k}]_{\text{coh}}^e$, which varies from loading step to loading step.

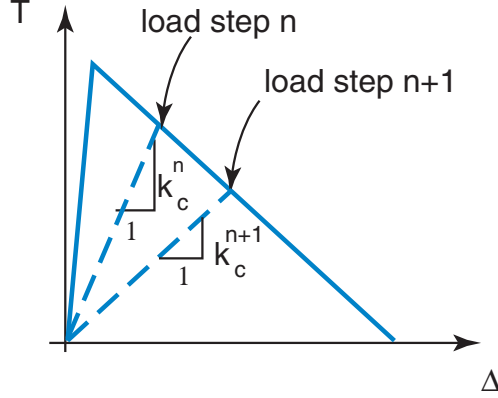


Figure 4.3: Cohesive element stiffness k_c varies with separation Δ .

Quasi-explicit Solution Scheme. At each time step n , the following system of equation is solved:

$$([\mathbf{K}_{\text{bulk}}] + [\mathbf{K}_{\text{coh}}]_n) \{\mathbf{u}\}_n = \{\mathbf{R}\}_n \quad (4.13)$$

Because $[\mathbf{K}_{\text{coh}}]_n$ that depends on solution of u_n is unknown, iteration is needed to approach a reliable solution. In this study, a quasi-explicit solution scheme with a simple iteration procedure is employed. First, $\{\mathbf{u}\}_n^0$ is solved using an approximation of $[\mathbf{K}_{\text{coh}}]_{n-1}$. Next, $[\mathbf{K}_{\text{coh}}]$ is updated using the updated $\{\mathbf{u}\}_n^0$. Finally, Equation (4.13) is solved again for $\{\mathbf{u}\}_n$. The iteration can be repeated to obtain a converged result, however in the current study, the one-iteration described above is sufficient, as long as the loading step is chosen appropriately.

We note that in the simple form of original quasi-explicit scheme, k_c evaluated using previous $\{\mathbf{u}\}$ will result in overestimated stiffness for the cohesive element. Under monotonically increasing loading, cohesive elements undergo increasing separation from loading step to loading step, which in turn result in decreasing stiffness k_c from step to step. Using k_c evaluated at previous load step yields higher stiffness. This leads to stiffer beam response and tougher fracture behavior (decelerated crack growth). This effect can be significant because once the $T - \Delta$ curve exceeds the elastic point, the separation Δ_n increases quickly with imposed loading, and thus k_c^n and k_c^{n+1} can be rather different, as shown in Figure 4.3.

A related issue is load step control. Insufficiently discretized load step also leads to the abovementioned effects. Cohesive element stiffness slope k_c varies from load step to load step discontinuously in a decreasing fashion, and if the load step is large, k_c^n is much different from k_c^{n+1} . Also this effect is additive; if at load step n k_c is overestimated, this leads to stronger cohesion force and smaller separation, and at the next load step k_c is further overestimated. Reasonable choice of load steps and element size are related; when using refined mesh, a smaller load step is required to achieve consistent results.

4.1.3 Verification

Analytical Solution. This simple problem provides an analytical solution for both the $P-u$ and $a-u$ curves. As shown in Figure 4.4, the $P-u$ relationship consists of two parts: before and after crack extension initiates. During the first stage, the energy release rate G provided by loading has not reached the fracture energy G_{Ic} , and P increases as loading u_{load} increases as

$$u_{load} = \frac{Pa_0^3}{3EI} \quad \text{or} \quad P = \frac{3EIu_{load}}{a_0^3} \quad (4.14)$$

where a_0 is the initial crack length. Crack growth begins at $G = G_{Ic}$,

$$\frac{3Eh^3u_{load}^2}{4a^4} = G_{Ic} \quad \implies \quad u_{load0} = \sqrt{\frac{4a_0^4G_{Ic}}{3Eh^3}}, \quad P_0 = \frac{3EIu_{load0}}{a_0^3} \quad (4.15)$$

During the crack growth stage, the $P-u$ curve is given by

$$P = \frac{3EIu_{load}}{a^3}, \quad \text{where} \quad a = \sqrt[4]{\frac{3Eu_{load}^2h^3}{4G_{Ic}}} \quad (4.16)$$

Convergence Analysis. For cohesive parameters in Table 4.1, a rough estimate of the cohesive zone size is given by a version of expression 4.1, i.e.,

$$\ell_{cz} = \frac{\pi}{8} \frac{EG_{Ic}}{(0.5T_{max})^2} = 0.3mm = 300\mu m \quad (4.17)$$

This predicts that

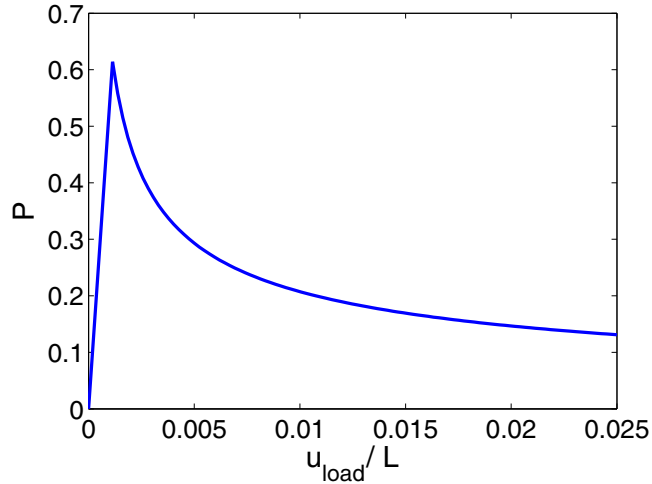


Figure 4.4: Analytical solution for reaction force P at the loading point versus imposed displacement u_{load} .

$$\ell_{\text{cz}} \propto E, G_{\text{Ic}}, 1/T_{\text{max}}^2. \quad (4.18)$$

In order to obtain a converged result within reasonable computation overhead, we wish to employ lower T_{max} value. However, the drawback of this approach is that as the value of T_{max} decreases, the specimen exhibits increasing compliance. Therefore, the very low T_{max} value adopted in reference [56] ($T_{\text{max}} = 0.761\text{MPa} \approx E/90670$) is not employed in this study.

Simulation results are reported for beam discretization of 30, 50, 100, 120 and 150 elements, respectively. The reaction force and imposed displacement relationship $P - u_{\text{load}}$ is plotted in Figure 4.5. As the number of elements increases, system response gradually converges. Due to artificial compliance, the numerical $P - u_{\text{load}}$ response at the hardening part (Equation(4.15)) is always more compliant than the analytical prediction. Mesh refinement does not improve compliance in this particular problem because the area of inserted cohesive elements remains the same for all mesh refinement levels.

Cohesive Zone Size Definition. As illustrated in Figure 4.6, we define the *trailing* point of the cohesive zone as the location where interface separation reaches the critical separation and cohesive traction T vanishes; and the *leading* point of the cohesive zone as the location where the cohesive law *begins* to soften and loses fracture resistance capacity as separation increases, i.e., where the traction T reaches

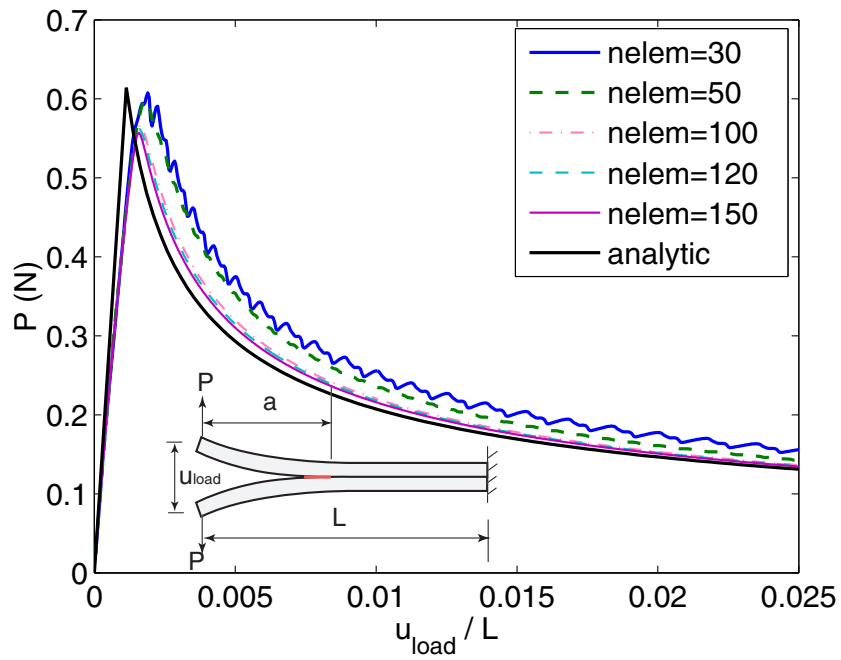


Figure 4.5: Comparison of DCB ($P-u$) response for different meshes with analytical solution.

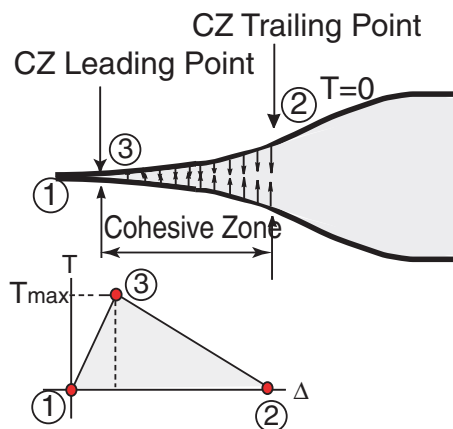


Figure 4.6: Definition of leading point and trailing point.

maximum value T_{\max} . Note that for intrinsic cohesive models it is not practical to define point ① as the leading point for the cohesive zone, because all cohesive elements in the mesh geometry separate to a finite value under loading. Although the separation for the elements outside the high stress region may be infinitesimal, point ① only exists in theory. On the other hand, extrinsic models allow a unique definition of cohesive zone leading point as the first uncracked node along the crack path. This will be discussed later in dynamic problems.

In the numerical application, the cohesive zone is thus defined as the length between the leading and trailing points. However, the definition of crack tip position is somewhat ambiguous when cohesive elements are active at the crack tip region. In reference [56], the authors choose this location somewhat arbitrarily.

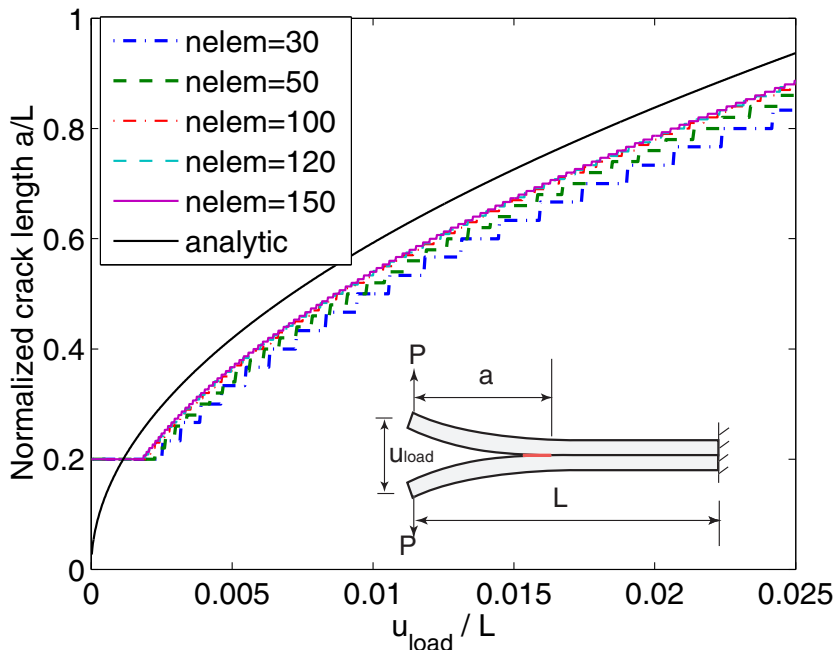


Figure 4.7: Crack growth vs. applied loading; crack tip is defined at the *trailing point* of the cohesive zone.

Crack Growth versus Applied Loading. Figure 4.7 compares the cohesive zone *trailing* point position versus the imposed loading for various meshes and analytical solution. Apparently, results converge as mesh is refined. However, the result does *not* converge to the analytical solution. This is because the analytical solution assumes that the free beam of length a is *clamped* at the end. When cohesive elements are present, the active cohesive elements experience separation, thus the beam in the

cohesive zone length region is actually *not clamped*.

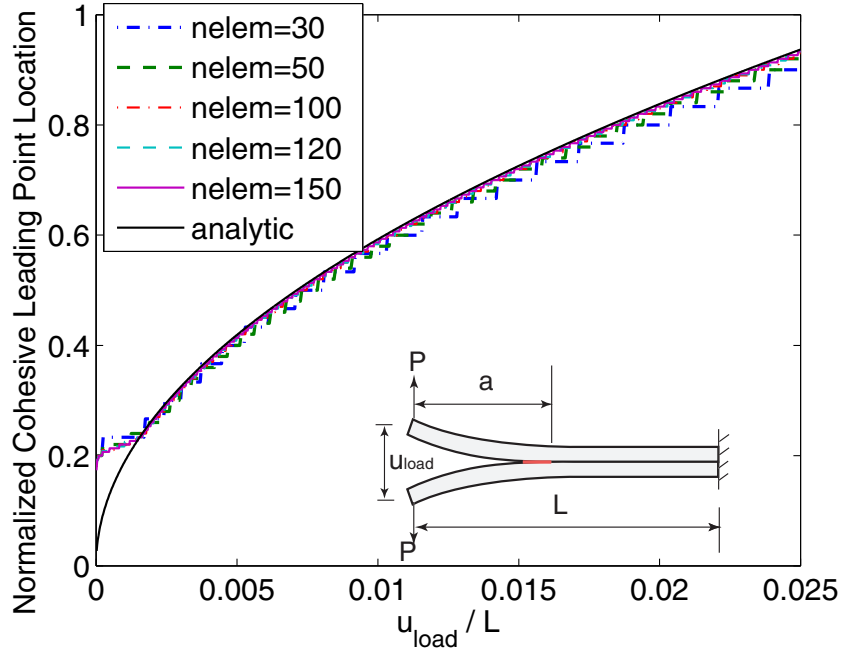


Figure 4.8: Crack growth vs. applied loading; crack tip is defined at the *leading point* of the cohesive zone.

In view of the above consideration, if we define the crack tip as the *leading point* of cohesive zone, result should reflect better agreement with the analytical solution. This is illustrated in Figure 4.8, which indicates both converged result and close approximation to the analytical solution.

Cohesive Zone Size. Figure 4.9 compares the cohesive zone size versus crack extensions for various mesh discretizations. Coarse mesh largely exaggerates cohesive zone size. For progressively refined meshes, the cohesive zone size converges to $l_{cz} \approx 0.5mm$. The oscillation present for all mesh levels is due to the discontinuous nature of cohesive interface separation: at each loading step, we check the separation value at the three Gauss points of each cohesive element. Inside a cohesive element close to the crack tip, once the Gauss point closest to the crack tip experiences the softening behavior, the other two Gauss points will follow in a few loading steps. Therefore, the position of the *leading point* advances. However, during the same loading steps, the location of the *trailing point* does not necessarily advance in exactly the same manner. Therefore an oscillatory behavior is observed.

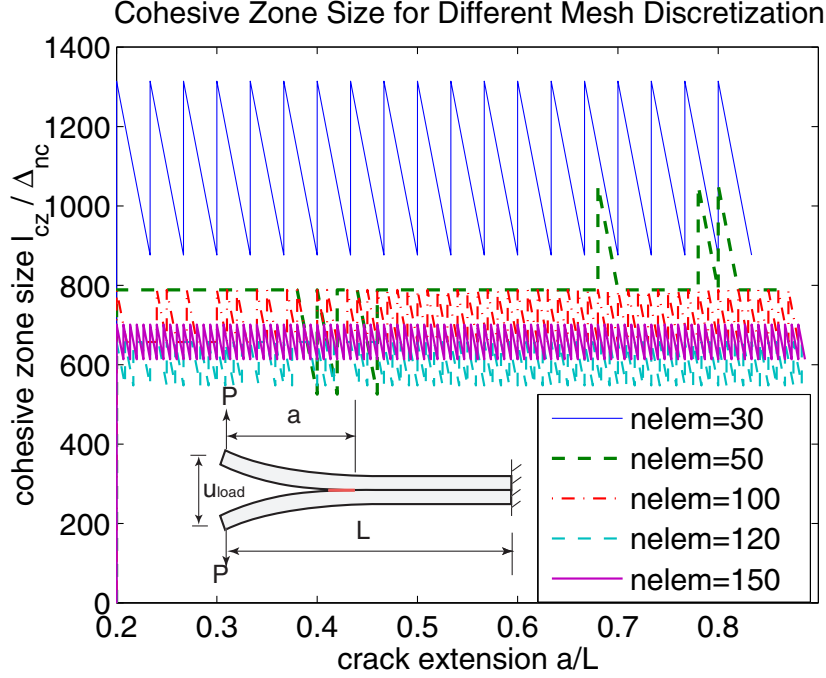


Figure 4.9: Normalized cohesive zone size versus imposed displacement loading for various meshes.

Figure 4.10 illustrates an example of cohesive zone size evaluation. The locations of the leading and trailing points are defined at nodal points. At loading step n , the leading and trailing points are four elements apart, hence $l_{cz} = 4\ell_{elem}$. At loading step $n + 1$, if the leading point advances while the trailing point remains stationary, then $l_{cz} = 5\ell_{elem}$. If the leading point remains stationary while the trailing point advances to the next node, then $l_{cz} = 3\ell_{elem}$. If both the leading and trailing points advance, then $l_{cz} = 4\ell_{elem}$.

Artificial Compliance and Influence of Loading Step. To obtain results closer to the analytical solution, artificial compliance introduced by cohesive elements needs to be reduced. We compare the above result with result for a initially stiffer cohesive law:

$$T_{max} = \frac{E}{200} = 345MPa, \quad \Delta_n = \frac{2G_{Ic}}{T_{max}} = 0.152\mu m. \quad (4.19)$$

Results for $P - u_{load}$ are plotted in Figure 4.11. It clearly shows that before the initial crack a_0 grows, the beam response is softer than analytical solution due to the

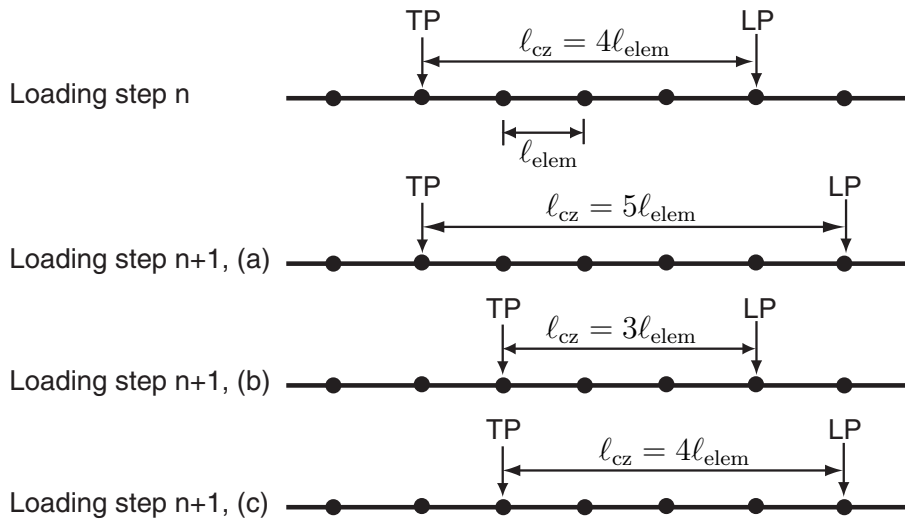


Figure 4.10: Schematic representation of cohesive zone size evaluation where the leading and trailing points are located at nodes; (a) the leading point (LP) advances while the trailing point (TP) remains stationary; (b) the leading point remains stationary while the trailing point advances to the next node; (c) both the leading and trailing points advance.

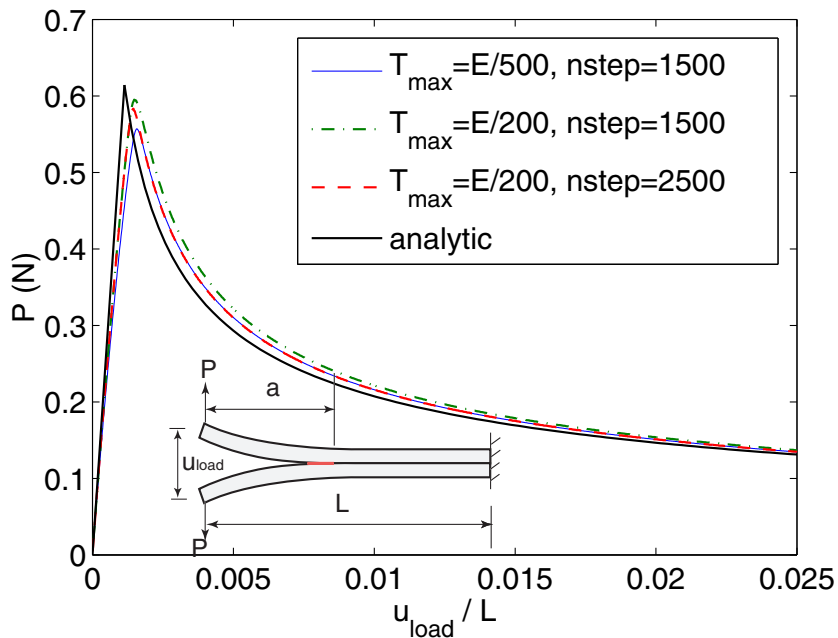


Figure 4.11: Comparison of DCB ($P-u$) response for two different T_{max} choice and different loading step.

presence of cohesive elements *a priori*. With a higher T_{\max}/Δ_n value, this discrepancy is reduced. On the other hand, using a smaller loading step can better capture the maximum load capacity. For $T_{\max} = E/200$, a larger load step (nstep=1500) results in more overshoot compared to a smaller load step (nstep=2500). During the crack extension stage, the two curves for ($T_{\max} = E/500$, nstep =1500) and ($T_{\max} = E/200$, nstep =2500) happen to coincide, because the former curve uses softer cohesive parameter and results in an underestimate of maximum load bearing capacity. These influencing factors intertwine and we must carefully evaluate the contribution of each.

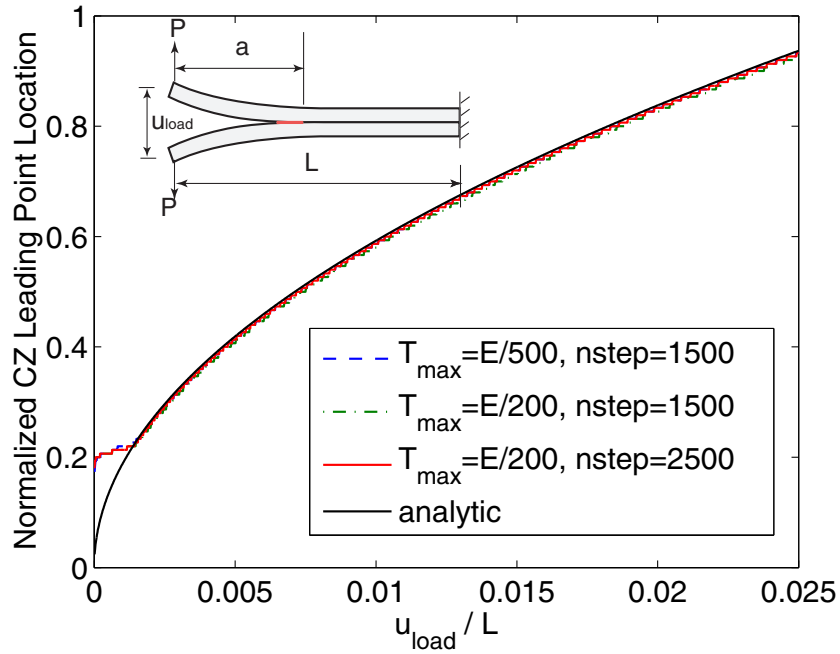


Figure 4.12: Comparison of DCB ($a-u$) response for two different T_{\max} choice and different loading steps. The crack tip is defined as the leading point of cohesive zone.

Figure 4.12 shows the normalized cohesive zone leading point versus loading curve. Although at closer inspection we see that the best approximation is obtained with parameters ($T_{\max} = E/200$, nstep =2500), the influence of the T_{\max} value and nstep are not significant.

4.1.4 Effect of the Cohesive Parameters

The static estimate (Equation (4.1)) indicates that cohesive zone size is proportional to G_{Ic} , and inversely proportional to T_{\max}^2 . In this section, we numerically evaluate

these relationships by conducting two types of parametric study.

1. Keep $G_{Ic} = T_{max}\Delta_n/2$ as constant while varying T_{max}

$$T_{max} = \frac{E}{200}, \quad \frac{E}{500}, \quad \frac{E}{1000}, \quad \frac{E}{1500}, \quad \frac{E}{5000}$$

2. Keep $T_{max} = E/500$ as constant while varying G_{Ic}

$$G_{Ic} = [1, 2, 5, 10]G_0, \quad G_0 = 52.5J/m^2$$

Vary Maximum Cohesive Strength. Results are plotted in Figures 4.13 to 4.16. The following observations are made based on these results:

- The parameter T_{max}/E controls the initial slope of the $P-u$ curve (Figure 4.13). Higher T_{max} value results in stiffer initial ($P-u$) response, thus closer to analytical solution.
- If the crack tip is defined as the trailing point of the cohesive zone, then results are different from the analytical solution, depending on the value of T_{max} , as shown in Figure 4.14. However, if the crack tip is defined as the leading point of the cohesive zone, all results are very close and agree well with the analytical solution, as shown in Figure 4.15.
- At the fixed cohesive energy level G_{Ic} , the cohesive zone size increases with decreasing T_{max} , as shown in Figure 4.16. The results are compared in Table 4.2. However, the relationship between ℓ_{cz} and E/T_{max} is not inverse square, as suggested by Equation (4.1). The difference between the numerical results and Equation (4.1) estimates are within a reasonable range (roughly of the same order) for the cohesive strength ranging between $T_{max} = E/1000$ to $E/500$, and became further apart outside this range.

Table 4.2: Cohesive zone size for various T_{max} values.

E/T_{max}	200	500	1000	1500	5000
ℓ_{cz} (mm)	0.3	0.5	0.65	0.8	1.5
$\ell_{cz_{Eqn.(4.1)}}$ (mm)	0.05	0.3	1.20	2.7	29.9

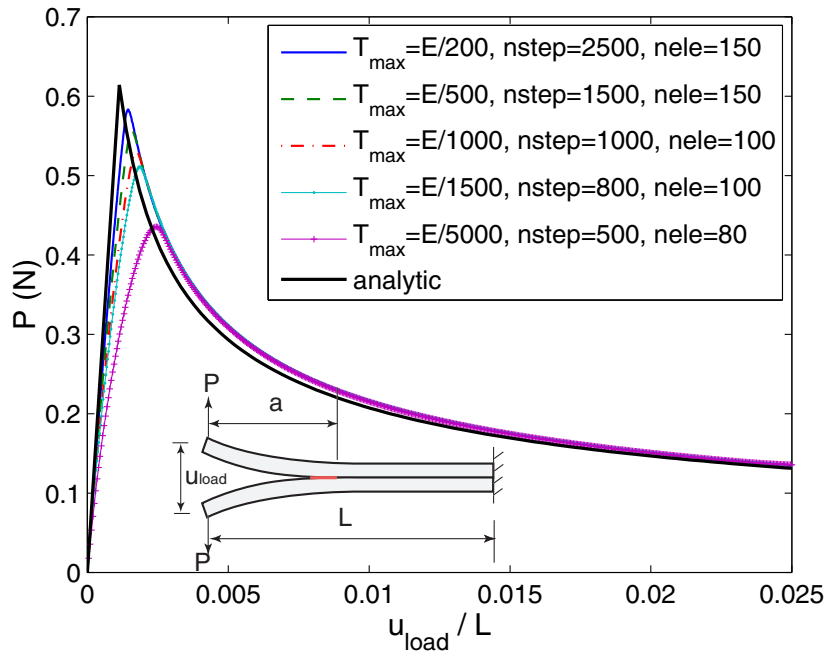


Figure 4.13: Comparison of DCB ($P-u$) response for various T_{\max} values.

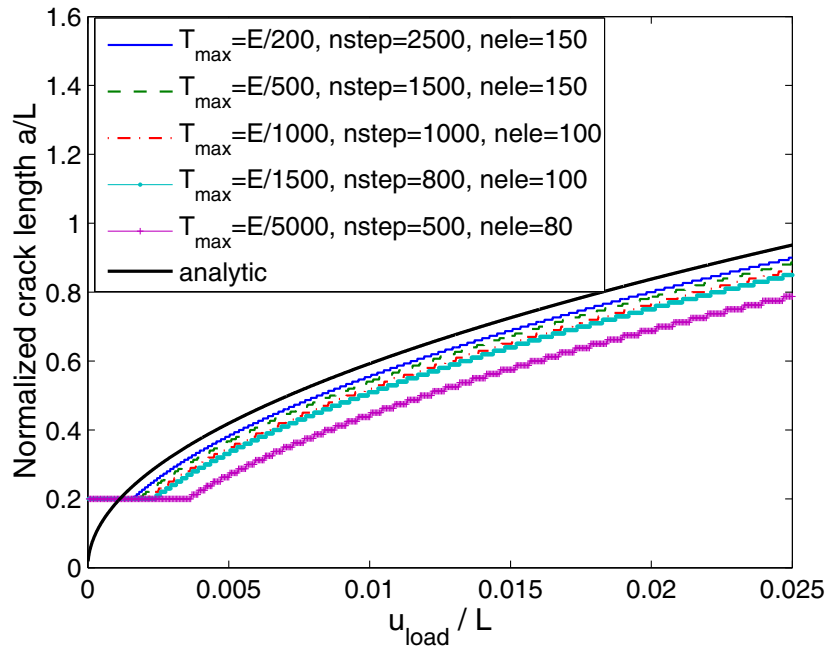


Figure 4.14: Comparison of DCB $a-u$ response for various T_{\max} values. Crack tip is defined as the *trailing point* of cohesive zone.

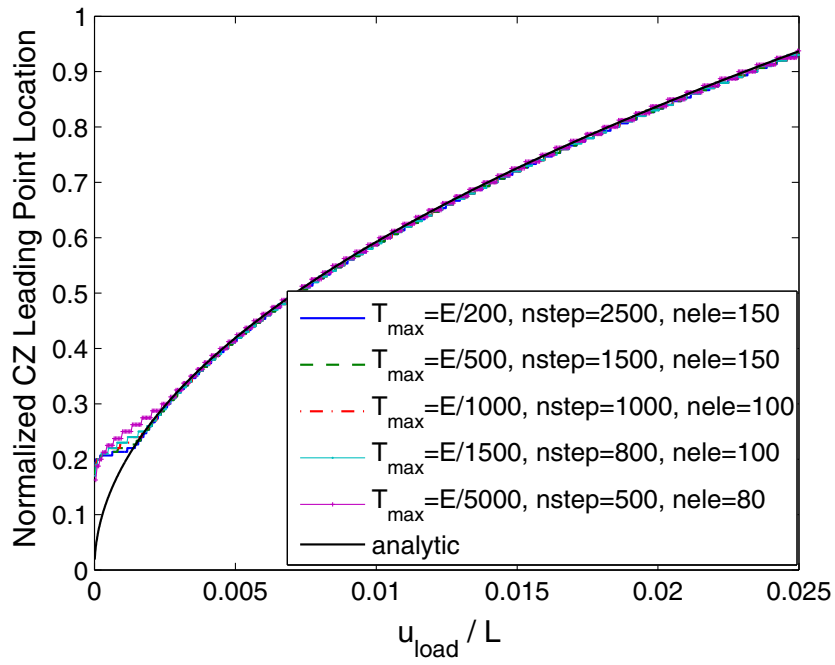


Figure 4.15: Comparison of DCB *leading point* position versus imposed loading for various T_{\max} values.

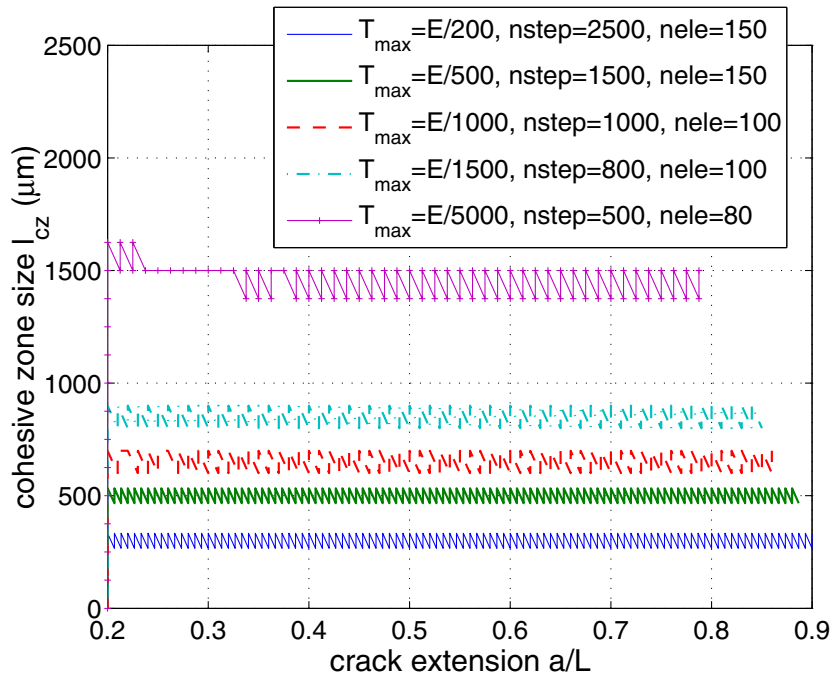


Figure 4.16: Comparison of DCB cohesive zone size versus crack length for various T_{\max} values.

Vary Critical Energy Release Rate. Results are plotted in Figures 4.17 to 4.20. The following observations are made based on the numerical results:

- Increasing G_{Ic} requires higher loading to be applied for crack to grow, as shown in Figure 4.17. The initial slopes for all curves are the same, since value of T_{max}/E is kept the same for these simulations. However, the discrepancy between numerical results and analytical prediction for load bearing capacity before crack extension is more significant for higher cohesive energy case.
- At the same imposed displacement, higher G_{Ic} value results in less crack extension, as shown in Figures 4.18 and 4.19. The crack growth versus loading results agree well with the analytical prediction for each G_{Ic} case when cohesive zone leading point is considered as the crack tip location (Figure 4.19).
- Higher cohesive energy value G_{Ic} results in longer cohesive zone size, as shown in Figure 4.20. The results are compared in Table 4.3. Clearly, the relationship between ℓ_{cz} and G_{Ic} is not linear, as indicated in Equation (4.1).

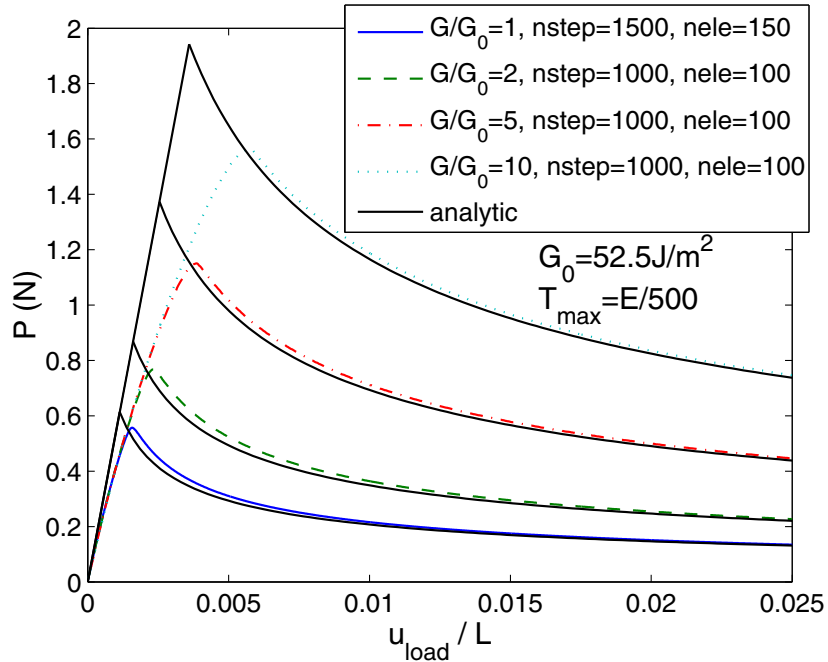


Figure 4.17: Comparison of DCB $P-u$ response for various G_{Ic} values.

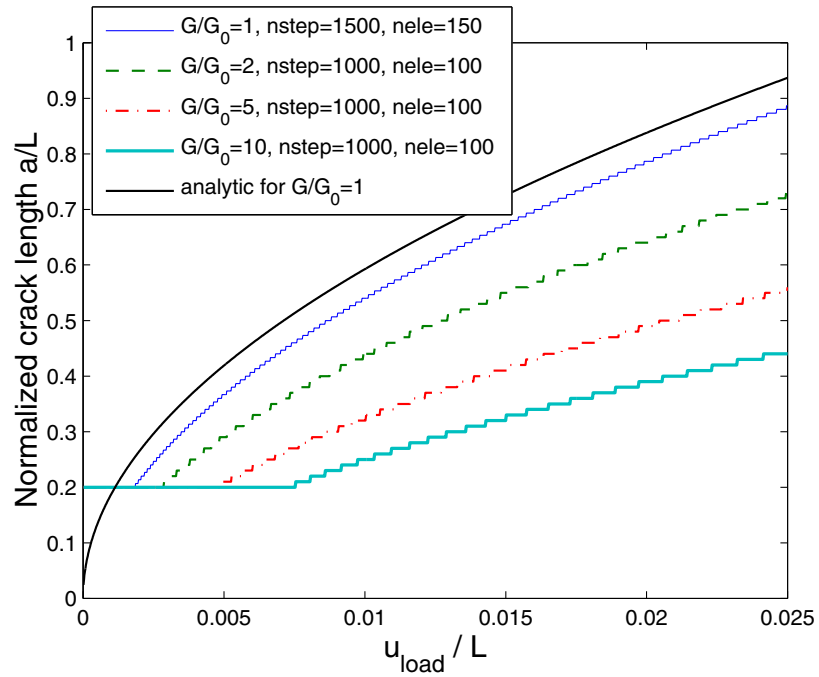


Figure 4.18: Comparison of DCB $a-u$ response for various G_{Ic} values.

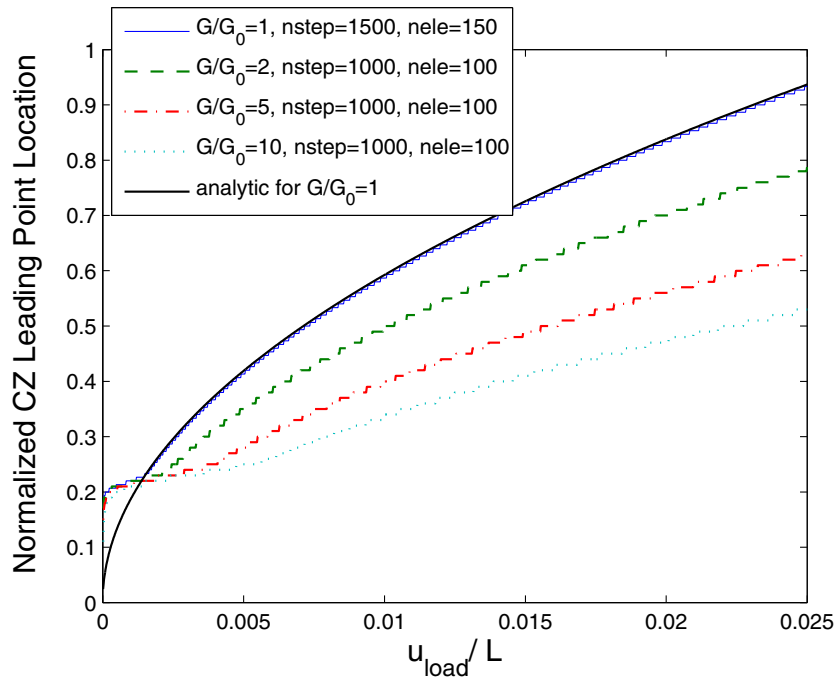


Figure 4.19: Comparison of DCB *leading point* position versus applied displacement loading for various G_{Ic} values.

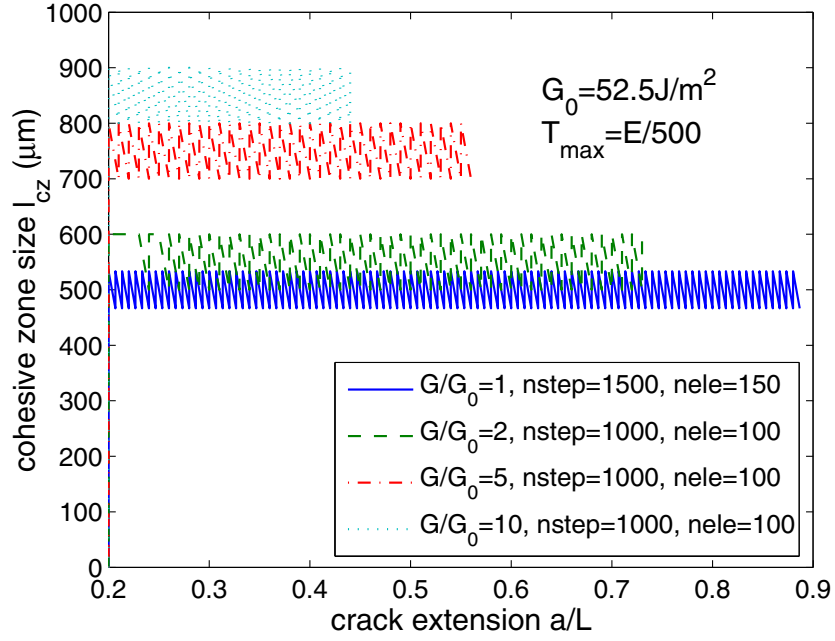


Figure 4.20: Comparison of DCB cohesive zone size versus crack length for various G_{Ic} values.

Table 4.3: Cohesive zone size for various G_{Ic} values.

G_{Ic}/G_0	1	2	5	10
l_{cz} (mm)	0.5	0.55	0.75	0.85
$l_{cz\text{Eqn.}(4.1)}$ (mm)	0.3	0.6	1.5	3.0

4.2 Dynamic Cohesive Zone Size

Clearly, under quasi-static loading for the DCB problem, the cohesive zone size remains constant as the crack grows as long as the material properties are constant for each problem (see Figures 4.9, 4.16, and 4.20). Next we are interested in finding out whether the cohesive zone size varies under dynamic loading condition.

Again, the same DCB specimen is employed in the following investigation, and the material properties are the same as those listed in Table 4.1. Displacement loading control is again employed, but the quasi-static condition is replaced by dynamic loading rates at the cantilever free tips:

$$V_{\text{load}} = 0.2m/s, \quad 1m/s, \quad 5m/s, \quad 10m/s.$$

In this section, we first develop an appropriate numerical method for the dynamic problem and verify dynamic crack growth solution. Afterwards, we look into the cohesive zone size and crack speed behavior for different loading rate cases.

4.2.1 Solution Method and Verification

For the dynamic problem under investigation, the explicit updating scheme outlined in Chapter 2 is still applicable. Because the present investigation employs beam elements, which are different from those used in the rest of the thesis, the difference in procedure is briefly described here.

Solution Method. The explicit updating scheme described in Equations (2.13–2.15) can still be applied. For completeness, the equations are again summarized here

$$\mathbf{u}_{n+1} = \mathbf{u}_n + \Delta t \dot{\mathbf{u}}_n + \frac{1}{2}(\Delta t)^2 \ddot{\mathbf{u}}_n \quad (4.20)$$

$$\ddot{\mathbf{u}}_{n+1} = \mathbf{M}^{-1}(\mathbf{F} + \mathbf{R}_{int_{n+1}} - \mathbf{R}_{coh_{n+1}}) \quad (4.21)$$

$$\dot{\mathbf{u}}_{n+1} = \dot{\mathbf{u}}_n + \frac{\Delta t}{2}(\ddot{\mathbf{u}}_n + \ddot{\mathbf{u}}_{n+1}) \quad (4.22)$$

where the unknowns \mathbf{u} , $\dot{\mathbf{u}}$ and $\ddot{\mathbf{u}}$ should incorporate both displacement and rotation degrees of freedom at each beam node (see Figure 4.2). Moreover, the beam element is discretized with “lumped mass” associated with the rotary inertia. The lumped (diagonal) mass matrix for a 2-node Euler beam element is

$$[\mathbf{m}]^e = \frac{m}{2} \begin{bmatrix} 1 & 0 & 0 & 0 \\ 0 & \ell_e^2/24 & 0 & 0 \\ 0 & 0 & 1 & 0 \\ 0 & 0 & 0 & \ell_e^2/24 \end{bmatrix} \quad (4.23)$$

where $m = \rho A \ell_e$ is the total element mass. The above expression assumes that the mass moment of inertia of a uniform slender bar of length $\ell_e/2$ and mass $m/2$ spinning about one end (see [22], p. 373).

In addition, the internal force vectors \mathbf{R}_{int} and cohesive force vector \mathbf{R}_{coh} in Equation (4.21) also include the moment contribution. These modifications are straightforward as the shape functions used in computing element stiffness matrix $[\mathbf{k}]^e$ and element cohesive force $\mathbf{R}_{\text{coh}}^e$ automatically account for the rotation contribution.

To achieve stable numerical results in the explicit dynamic procedure with cohesive elements, the time step is chosen as

$$\Delta t = 0.1 \ell_e / C_d \quad (4.24)$$

where $C_d = \sqrt{E/\rho} = 5055 \text{ m/s}$ is the dilatational wave speed. The coefficient 0.1 is adopted to ensure a stable result at the presence of cohesive elements. Based on the static problem investigation, the beam is discretized into 100 beam elements.

Code Verification. To verify the numerical procedure, we simulate crack propagation in the DCB specimen under a slow loading velocity at the free tip. When the loading is sufficiently slow, the inertia effect is negligible and crack growth behavior should approach that of the quasi-static problem. We verify this assumption through the crack extension vs. displacement loading relationship and crack tip velocity history.

A loading rate of $V_{\text{load}} = 0.2 \text{ m/s}$ is chosen, and the crack length vs. loading ($a - u_{\text{load}}$) relationship is plotted in Figure 4.21. The cohesive zone leading point position at each loading step is very close to that of the quasi-static solution. We also notice that similarly to the quasi-static problem, the cohesive zone trailing point lags behind the trailing point for each loading step. The difference between the two locations, defined as dynamic cohesive zone length, will be reviewed in the next section.

Figure 4.22 plots the crack speed profile for the $V_{\text{load}} = 0.2 \text{ m/s}$ problem. Before crack initiation, crack speed remains 0, and then rises to a finite value of about 15 m/s ,

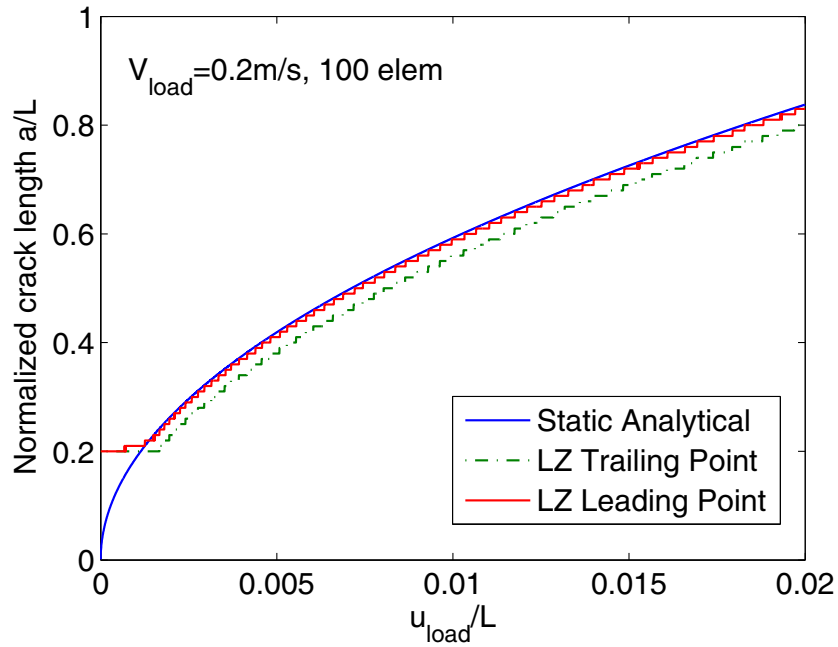


Figure 4.21: Crack tip location vs. applied displacement at free tip for the dynamic DCB problem and loading rate $V_{\text{load}} = 0.2\text{m/s}$.

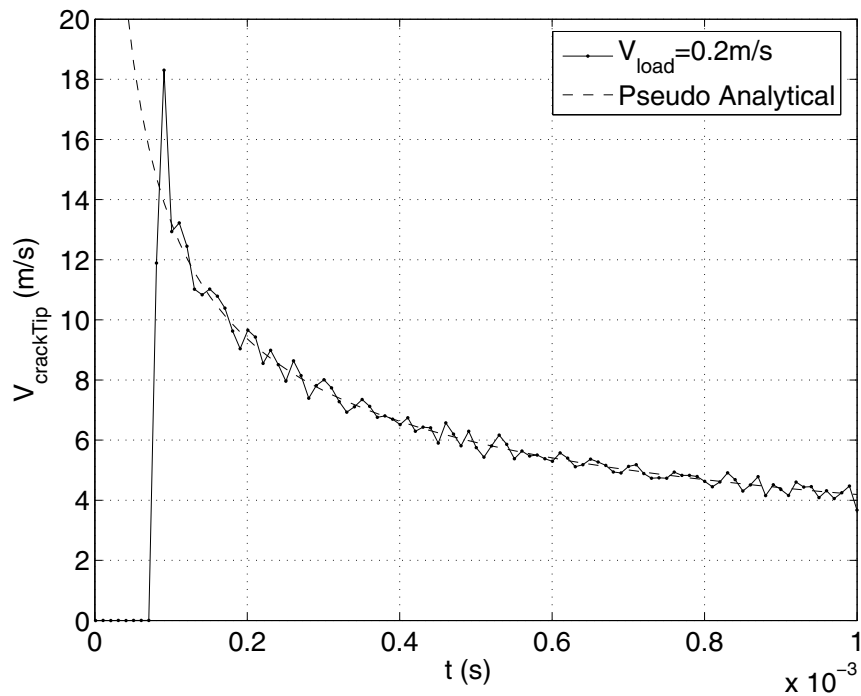


Figure 4.22: Crack tip velocity history for dynamic DCB problem at loading rate $V_{\text{load}} = 0.2\text{m/s}$. Pseudo analytical result indicates corresponding quasi-static case result derived from $a-u_{\text{load}}$ curve shown in Figure 4.21.

and gradually decreases afterwards. The crack speed ranges between 5 to 15m/s, which is relatively slow for a dynamic crack problem. As the crack growth profile is very close to a quasi-static case, we further derive the corresponding “pseudo” crack tip velocity v_{pseudo} for the quasi-static case based on the analytical $(a - u_{load})$ relationship (Equation (4.16)) as shown in Figure 4.21.

$$\begin{aligned}
v_{pseudo} &= \frac{da}{dt_{pseudo}} = \frac{d}{dt_{pseudo}} \left(\sqrt[4]{\frac{3Eu_{load}^2 h^3}{4G_{Ic}}} \right) \\
&= \sqrt[4]{\frac{3Eh^3}{4G_{Ic}}} \frac{1}{2\sqrt{u_{load}}} \frac{du_{load}}{dt} = \frac{a}{\sqrt{u_{load}}} \frac{1}{2\sqrt{u_{load}}} V_{load} \\
&= \frac{a}{2u_{load}} V_{load} = \frac{a}{2t_{pseudo}}
\end{aligned} \tag{4.25}$$

In the above expression, the subscript “pseudo” for v and t refers to the fact that although the quasi-static problem does not involve time history, we use the slow loading rate (here taken as $V_{load} = 0.2m/s$) as a “pseudo” loading rate and compute the pseudo-dynamic result based on the $(a - u_{load})$ relationship for the quasi-static analysis. Figure 4.22 thus indicates that the crack velocity history for the $V_{load} = 0.2m/s$ dynamic problem approaches that of a corresponding quasi-static case very well.

Figure 4.23 plots the reaction force P at the loading point versus imposed displacement u_{load} for the $V_{load} = 0.2m/s$ case. The analytical solution of the $(P - u_{load})$ curve for the quasi-static problem is also included for comparison purposes. The overall reaction force history mimics that of the quasi-static case. It also exhibits high-frequency oscillation, which is due to the inertia effect and the existence of cohesive elements.

We regard the above comparisons with the analytical solution as verification evidence that the numerical procedure is correct. Next, we proceed to investigate the cohesive zone size dependence on loading rate.

4.2.2 Effect of Loading Rates

We investigate the following dynamic crack growth events with four different velocity loading rates at the cantilever free tip:

$$V_{load} = 0.2m/s, \quad 1m/s, \quad 5m/s, \quad 10m/s.$$

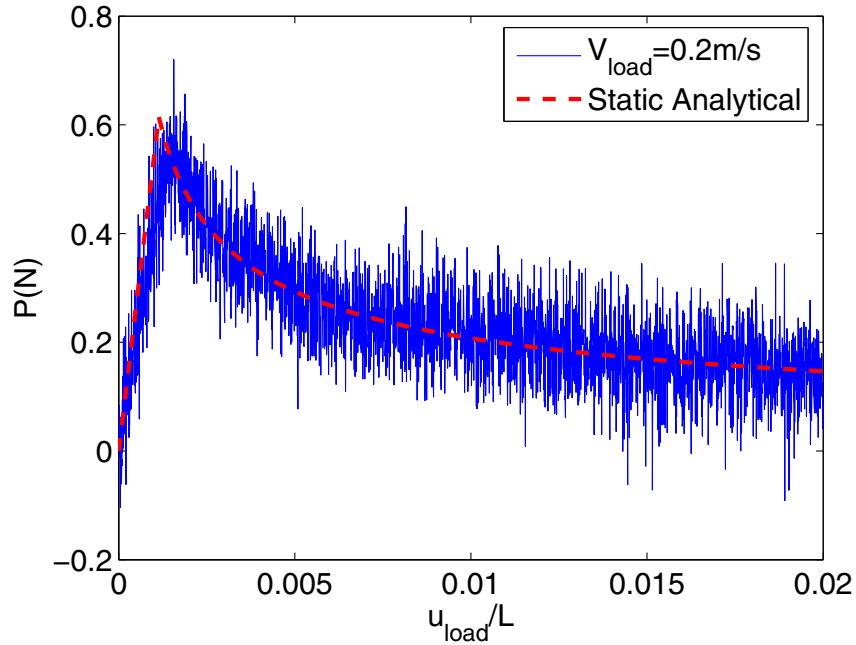
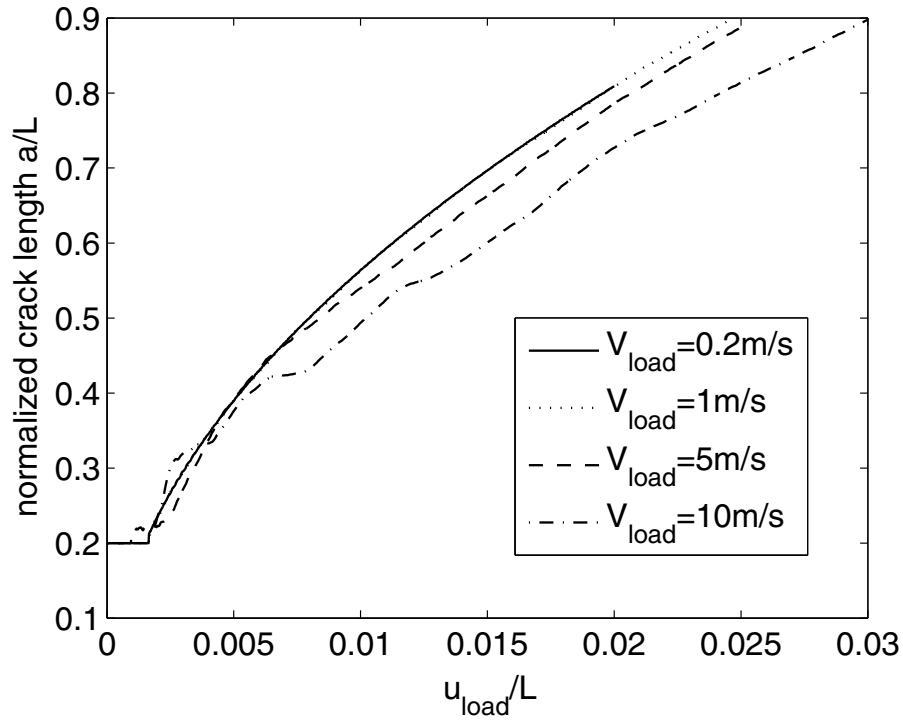


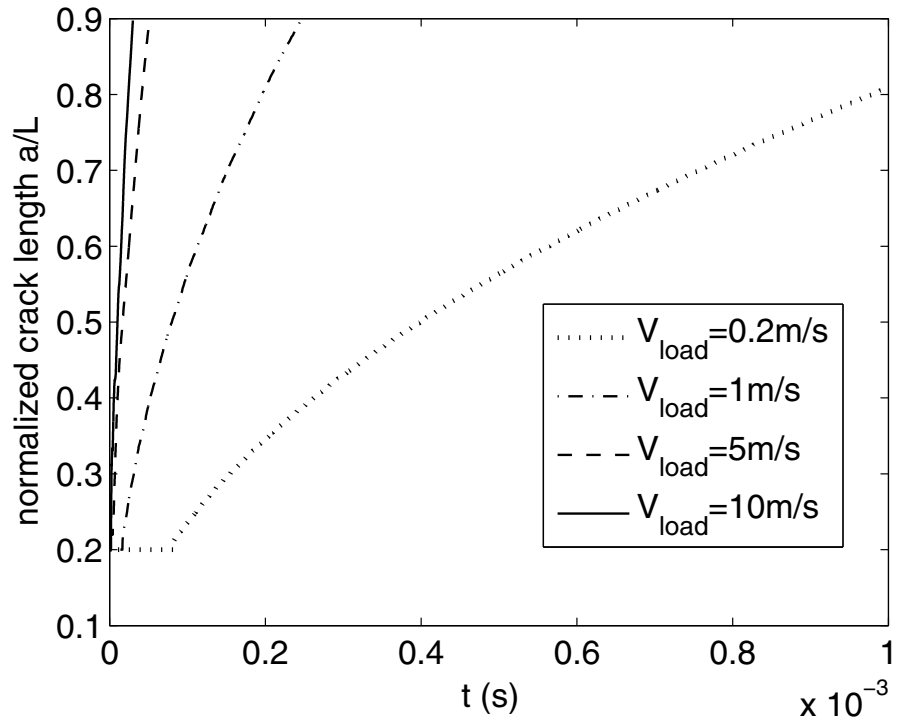
Figure 4.23: Numerical result for reaction force P at the loading point versus applied displacement u_{load} for $V_{\text{load}} = 0.2\text{m/s}$ case compared to analytical solution for the quasi-static problem.

which spans a loading rate difference of 500 times. As the loading rate increases, the inertia effect becomes more significant and crack velocity usually exhibits stronger oscillation. These effects are shown in Figures 4.24–4.29.

Crack Growth History. Figure 4.24 (a) shows crack length, defined as the location of cohesive zone trailing point, vs. imposed displacement loading. Crack growth profiles at slow loading rates ($V_{\text{load}} = 0.2\text{m/s}$ and $V_{\text{load}} = 1\text{m/s}$) are smooth and very close to the quasi-static case. As the loading rate increases, the crack growth exhibits more oscillation. For the same displacement applied at the free tip, the crack tip location for a higher loading rate is *behind* that of a lower loading rate. This is due to the dynamic effect; it takes time for the loading at free tip to “propagate” its effect to the crack tip and drive the crack to grow. For the static case, the loading at the free tip can instantaneously translate to tearing effect at the crack tip, as no time is involved. For dynamic problems, however, it takes time for the same effect to occur. Figure 4.24 (b) more intuitively reveals the crack growth vs. time for the different loading cases. Clearly, at high loading, crack advances faster, as the slope of each curve indicates.



(a)



(b)

Figure 4.24: Crack length history for loading cases $V_{load} = 0.2$ m/s, 1m/s, 5m/s, 10m/s; (a) normalized crack length vs. normalized imposed displacement. Solid line for $V_{load} = 0.2m/s$ and dotted line for $V_{load} = 1m/s$ are virtually indistinguishable; (b) normalized crack length vs. time.

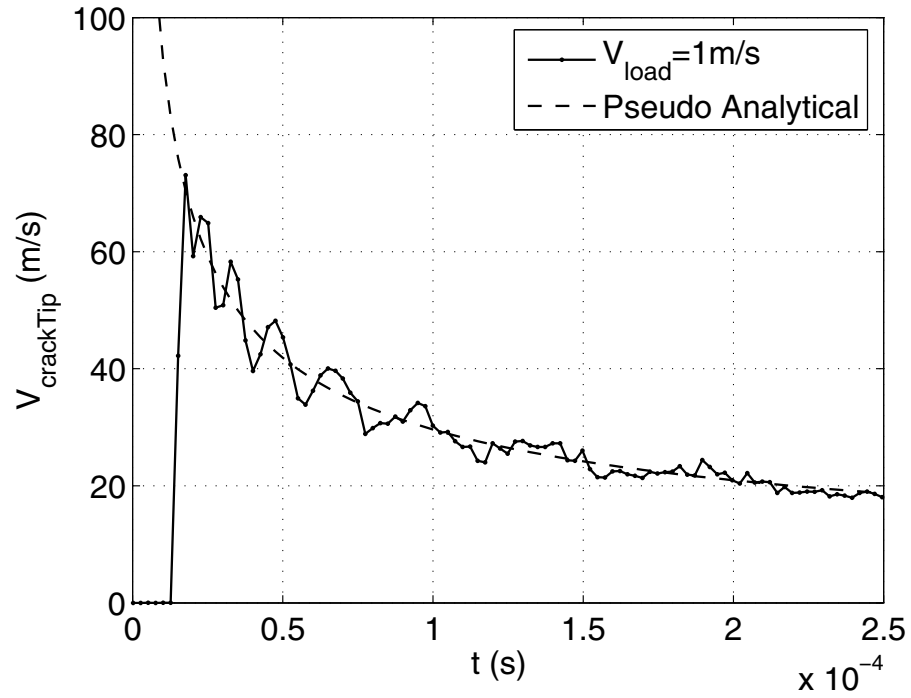


Figure 4.25: Crack tip velocity history for dynamic DCB problem at loading rate $V_{load} = 1m/s$.

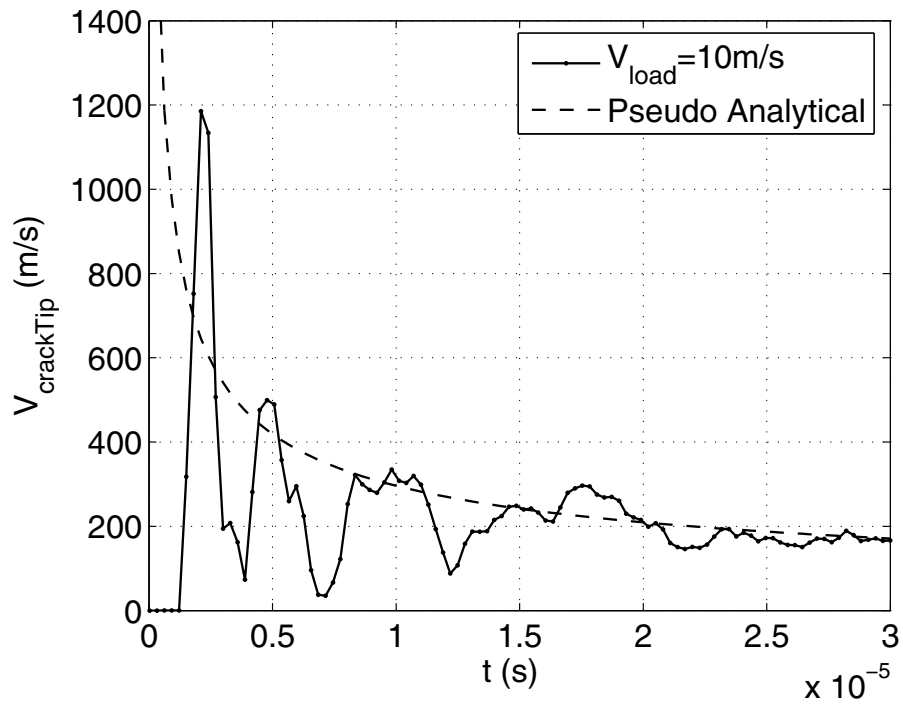


Figure 4.26: Crack tip velocity history for dynamic DCB problem at loading rate $V_{load} = 10m/s$.

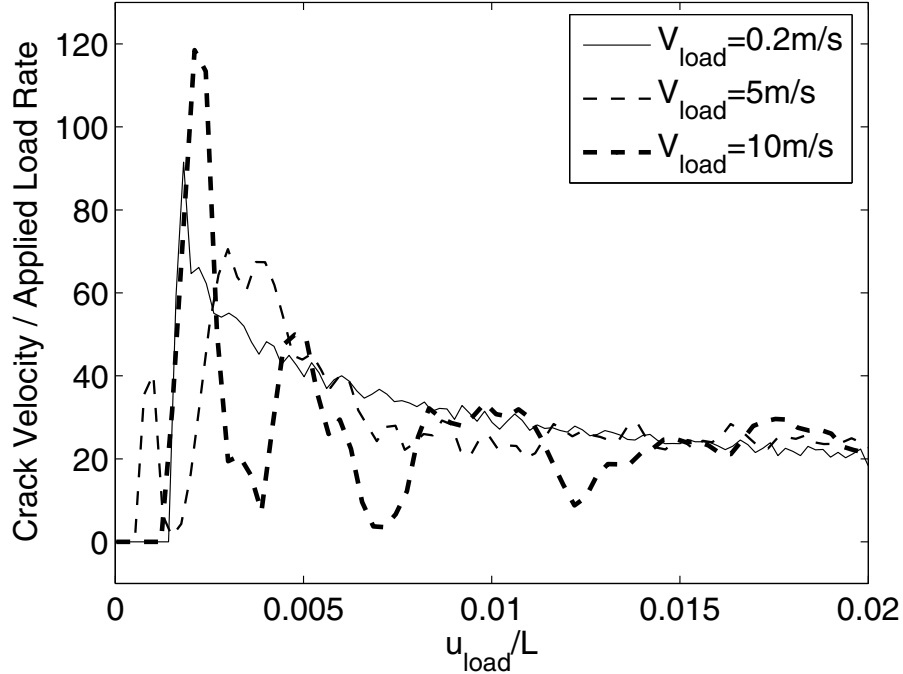


Figure 4.27: Comparison of crack velocity history for loading cases $V_{\text{load}} = 0.2 \text{ m/s}$, 1 m/s , 5 m/s , 10 m/s . Velocity profile is scaled by the applied loading rate of each case.

Crack Tip Velocity History. Figures 4.25 and 4.26 plot crack tip velocity for $V_{\text{load}} = 1 \text{ m/s}$ and $V_{\text{load}} = 10 \text{ m/s}$, respectively. The “pseudo” velocity described in previous section for each case is also provided for comparison. At a low loading rate ($V_{\text{load}} = 1 \text{ m/s}$), crack velocity exhibits periodic oscillation around the pseudo analytical results, and the oscillation gradually dies out in the long run. At a high loading rate ($V_{\text{load}} = 10 \text{ m/s}$), the highest crack velocity reaches around 1200 m/s , which is around 40% of the Rayleigh wave speed (2820 m/s). Such dynamic behavior undoubtedly is accompanied by more oscillation in the crack profile. The crack velocity in Figure 4.26 varies significantly, although we can still discern its trend of following around the pseudo analytical solution, especially at a later stage of the crack growth.

Crack growth velocity is directly related to the loading velocity. Figure 4.27 compares the crack velocity profiles for $V_{\text{load}} = 0.2, 5$ and 10 m/s cases by scaling each crack velocity with its respective loading rate. At crack initiation, crack velocity is about 80 to 100 times that of the loading rate, and then gradually decreases to about 30 times that of the loading rate.

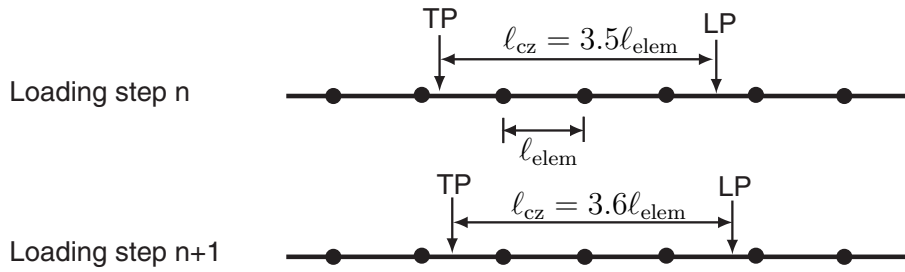


Figure 4.28: Schematic representation of cohesive zone size evaluation where the leading and trailing points are interpolated between nodes.

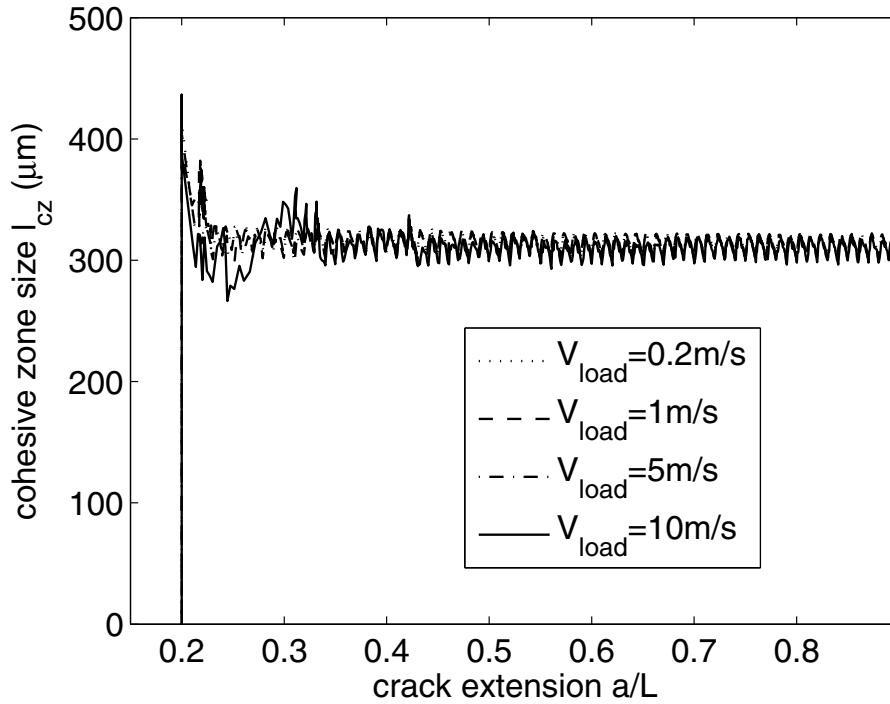


Figure 4.29: Cohesive zone size for loading cases $V_{load} = 0.2, 1.5$ and 10 m/s .

Cohesive Zone Size. *The dynamic cohesive zone size is calculated as the difference between the leading and trailing points of the cohesive zone.* The locations of the leading and trailing points are interpolated between nodes, as schematically shown in Figure 4.28. At loading step n , $l_{cz} = 3.5l_{\text{elem}}$. At loading step $n + 1$, both the leading and trailing points advance, and $l_{cz} = 3.6l_{\text{elem}}$. This approach provides a more precise evaluation of the cohesive zone size compared to the approach shown in Figure 4.10 in Section 4.1.3.

For different loading cases, the cohesive zone size is retrieved and compared in Figure 4.29. Despite a very different loading rate, the cohesive zone size results are virtually the same for all cases except for the brief crack initiation stage. Small oscillation (around $20\mu m$) appears due to numerical effects, and are the same for all cases.

Discussion. The fact that cohesive zone size is independent on the loading rate appears to be counterintuitive at first. However, when we closely review the solution procedure, it becomes clear that rate-dependent behavior is absent from the constitutive law of the material description itself, thus we may not expect to find rate-dependent dynamic behavior in cohesive zone. In the next section, we investigate the rate effect that is built into the cohesive law, which results in rate-dependent crack growth behavior as well as rate-dependent cohesive zone size.

4.3 Rate Effects

Introducing rate-dependence in the cohesive modeling of fracture has been an active research area [95, 59, 118]. The original cohesive model introduced by Dugdale [27] and Barenblatt [6] is rate-independent, for which the cohesive traction depends only on cohesive interface separation. However, many material exhibits rate sensitivity during fracture process. For example, Sharon and Fineberg [97] reported that higher energy is dissipated for a crack to propagate at faster speed in brittle materials like PMMA, as shown in Figure 4.30 (a). As the crack velocity increases from 200m/s to 650m/s, energy flux increases about 9 to 10 times in an exponential fashion.

The apparent rate-toughening behavior, i.e., fracture energy increasing with crack speed, is explained by the formation of multiple micro-cracks in brittle materials. At higher crack speed, more micro-cracks appear along the main crack, thus increasing total fracture surface area. Figure 4.30 (b) illustrates a roughly linear relationship between the total crack surface area and energy input. A detailed numerical study of

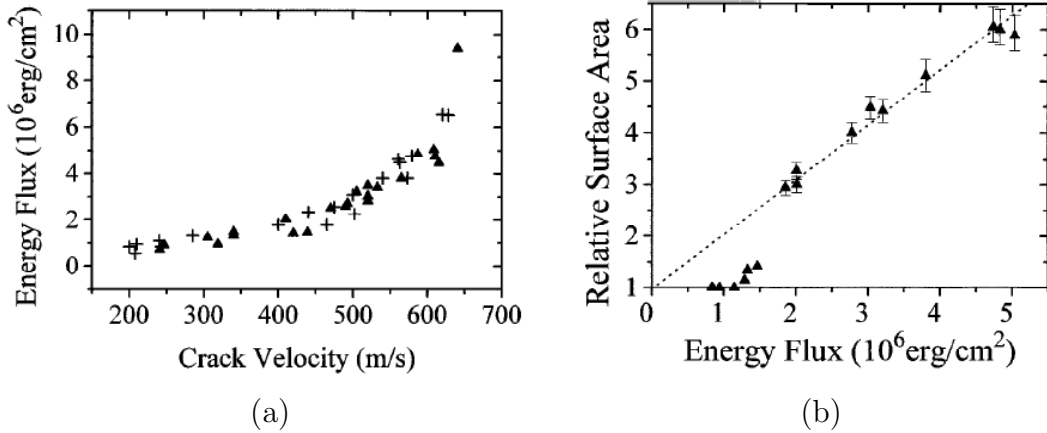


Figure 4.30: Rate-dependent fracture behavior in dynamic crack propagation in PMMA [97]. (a) the energy flux into the crack tip (G) as a function of steady-state crack velocity (Fig. 3 in [97]); (b) the relative surface area (A) created by a crack as a function of the energy flux G into the crack tip. The linear dependence above v_c indicates that nearly all of the energy goes into creating new surface, while the energy cost per unit surface area is unchanged. A linear fit (line) to the data yields $A = 1.0 + 1.05 \times 10^{-6}G$ (Fig. 4 in [97]).

such micro-branching phenomena involved in experiment [97] is studied in Chapter 5 and reference [117], using an extrinsic rate-independent cohesive model. In the present study, on the other hand, we adopt a rate-toughening model to investigate the crack evolution and cohesive zone size.

4.3.1 Phenomenological Rate-dependent Models

As discussed above, the rate-toughening in brittle materials at a higher crack speed can be successfully captured by using appropriate cohesive model [117], albeit rate-independent. In the present study, however, we approach the dynamic crack rate-dependency using a *phenomenological* rate-dependent models to represent the rate-toughening behavior without resorting to simulating micro-crack details.

Rate-dependent Model Inspired by Polymer Literature. Rate-dependent fracture behavior in viscoelastic materials, such as polymers, has been extensively studied experimentally [7, 8, 34, 40, 65, 103]. The velocity-dependent critical energy release rate (G) in a peeling test typically exhibits power-law relationship, for example [34],

$$\frac{G}{G_0} = 1 + \left(\frac{v}{v_0}\right)^n \quad (4.26)$$

where G_0 is the critical energy release rate at a peeling velocity v approaching zero, v_0 denotes the reference peeling velocity at which the critical energy release rate doubles to G_0 , and the exponent n is a parameter determined from experiments. These parameters may also be temperature dependent, due to the viscoelastic behavior.

Rate-dependent Model Proposed by Zhou and Coworkers. Motivated by the exponential-type energy-crack speed behavior shown in Figure 4.30 (a), reference [118] presents the following rate-toughening cohesive zone model

$$G_c(v_{\text{crack}}) = G_0 \log\left(\frac{v_L}{v_L - v_{\text{crack}}}\right) \quad (4.27)$$

which directly correlates fracture energy G_c increase with macroscopic crack tip velocity v_{crack} . This model uses two parameters G_0 and v_L , which are obtained using curve fitting to PMMA dynamic fracture experimental data [97]. This approach harbors the following assumptions:

- In the experiment, all input energy (strain energy) converts into fracture energy.
- Kinetic energy is negligible.
- Fitting curve indicates $G_c = 0$ at $v_{\text{crack}} = 0$ while static PMMA fracture energy is around $300N/m$.

Rate-dependent Model Proposed by Zhang and Paulino. Some of the above considerations are arguable, yet not particularly pertinent to our current investigation, therefore not to be further debated. In the present study, we propose a more intuitive rate-toughening cohesive model

$$G_c(v_{\text{crack}}) = G_0 \alpha \frac{v_{\text{crack}}}{v_0} \quad (4.28)$$

where G_0 is the static fracture energy, while parameters α and v_0 control rate-dependency behavior. For $\alpha = 1$, the model degrades to a rate-independent model. Figure 4.31 represents such behavior where the rate-dependent fracture energy increases with crack velocity with parameters $\alpha = 1.5$ and $v_0 = 100m/s$. We also point

out that in this model, the two parameters α and v_0 are not independent. They can be combined into a single parameter by introducing

$$\alpha^{1/v_0} = e^{\log_\alpha/v_0} \quad (4.29)$$

Figure 4.31 indicates that fracture energy retains a static value for $v_{\text{crack}} = 0$, and increases exponentially with higher crack velocity, which is similar to Figure 4.30 (a). Because no specific experimental data is available for the current investigation, the present study uses hypothetical parameter values. For problems with experimental data, we may consider different velocity-toughening behavior.

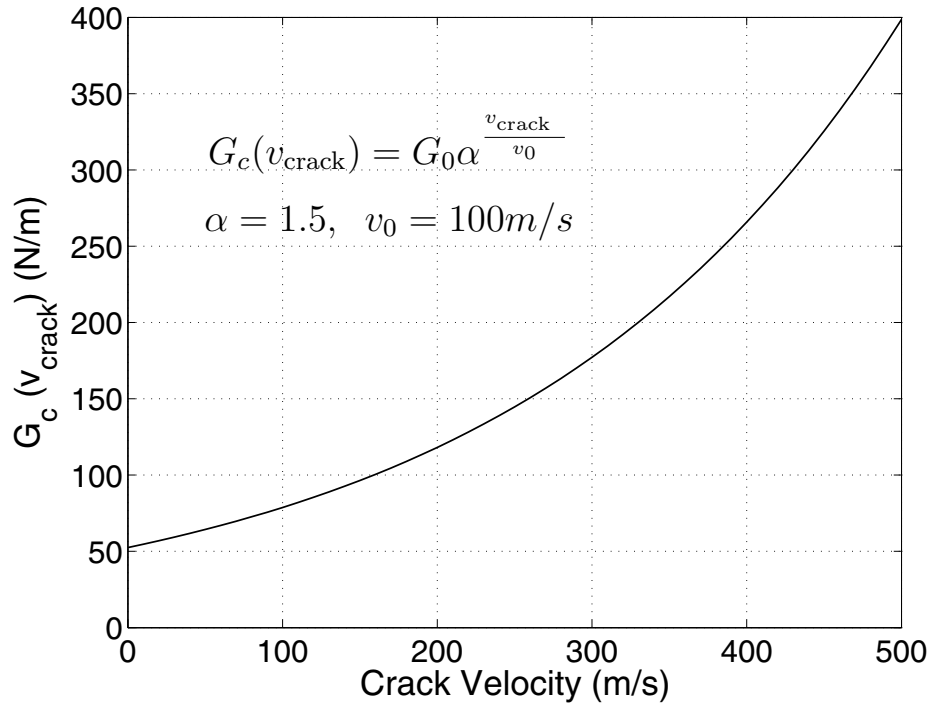


Figure 4.31: Phenomenological rate-dependent cohesive model.

Cohesive Zone Shape. We next choose the shape of the rate-dependent cohesive model. A bilinear intrinsic model is used throughout the study. Among the three cohesive parameters, i.e., cohesive energy G , cohesive strength T_{max} and critical separation δ_c , only two are independent, and $G = 0.5T_{\text{max}}\delta_c$. Therefore, fracture energy increasing with crack velocity implies either T_{max} , or δ_c , or both, increasing with crack velocity. Therefore, the increase of fracture energy can be translated into an increase of critical separation. Experiments do not indicate much increase of

critical strength of material (i.e., cohesive strength) at a higher crack velocity [118]. For example, for ceramic, failure strength increases nominally (10 to 15%) when strain rate increases from $40s^{-1}$ to $5000s^{-1}$. On the other hand, from a physics point of view, at a higher crack speed, more microscopic crack formation surrounding macroscopic crack tip region implies a larger damage zone. Therefore, we adopt the following rate-dependent critical separation model:

$$\delta_c(v_{\text{crack}}) = \delta_0 \alpha \frac{v_{\text{crack}}}{v_0} \quad (4.30)$$

where δ_0 is the static critical separation, i.e., in rate-independent. Figure 4.32 illustrates such concept. Note that cohesive strength T_{max} remains constant as the shape of the cohesive model “elongates” with increasing velocity.

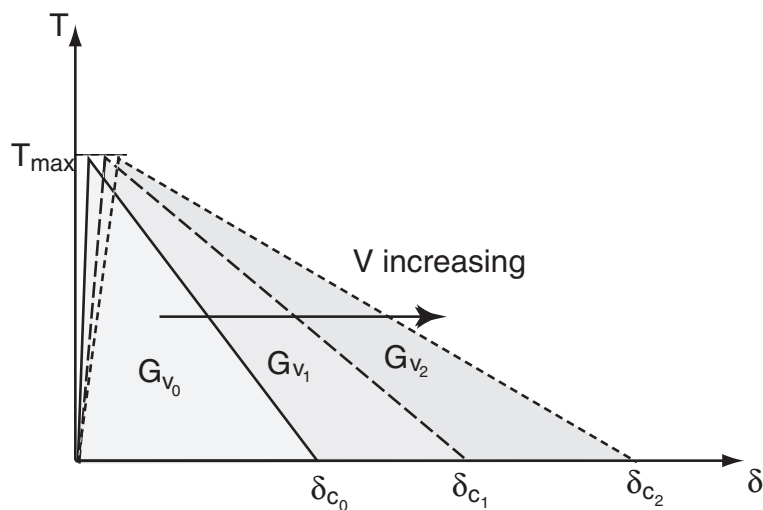


Figure 4.32: Rate-dependent intrinsic bilinear cohesive zone with constant cohesive strength and varying fracture energy.

4.3.2 Numerical Implementation Issues

The proposed rate-toughening model (Equation (4.28)) that directly correlates fracture energy increase with higher crack velocity is both intuitive and straightforward, as well as supported by experimental observations [97]. However, such a method poses difficulty in numerical implementation for an arbitrary dynamic fracture problem, especially when multiple crack paths are present.

Ideally, cohesive parameters in such simulations are no longer constant, but rather varying during simulation, depending on the instantaneous crack velocity. When more

than one crack front is present, it is difficult, and sometimes impractical for numerical studies, to track each crack tip and compute its respective velocity. Even for a simpler case involving a single crack, as in the present study, accurate computation of crack speed and subsequent assignment of cohesive parameters can still be challenging. For example, Figure 4.26 indicates that crack velocity oscillates very rapidly between $1200m/s$ and $100m/s$ during the beginning stage. Following Equation (4.28), such oscillation results in fracture energy variation of over 100 times along a short distance of crack path. If such method is directly applied, the numerical results can be rather erratic since the definition of critical separation varies too fast for a consistent track of crack tip position and consequently crack speed calculation.

Such a method, therefore, applies best in a single crack problem where crack speed variation is moderate, as in the work by Zhou et al. [118]. In the present study, we simplify the implementation by pre-assigning cohesive properties for all cohesive elements, instead of computing the parameters during simulation. Such consideration is adopted primarily to avoid the oscillation issue discussed above. Two approaches are considered:

- *Pre-assign constant rate-toughening cohesive properties along crack path.* This approach first adopts the mean crack velocity obtained from the *rate-independent* dynamic investigation as the average crack speed, then retrieves corresponding rate-toughening fracture energy following Equation (4.28), and assigns the *same* cohesive parameter to *all* cohesive elements along the crack path.
- *Pre-assign pseudo-analytical rate-toughening cohesive properties along crack path.* This approach first computes the *pseudo-analytical* crack velocity for different loading cases, as explained in Section 4.2.1. Next, the rate-dependent cohesive properties are obtained based on the *assumed* crack velocity. Cohesive properties obtained this way possess a continuously varying profile along the crack path, thus avoiding the excessive oscillation discussed above.

4.3.3 Constant Cohesive Rate-toughening

The average crack velocity in a dynamic DCB problem for different loading cases ($V_{load} = 0.2, 1, 5, 10m/s$) is obtained from the rate-independent cohesive model investigation in Section 4.2. According to the rate-toughening model of Equation (4.28) with parameters $\alpha = 1.5$ and $v_0 = 100m/s$, the corresponding fracture energies for these case are listed in Table 4.4:

Table 4.4: Average crack velocity from rate-independent analysis and corresponding rate-toughening fracture energy

V_{load} (m/s)	0.2	1	5	10
Avg. v_{crack} (m/s)	7	29	150	250
$G(v_{\text{crack}})$ (N/m)	54.0	59.0	96.4	144.7

Apparently at a low applied velocity the rate-toughening effect is almost negligible. Therefore, we investigate the crack growth behavior and cohesive zone size for the following loading rates: $V_{\text{load}} = 1, 5, 10\text{m/s}$.

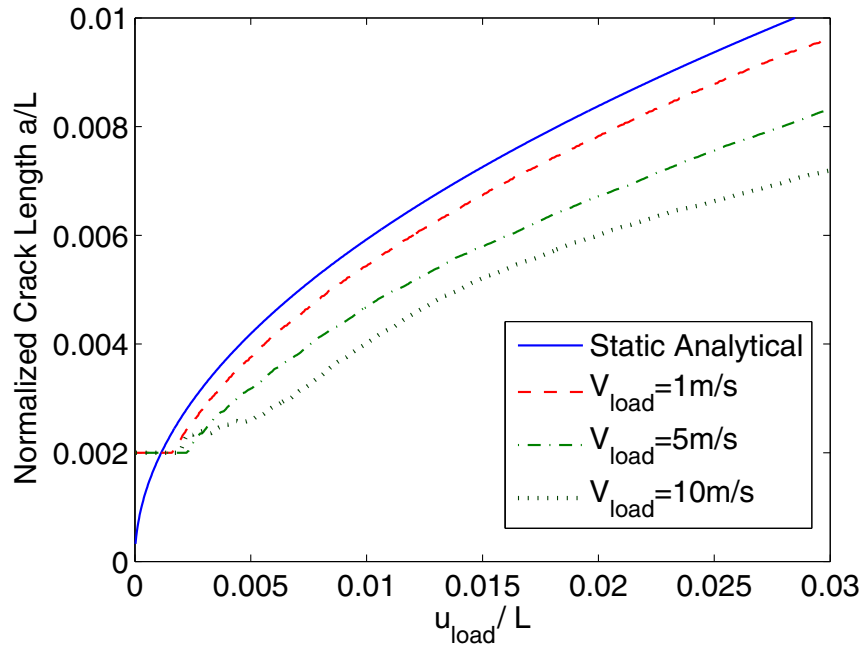


Figure 4.33: Crack evolution vs. applied displacement for $V_{\text{load}} = 1, 5$ and 10m/s . Rate toughening effect is considered by assuming a constant velocity throughout each simulation.

Figure 4.33 compares the crack evolution versus applied displacement loading for different loading rates. Crack length here is based on the trailing point of the cohesive zone where complete separation occurs. For comparison purposes, the static analytical solution is also provided. At a lower loading velocity, crack growth mimics the static solution well. At increased loading, crack growth “lags” behind the static case, as explained in Section 4.2. The crack growth exhibits smaller oscillation compared to the rate-independent investigation (see Figure 4.24 (a)).

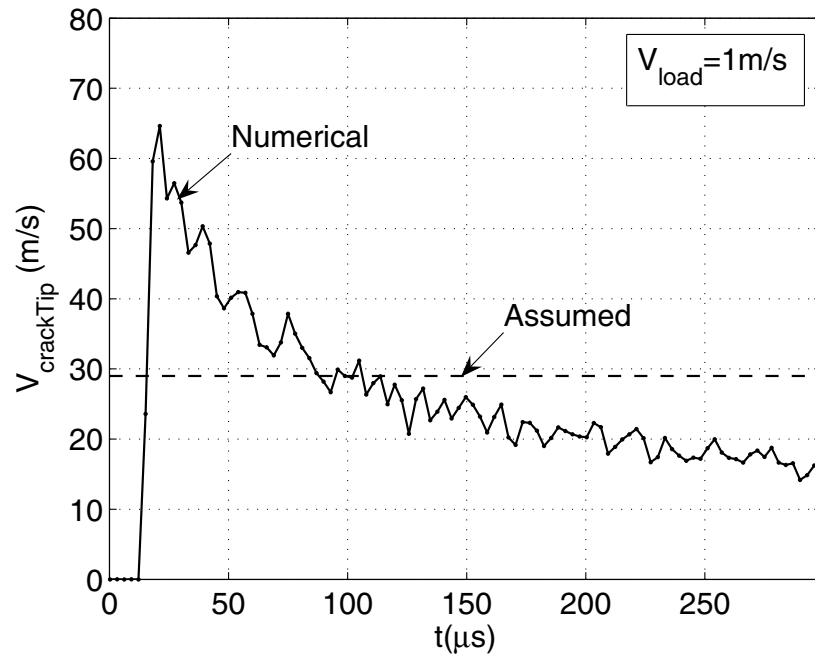


Figure 4.34: Crack velocity history for $V_{load} = 1\text{ m/s}$. Fracture energy for all cohesive elements (59 N/m) is based on assumed velocity (29 m/s) obtained from rate-independent study.

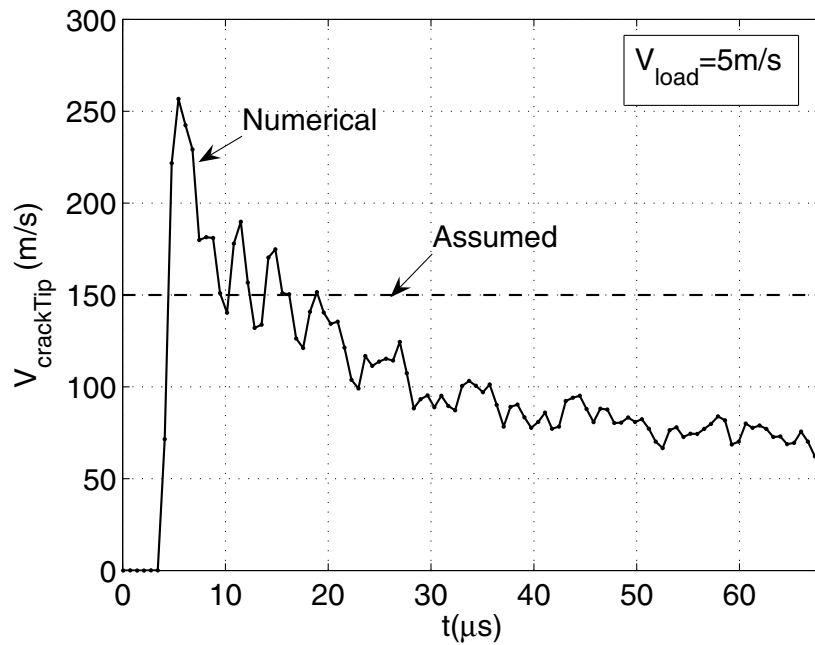


Figure 4.35: Crack velocity history for $V_{load} = 5\text{ m/s}$. Fracture energy for all cohesive elements (96 N/m) is based on assumed velocity (150 m/s) obtained from rate-independent study.

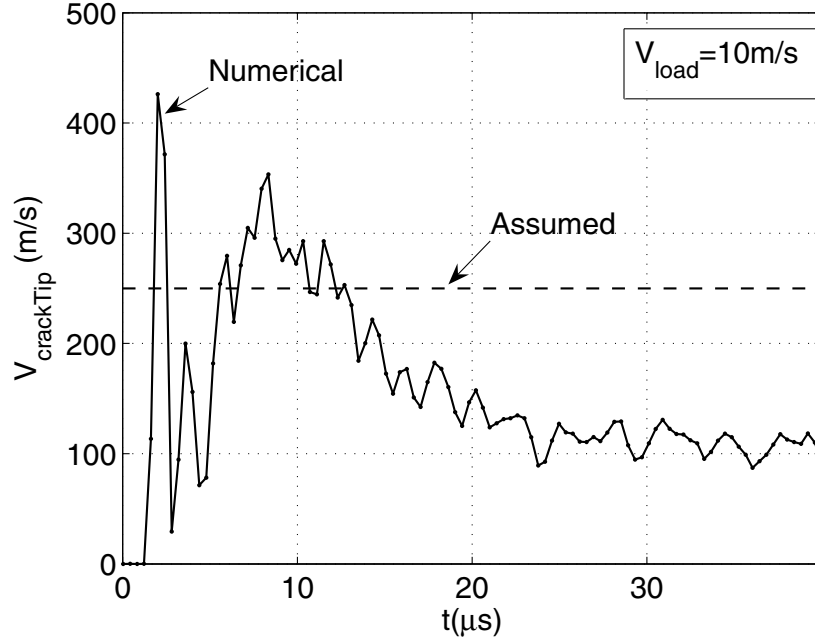


Figure 4.36: Crack velocity history for $V_{\text{load}} = 10\text{m/s}$. Fracture energy for all cohesive elements (145N/m) is based on assumed velocity (250m/s) obtained from rate-independent study.

Crack Velocity. Figures 4.33 and 4.34 compare the *simulated* velocity history and *assumed* velocity for each loading cases. For slow loading rate $V_{\text{load}} = 1\text{m/s}$, velocity profile is very similar to that obtained from the rate-independent analysis (see Figure 4.25), as expected. However, for faster loading rates $V_{\text{load}} = 5\text{m/s}$ and 10m/s , the crack speed is much slower compared to the rate-independent analysis. The peak velocity dropped from 350m/s to 250m/s for $V_{\text{load}} = 5\text{m/s}$ case, and from 1200m/s to 400m/s for $V_{\text{load}} = 10\text{m/s}$ case. Not surprisingly, crack velocity oscillation also dropped in each loading case compared to the rate-independent study. As the expected outcome from the present modeling approach, for all loading cases, the crack propagates at a decelerating speed over time, which is obviously different from the assumed constant velocity.

Cohesive Zone Size. Figure 4.37 compares the cohesive zone size for different loading cases. The rate-toughening effect is evident compared to the rate-independent cohesive law investigation (see Figure 4.29). The cohesive zone size remains constant throughout crack propagation history for each loading case, due to the assumed constant cohesive property along the crack path. The average cohesive zone size is $\ell_{cz} = 325, 360, 400\mu\text{m}$ for $V_{\text{load}} = 1, 5, 10\text{m/s}$, respectively.

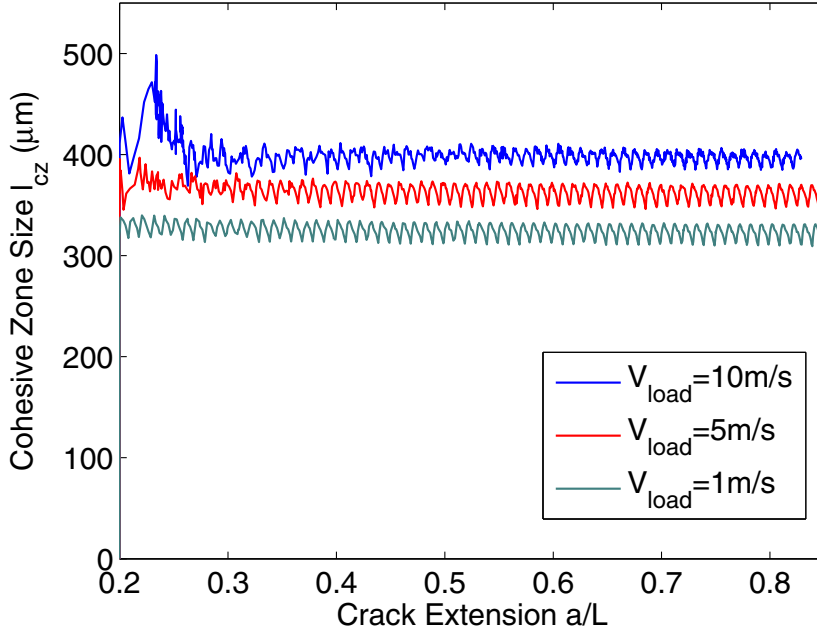


Figure 4.37: Cohesive zone size for different loading cases $V_{\text{load}} = 1, 5$ and 10m/s . Rate-toughened fracture energy for each case is 59, 96 and 145N/m .

4.3.4 Pseudo-analytical Cohesive Rate-toughening

In Section 4.2 we derived the “pseudo-analytical” crack speed for a rate-independent dynamic DCB problem. Figures 4.22, 4.25 and 4.26 suggest a general agreement between the pseudo-analytical velocity with numerical solution. Therefore, we consider using similar *pseudo-analytical* velocity as a guideline for determination of rate-toughening cohesive energy along crack path.

For rate-independent study, the *pseudo-analytical* velocity is easy to obtain because cohesive energy is assumed to be constant. However, for rate-dependent analysis, such derivation is more involved, and a closed-form solution may not be directly obtained. Because a reliable prediction of crack speed (i.e., pseudo-analytical velocity in the current study) must account for varying cohesive energy along crack path (thus time history), which in turn depends on crack velocity, such derivation process exhibits an iterative nature. Therefore, numerical approximations at certain stages are employed in the following study.

Predicted velocity. The previous v_{pseudo} to crack length a relationship (Equation (4.25)) may not be directly used when G_c is no longer a constant. In the following we derive the pseudo-analytical crack speed when considering variable fracture energy

along the crack path. Thus,

$$a(u(t)) = \int_0^{u_{\text{load}}} da(u) = \int_0^t d \left(\sqrt[4]{\frac{3Eu(t)^2h^3}{4G_c(v(t))}} \right) \quad (4.31)$$

$$\begin{aligned} v_{\text{crack}}^{\text{pseudo}} &= \frac{da(u(t))}{dt} = \frac{d}{dt} \left(\sqrt[4]{\frac{3Eu^2(t)h^3}{4G_c(v(t))}} \right) = \sqrt[4]{\frac{3Eh^3}{4G_0}} \frac{d}{dt} \left(\frac{\sqrt{u(t)}}{\sqrt[4]{\alpha \frac{v_{\text{crack}}(t)}{v_0}}} \right) \\ &= \sqrt[4]{\frac{3Eh^3}{4G_0}} \left\{ \frac{1}{\sqrt[4]{\alpha \frac{v_{\text{crack}}(t)}{v_0}}} \frac{1}{2\sqrt{u(t)}} V_{\text{load}} - \frac{\sqrt{u(t)}}{\sqrt[4]{\alpha \frac{v_{\text{crack}}(t)}{v_0}}} \ln \alpha \frac{\dot{v}_{\text{crack}}(t)}{4v_0} \right\} \\ &= \sqrt[4]{\frac{3Eh^3}{4G_c(v(t))}} \left\{ \frac{V_{\text{load}}}{2\sqrt{u(t)}} - \sqrt{u(t)} \ln \alpha \frac{\dot{v}_{\text{crack}}(t)}{4v_0} \right\} \quad (4.32) \\ &= \text{Term1} + \text{Term2} \end{aligned}$$

where $u(t) = u_{\text{load}}(t)$ is the applied displacement, $V_{\text{load}} = \dot{u}(t) = du(t)/dt$ is the applied velocity, and $\dot{v}_{\text{crack}}(t)$ denotes the differentiation of crack velocity with respect to time, i.e., crack acceleration rate. The above expression is an ordinary differential equation with variable coefficients. In general, solving such an equation requires a numerical procedure. For practical purposes, the current investigation focuses on deriving a ‘‘pseudo-analytical’’ solution, such that an involved numerical procedure is avoided. To understand the implication of the above equation, we first examine the behavior of the two terms in Equation (4.32).

- **Term 1.** The first term is similar to the rate-independent pseudo-analytical ($v_{\text{crack}}^{\text{pseudo}} - u_{\text{load}}$) relationship in Equation (4.25), but with varying fracture toughness. For instance, this term gives the general velocity profile similar to that shown in Figure 4.22. We denote this term as $v_{\text{crack}}^{\text{pseudo}*}$.
- **Term 2.** The second term originates from the rate-dependency term $G_c(v)$. This term vanishes for $\alpha = 1$, i.e., when considering rate-independent behavior. Moreover, for $\dot{v}_{\text{crack}}(t) > 0$ (i.e., crack velocity increases), this term is negative, thus $v_{\text{crack}}^{\text{pseudo}} < v_{\text{crack}}^{\text{pseudo}*}$, and vice-versa. Apparently, this rate-dependency term tends to reduce crack velocity oscillation in otherwise rate-independent analysis by providing more resistance at faster crack velocity and vice-versa.

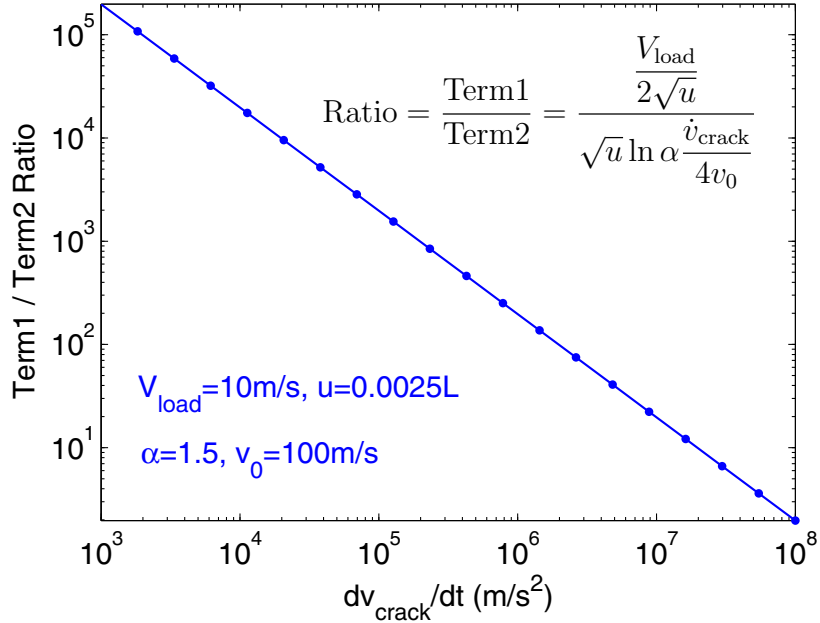


Figure 4.38: Ratio of the two terms in Equation (4.32) for varying crack acceleration rate \dot{v}_{crack} .

Whether the second term contributes significantly to the total $v_{\text{crack}}^{\text{pseudo}}$ depends mainly on the crack acceleration \dot{v}_{crack} . Figure 4.38 illustrates the ratio of the two terms vs. \dot{v}_{crack} on logarithmic scale. At relatively low crack velocity variation, contribution of $v_{\text{crack}}^{\text{pseudo}*}$ (Term 1) is dominant. At a high velocity variation rate (around 10^8 m/s^2), the two terms contribute to the total $v_{\text{crack}}^{\text{pseudo}}$ at a similar magnitude.

In the current analysis, we assume the acceleration is moderate, and thus neglect the second term. Therefore, Equation (4.32) is substantially simplified to the following form:

$$v_{\text{crack}}^{\text{pseudo}} = \sqrt[4]{\frac{3Eh^3}{4G_c(v(t))} \frac{V_{\text{load}}}{2\sqrt{u(t)}}} \quad (4.33)$$

Note that in above expression, v_{crack} , $G_c(v(t))$ and $u(t)$ are functions of the “pseudo-time” t . Our objective here, however, is to obtain a “realistic” assumed velocity in terms of the $v_{\text{crack}} - a$ relationship, so that the rate-toughened cohesive property G may be prescribed along the crack path a accordingly. Obviously, v_{crack} , $G_c(v)$ and u are implicit unknown functions of crack length a . To find out $v_{\text{crack}} - a$ as well as $G - a$ relationships, we consider introducing crack length a into the above expression

using an approximate $u-a$ relationship.

To this end, we borrow the quasi-static *rate-independent* relationship of $u-a$,

$$u_{\text{rate-independent}} = \sqrt{\frac{4a^4 G_c}{3Eh^3}} \quad (4.34)$$

which assumes *constant* fracture resistance, and use similar form

$$u_{\text{rate-dependent}}^{\text{approx}} = \sqrt{\frac{4a^4 G_c(v)}{3Eh^3}} \quad (4.35)$$

as an *approximation* of the *rate-dependent* $u-a$ relationship. The approximation originates from the fact that instead of being constant, for the current rate-dependent analysis, $G_c(v)$ varies along a , depending on assumed velocity v . The actual $u-a$ relationship can only be accurately solved as an integration process over history, and expression (4.35) *underestimates* u at given a compared to the actual relationship (to be discussed in more detail later). Bearing this fact in mind, next we substitute expression (4.35) into Equation (4.33) and obtain

$$v_{\text{approx}} = \sqrt[4]{\frac{3Eh^3}{4G_c(v)}} \frac{V_{\text{load}}}{2\sqrt[4]{\frac{4a^4 G_c(v)}{3Eh^3}}} = \frac{V_{\text{load}}}{4a} \sqrt{\frac{3Eh^3}{G_c(v)}}. \quad (4.36)$$

Note that a direct solution to Equation (4.36) provides merely an approximation of the pseudo-analytical velocity that we actually seek. In the following, three methods are attempted to approach the problem, motivated by consideration of balancing simplicity and accuracy.

- *Method 1: Direct Solution of Equation (4.36).* Substitute $G_c(v) = G_0 \alpha^{\frac{v}{v_0}}$ into Equation (4.36) and rearrange terms:

$$v \alpha^{\frac{v}{2v_0}} = \frac{V_{\text{load}}}{4a} \sqrt{\frac{3Eh^3}{G_0}}. \quad (4.37)$$

Although a solution in closed form is not readily available, a simple numerical solution can be obtained easily (e.g., using Matlab). The solution of v_{pseudo} vs. time t is plotted in Figure 4.39.

- *Method 2: Solving Equation (4.36) and correcting $(u-a)$ relationship in Equation 4.35.* In the rate-independent DCB problem, G_c is constant and Equation (4.35) strictly holds for quasi-static analysis. In the rate-dependent DCB

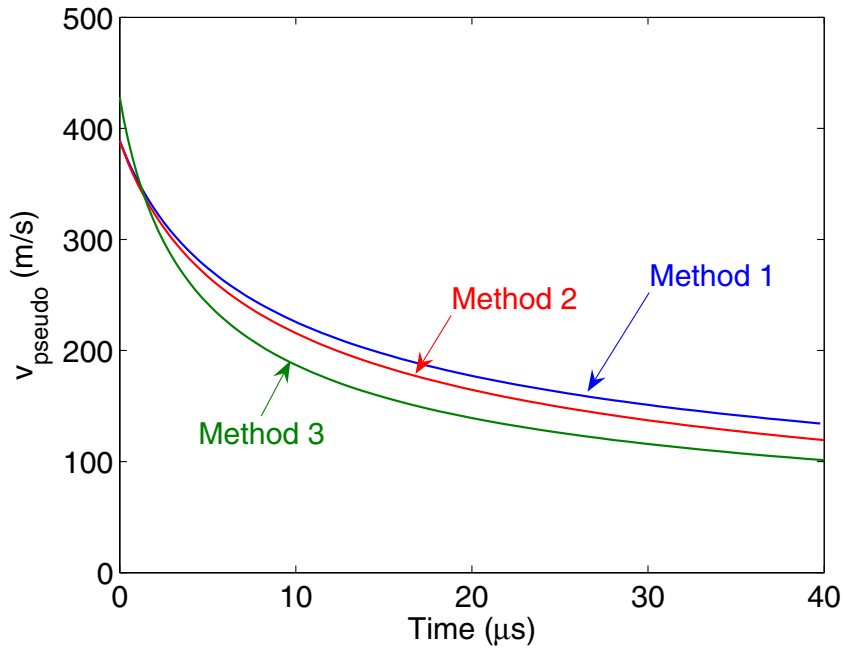


Figure 4.39: Pseudo-velocity by solving Equation (4.36) and considering the rate-toughening effect on velocity reduction using different method. Method 1: no reduction; Method 2: linear decreasing from 1 to 0.9 as crack location from a_0 to L ; Method 3: use half of the velocity predicted using rate-independent G_c value.

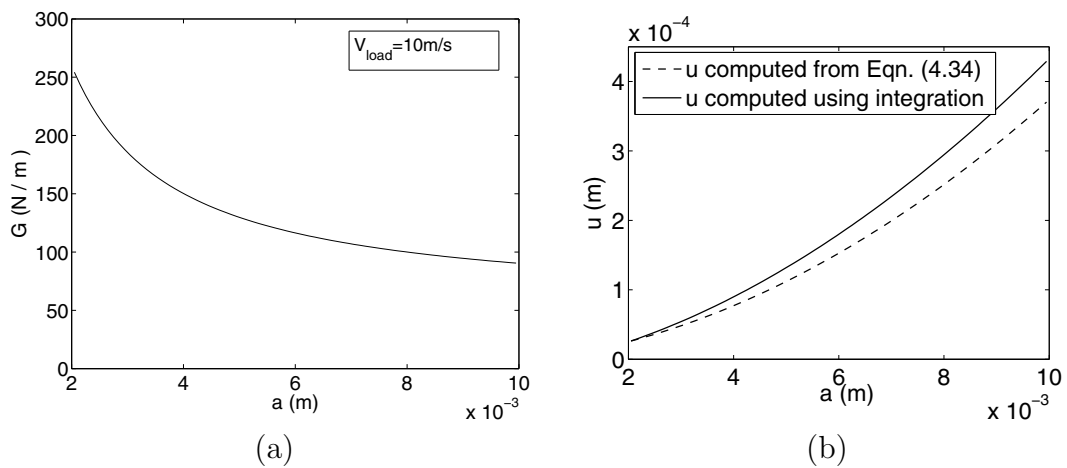


Figure 4.40: Method 2 corrects for underestimated u in Equation (4.35); (a) fracture resistance G variation along crack path a based on Method 1 solution; (b) comparison of u – a relationship obtained using Equation (4.35) approximation and more accurate numerical integration process.

problem, $G_c(v)$ gradually decreases along the x direction when crack grows, as shown in Figure 4.40 (a), which is based on Method 1 result for $V_{\text{load}} = 10m/s$ case. At $a = a_0$, $G = 250N/m$, and gradually decreases to around $90N/m$ at $a = L$.

Because the material property is not constant, u at any given a location should be calculated as an integration of all “previous” Δu . The approximation given in Equation (4.35) thus underestimates actual u at given a . This is analyzed in the following: at any given location a , all “previous” G_c (prior to this point) are larger than the current G_c . This also implies that all “previous” Δu required for crack to grow to current stage is larger than what Equation (4.35) predicts using the “current” G_c . We denote the more realistic u as u^* and $u^* > u_{Eqn. (4.35)}$. Hence we can improve the expression of Equation (4.36):

$$\begin{aligned} v &= \sqrt[4]{\frac{3Eh^3}{4G_c(v)} \frac{V_{\text{load}}}{2\sqrt{u^*}}} = \beta(a) \sqrt[4]{\frac{3Eh^3}{4G_c(v)} \frac{V_{\text{load}}}{2\sqrt{u_{Eqn. (4.35)}}}} \\ &= \beta(a) \frac{V_{\text{load}}}{4a} \sqrt{\frac{3Eh^3}{G_c}}. \end{aligned} \quad (4.38)$$

where $\beta(a)$ accounts for the reduction effect discussed above. This coefficient takes the value of 1 at $a = a_0$ as no error occurs due to underestimated “previous” Δu , and gradually decreases along a . The value of $\beta(a)$ depends on the variation of fracture resistance G along crack path a . Higher variation leads to more reduction effect, and hence a lower β value. As an example, we numerically compute the $u - a$ relationship using an integration process (thus the more accurate u^*), and compare it with Equation (4.35) result in 4.40 (b). Clearly, Equation (4.35) underestimates $u - a$ relationship, although the difference is not significant in this case (about 15% at $a = L$). Based on the example, we assume $\beta(a)$ to be linearly degrading from 1 to 0.9 for $V_{\text{load}} = 10m/s$ case.

- *Method 3: Solving Equation (4.36) with rate-independent G_0 value and applying coefficient for velocity reduction.* This approach borrows the rate-independent static result, then introduces a reduction coefficient based on the argument that the rate-toughening effect will slow down crack velocity compared to rate-independent case. The solution is thus

$$v^{\text{pseudo}} = \beta \frac{V_{\text{load}}}{4a} \sqrt{\frac{3Eh^3}{G_0}} \quad (4.39)$$

For the $V_{\text{load}} = 10m/s$ case, β value is assumed to be 0.5. The value is based on comparing the rate-independent and rate-dependent (assuming constant toughening) results shown in Figures 4.26 and 4.36. Crack velocity ranges from 1200 to 200 m/s , and 400 to 100 m/s in rate-independent and rate-dependent cases, respectively. Therefore an overall reduction coefficient 0.5 is used here.

Figure 4.39 compares the pseudo-velocity results using above three methods. Methods 1 and 2 predict the same velocity in the beginning, and then Method 2 gradually deviates from Method 1 due to the reduction effect. Method 3 predicts a slightly higher initial velocity and then quickly decreases to lower values than the Method 2 result.

Numerical vs. Predicted Velocity. We first examine the velocity results using $G_c(v)$ based on predicted pseudo-velocity described previously. Figures 4.41 to 4.43 compare the numerical solution with the assumed velocity for the three methods. The numerical results are similar for all three methods. Crack initiates at around $5\mu s$, when crack velocity arises to around $400m/s$, and gradually decreases to $150m/s$ in the end. The difference between Figures 4.41 and 4.42 is nearly negligible, because the “reduction coefficient” effect between Methods 1 and 2 is small for this loading case. Method 3 slightly underestimates the crack velocity in the beginning but follows the general trend well. The above examples suggest that for crack propagating at low to moderate velocities, either method may be used as a reliable prediction. For problems involving high velocities, thus higher variation of fracture resistance along the crack path, Method 2 provides more a accurate prediction.

Rate-dependent Cohesive Zone Size. Figure 4.44 compares cohesive zone size for different loading cases. Method 2 is used for the reported results. The rate-toughening effect is evident compared to the quasi-static case (Equation 4.1), the rate-independent cohesive law investigation (Figure 4.29), and also the case with constant rate toughening cohesive properties along the crack path (Figure 4.37). Cohesive zone size varies as crack grows. At crack initiation, the cohesive zone size is $\ell_{cz} = 370, 450$ and $550\mu m$ for $V_{\text{load}} = 1, 5$ and $10m/s$, respectively. As the crack grows, cohesive zone size decreases. and when the crack reaches $a = 0.9L$, $\ell_{cz} = 320, 340$ and $360\mu m$ for

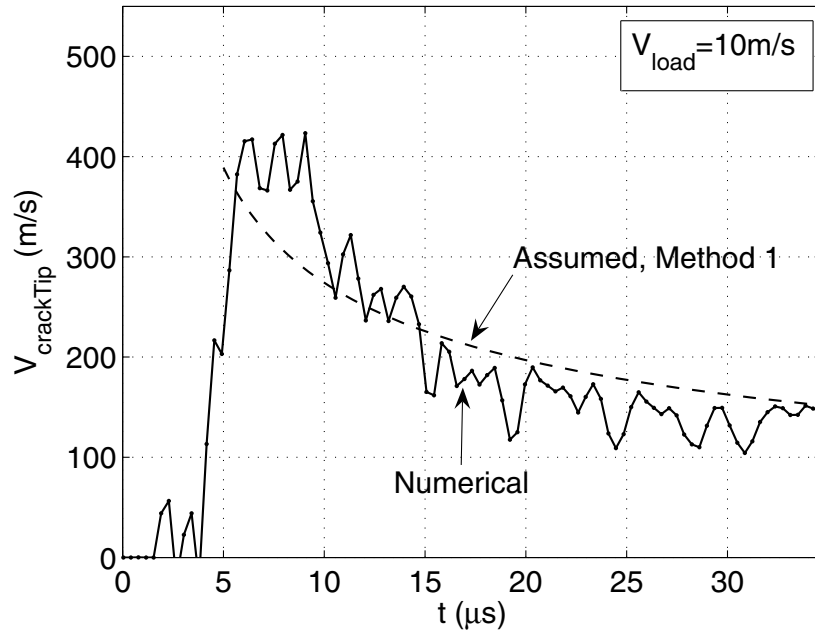


Figure 4.41: Crack velocity history for $V_{load} = 10m/s$. Fracture energy $G_c(v)$ is based on assumed velocity obtained from *Method 1*.

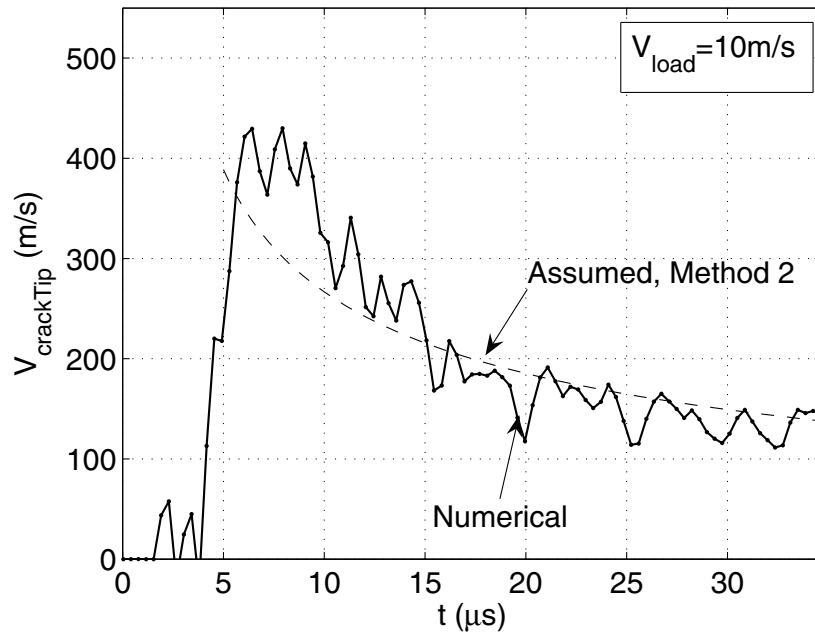


Figure 4.42: Crack velocity history for $V_{load} = 10m/s$. Fracture energy $G_c(v)$ is based on assumed velocity obtained from *Method 2*.

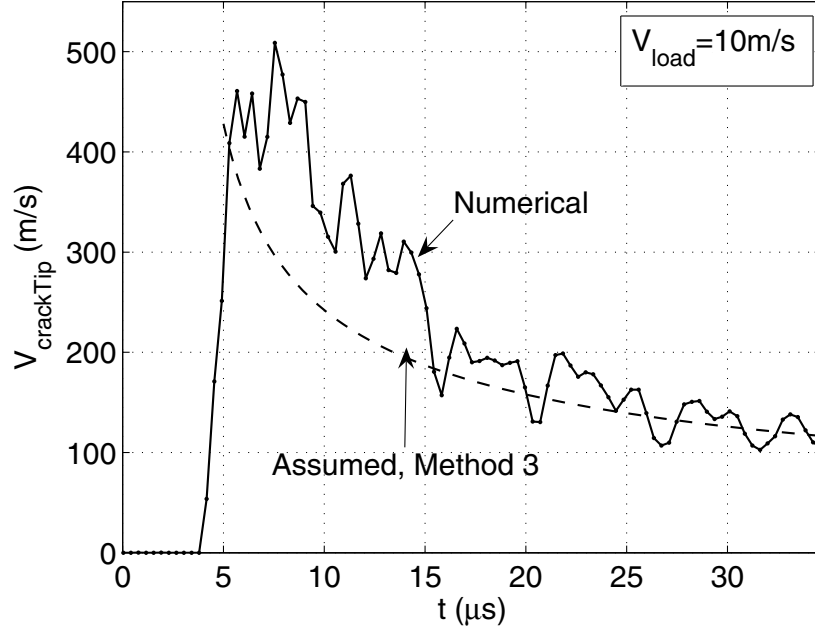


Figure 4.43: Crack velocity history for $V_{\text{load}} = 10\text{m/s}$. Fracture energy $G_c(v)$ is based on assumed velocity obtained from *Method 3*.

$V_{\text{load}} = 1, 5$ and 10m/s , respectively. Clearly, the cohesive zone size variation is more significant in higher loading cases ($190\mu\text{sm}$ for $V_{\text{load}} = 10\text{m/s}$, compared to $50\mu\text{sm}$ for $V_{\text{load}} = 1\text{m/s}$) due to higher variation in velocity history.

4.3.5 Discussion

In the present study we examined crack growth behavior and cohesive zone size for static, rate-independent dynamic and rate-dependent dynamic problems using a DCB example. The numerical procedure is carefully verified for each category of problems. The major findings are summarized in the following:

- The numerical procedure using simple beam element and 1D cohesive elements provides excellent numerical results for the classical DCB problem. Parametric study indicates that the widely used cohesive zone estimate may be far away from that actually obtained from numerical solution. Therefore the application of the estimate in deciding cohesive element size must be exercised with caution.
- A rate-independent cohesive zone model cannot capture the rate-toughening effect observed in a dynamic fracture experiment. Rate-dependency must be considered in the constitutive level in order to capture rate-dependent behavior

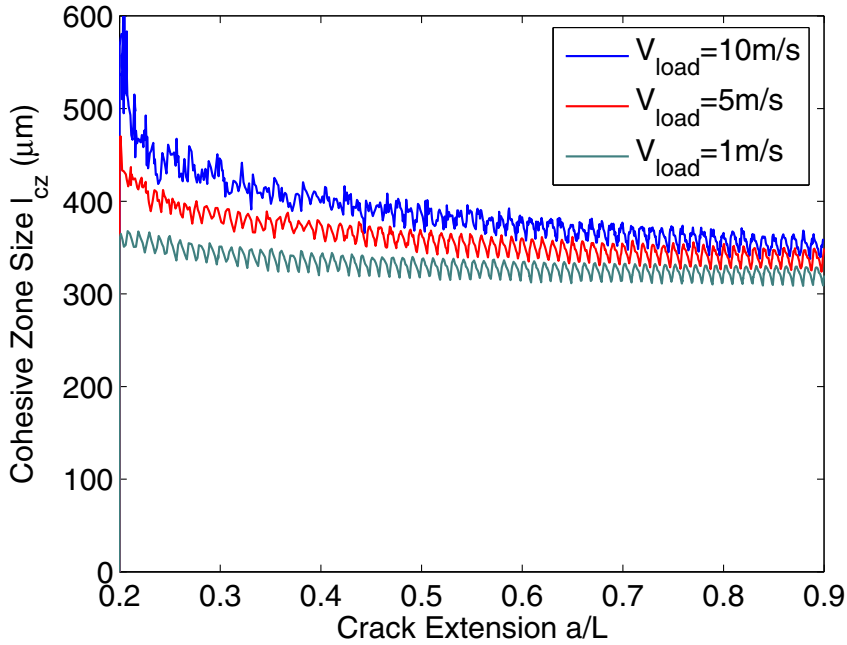


Figure 4.44: Cohesive zone size for different loading cases $V_{\text{load}} = 1, 5$ and 10m/s considering the rate toughening effect.

in dynamic fracture. However, when dissipation of extra energy at high crack velocity is due to creation of micro-cracking (e.g., in brittle fracture), such behavior can be captured by rate-independent cohesive model combined with micro-branching capability in the numerical scheme. This will be discussed in detail in Chapter 5.

- The rate-dependent cohesive zone model used in the present study directly relates fracture toughness increase with higher crack velocity. Though intuitive, such a method is not straightforward in terms of numerical implementation, mainly due to the difficulty of tracking crack tip velocity during simulation, especially when multiple crack fronts are present. A model based on local rate quantities, for example, the cohesive interface separation rate, may be an alternative candidate for such analysis.

Chapter 5

Dynamic Fracture and Microbranching Instability in Brittle Materials

This Chapter investigates dynamic crack microbranching processes in brittle materials. Experiments indicate presence of a limiting crack speed for dynamic crack in brittle materials as well as increasing fracture resistance with crack speed. These phenomena are numerically investigated by means of the extrinsic cohesive zone approach facilitated by the topological data structure TopS presented in Chapter 3. Extrinsic CZMs involve additional issues both in implementing the procedure and in interpreting simulation results. These include time discontinuity in stress history, fracture pattern dependence on time step control, and numerical energy balance. These issues are investigated in detail through a “quasi-steady-state” crack propagation problem in Polymethylmethacrylate (PMMA). The simulation results compare reasonably well with experimental observations both globally and locally, and demonstrate certain advantageous features of the extrinsic CZM with respect to the intrinsic CZM.

5.1 Introduction

Dynamic fracture instability in brittle materials has been a field of much interest and research during the past decades [24]. Experiments have been performed on various amorphous brittle materials to investigate dynamic fracture behavior; for instance, Homalite-100 [84, 85, 86, 87], PMMA [96, 88], Solithane-113 and polycarbonate [88]. These experiments provide valuable information for improved understanding of dynamic fracture phenomena in the brittle materials, particularly with respect to the process of nucleation, growth, and coalescence of microcracks. Two phenomena remained the focus of interest among these observations: first, crack surface roughens as crack speeds up, as the “mirror-mist-hackle” stages described in [86]; second, the onset of instability occurs at a speed well below the theoretical limiting speed predicted by classical linear elastodynamics. A dynamic fracture experiment with focus on microbranch formation in PMMA is found in [96], which further investigated

the transitional stage when microbranches occur and grow longer with increasing crack speed, as shown in Figure 5.1. Although crack instability at high speed is predicted by the conventional linear elastodynamic theory, these experimental observations reveal significant deviation of fracture behavior in the brittle material from those conditions suggested by the linear theory.

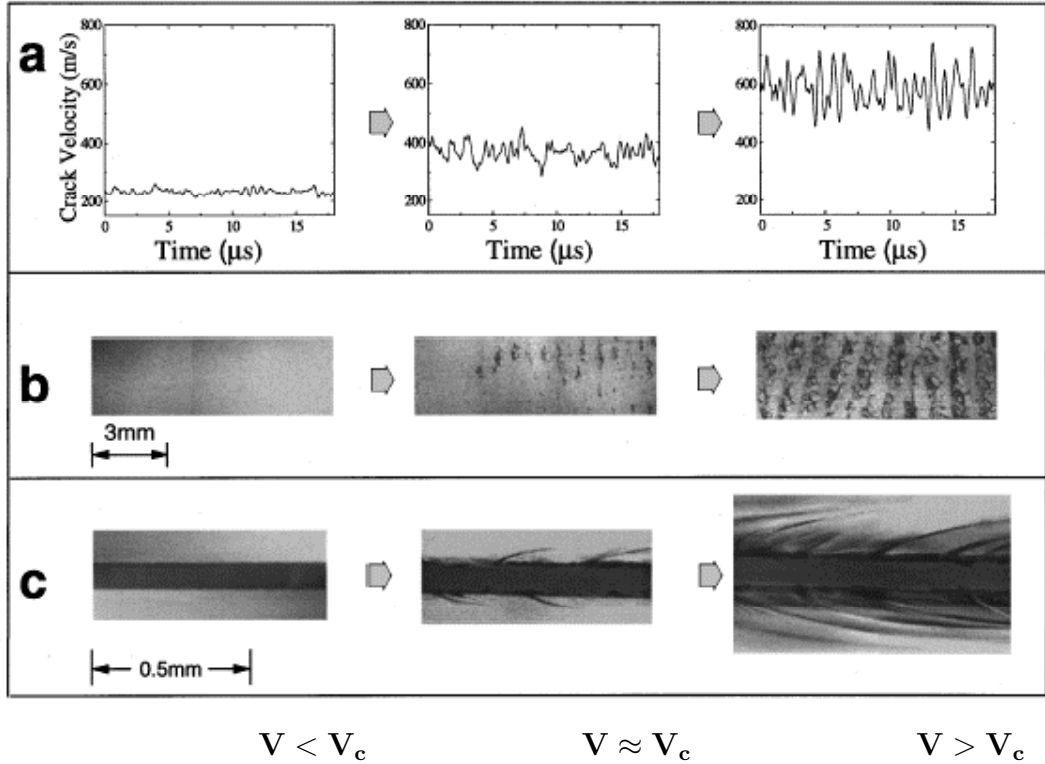


Figure 5.1: Experimental observation of branching instability as crack propagates in PMMA. Figure reproduced from Figure 4 of Sharon and Fineberg [96]. The critical crack speed at which microbranch appears is denoted as V_c . (a) the velocity of the crack is a smooth function of time for $V=300$ m/s $< V_c$ (left), at $V=400$ m/s $\approx V_c$ the crack velocity starts to oscillate (center), the oscillation amplitudes increase at higher velocity (right); (b) for $V=300$ m/s $< V_c$ the fracture surface is smooth (left), at $V \approx 400$ m/s small regions of different texture are distributed along the surface (center), at $V \approx 600$ m/s these regions coalesce, forming a periodic pattern with wavelength on the order of 1 mm (right); (c) A single crack is observed (left) for $V < V_c$. Microbranches appear at $V \approx V_c$ (center), and increase in length at higher velocities (right).

This work investigates dynamic crack microbranching processes by incorporating a cohesive zone model (CZM) in the finite element method to characterize the fracture process. One major challenge in simulating branching phenomena is how to allow multiple cracks to form “freely” in a finite discretization. Among the set of numerical schemes in the literature, the CZM has the advantage of allowing multiple crack

formation. Between the two classes of CZMs, i.e., “*intrinsic*” and “*extrinsic*” models, the latter is adopted in the study as this approach avoids a number of disadvantages of the former, including the so-called “artificial compliance”, which may result in significant reduction of stiffness of the modelled specimen. Compared to intrinsic CZMs, which include a hardening segment in the traction-separation curve, extrinsic CZMs involve additional issues both in implementing the procedure and in interpreting simulation results. These include time discontinuity in stress history, fracture pattern dependence on time step control, and numerical energy unbalance.

5.2 Related Work

The analytical solution for a crack moving at constant velocity based on linear elastic fracture analysis dates back to the middle of last century [111], which predicted crack velocity limit as the Rayleigh wave speed (c_R) for mode-I problems. Such analysis assumes ideal brittle fracture model in which the crack moves at constant speed along its initial direction through an infinite strip. Freund [36] provides a more detailed description of the ideal model with further consideration of nonuniform crack tip motion. Moreover, this theoretical model also predicts dynamic crack instability. For quasi-static crack propagation, the maximum circumferential (“hoop”) stress criterion predicts the deviation angle $\theta=0$, i.e., the crack tends to propagate along the initial crack path. For dynamic crack propagation, however, the angular distribution of circumferential stress depends on crack velocity. As crack tip velocity increases, the maximum stress may not necessarily occur at $\theta=0$. When the crack tip velocity reaches about two thirds of the Rayleigh wave speed, the hoop stress varies less than 10% within an angular range from -45° to 45° (see, e.g. [36], Figure 4.2). When crack tip velocity reaches about three fourths of the Rayleigh wave speed, the hoop stress varies only marginally within the angular range from -60° to 60° . This solution suggests that crack path becomes unstable at high crack tip speed and branching may occur. Although this linear elastodynamic based analysis is significant in revealing the onset of fracture path instability, the predicted critical crack velocity does not agree well with experimental observations ([86], [88] and [96]), which reveal that the limiting crack speed is about half of the Rayleigh wave speed, and that the specimen develops increasing fracture surface roughness with increasing fracture velocity.

Motivated by the experimental observations, Gao [37] proposed an explanation through the correlation between *micro*-crack speed and *macro*-crack speed. At high

velocity, the crack tends to propagate through a “wavy” path so as to maximize the energy flux into the crack tip while maintaining the average crack speed below 50% of the Rayleigh wave speed. The microcracks can propagate at higher speed, with the limit predicted by the Yoffe solution [111]. Gao’s work [37] also pointed out the importance of “T-stress” in the dynamic crack propagation process. A negative T-stress that is parallel to the crack path tends to stabilize the crack path along its original surface, while a positive T-stress results in the opposite behavior. Rice et al. [92] later pointed out that this stabilization effect is limited; at crack velocity greater than 75% Rayleigh wave speed, the crack path will be destabilized and any deviation from straightness then gets amplified. Rice et al. [92] also observed that the analyses by Eshelby [31] and Freund [35] indicate that there is enough energy available to create two crack surfaces as was available to create one when the crack speed is about 75% Rayleigh wave speed.

A theory of local limiting speed was postulated by Gao [38] through consideration of nonlinear elastic response at crack tip, which governs the *local* crack limiting speed. The local limiting speed is found to be $c_s \sqrt{\sigma_{max}/\mu}$, where c_s is the macroscopic shear wave speed, μ is the shear modulus and σ_{max} is the equibiaxial cohesive strength of the solids. The local limiting speed provides an explanation for the onset of mirror-mist transition of fracture surface. Gao [38] also developed a steady-state maximization algorithm to compute atomistic responses near the tip of a crack moving with constant speed in a 6-12 Lenard-Jones lattice. The critical velocity at the onset of local crack branching is in agreement with molecular dynamics simulation study of Abraham et al. [3], and is about 80% of the calculated local limiting speed.

Brittle fracture instability was also investigated through numerical means, including the finite element method (FEM) [108, 56, 13], the boundary element method (BEM) [83], and molecular dynamics [3]. Xu and Needleman [108] did FEM simulation of macro-branch occurrence in a center-cracked plate subjected to tensile displacement loading. Their work uses intrinsic cohesive zone models, which involve embedded interface elements in the mesh that allow separation between triangular-shaped area elements. Although the method suffers from mesh dependence and the crack speed is artificially increased due to so-called “lift-up” effect, the simulation result is significant in revealing the branching dependence on applied loading, and in qualitatively matching the experimental observations. Klein et al. [56] simulated microbranch occurrence using a nonlinear continuum “virtual internal bond” model, which considers material weakening at the strain localization region. The simulation produced average crack speed and microbranch pattern that qualitatively match the

experimental measurements. Belytschko et al. [13] investigated crack bifurcation using the extended FEM (X-FEM) combined with the loss of hyperbolicity condition for the crack initiation criterion. This work focused more on method development rather than reproducing observed experiments, and the authors pointed out that this method neither simulates roughness in the crack path, nor treats the microbranches. Rafiee et al. [83] employed boundary integral method to investigate the crack bifurcation and trifurcation under bi-axial loading case. Crack branching criterion used in that study is attainment of a critical stress intensity factor (SIF), which is much higher than the static material toughness. Therefore velocity toughening effect is considered in the model. Abraham et al. [3] investigated crack tip instability using molecular dynamics involving 10^6 atoms. Although at substantially smaller time and length scales, the atomistic simulation produced “wavy” crack path as observed in experiments.

5.3 Simulation of Sharon and Fineberg’s Experiment

In the following, the crack propagation in a pre-stretched narrow strip is investigated for PMMA material. The prescribed geometry and boundary conditions result in so called “quasi-steady-state crack propagation” [97] problem, i.e. the crack runs at a relatively constant speed throughout the strip. The numerical investigation uses a geometry of reduced dimension in comparison with the original experiment, however, most of the features of the experiment are well reproduced. First, the mesh convergence of the numerical method is investigated. Results of the crack tip velocity suggest that the criterion for mesh size versus crack tip process zone size depends upon not only material property but also boundary conditions. Next, the relationship between fracture behavior and applied load is analyzed and compared with experimental observations. Finally, energy balance is investigated in detail, which also provides verification of the numerical implementation.

5.3.1 Problem Description

Sharon and his co-workers [98, 96, 97] investigated “quasi-steady-state crack propagation”, focusing on characterization of the relationship between microcrack pattern, crack surface characteristics and crack speed. The experimental setting is schematically shown in Figure 5.2. The upper and lower boundaries are clamped, and uniform

stress of magnitude of $\sigma = 10$ to 18MPa is applied. Afterwards, the boundaries are held fixed, and a sharp crack is introduced along the blunt pre-notch using razor blade. The energy stored in the system thus spur crack propagation through the strip.

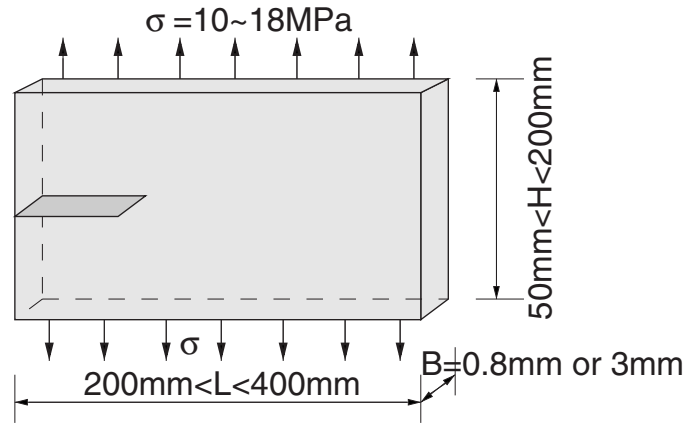


Figure 5.2: Model of the experimental setting by Sharon and Fineberg [96]; the length to height ratio (L:H) is maintained between 2 to 4, in order to represent steady-state crack propagation condition.

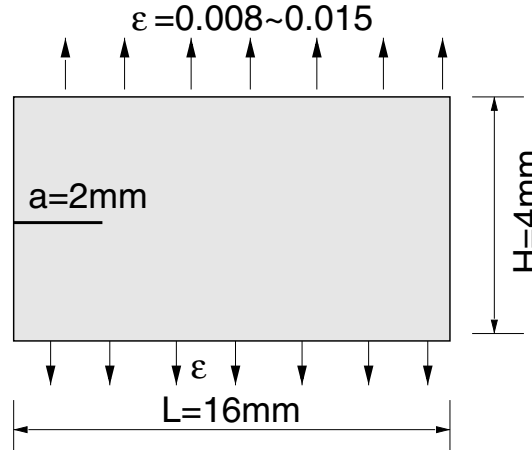


Figure 5.3: Schematic representation of the geometry and boundary condition for the 2-D steady-state crack propagation problem, using reduced dimension based on Sharon and Fineberg [96]; the length to height ratio (L:H) is 4.

Since the cohesive model approach requires fine mesh size to capture the nonlinear behavior at the crack tip region, the original experiment size is reduced in proportion in the numerical analysis. Figure 5.3 shows the geometry and boundary conditions used in the study.

The strip is initially stretched uniformly by imposing an initial displacement field

$$u(x, y; t = 0) = 0, \quad v(x, y; t = 0) = \varepsilon y \quad (5.1)$$

which results in a uniform strain field at the initial time. The upper and lower surfaces are held fixed and a small crack length a is introduced at the left edge at time $t = 0$. The material used is Polymethylmethacrylate (PMMA) [108], and its properties are given in Table 5.1. In the numerical simulations G_{IIc} is assumed to be equal to G_{Ic} ($G_{IIc} = G_{Ic}$).

Table 5.1: Properties of PMMA [108] strip subjected to initial stretch.

E (GPa)	ν	ρ (kg/m^3)	G_{Ic} (N/m)	$T_n^{\max} = T_t^{\max}$ (MPa)	$\delta_n = \delta_t$ (μm)	η	c_R (m/s)
3.24	0.35	1190	352.3	129.6	5.44	1	939

5.3.2 Reduced Dimension Model

The cohesive model approach demands highly refined mesh around the crack tip region. Since the present problem involves numerous branchings without pre-defined paths across the entire strip, the strip is meshed with very fine elements. Moreover, small element size ensues use of small time step, which is required by explicit updating scheme. As a consequence, the numerical simulation becomes enormously heavy if the original experimental model is used, which results in a FE model consisting of 20 millions of nodes and 10 millions bulk elements when the fine mesh discretization is used. Such large scale computation is better suited for super-computers, which were not available for the present study. Therefore, in order to achieve a numerical study that reasonably represents the original problem while keeping the computation overhead under control, the reduced model in Figure 5.3 is adopted in the study, which is the same model dimension used by Miller et al. [67].

Material properties listed in Table 5.1 follow those of Miller et al. [67], except for cohesive strength T_n^{\max} and characteristic separation δ_n . Miller et al.'s work [67] uses an exponential-form intrinsic cohesive model which assumes a high cohesive strength (1/10 of Young's modulus for PMMA). Adoption of the high value is motivated more by trying to control the artificial compliance, which is unavoidably associated with the intrinsic model, rather than experimental evidence. Admittedly, cohesive strength can rarely be obtained from experiment with high reliability [56], yet the available

reported tensile strength of PMMA ($62.1MPa$) is much lower than that used by Miller et al. [67] ($324MPa$). The mode mixity factor is taken as $\eta = 1$.

The selection of cohesive strength in the present study is related to the reduced dimension problem, which does not represent the original experiment completely because of the material-dependent length scales. *The guideline of modeling the problem is to maintain the same amount of strain energy per unit length along the strip for the original experiment and the reduced dimension problem.* This consideration results in adaption of applied loading compared to the experiment. In the experiment, the initial load results in an amount of stored strain energy per unit length of approximately $800 - 5000Nm/m^2$ [96], and a stretch of approximately $\varepsilon = 0.0027$ to 0.0049 along the vertical direction at initial time. To maintain the same energy stored per unit length in the numerical analysis as in the experiment, the stress and strain applied at the initial time are much higher in the former case (numerics) than the latter (experiments). The applied load in the experiment (10 to $18MPa$) is much lower than material tensile strength ($62.1MPa$), while in numerical analyses the initial uniform stress (37 to $96MPa$) is close or even higher than material tensile strength. As a consequence, if the material tensile strength is chosen as the cohesive strength, numerous interfaces will break at the initial loading, which is confirmed by the authors' numerical study (results not reported here). Therefore, to avoid unwanted fracture at locations without stress concentration, the cohesive strength used in the present study ($E/25=129.6MPa$) is chosen to be higher than the boundary loading. This value does not match the real material tensile strength ($62.1MPa$), and the difference between the actual and reduced dimension must be considered in interpreting the numerical results.

5.3.3 Mesh Convergence

The domain is uniformly discretized by T6 elements of various element sizes as shown in Figure 5.4 and Table 5.2. Time step Δt is chosen as a fraction (around 10%) of that required by the Courant condition for explicit updating scheme, to ensure stable computation when cohesive elements are present. Cohesive elements are adaptively inserted in the finite element mesh, which allow crack to spontaneously grow and branch.

Driven by the strain energy stored in the pre-stretched strip, the crack propagates towards right edge of the strip. In actual experiments, unless the crack path is constrained, the crack tip speed can hardly reach 50% of Rayleigh wave speed due

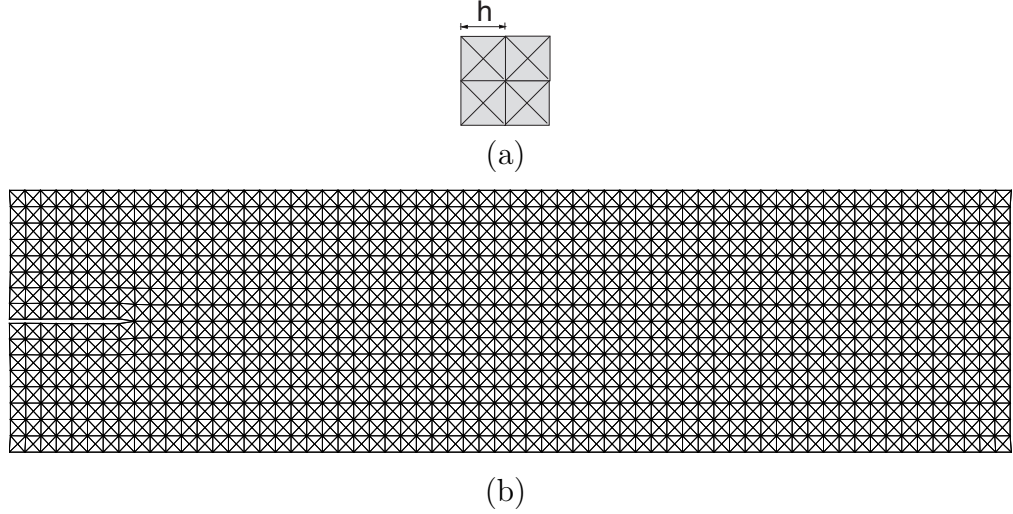


Figure 5.4: Mesh discretization with T6 elements for pre-cracked PMMA strip subjected to initial stretch; (a) mesh pattern and characteristic length h , which is defined as grid spacing; (b) mesh with grid 16×64 , $h=250\mu\text{m}$. Other meshes with grid 32×128 ($h=125\mu\text{m}$), grid 48×192 ($h=83\mu\text{m}$) and grid 64×256 ($h=62.5\mu\text{m}$) use the same mesh pattern with different levels of refinement .

Table 5.2: Mesh discretization and time step control associated with Figure 5.4.

Mesh	$h(\mu\text{m})$	Grid	# Nodes at t=0	# Bulk elements	$\Delta t (\mu\text{s})$
(a)	250	16×64	8,369	4,096	8×10^{-3}
(b)	125	32×128	33,121	16,384	4×10^{-3}
(c)	83	48×192	74,257	36,864	3×10^{-3}
(d)	62.5	64×256	131,777	65,536	2×10^{-3}

to energy dissipation mechanisms, for example, from micro crack formation at the immediate crack tip vicinity. The energy dissipation mechanism is simulated by the formation of microbranching at crack tip.

Various mesh discretizations are employed to investigate the convergence of the numerical scheme in terms of the relationship between the characteristic cohesive length scale δ and mesh size h . Here h is defined as the grid spacing (see Figure 5.4). Previous researchers who have used intrinsic cohesive models [41, 56] recommend that at least two to three cohesive elements be present inside the cohesive zone, whose size is estimated by [91]

$$\ell_{cz} = \frac{\pi}{8} \frac{E}{1 - \nu^2} \frac{G_{Ic}}{\sigma_{ave}^2} \quad (5.2)$$

where for the cohesive law employed, $\sigma_{ave} = 0.5T_n^{max}$. For the material property chosen (Table 5.1), the estimated cohesive zone size is $\ell_{cz} = 122\mu\text{m}$. However, this

estimate originated from a *static* problem [91]. The investigation in Chapter 4 reveals that numerically evaluated cohesive zone size may differ markedly from the above estimate. In an earlier study [110], it was noted that for *dynamic* fracture analysis, the process zone size varies with loading rate. Although this result is obtained with mode-III problem, it is reasonable to suspect that dynamic cohesive zone size depends on more factors other than cohesive properties. Moreover, in a previous study by the authors [116], numerical simulation results for crack propagation along pre-defined path also reveal that mesh convergence is achieved at different levels of mesh refinement for different loading conditions, although the cohesive element properties are identical.

An intrinsic time scale implied in the cohesive model was discussed in a series of papers by Ortiz and his co-workers [16, 74, 73]. This *characteristic time* is defined as

$$t_c = \frac{\rho c_d \delta_n}{2T_n^{max}} \quad (5.3)$$

where ρ and c_d denote mass density and dilatational wave speed, respectively. Pandolfi et al. [74] indicated that the characteristic time influences crack initiation and propagation. Moreover, we also observe that the characteristic time scale influences minimum time step Δt required for convergent numerical result. For higher cohesive strength T_n^{max} (thus smaller critical opening), characteristic time is lower, and so is time step Δt . The characteristic time scale for the cohesive law employed is $t_c = 0.052\mu s$, while $\Delta t = 0.002\mu s$ to $0.008\mu s$ for the computation (Table 5.2), which is about one order lower than the characteristic time.

The influence of mesh size on the evolution of the crack propagation pattern is shown in Figure 5.5 for an initial stretching parameter $\varepsilon = 0.015$. Evidently, the fracture and branching patterns are influenced by mesh refinement. The numerical result for coarse mesh (Figure 5.5 (a)) indicates few major branching. A close study reveals that minor branching do occur at almost every element intervals as the main crack advances, however the majority of these branches close afterwards, except for a few. For more refined meshes, Figure 5.5 (b) and (c) reveal similar fracture patterns both in branching angle and major branching spacing. Minor branches emanate from the main crack every couple of elements in a random pattern, and then arrest after running one or at most a few elements length. On the other hand, major (longer) branches appear between a certain distance, growing alternatively on each side of the main crack. These major microbranches extend about 0.5 to 1 mm and then arrest. This pattern is similar in both Figure 5.5 (b) and (c). The present

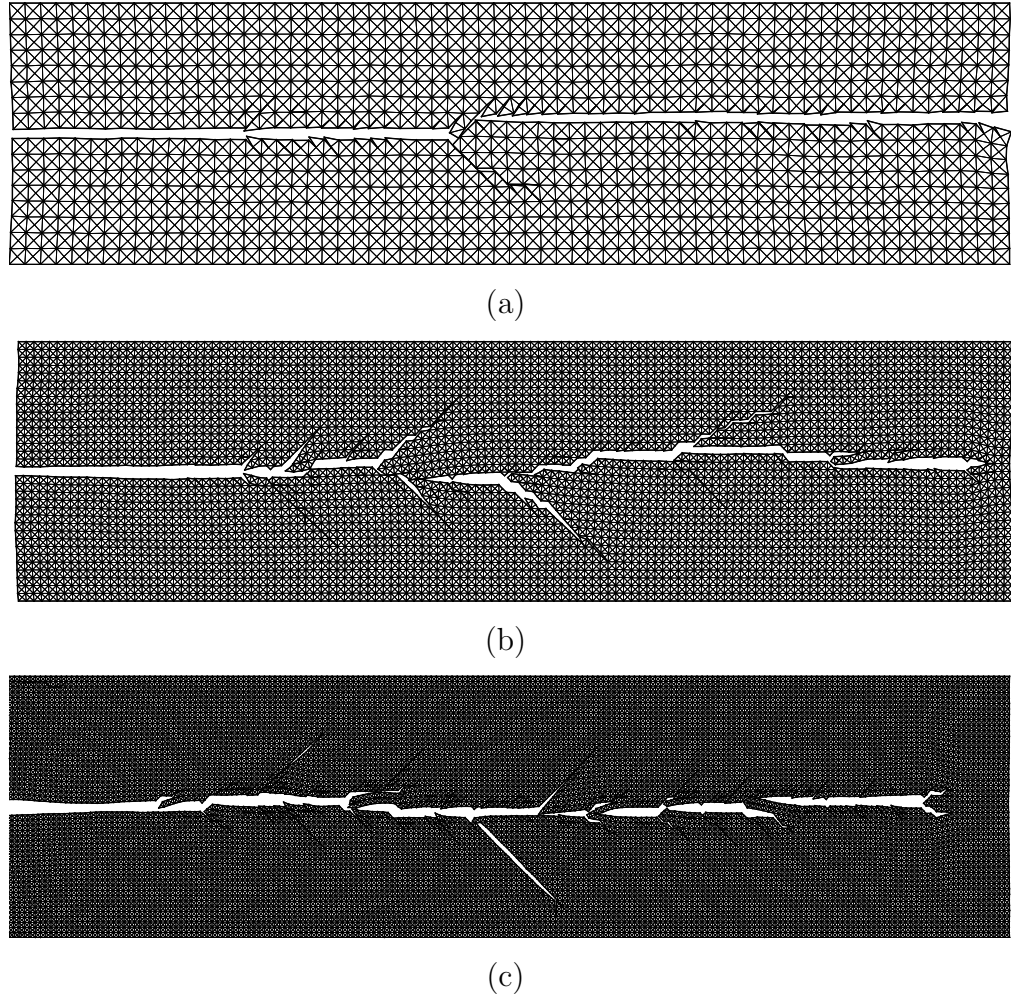


Figure 5.5: Mesh size influence on fracture pattern for applied stretch $\varepsilon = 0.015$; (a) 16×64 grid, simulation time $t=24\mu s$; (b) 32×128 grid, simulation time $t=22\mu s$; (c) 48×192 grid, simulation time $t=21\mu s$. Notice that the crack branches arrest, as in the experiments by Sharon and Fineberg [96] – this is due to extrinsic CZM framework using TopS.

computational framework clearly demonstrates that the crack branches arrest, as shown in the experiments by Sharon and Fineberg [96]. In contrast, the crack branches do not get arrested in the work by Miller et al. [67] (see Figure 6).

Table 5.3: Crack initiation time and average crack speed for loading case $\varepsilon = 0.015$ using different mesh discretizations.

Mesh	$h(\mu m)$	Grid	Crack initiation time (μs)	Average crack velocity (m/s)
(a)	250	16×64	1.12	633
(b)	125	32×128	0.67	642
(c)	83	48×192	0.47	642

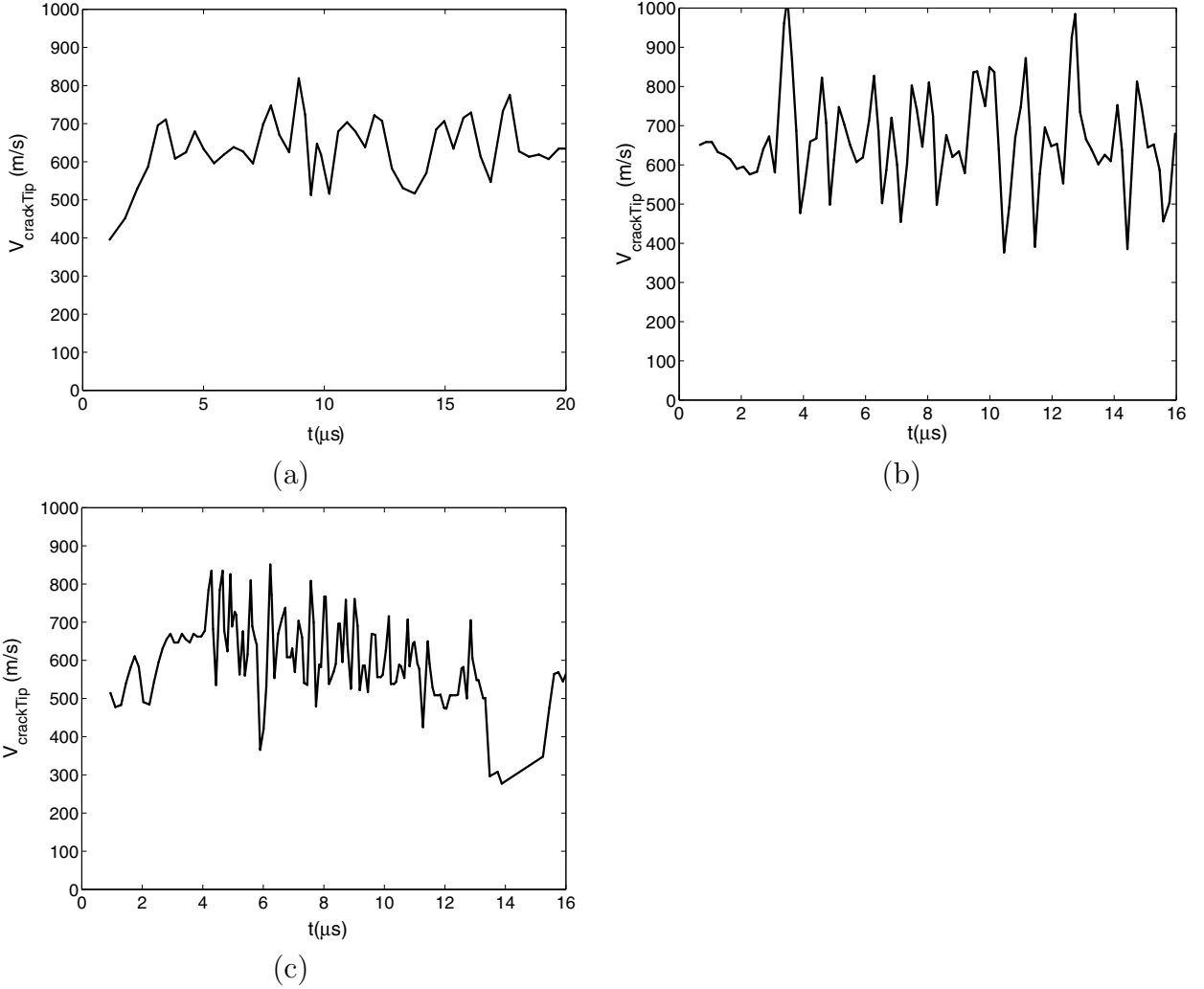


Figure 5.6: Crack velocity versus time considering initial stretch $\varepsilon = 0.015$ and various levels of mesh refinement; (a) grid 16×64 ; (b) grid 32×128 ; (c) grid 48×192 .

The influence of mesh size on crack propagation velocity is shown in Figure 5.6. Since there are usually more than one crack (including major and minor branches) during the simulation time, the velocity reported in Figure 5.6 is for the main crack, which is associated with the currently most advanced crack tip. Oscillation pattern is observed in all three mesh cases, which is accompanied by occurrence of microbranching. When a new microbranch appears, velocity for the main crack drops as energy released from stored strain energy in the strip flows into more channels. As the main crack advances and the microbranch closes at its trail, more energy flows back to the main crack and it accelerates. Depending on the frequency of microbranch occurrence and the length each microbranch runs, oscillation pattern appears repeatedly throughout the simulation. For refined mesh, more microbranches

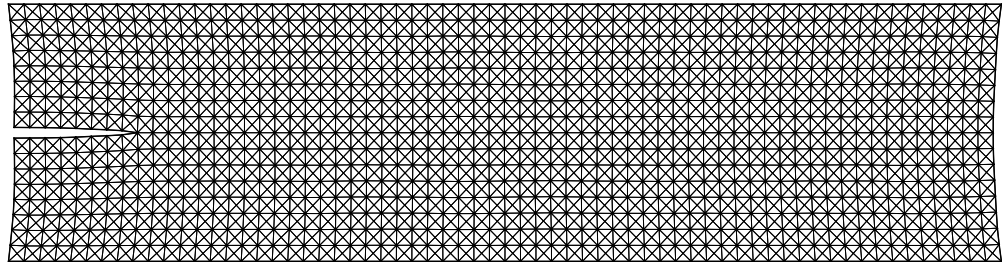
occur with sharper fluctuation in the velocity history (Figure 5.6). However, the main crack velocity oscillates along an “average” value, which is roughly the same for different meshes (633m/s, 642m/s and 642m/s for the three meshes). Table 5.3 compares the initial crack propagation time and average crack speed for different mesh sizes for the same problem. For refined mesh, crack initiation occurs relatively earlier (Table 5.3). Note that for the specific applied load, the results are meaningful and consistent despite the fact that the mesh sizes used do not strictly satisfy the recommended relationship between mesh size and statically estimated cohesive zone size [41, 56] mentioned above. Again, such estimated cohesive zone size provides merely a guidance in dynamic fracture problems. A previous investigation for mesh convergence in single crack propagation problem [115] also suggested that this requirement is problem dependent and can be relaxed under certain conditions.

Similar investigations are carried out for various initial stretches, which indicate that mesh size criterion is more stringent for problems of lower stretch loading. For example, for initial stretch $\varepsilon = 0.012$ as shown in Figure 5.7, the coarse mesh (16×64 grid, Figure 5.7 (a)) is not sufficient to initiate crack propagation, while for subsequently refined mesh, results of similar trend are obtained. Microbranching pattern for 48×192 grid mesh (Figure 5.7 (c)) is slightly different: a major bifurcation occurs at about $1/3$ of the strip length and the upper branch dominates later while the lower one closes after extending for about 3mm. However, the overall branching pattern, in terms of microbranch extension length and interval, as well as average crack propagation speed, is similar to the other two meshes (32×128 grid and 64×256 grid, Figure 5.7 (b) and (d)).

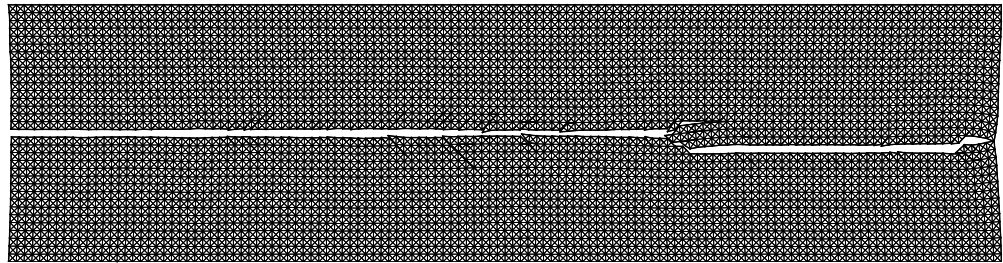
For initial stretch $\varepsilon = 0.01$, the coarse mesh is not sufficient to initiate crack propagation, as shown in Figure 5.8 (a). With refined mesh, crack propagates at an average speed of around 572m/s through the strip (Figure 5.8 (b) and (c)).

5.3.4 Influence of Applied Load on Microbranch Patterns

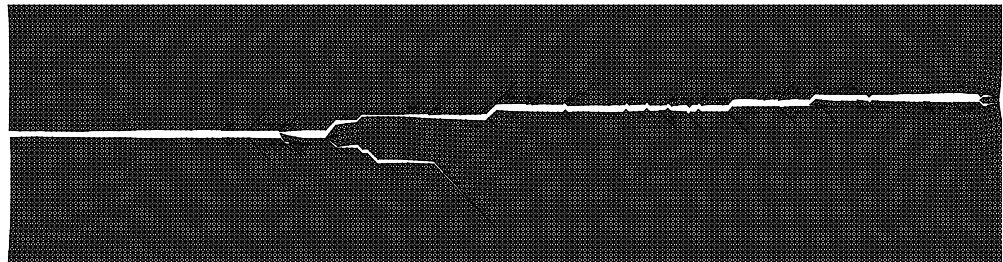
Experiments [96] indicate that with increasingly stored energy, the crack runs at higher velocity and generates longer and more noticeable microbranches. Figure 5.9 demonstrates the transition from smooth crack to more roughened crack with significant microbranches as initial stretch increases. The branches plotted in the figure consist of all the completely separated cohesive surfaces. The condition for cohesive element failure is defined such that all three Gauss points of the elements have experienced complete decohesion (in terms of separation Δ_{eff}). Therefore, some cohesive



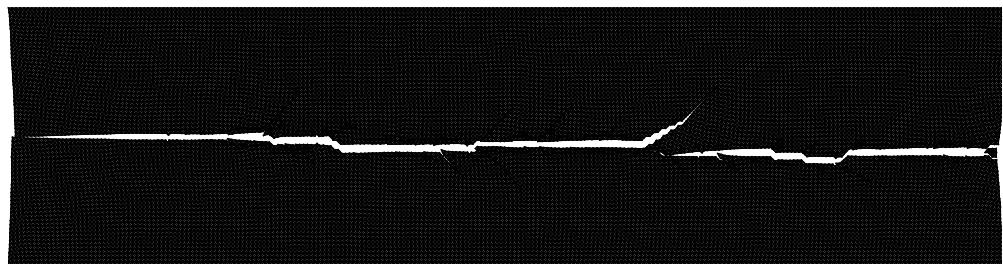
(a)



(b)

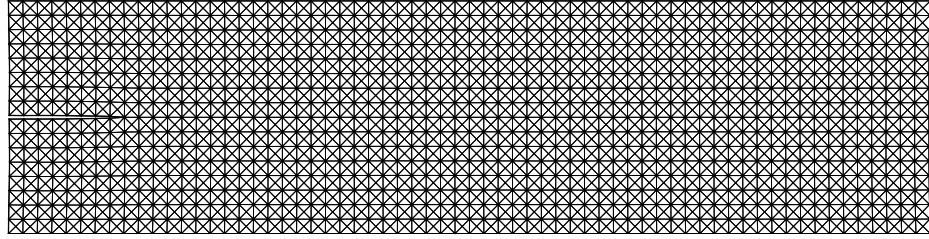


(c)

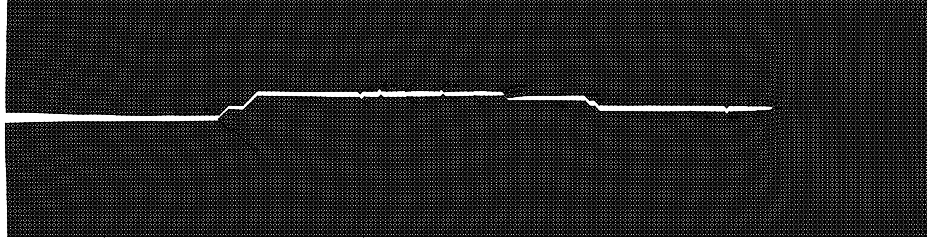


(d)

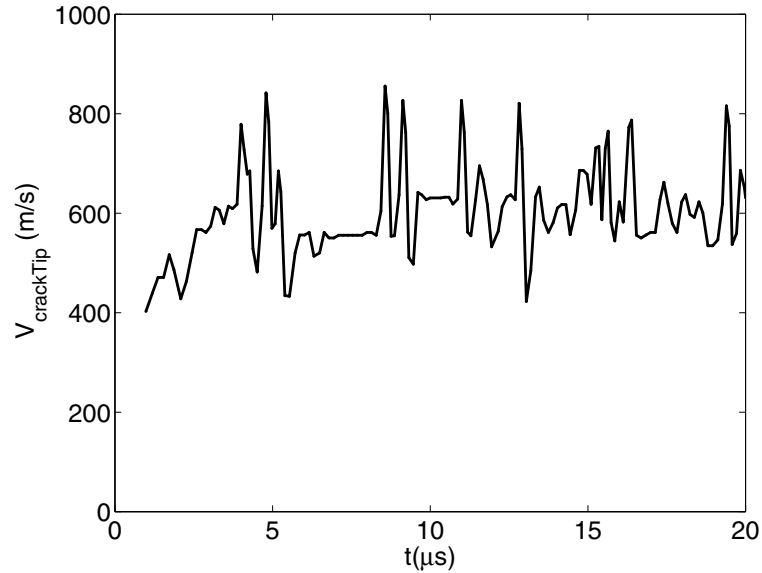
Figure 5.7: Mesh size influence on fracture pattern for applied stretch $\varepsilon = 0.012$; (a) 16×64 grid, simulation time $t=32\mu s$; (b) 32×128 grid, simulation time $t=24\mu s$; (c) 48×192 grid, simulation time $t=24\mu s$; (d) 64×256 grid, simulation time $t=23.4\mu s$.



(a)



(b)



(c)

Figure 5.8: Mesh size influence on fracture pattern for applied stretch $\varepsilon = 0.01$; (a) crack arrests for coarse mesh (16×64 grid); (b) crack pattern for refined mesh (48×192 grid); (c) associated crack velocity history for refined mesh (48×192 grid).

surfaces that are still active (i.e., not all Gauss points have reported decohesion), are not included. Consequently, a “smooth” crack in the plot does not indicate non-existence of any microbranch, rather, it means that even though microbranch may occur, they arrest before running more than one element length. With this understanding, Figure 5.9 (a) indicates that for $\varepsilon = 0.0085$ case, the main crack runs

smoothly through the entire strip, while more microbranches appear for $\varepsilon = 0.009$ and $\varepsilon = 0.01$ cases (Figure 5.9 (b) and (c), respectively). As applied loading increases, the microbranches also extend longer, as shown in Figure 5.9 (d). This overall trends are in agreement with the experiments by Sharon and Fineberg [96].

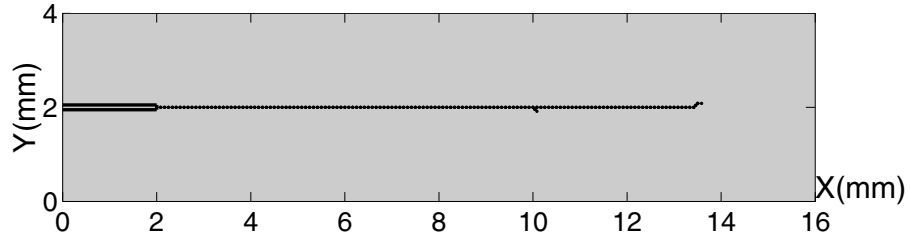
5.3.5 Influence of Applied Load on Crack Velocity

Comparison of crack initiation time and average crack speed for the simulations in Figure 5.9 is provided in Table 5.4. To avoid boundary effect influence on the calculated velocity result, average velocity is computed using only the central segment of crack, taken as $x=4$ to 12mm. Results in Table 5.4 clearly indicates that the larger the applied load, the earlier the crack propagation initiates, and the higher the average crack velocity.

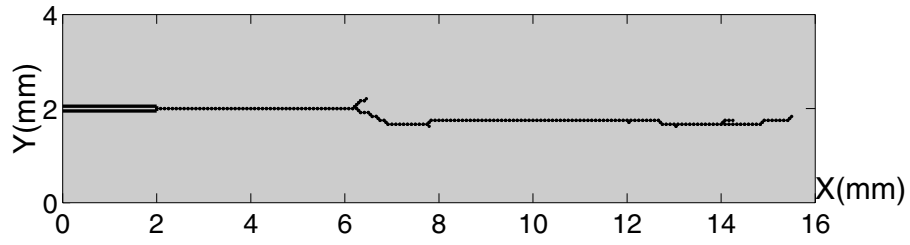
Table 5.4: Comparison of crack initiation time and average crack speed for different loading cases as shown in Figure 5.9.

Initial stretch ε	Mesh grids	Crack initiation time (μs)	Average crack velocity (m/s)
0.0085	48×192	1.61	518
0.009	48×192	1.23	558
0.010	48×192	0.98	572
0.012	48×192	0.71	597
0.015	48×192	0.47	642

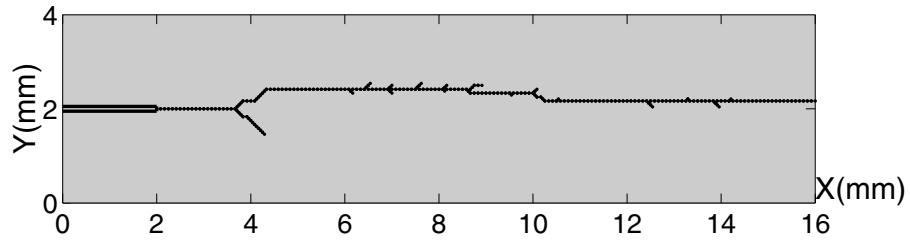
In the experiment [96], velocity oscillation level increases with higher loading due to presence of more frequent occurrence and longer length of microbranches. This trend can also be observed in the velocity profile, however it is clouded by additional numerical issues. Consider loading cases $\varepsilon = 0.01$ and $\varepsilon = 0.015$ for example. Since at lower loading rate ($\varepsilon = 0.01$) less microbranching occur compared to higher loading ($\varepsilon = 0.015$), there are noticeably longer periods of smooth velocity history in the former case (Figure 5.8(c)) than in the latter (Figure 5.6(c), using the same 48×192 grid mesh). As for the velocity amplitude oscillation, both velocity profiles vary between 500m/s and 800m/s, although the higher loading rate results in more peaks in the higher velocity amplitude than the lower loading rate case. A closer study of the velocity calculation and the microbranch pattern reveals that the computed velocity is highly sensitive to the insertion of each new cohesive element, when a sharp drop in the crack velocity history occurs. Since the crack velocity is computed as crack length variation over time step duration, it depends much on the choice of time step. In the present study, the time step is extremely small (of the order of $10^{-3}\mu s$), and



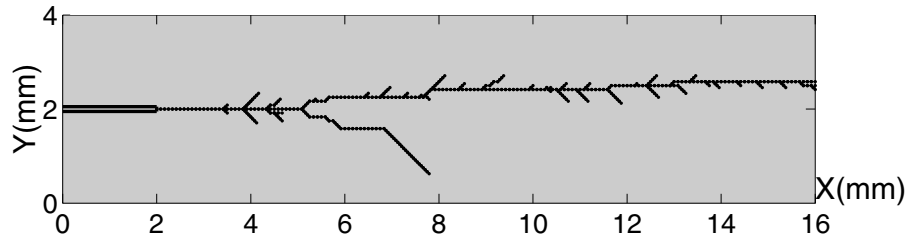
(a) $\varepsilon = 0.0085$



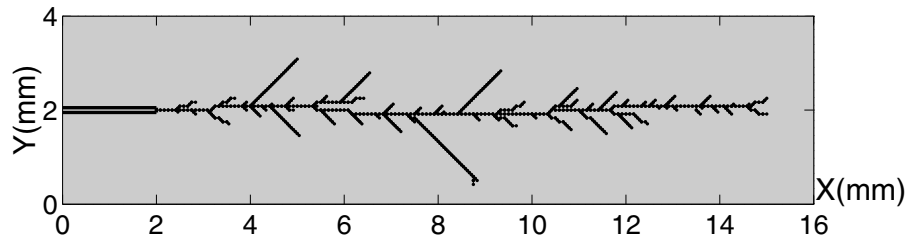
(b) $\varepsilon = 0.009$



(c) $\varepsilon = 0.010$



(d) $\varepsilon = 0.012$

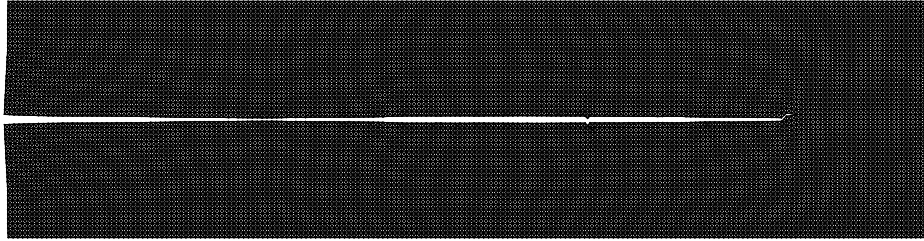


(e) $\varepsilon = 0.015$

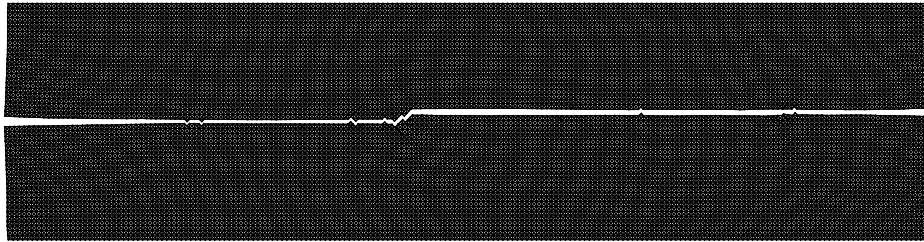
Figure 5.9: Comparison of branch patterns for various loading cases considering different applied strains (ε) and using an initial mesh discretization consisting of a 48×192 grid. (a) $\varepsilon = 0.0085$; (b) $\varepsilon = 0.009$; (c) $\varepsilon = 0.010$; (d) $\varepsilon = 0.012$; (e) $\varepsilon = 0.015$.

thus even though the crack length varies only marginally between two time steps, the calculated velocity variation is much amplified. Therefore, the high fluctuation in the velocity history is not only due to microbranching, but also to numerical artifacts.

5.3.6 Influence of Check-Time Intervals for Cohesive Element Insertion



(a) $\varepsilon = 0.0085$, nstep = 10

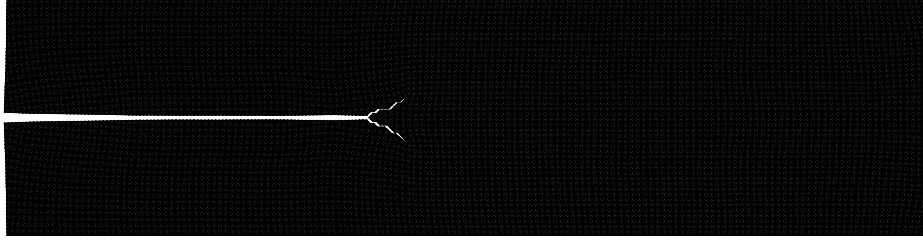


(b) $\varepsilon = 0.0085$, nstep = 1

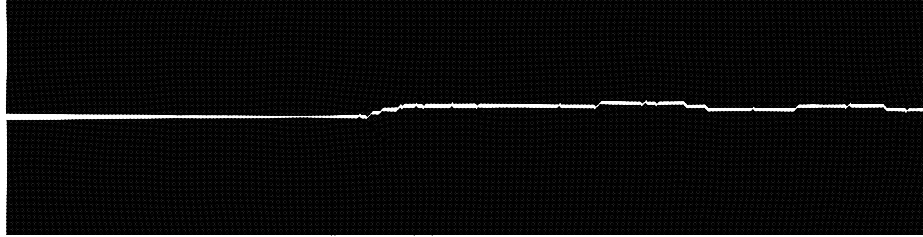
Figure 5.10: Comparison of branch patterns at $t = 19.8\mu s$ for applied initial stretch $\varepsilon = 0.0085$ using different cohesive element insertion checking intervals. (a) cohesive element insertion checked at every 10 time steps; (b) cohesive element insertion checked at every time step.

The numerical results are influenced by the time intervals at which the cohesive element insertion criterion is checked. Since the evaluation of cohesive element insertion at each element edge at each time step is computationally heavy, the procedure is usually carried out every certain time steps. In this study, the results reported so far are obtained using a time step interval of 10, i.e., the cohesive element insertion is checked every 10 time steps. To evaluate the influence of this issue, further simulations are carried out in which cohesive element insertion check are performed at every time step. Two cases of interest are investigated, one with higher initial stretch ($\varepsilon = 0.0085$) and another with lower initial stretch ($\varepsilon = 0.008$).

Figures 5.10 (a) and (b) compare the results with initial stretch of $\varepsilon = 0.0085$, using different time intervals. When cohesive element insertion is checked frequently



(a) $\varepsilon = 0.008$, $nstep = 10$



(b) $\varepsilon = 0.008$, $nstep = 1$

Figure 5.11: Comparison of branch patterns at $t = 25.4\mu s$ for applied initial stretch and $\varepsilon = 0.008$ using different cohesive element insertion checking intervals. (a) cohesive element insertion checked at every 10 time steps; (b) cohesive element insertion checked at every time step.

(e.g. at each time step), upon satisfaction of the criterion, a new cohesive surface is introduced, and local stress concentration is released. In contrast, when cohesive element insertion is checked less frequently, although local stress around crack tip is high enough to initiate new interface, the cohesive element cannot be inserted immediately, and local stress builds up, therefore at the time of cohesive element checking, more interfaces around the current crack tip may satisfy the separation criterion. Consequently, more microbranches form. This is revealed in Figure 5.10, which indicate that more microbranches (but short and heal soon after main crack runs forward) appear when cohesive element insertion is checked every 10 time steps (Figure 5.10 (a)), compared to the case for which cohesive element insertion is checked at each time step (Figure 5.10 (b)). More frequent check of cohesive elements also results in increased crack velocity, since the new crack surface does not need to “wait” up to 10 time steps. Therefore, at time $t = 19.8\mu s$, crack has run through the whole strip in Figure 5.10 (b), but not in Figure 5.10 (a). On the other hand, the overall crack patterns remain similar for this loading case.

In another test with initial stretch of $\varepsilon = 0.008$, the simulation results are different. Since this loading is relatively low, when two microbranches occur simultaneously (Figure 5.11 (a)), the energy flowing into the two branches is divided into similar

magnitude for each, and none is enough to drive the branch grow further. Consequently, both branches arrest. On the other hand, in Figure 5.11 (b), simultaneous branches of similar strength did not occur, but one crack is dominant, and the crack propagates through the strip.

5.3.7 Energy Evolution

Sharon and Fineberg [96] assumed that in the experiment carried out, all initial strain energy has been dissipated for fracture surface formation. At higher input energy, the apparent increase in fracture resistance is explained by the formation of undulated crack surface and formation of significantly increased microbranches. The assumption is supported by the measurement of microcrack surface being proportional to the input energy. In the current study, we may not be able to make the same assumption, as the strain energy density is much higher in the reduced dimension problem in comparison to the original experiment. However, it is necessary to check the energy evolution history.

The energy components of interest are listed below. i.e.,

- External work (\mathcal{E}_{ext}): work done by external loading.
- Kinetic energy (K): energy of motion.
- Strain energy due to elastic deformation of the bulk elements (U_{bulk}): elastic energy stored in the bulk material.
- Deformation energy due to elastic deformation of the cohesive elements (U_{coh}): elastic energy stored in the cohesive surfaces. This recoverable strain energy is depicted in Figure 5.13, where permanent damage and partial “relaxation” of the interface have occurred.
- Fracture energy (\mathcal{E}_{frac}): energy dissipated by the generation of new surfaces to form advancing crack(s).
- Total cohesive energy (\mathcal{E}_{coh}): sum of elastic cohesive energy (recoverable) and dissipated fracture energy (irrecoverable). $\mathcal{E}_{coh} = U_{coh} + \mathcal{E}_{frac}$.

For the current problem under discussion, the external work is kept constant, with value equal to the initial strain energy due to deformation. At any time instant, the total energy in the system is conserved, i.e.,

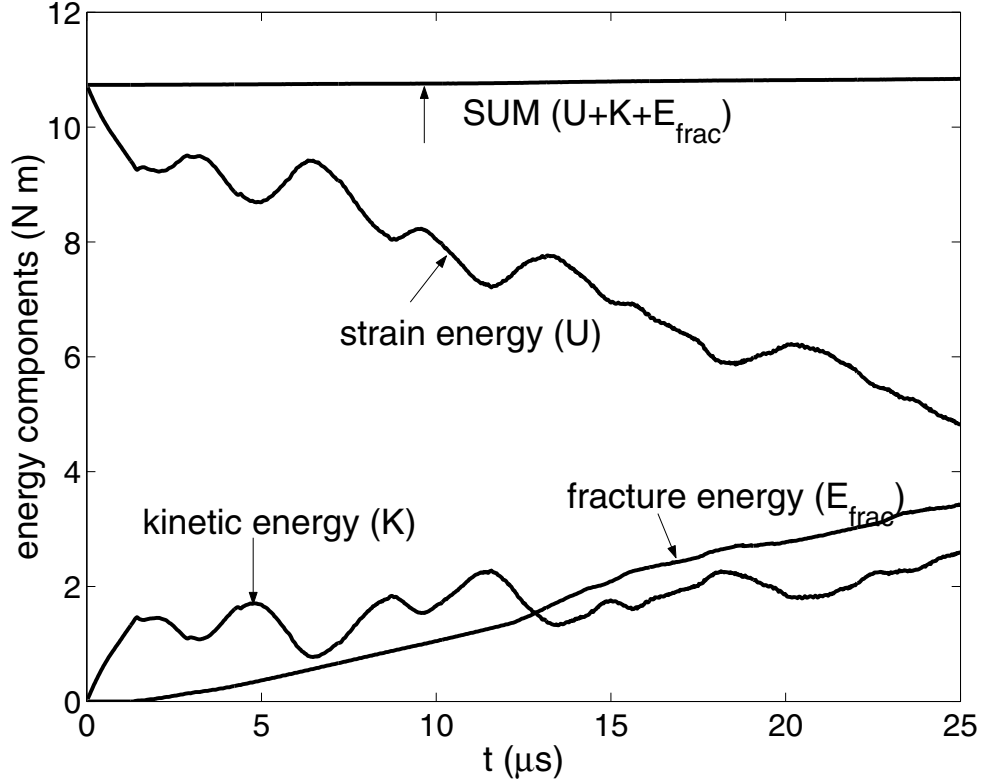


Figure 5.12: Energy components evolution with time for crack propagation problem with initial stretch $\varepsilon = 0.008$. Mesh used is 64×256 grids, cohesive element insertion is checked at every 10 time steps.

$$\mathcal{E}_{ext} = \mathcal{E}_{tot} = U + K + \mathcal{E}_{frac} = \text{constant}, \quad U = U_{bulk} + U_{coh} \quad (5.4)$$

where U represents the total recoverable elastic energy of the system.

Figure 5.12 shows the evolution of various energy components for the crack propagation simulation in the PMMA strip with $\varepsilon = 0.008$, including the total elastic energy U , kinetic energy K , energy dissipated by fracture \mathcal{E}_{frac} . Apparently, part of the strain energy initially stored in the system gradually converts to fracture energy and drives the crack to propagate. A portion of strain energy is converted to kinetic energy, which oscillates in equilibrium with the strain energy. During the dynamic simulation, some elastic energy U_{coh} is stored in the cohesive elements, which consists only of a nominal fraction of the total recoverable energy U . The total cohesive energy \mathcal{E}_{coh} can be decomposed into recoverable elastic part U_{coh} and dissipated fracture energy \mathcal{E}_{frac} .

Energy conservation is not perfectly retained in the numerical study, but is accept-

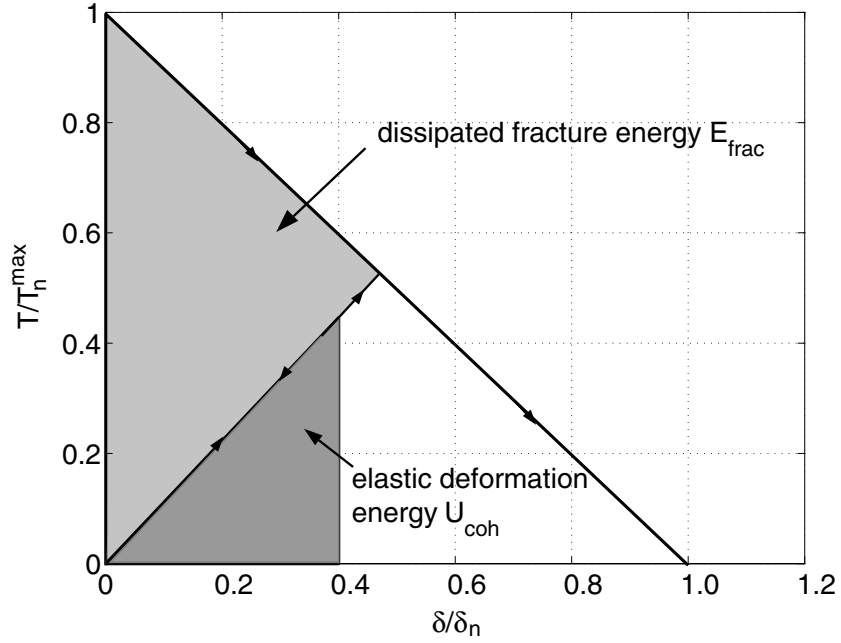


Figure 5.13: Components of the cohesive energy.

able. Source of the error is the discontinuous nature of the cohesive model adopted. As can be seen in Figure 1.4, the traction-separation is discontinuous at separation close to 0. As fracture energy is numerically evaluated by summation of the integral of cohesive energy rate over time for each cohesive surface, the strong discontinuity results in inevitable error in the results. The error can be reduced by decreasing time step so as to better approximate the jump in the cohesive model, however this issue is innate to the numerical scheme and cannot be completely eliminated. A recent proposal for a time continuous CZM has been presented by Papoulia et al. [77].

Chapter 6

Three-Dimensional Crack Initiation and Propagation

In this Chapter, the crack propagation in a pre-notched three point bending (TPB) concrete beam [49] is investigated. The objective of the original experiment was to reveal the influence of initial notch position on the crack propagation profile. Ruiz et al. [93] also simulated this problem using a three-dimensional finite element framework with extrinsic cohesive zone modeling. However, the numerical results did not fully capture the crack propagation paths in the experiment. The present work addresses the mesh quality issue in detail and reveals that the discrepancy between numerical results [93] and experimental observation [49] is due to insufficient mesh discretization. Another research work carried out by Sam et al. [94] also simulated this problem using a two-dimensional finite element settings. In this study, focus will be given to three-dimensional analysis.

Simulation results indicate that most of the features of the experiment are well reproduced. First, the mesh quality issue is investigated in detail, with focus on structured vs. unstructured mesh. Next, a damage zone analysis is presented, and crack propagation paths are compared for different initial notch positions. Finally, load history energy balance is investigated, which also provides verification of the numerical implementation.

6.1 Problem Description

John and Shah [49] tested pre-notched three-point-bend beam (TPB) specimens as shown in Figure 6.1. In order to test cases of different fracture mode mixity (combined tensile and shear mode), experiments [49] were carried out using specimens of different initial notch positions. John and Shah tested for both quasi-static and dynamic loading cases. In the present study, dynamic loading cases are considered.

By increasing the initial notch offset (represented by parameter γ where $0 < \gamma < 1$), the pre-notch was subjected to increasingly mode-II fracture conditions, and the trajectory of the crack varied accordingly. Two competing crack mechanisms drove

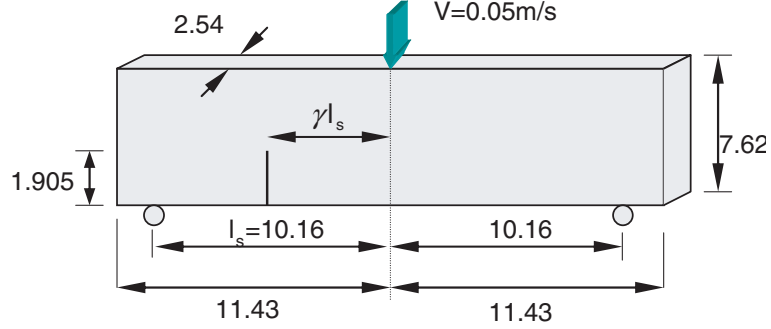


Figure 6.1: Geometry and loading condition of three-point-bending beam experiment [49]. Initial notch position is described by parameter γ which measures relative notch position from midspan to the left support.

fracture initiation and growth in the specimen, as illustrated in Figure 6.2: the crack growth initiated from the pre-crack; and the nucleation of crack at the lower center cross-section and its subsequent growth. The experiment indicates that for $\gamma < 0.77$, crack pattern is dominated by the growth of pre-crack, while for $\gamma > 0.77$ crack initiation and growth of center crack become dominant and shields the growth of pre-crack. The value $\gamma = 0.77$ is thus denoted as *transition stage* γ_t .

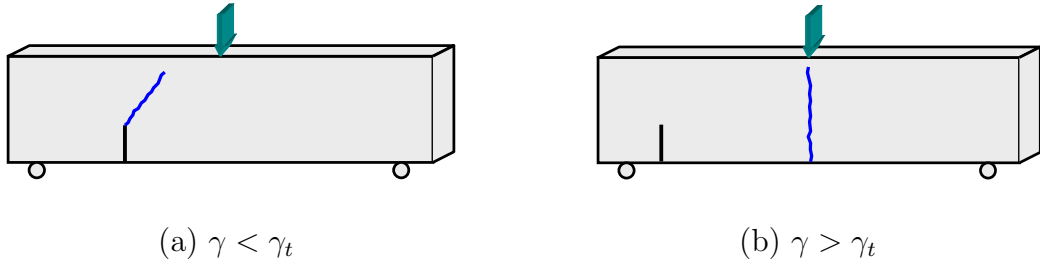


Figure 6.2: Possible crack propagation location and effect of pre-notch position on final failure; (a) crack grows from pre-notch tip for $\gamma < \gamma_t$ cases; (b) crack initiates from midspan and continues to grow until specimen failure for $\gamma > \gamma_t$ cases.

The experimental specimens [49] used type I ordinary Portland cement and crushed-limestone aggregate. The maximum aggregate size was 3/8 in. (9.5mm). The specimens were cast using a 1:2:2:0.5 mix (cement:sand:coarse aggregate:water, by weight). The notches were cut using a circular diamond saw after the 35-day curing period. In the present study, the bulk material was assumed to be linear elastic, which follows that of [93], as in Table 6.1. Cohesive model parameters follow those of [94]. Most of the numerical simulations are carried out assuming G_{IIc} to be equal to G_{Ic} ($G_{IIc} = G_{Ic}$).

Because the cohesive model approach requires fine mesh size to capture the nonlin-

Table 6.1: Material properties of concrete beam specimen [49].

E (GPa)	ν	ρ (kg/m^3)	G_{Ic} (N/m)	G_{IIc} (N/m)	T_n^{\max} (MPa)	T_t^{\max} (MPa)	c_R (m/s)
29	0.24	2400	22	22	8	22	2028

ear behavior at the crack tip region, the possible crack development region is typically more refined.

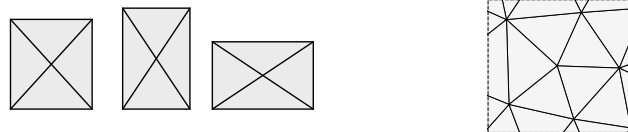
6.2 Structured vs. Unstructured Mesh

For arbitrary crack growth problem (i.e., crack not be defined *a priori*), element types adopted are usually triangles for 2D and tetrahedra for 3D. These elements allow more flexible crack propagation paths compared to 2D quadrilateral and 3D brick elements, since the latter ones only allow crack growth along either original direction or an abrupt 90° diversion.

Moreover, additional challenge in mesh generation remains regarding whether to use structured or unstructured mesh. Structured mesh is usually adopted when crack path is pre-defined and/or investigation targets on mesh convergence issues (see, e.g. [116]). However, structured mesh tends to confine crack propagation paths and lead to different crack profiles with different mesh orientations. We address this issue in detail in this section.

6.2.1 3D Structured Mesh Generation

The difference between structured and unstructured triangular meshes in 2D scenario is distinctive, as illustrated in Figure 6.3. Structured triangular mesh represents regular mesh patterns, although the grid aspect ratio may vary. Unstructured mesh, on the other hand, displays rather irregular mesh patterns.



(a) Structured 2D mesh

(b) Unstructured 2D mesh

Figure 6.3: Illustration of structured and unstructured 2D mesh; (a) structured mesh consisting of grid mesh divided into triangles; grid can have different aspect ratios; (b) unstructured mesh.

In 3D case, however, terms “structured” and “unstructured” alone may not be sufficient to describe mesh orientation possibilities. Here we first define “structured-through-thickness” mesh in the following. As illustrated in Figure 6.4, first a surface mesh is generated, regardless of it being structured or unstructured. In Figure 6.4, a structured surface mesh is used. Next, all the *lines* on the surface are “extruded” along thickness direction to form *surfaces*, as the darker surfaces represent. Finally, the volume is divided into Tetrahedron elements. This approach thus guarantees that if crack forms along the surface lines in 2D, it is possible for the crack to grow *through-thickness* following the same path in 3D.

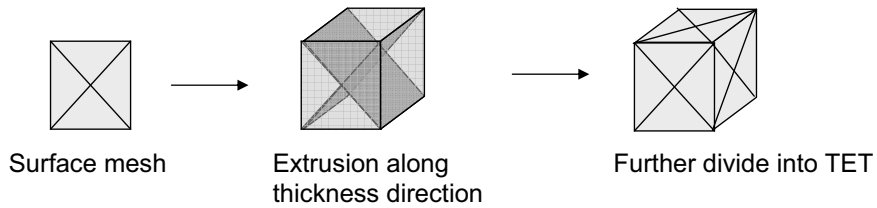


Figure 6.4: Creation of structured mesh through thickness direction.

Depending on whether mesh generation considers regular pattern in-plane and through-thickness, we can define four combinations of “structured” and “unstructured” mesh:

1. S-S mesh (fully structured mesh): structured both in-plane and through-thickness, as is the case in Figure 6.4.
2. U-S mesh: Unstructured in-plane but structured through-thickness.
3. S-U mesh: Structured through-thickness but unstructured through-thickness.
4. U-U mesh (fully unstructured mesh): unstructured both in-plane and through-thickness.

6.2.2 Fully Structured Mesh

Figure 6.5 shows a typical fully structured 3D mesh used in our study. The central zone where crack may potentially grow is discretized using fine mesh, with in-plane mesh grids of $2\text{mm} \times 2\text{mm}$. Structured mesh is generated as described in Section 4.2.1, and mesh size along thickness direction is 2.1mm. The mesh consists of 66,443 nodes and 293,658 4-node tetrahedron elements.

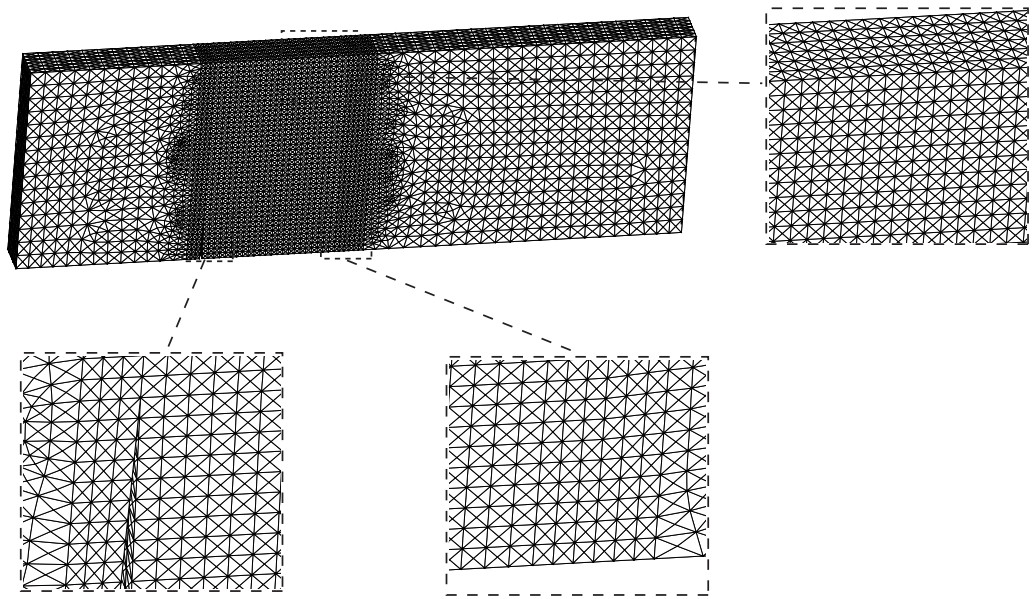
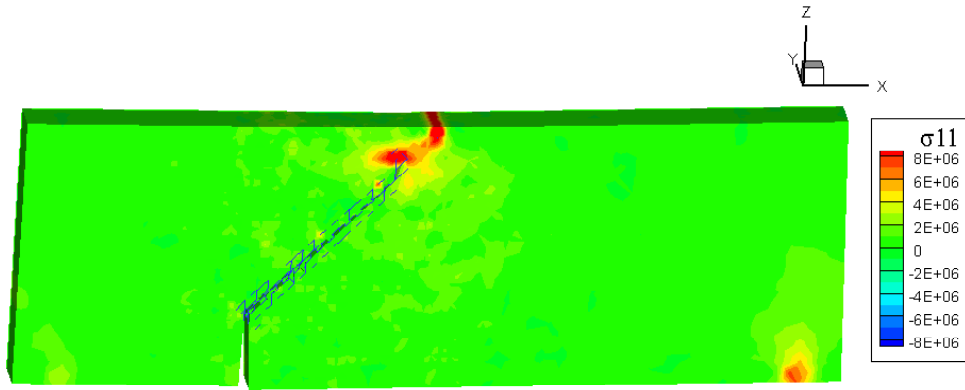
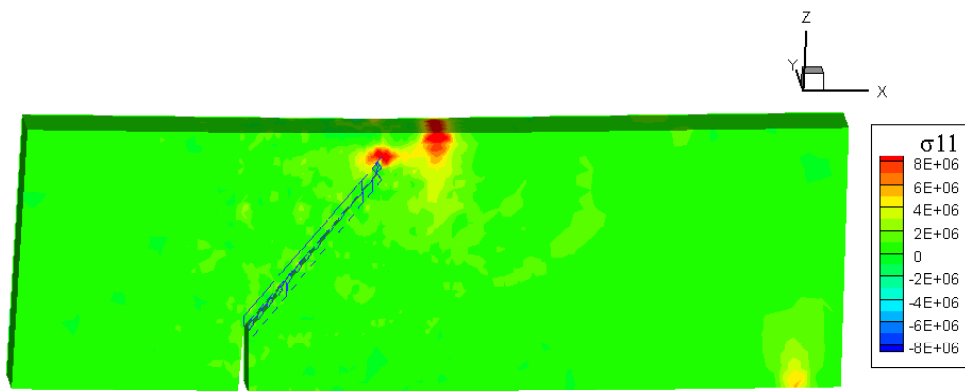


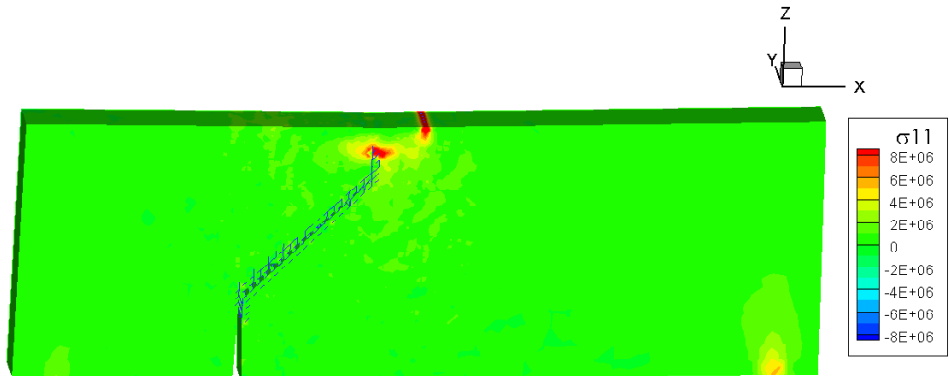
Figure 6.5: Sample fully structured 3D mesh, $\gamma = 0.5$, mesh grid size is $2\text{mm} \times 2\text{mm}$ within central zone where fracture may occur. Largest in-plane grid size outside central zone is $5\text{mm} \times 5\text{mm}$.



(a) mesh grid $3\text{mm} \times 3\text{mm}$



(b) mesh grid $2.5\text{mm} \times 3.3\text{mm}$



(c) mesh grid $2\text{mm} \times 2\text{mm}$

Figure 6.6: Results comparison for fully structured mesh; (a) mesh grid $3\text{mm} \times 3\text{mm}$, 110,540 Tet4 elements and 26,015 nodes; (b) mesh grid $2.5\text{mm} \times 3.3\text{mm}$, 100,600 Tet4 elements and 23,713 nodes; (c) mesh grid $2\text{mm} \times 2\text{mm}$, 293,658 Tet4 elements and 66,443 nodes.

We investigated three fully structured meshes of different orientation (mesh aspect ratio) and mesh size for the beam problem:

- $\gamma = 0.5$, in-plane mesh grid size $3\text{mm} \times 3\text{mm}$, through-thickness grid size 3.1mm .
- $\gamma = 0.5$, in-plane mesh grid size $2.5\text{mm} \times 3.3\text{mm}$, through-thickness grid size 3.1mm .
- $\gamma = 0.5$, in-plane mesh grid size $3\text{mm} \times 3\text{mm}$, through-thickness grid size 2.1mm .

Figure 6.6 compares the simulation results for the three meshes. For $\gamma = 0.5$, cracks initiate from notch tip and grow towards the loading point, which is roughly consistent with the experiment. However, numerical results are clearly mesh dependent: fracture grows along straight line following the mesh orientation. For the square grids (Figure 6.6 (a) and (c)), the crack plane follows a 45° diagonal plane. For length:height=3:4 mesh grid (Figure 6.6 (b)), the crack plane follows a 53° diagonal plane. The problem is not due to mesh size, since Figure 6.6 (a) and (c) indicates the same behavior. Such mesh-dependent behavior is obviously not desirable, and we conclude that fully structured 3D mesh should be avoided in cohesive fracture applications.

6.2.3 Unstructured In-plane and Structured Through-thickness Mesh

In this section, we examine U-S (Unstructured in-plane and Structured through-thickness) mesh. This type of mesh appears to be unstructured on plane surface, while provides possibility of crack growing through flat planes through thickness direction. Four meshes are examined:

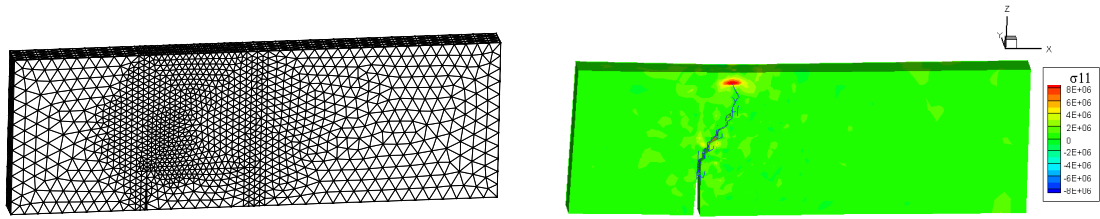
- $\gamma = 0.5$, in-plane mesh size 3mm , through-thickness grid size 3.1mm .
- $\gamma = 0.5$, in-plane mesh size 2mm , through-thickness grid size 2.1mm .
- $\gamma = 0.6$, in-plane mesh size 2mm , through-thickness grid size 2.1mm .
- $\gamma = 0.7$, in-plane mesh size 2mm , through-thickness grid size 2.1mm .

Figure 6.7 summarizes crack patterns for the above cases. The number of elements and nodes for different mesh level are comparable to those in the previous section.

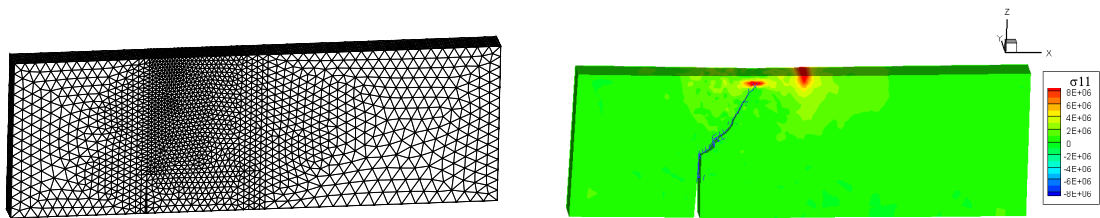
Clearly the crack pattern appears to be more “natural” compared to those in the previous section, and no longer grow along straight lines. The overall crack path angles also compare well with those obtained from experiment [49].

However, results still suggest mesh dependency, as shown in Figure 6.7 (a) and (b). The more refined mesh in Figure 6.7 (b) does not lead to better result compared to a coarser mesh in Figure 6.7 (a). Figure 6.7 (b) indicates vertical crack growth immediately after initiation, which is not consistent with the experiment. Such behavior is due to the mesh construction.

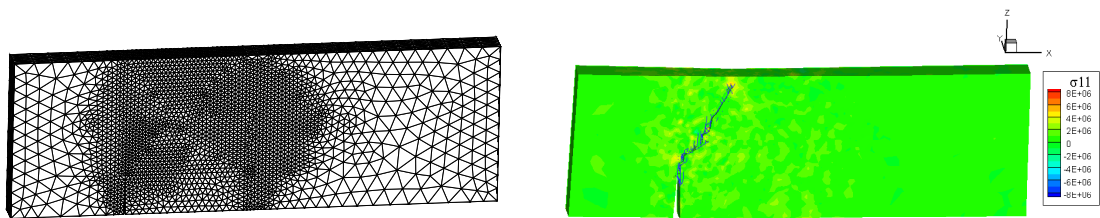
The U-S type of mesh allows through-thickness growth of surface crack pattern. The final crack patterns in Figure 6.7 reveal few micro-cracks along the main-crack, which indicates that crack growth is indeed confined along through-thickness planes. Therefore the final crack pattern is still strongly dependent upon in-plane surface mesh: whether the numerical result may capture the experiment depends on if the surface mesh allows a “nice” crack propagation direction that approximates the *real* crack in experiment. The reason that Figure 6.7 (b) shows an unsatisfactory result is that crack cannot “find” a proper propagation angle due to limited *surface* mesh orientation choices within that region. Such behavior again limits the applicability of the cohesive fracture approach, thus this type of mesh should also be avoided.



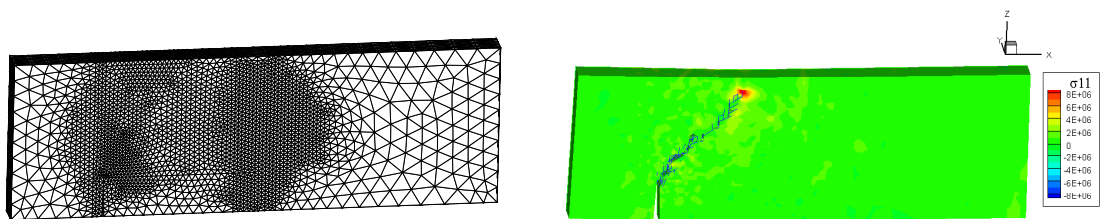
(b) $\gamma = 0.5$, 3mm U-S mesh



(b) $\gamma = 0.5$, 2mm U-S mesh

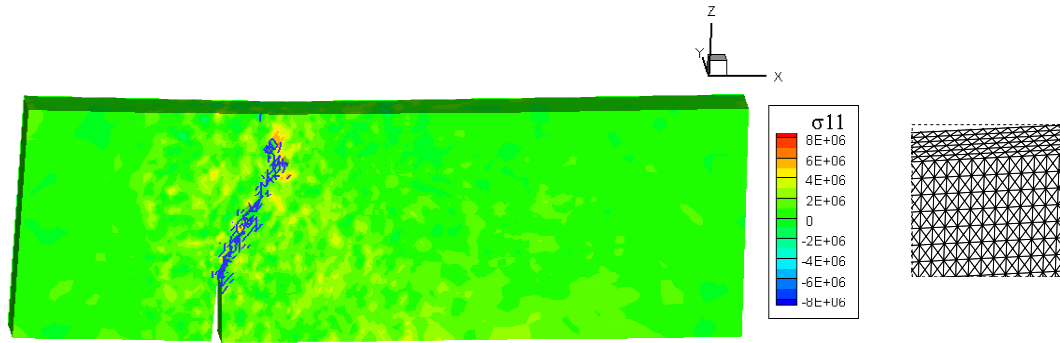


(c) $\gamma = 0.6$, 2mm U-S mesh

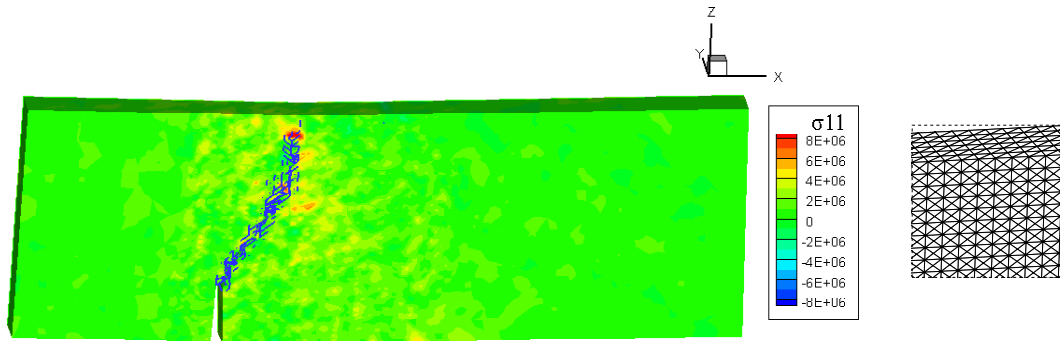


(d) $\gamma = 0.7$, 2mm U-S mesh

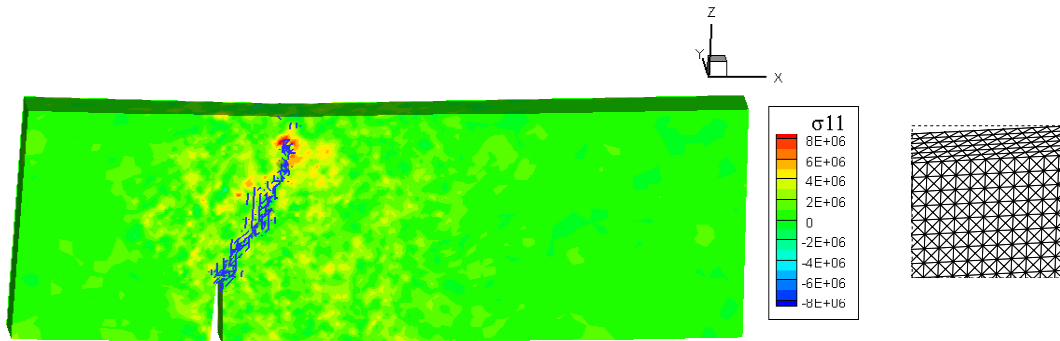
Figure 6.7: Unstructured in-plane and structured through-thickness meshes and results, mesh size inside crack propagation region is 2mm except for case (a), which uses 3mm; (a) $\gamma = 0.5$, 101,684 Tet4 elements and 20,220 nodes; (b) $\gamma = 0.5$, 209,418 Tet4 elements and 40,638 nodes; (c) $\gamma = 0.6$, 300,495 Tet4 elements and 57,914 nodes; (d) $\gamma = 0.7$, 305,184 Tet4 elements and 58,691 nodes.



(a) In-plane mesh grid $1.7\text{mm} \times 2.3\text{mm}$, $t=2.0\text{ms}$



(b) In-plane mesh grid $2.3\text{mm} \times 1.7\text{mm}$, $t=2.25\text{ms}$



(c) In-plane mesh grid $2\text{mm} \times 2\text{mm}$, $t=2.2\text{ms}$

Figure 6.8: Results comparison for structured in-plane and unstructured through-thickness meshes; (a) In-plane mesh grid $1.7\text{mm} \times 2.3\text{mm}$, 161,593 Tet4 elements and 32,189 nodes; (b) In-plane mesh grid $2.3\text{mm} \times 1.7\text{mm}$, 171,061 Tet4 elements and 33,876 nodes; (c) In-plane mesh grid $2\text{mm} \times 2\text{mm}$, 180,297 Tet4 elements and 35,308 nodes.

6.2.4 Structured In-plane and Unstructured Through-thickness Mesh

As the previous results show, meshes that are structured through-thickness direction usually lead to mesh dependency issues. In this section, we study the S-U mesh, here defined as Structured in-plane and Unstructured through-thickness mesh. Results are presented for different in-plane mesh grid aspect ratios:

- $\gamma = 0.5$, in-plane mesh grid $1.7\text{mm} \times 2.3\text{mm}$.
- $\gamma = 0.5$, in-plane mesh size $2.3\text{mm} \times 1.7\text{mm}$.
- $\gamma = 0.5$, in-plane mesh size $2.0\text{mm} \times 2.0\text{mm}$.

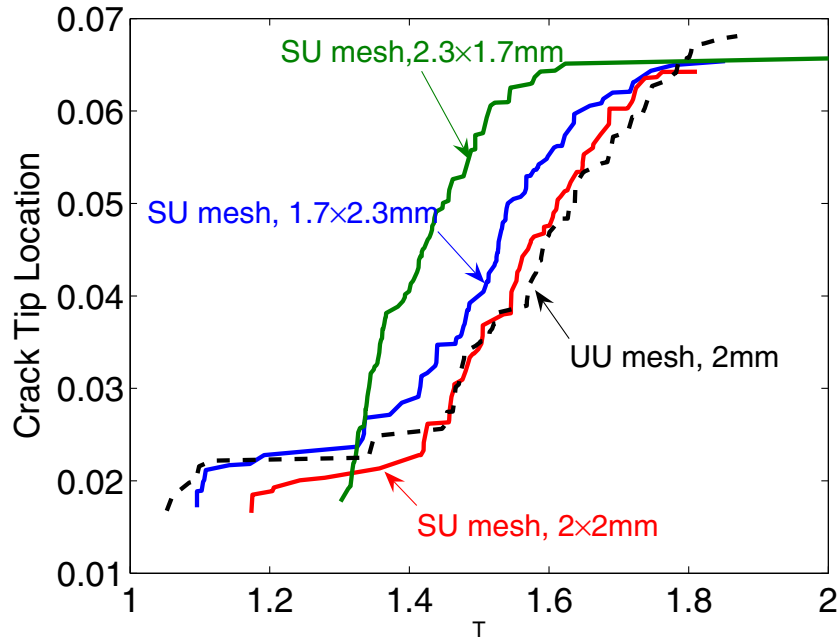


Figure 6.9: Time history of crack tip height for $\gamma = 0.5$ with S-U meshes of different in-plane mesh aspect ratios. Result for Fully Unstructured (U-U) mesh is plotted using dotted line for comparison purpose.

Figure 6.8 compares the final fracture patterns of the three cases. For $\gamma = 0.5$, the experiment indicates a roughly straight crack propagation angle of around 30° measured from the initial crack plane. Despite the in-plane mesh grid orientation biases, cracks in all three cases find similar paths propagating towards the top surfaces of specimens.

Difference between current results and those obtained using structured through-thickness meshes is distinctive. There is a broader band of damage zone along the fracture path, due to the unstructured mesh nature. Crack tries to find a straight path (as the experiment shows), yet due to interior mesh roughness, it has to damage a broader zone in order to propagate through.

Figure 6.9 compares the crack tip height locations for the three cases, as well as fully unstructured (U-U) mesh for the same notch position. Apparently, cracks initiation vary from case to case. Once crack picks up speed, however, crack growth speeds (curve slopes) are similar. Therefore we conclude that S-U mesh results in overall mesh-independent crack path, but crack evolution history still depends on individual mesh construction.

6.2.5 Fully Unstructured Mesh

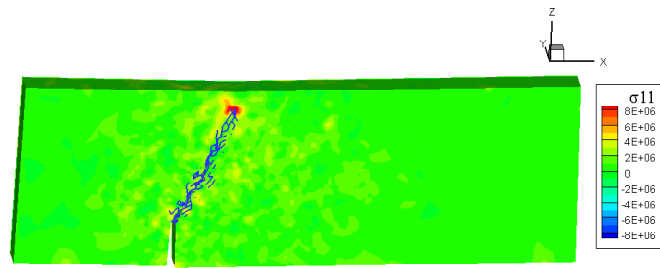
Based on results presented in previous sections, we conclude that unstructured mesh is most appropriate for the present investigation. Figure 6.10 summarizes final crack patterns obtained using fully unstructured meshes for $\gamma = 0.5, 0.6, 0.7$ and 0.8 , with mesh size 2mm inside the central region.

Crack initiates and propagates from the pre-notch tip up to $\gamma = 0.7$. For $\gamma = 0.5$ and $\gamma = 0.6$ (Figure 6.10 (a) and (b)), no damage occurs at the midspan. For $\gamma = 0.7$ (Figure 6.10 (c)), midspan damage occurs, but was shielded by the main crack from the pre-notch. For $\gamma = 0.8$ (Figure 6.10 (d)), cracks initiate from both the midspan and pre-notch, and the midspan crack finally becomes dominant.

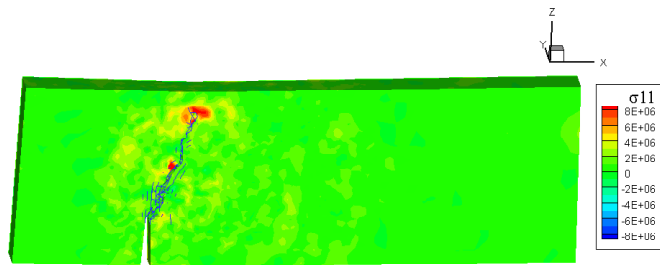
Crack behavior can be further understood with the time history of crack tip location shown in Figure 6.11. As expected, crack initiation time is earlier for smaller γ value, since the competition between the two sites are less significant. Moreover, average crack speed is faster for higher γ value. The experiment [49] did not report crack speed, therefore no direct comparison is available for the current study. We thus compare with the 2D simulation results presented in [94], which indicate crack speed between 80m/s to 240m/s for various γ values. The average crack speed shown in Table 6.2 is consistent with those in [94] too.

6.3 Cohesive Damage Zone Development

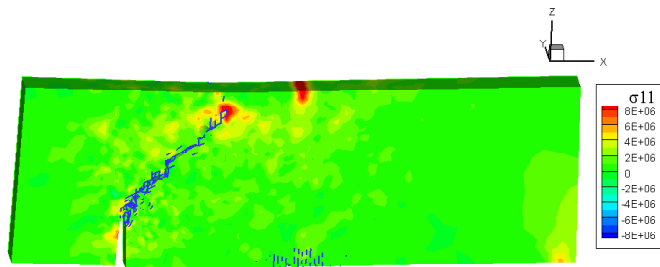
Cohesive zone concept represents existence of a damage zone, in which material is neither fully damaged nor intact. Accordingly, only those cohesive interfaces that



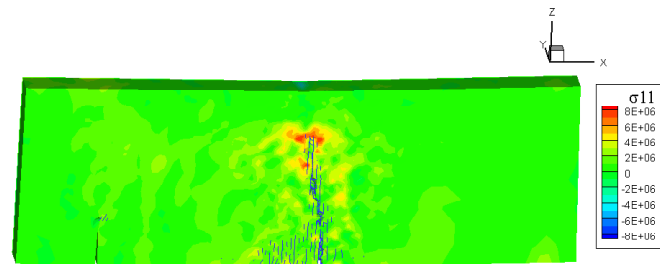
(a) $\gamma = 0.5, t=1.9\text{ms}$



(b) $\gamma = 0.6, t=1.8\text{ms}$



(c) $\gamma = 0.7, t=2.2\text{ms}$



(d) $\gamma = 0.8, t=2.3\text{ms}$

Figure 6.10: Crack patterns for fully unstructured meshes; (a) $\gamma = 0.5$, 98,123 Tet4 elements and 19,915 nodes; (b) $\gamma = 0.6$, 107,113 Tet4 elements and 21,599 nodes; (c) $\gamma = 0.7$, 96,003 Tet4 elements and 19,363 nodes; (d) $\gamma = 0.8$, 105,289 Tet4 elements and 21,169 nodes;

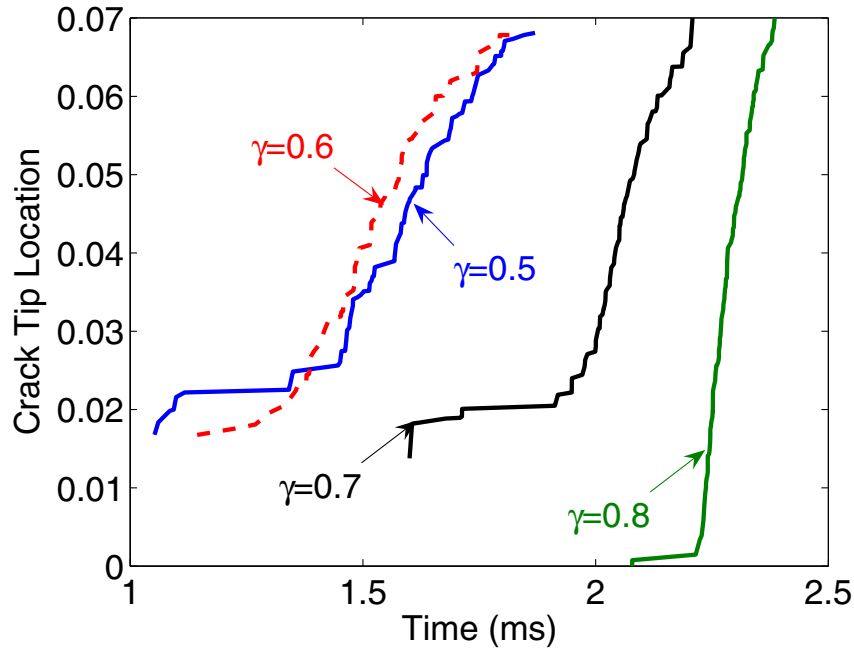


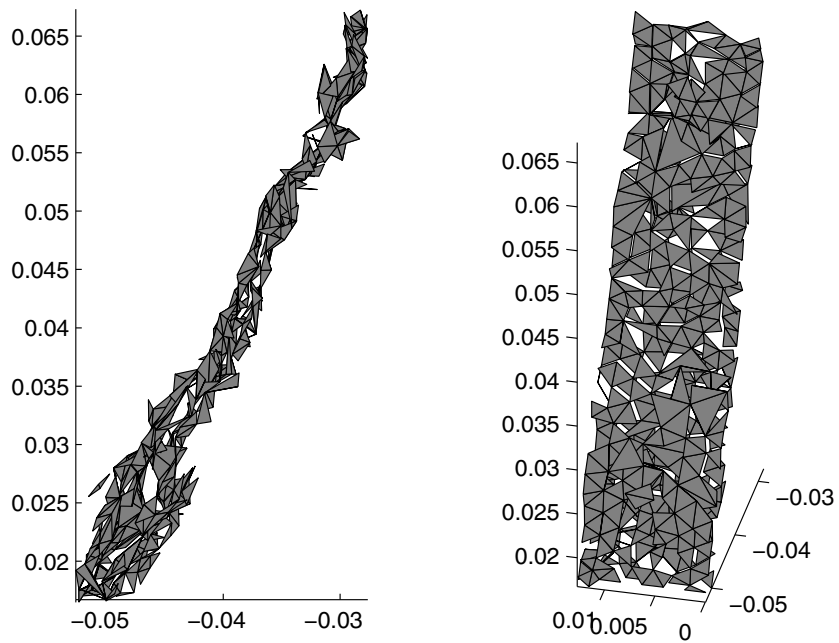
Figure 6.11: Time history of crack tip height for $\gamma = 0.5, 0.6, 0.7, 0.8$. Fully unstructured mesh.

Table 6.2: Crack initiation time and crack velocity for $\gamma = 0.5, 0.6, 0.7, 0.8$.

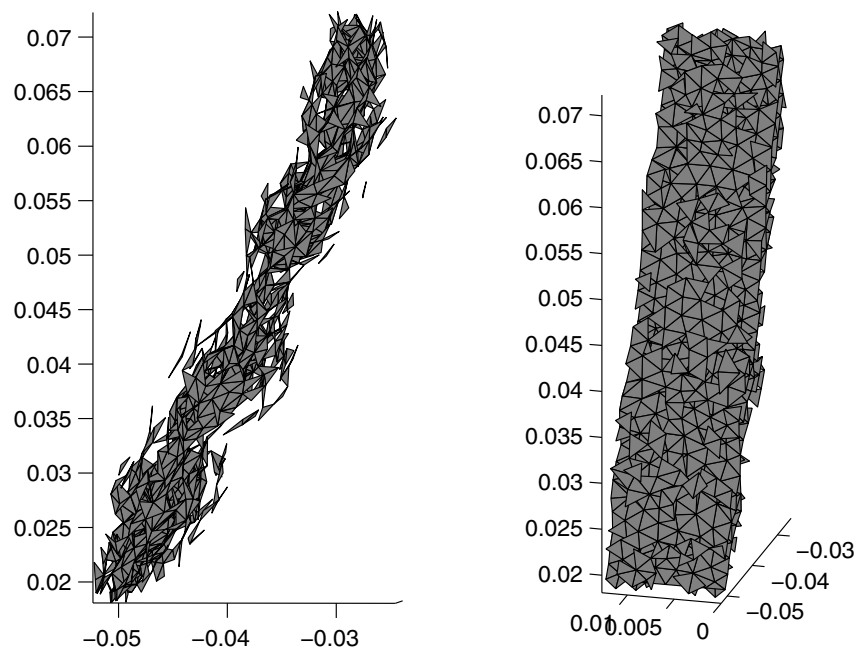
γ	t_{init} (ms)	v_{crack} (m/s)
0.5	1.052	62.8
0.6	1.144	74.4
0.7	1.601	86.8
0.8	2.078	234.4

have undergone complete separation represent fully cracked surfaces, while others represent damaged surfaces. Figure 6.12 illustrates such concept for the $\gamma = 0.5$ case using fully unstructured (U-U) mesh. All fully separated cohesive elements are plotted in Figure 6.12 (a), from the front and side viewing angles. Figure 6.12 (b) represents *all* cohesive interfaces, regardless of fully fractured or not. Clearly, a damage zone develops across a certain width band along the cracked surfaces, and only around 1/3 (537 out of 1530) of cohesive interfaces are fully damaged.

A further comparison is made in Figure 6.13. The damage index d_{coh} is defined as the ratio of current effective separation to material critical separation value. Therefore, $d_{coh}=0$ indicates no damage, while $d_{coh}=1$ indicates full separation. Figure 6.13 (a) plots all cohesive interfaces with damage indexed as gray scale. Clearly, the central ones are fully damaged (black), and the damage band (different gray scale) spreads



(a) All completely separated cohesive elements



(b) All cohesive elements inserted during simulation

Figure 6.12: Comparison of (a) crack surfaces representing full decohesion and (b) all inserted cohesive surfaces during simulation.

over a certain distance surrounding the central crack path. Figure 6.13 (b) plots the damage zone in the beam, and a similar damage band can be observed.

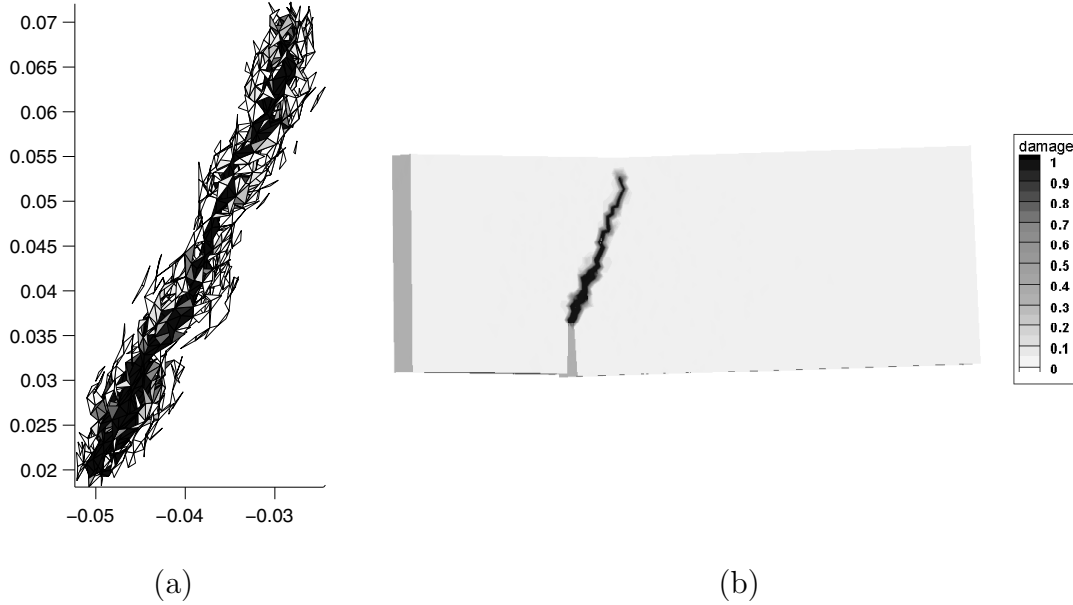


Figure 6.13: Cohesive damage zone of $\gamma = 0.5$ case using fully unstructured mesh; (a) gray scale representation of damage development in all cohesive elements; (b) damage zone contour in beam.

Damage zone plots for all $\gamma = 0.5, 0.6, 0.7, 0.8$ cases are illustrated in Figure 6.14. We point out that in the case of $\gamma = 0.7$, although damage begins to develop in the midspan zone, those cohesive elements are merely damaged, but never went through complete decohesion. Moreover, some fragmentation and debris can be observed in the case of $\gamma = 0.8$ around the midspan region.

6.4 Energy Evolution

John and Shah [49] did not report energy terms, yet for verification purpose, it is necessary to check the energy evolution history. The energy components of interest are listed below. i.e.,

- External work (\mathcal{E}_{ext}): work done by external loading.
- Kinetic energy (K): energy of motion.
- Strain energy due to elastic deformation of the bulk elements (U_{bulk}): elastic energy stored in the bulk material.

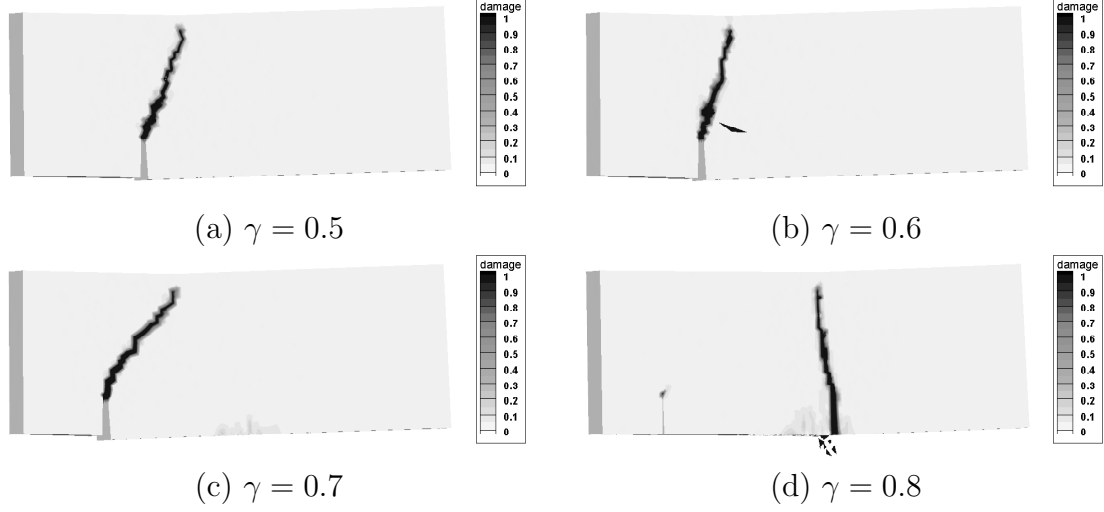


Figure 6.14: Damage zone plots for (a) $\gamma = 0.5$; (b) $\gamma = 0.6$, (c) $\gamma = 0.7$, (d) $\gamma = 0.8$.

- Deformation energy due to elastic deformation of the cohesive elements (U_{coh}): elastic energy stored in the cohesive surfaces.
- Fracture energy (\mathcal{E}_{frac}): energy dissipated by the generation of new surfaces to form advancing crack(s).
- Total cohesive energy (\mathcal{E}_{coh}): sum of elastic cohesive energy (recoverable) and dissipated fracture energy (irrecoverable). $\mathcal{E}_{coh} = U_{coh} + \mathcal{E}_{frac}$.

Energy conservation dictates that at any time instant, the total energy in the system is conserved, i.e.,

$$\mathcal{E}_{ext} = \mathcal{E}_{tot} = U + K + \mathcal{E}_{frac}, \quad U = U_{bulk} + U_{coh} \quad (6.1)$$

where U represents the total recoverable elastic energy of the system.

Figure 6.15 shows the evolution of various energy components for the crack propagation simulation in the TPB with $\gamma = 0.5$ using fully unstructured mesh, including the total elastic energy U , kinetic energy K , energy dissipated by fracture \mathcal{E}_{frac} . Comparing $\mathcal{E}_{\uparrow\downarrow}$ and $\mathcal{E}_{\downarrow\downarrow}$ indicates that energy balance is preserved. Apparently, in the beginning stage, as load increases and beam bending increases, majority of external work converts to strain energy in the system. By time $t \approx 1.1ms$, crack initiates, and fracture energy value \mathcal{E}_{frac} begins to increase. At time $t \approx 1.4ms$, crack speed picks up and energy absorbed by increasing amount of cohesive interfaces increases more rapidly. As the crack grows, deformation energy in the bulk body is

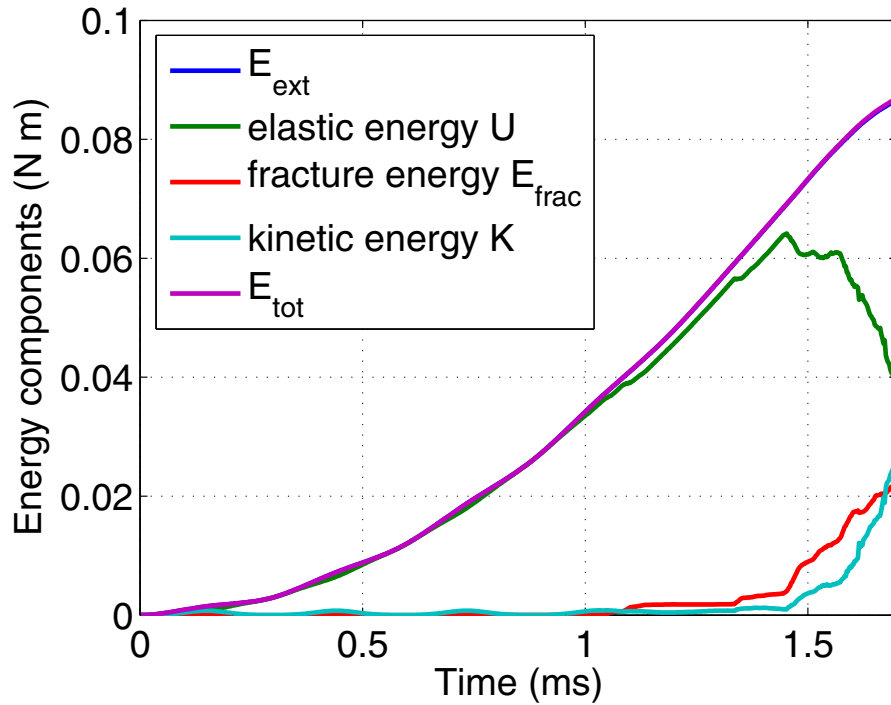


Figure 6.15: Energy components evolution with time for $\gamma = 0.5$, fully unstructured mesh.

releases, thus elastic energy U drops. During the dynamic simulation, some elastic energy U_{coh} is stored in the cohesive elements, which consists only of a nominal fraction of the total recoverable energy U . The total cohesive energy \mathcal{E}_{coh} can be decomposed into recoverable elastic part U_{coh} and dissipated fracture energy \mathcal{E}_{frac} .

6.5 Load History

The experiment [49] employed displacement control loading with a dynamic loading rate of 0.05m/s. In the numerical simulation, we may retrieve reaction force at the loading site and investigate load capacity for different notch position cases.

Figure 6.16 plots the reaction force for the $\gamma = 0.5$ case. As the solid line shows, the reaction force increases at the beginning stage with periodic oscillation. In the static case, the reaction force would increase monotonically with increasing displacement loading until the specimen reaches maximum loading capacity. In the dynamic case, however, the beam vibration results in the oscillation in force profile. At round time $t \approx 1.1ms$, the periodic pattern is broken, as beam damage begins to occur and crack initiates. For comparison purposes, the fracture energy term \mathcal{E}_{frac} discussed in

previous section is also plotted, which clearly shows that the crack initiation stage coincides with the reaction force changing point. Afterwards, the beam can still sustain small amount of loading increment, while at around time $t \approx 1.4$ to 1.5 ms, crack begins to grow rapidly (dotted fracture energy curve grows sharply), thus the beam reaches its maximum loading capacity, which then drops with crack growth.

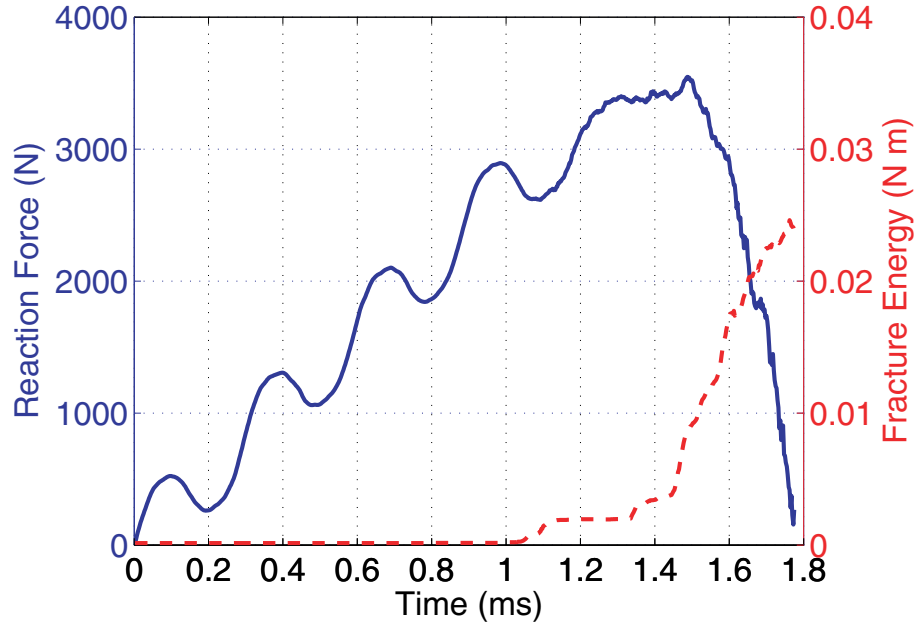


Figure 6.16: Reaction force at loading point evolution with time for $\gamma = 0.5$, fully unstructured mesh.

Reaction force evolutions for different initial notch positions ($\gamma = 0.5, 0.6, 0.7, 0.8$) are plotted in Figure 6.17. Unstructured meshes are used. The initial oscillation in force history is observed in each case, and the force magnitudes are very close before crack initiation occurs. This indicates that at the beginning, despite the different notch position, the force responses to displacement loadings are similar in all cases. However, the final loading capacities are different, depending on when crack initiation starts. Increasing γ delays crack initiation, and thus results in a higher final loading capacity. The loading capacity is summarized in Table 6.3.

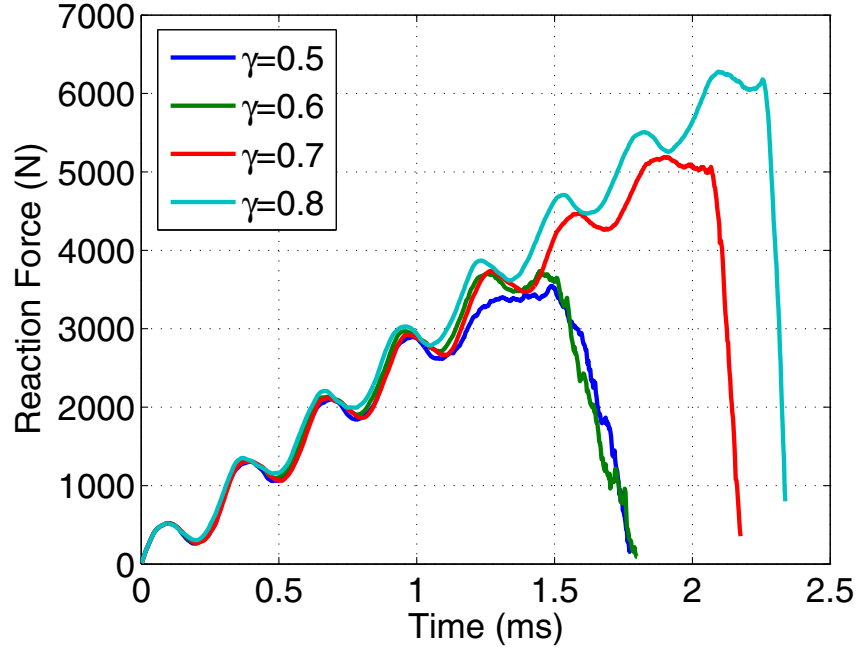


Figure 6.17: Comparison of reaction force at loading point evolution with time for $\gamma = 0.5, 0.6, 0.7, 0.8$, fully unstructured mesh.

Table 6.3: Crack initiation time and load capacity $\gamma = 0.5, 0.6, 0.7, 0.8$.

γ	t_{init} (ms)	Load capacity (N)
0.5	1.052	3500
0.6	1.144	3800
0.7	1.601	5200
0.8	2.078	6200

Chapter 7

Conclusions and Future Work

In this study, the dynamic fracture phenomena in homogeneous and nonhomogeneous materials under impact loading are investigated, which include 2D and 3D problems. A research code is developed using *explicit* dynamic scheme. Both intrinsic and extrinsic cohesive models are employed and their capabilities explored, with focus placed on the latter. As illustrated in the study, the cohesive approach, which is based on a cohesive view of material fracture, is promising for modeling generalized fracture without predefined fracture criteria. It proves to be an attractive alternative approach for investigating a broad range of fracture phenomena, especially for dynamic fracture propagation problems involving branching and fragmentation, which are not handled properly by other models.

In this Chapter, a brief summary of the content and contribution of the study is presented, followed by a number of suggestions for the future work.

7.1 Concluding Remarks

This work first provides some background information, including an overview of the numerical approach adopted in the study, explanation of the cohesive zone modeling concept, and how this model is implemented in the numerical scheme. A number of existing CZMs are critically reviewed to show the general capability of CZMs, as well as the advantages and potential caveats of each model. After that, the dynamic behavior of homogeneous and graded materials *without* cracks are investigated. The explicit scheme is used in this study, with adaptation of the time step control due to varying wave speed in FGMs. Graded elements are introduced by means of a generalized isoparametric formulation including material gradation at the element level. Examples are presented to validate the code and assess the bulk behavior under dynamic loading for homogeneous and functionally graded materials. A careful study of one-dimensional wave propagation problem in homogeneous and FGM beams reveals the effect of smooth material gradation on stress concentration reduction.

An intrinsic cohesive fracture problem is then presented for a mixed-mode crack propagation problem, for which the initial slope of cohesive model was carefully controlled to reduce the mesh dependency issue.

The focus of the study is placed on extrinsic cohesive model, which requires a robust and efficient data structure to support adaptive cohesive interface insertion. A topological framework for supporting both intrinsic and extrinsic fragmentation simulation is then presented in detail. This data structure proposes a new systematic topological classification of fracture facet, thus achieving a general algorithm that works for 2D and 3D models, including both linear and quadratic elements. Computational experiments demonstrate the scalability and correctness of the proposed approach. The insertion of cohesive elements is based on local topological operations. As a consequence, the time needed to insert cohesive elements at all facets of a model is linearly proportional to the number of inserted elements. The numerical fracture analysis code is then built on the data structure through a transparent interface. Numerical examples in Chapters 5 and 6 illustrate the power and versatility of this data structure.

An important yet so far inadequately investigated physical length scale in fracture problem is the damage zone size. Chapter 4 is devoted to numerically evaluated cohesive zone size problem by investigating a simple double-cantilever beam problem. Both static and dynamic cases are investigated, as well as rate effect influence on cohesive zone size. Results strongly suggest that the commonly adopted cohesive zone size estimate in literature may be misleading in deciding adequate element size to resolve crack tip nonlinearity. A further mesh quality study in Chapter 6 also supports this conclusion.

With the support of a topological data structure, a number of numerical simulations are carried out, for both 2D and 3D dynamic fracture problems under impact loading, and considering crack propagation along arbitrary paths with crack nucleation capability. Comparison of results of numerical simulation with those from experiments indicates that the extrinsic cohesive zone approach is capable of capturing the fracture microbranching instability characteristics, and provide better results compared to intrinsic models. Another 3D numerical example also successfully reproduces experimental observation of crack nucleation, propagation and competition mechanisms in concrete beam fracture problems.

The primary contributions in this study are briefly summarized as follows:

- Extension of bilinear CZM to nonhomogeneous materials that employs separate

laws for normal and tangential quantities rather than using effective quantities. A similar approach is also proposed for extrinsic CZM.

- Implementation of fracture analysis code in conjunction with topological data structure to support adaptive cohesive interface insertion during simulation. Both 2D and 3D research codes are developed.
- Investigation of difference between intrinsic and extrinsic CZMs.
- Investigation of cohesive zone size using numerical examples.
- Investigation of arbitrary crack propagation and microbranching instability issues in brittle materials under impact loading.
- Investigation of crack nucleation, propagation and competition phenomena in brittle concrete beams under impact loading, and detailed mesh quality analysis.

7.2 Suggestions for Future Work

Some open problems that call for closer attention and careful treatment for the CZM approach are discussed below. The topics are listed from a more specific to a more general computational perspective.

Mesh dependence and cohesive zone size. Xu and Needleman [108] have reported that distinctively different crack propagation profiles are generated with different mesh orientation patterns. In reference [56], similar results have been presented, and the reason for this phenomenon was ascribed to mesh size. To ensure that the crack propagates in a continuum way rather than in a discrete manner, certain upper limit for mesh size needs to be prescribed. However this limit requires the mesh size to be of the same scale of the material characteristic length, for which the computation overhead is enormous. No results have yet been reported to demonstrate that violation of this condition is indeed responsible for mesh dependence. Thus a systematic study needs to be conducted to address mesh dependence in CZMs, including recommendation for practical simulation frameworks. A related issue is a realistic estimate of cohesive zone size for the numerical analysis. The current study provides a basic investigation of this issue, however no specific recommendation has been made yet.

Retrieve cohesive law directly from experiments. Recent studies suggest a promising new direction in the experimental determination of cohesive law through digital image correlation (DIC) techniques. Kubair et al. [102] employed DIC to obtain matrix/particle interface cohesive property of high explosives by directly recording local crack tip displacement and deriving stress field, thus retrieving cohesive law. By combining forward and inverse computations, it is possible to calibrate detailed material parameters and crack front behaviors.

Fragmentation and Contact. The current study focuses on dynamic fracture behavior under low or mid-velocity loadings. Under high-velocity loading (e.g., bullet penetrating body armor), contact and fragmentation mechanisms need to be considered. The CZM itself is capable of preventing unrealistic penetration between *paired* cohesive interfaces, however, it does not guarantee proper contact behavior in general. Such physical process can only be realistically simulated through an integrated framework that considers contact, friction, friction generated heat effect, plasticity, large deformations, and fragmentation.

Parallel Computing. Parallelization of program code is mandatory for large-scale simulation, particularly for 3D dynamic fracture simulation. In 3D simulation, the number of degrees of freedom (DOF) is usually high, and CZM parameters also dictate an upper limit of mesh size. Thus a large number of DOFs in the bulk area is generated. Moreover, the presence of cohesive elements again increases the number of DOFs of the finite element model by introducing multiple nodes at the same location, and requires a smaller time step to obtain stable results. All these factors lead to huge computation overhead, hence parallel computing must be employed. Moreover, by incorporating the topological data structure into the numerical scheme, the parallel computing also requires parallelization of the data structure as well as efficient information transfer and optimal load balancing with a changing topology.

Scientific Visualization. Rich fracture phenomena, e.g., crack tunneling, branching and fragmentation, can be captured with CZM approach. This also adds to the complexity in the understanding and explanation of the results, especially in 3D simulations. To help understand the mechanical phenomena at various scales and regions of the body under investigation, scientific visualization tools need to be employed, including virtual reality. Various means involving visual and audio effects can be pursued. This further requires development of the finite element code to

accommodate these features, e.g., real-time data retrieving, and data postprocessing.

References

- [1] J. Aboudi, M.-J. Pindera, and S.M. Arnold. Higher-order theory for functionally graded materials. *Composites: Part B (Engineering)*, 30(8):777–832, 1999.
- [2] J. Aboudi, M.-J. Pindera, and S.M. Arnold. Higher-order theory for periodic multiphase materials with inelastic phases. *International Journal of Plasticity*, 19(6):805–847, 2003.
- [3] F.F. Abraham, D. Brodbeck, R.A. Rafey, and W.E. Rudge. Instability dynamics of fracture: A computer simulation investigation. *Physical Review Letters*, 73:272–276, 1994.
- [4] T.L. Anderson. *Fracture Mechanics: Fundamentals and Applications*. CRC Press, Boca Raton, Florida, 3rd edition, 2005.
- [5] G.I. Barenblatt. The formation of equilibrium cracks during brittle fracture: General ideas and hypothesis, axially symmetric cracks. *Applied Mathematics and Mechanics (PMM)*, 23:622–636, 1959.
- [6] G.I. Barenblatt. The mathematical theory of equilibrium cracks in brittle fracture. In: Dryden, H. L., von Karman, T. (Eds.). *Advances in Applied Mechanics*, 7:55–125, 1962.
- [7] M. Barquins and M. Ciccotti. On the kinetics of peeling of an adhesive tape under a constant imposed load. *International Journal of Adhesion and Adhesives*, 17:65–68, 1997.
- [8] E. Barthel and S. Roux. Velocity-dependent adherence: An analytical approach for the JKR and DMT models. *Langmuir*, 16(21):8134–8138, 2000.
- [9] Z.P. Bažant and L. Cedolin. *Stability of Structures: Elastic, Inelastic, Fracture and Damage Theories*. Oxford University Press, New York, 1991.
- [10] Z.P. Bažant and J. Planas. *Fracture and Size Effect: in Concrete and Other Quasibrittle Materials*. CRC Press, New York, 1998.
- [11] J. Baylor. A numerical simulation of impact-induced damage of composite materials. Master’s thesis, University of Illinois at Urbana-Champaign, 1998.

- [12] M.W. Beall and M.S. Shephard. A general topology-based mesh data structure. *International Journal of Numerical Methods in Engineering*, 40:1573–1596, 1997.
- [13] T. Belytschko, H. Chen, J. Xu, and G. Zi. Dynamic crack propagation based on loss of hyperbolicity and a new discontinuous enrichment. *International Journal of Numerical Methods in Engineering*, 58:1873–1905, 2003.
- [14] T. Belytschko, R.L. Chiapetta, and H.D. Bartel. Efficient large scale non-linear transient analysis by finite elements. *International Journal of Numerical Methods in Engineering*, 10:579–596, 1976.
- [15] V. Birman and L. W. Byrd. Modeling and analysis of functionally graded materials and structures. *Applied Mechanics Reviews*, 60(5):195–216, 2007.
- [16] G.T. Camacho and M. Ortiz. Computational modeling of impact damage in brittle materials. *International Journal of Solids and Structures*, 33:2899–2938, 1996.
- [17] G.F. Carey, M. Sharma, and K.C. Wang. A class of data structures for 2-D and 3-D adaptive mesh refinement. *International Journal of Numerical Methods in Engineering*, 26:2607–2622, 1988.
- [18] W. Celes, G.H. Paulino, and R. Espinha. A compact adjacency-based topological data structure for finite element mesh representation. *International Journal of Numerical Methods in Engineering*, 64(11):1529–1556, 2005.
- [19] W. Celes, G.H. Paulino, and R. Espinha. Efficient handling of implicit entities in reduced mesh representations. *Journal of Computing and Information Science in Engineering, Special Issue on Mesh-Based Geometric Data Processing*, 5(4):348–359, 2005.
- [20] A. Chakraborty and J. Gopalakrishnan. A spectrally formulated finite element for wave propagation analysis in functionally graded beams. *International Journal of Solids and Structures*, 40(10):2421–2448, 2003.
- [21] E.S.C. Chin. Army focused research team on functionally graded armor composites. *Materials Science and Engineering*, A259:155–161, 1999.
- [22] R.D. Cook, D.S. Malkus, and M.E. Plesha. *Concepts and Applications of Finite Element Analysis*. John Wiley & Sons, New York, 3rd edition, 1989.
- [23] F. Costanzo and J.R. Walton. A study of dynamic crack growth in elastic materials using a cohesive zone model. *International Journal of Engineering Science*, 35:1085–1114, 1997.
- [24] B.N. Cox, H. Gao, D. Gross, and D. Rittel. Modern topics and challenges in dynamic fracture. *Journal of the Mechanics and Physics of Solids*, 53:565–596, 2005.

- [25] L. De Floriani and A. Hui. A scalable data structure for three-dimensional non-manifold objects. In *Eurographics Symposium on Geometry Processing*, pages 72–82, 2003.
- [26] J.E. Dolbow and M. Gosz. On the computation of mixed-mode stress intensity factors in functionally graded materials. *International Journal of Solids and Structures*, 39(9):2557–2574, 2002.
- [27] D.S. Dugdale. Yielding of steel sheets containing cracks. *Journal of the Mechanics and Physics of Solids*, 8:100–104, 1960.
- [28] J.W. Eischen. Fracture of non-homogeneous materials. *International Journal of Fracture*, 34:3–22, 1987.
- [29] J.W. Eischen. An improved method for computing the J_2 integral. *Engineering Fracture Mechanics*, 26(5):691–700, 1987.
- [30] F. Erdogan. Fracture mechanics of functionally graded materials. *Composites Engineering*, 5:753–770, 1995.
- [31] J.D. Eshelby. Energy relations and the energy-momentum tensor in continuum mechanics. In W.F. Kanninen, A.R. Rosenfield, and R.I. Jaffe, editors, *Inelastic Behavior of Solids*, pages 77–115. McGraw-Hill, New York, 1970.
- [32] H.D. Espinosa and P.D. Zavattieri. A grain level model for the study of failure initiation and evolution in polycrystalline brittle materials. Part 1: Theory and numerical implementation. *Journal of Materials*, 35:333–364, 2003.
- [33] M.L. Falk, A. Needleman, and J.R. Rice. A critical evaluation of cohesive models of dynamic fracture. *Journal de Physique IV*, 11:Pr5–43–50, 2001.
- [34] X. Feng, M.A. Meitl, A.M. Bowen, Y. Huang, R.G. Nuzzo, and J.A. Rogers. Competing fracture in kinetically controlled transfer printing. *Langmuir*, 2007, in press.
- [35] L.B. Freund. Crack propagation in an elastic solid subject to general loading - I, constant rate of extension. *Journal of the Mechanics and Physics of Solids*, 20:129–140, 1972.
- [36] L.B. Freund. Dynamic fracture mechanics. In F.R.S Batchelor, C. Wushch, and J. Rice, editors, *Cambridge Monographs on Mechanics and Applied Mathematics*. Cambridge University Press, New York, 1990.
- [37] H. Gao. Surface roughening and branching instabilities in dynamic fracture. *Journal of the Mechanics and Physics of Solids*, 41:457–486, 1993.
- [38] H. Gao. A theory of local limiting speed in dynamic fracture. *Journal of the Mechanics and Physics of Solids*, 44:1453–1474, 1996.

- [39] R.V. Garimella. Mesh data structure selection for mesh generation and FEA applications. *International Journal of Numerical Methods in Engineering*, 55:451–478, 2002.
- [40] A. Gent and J. Schultz. Effect of wetting liquids on the strength of adhesion of viscoelastic materials. *Journal of Adhesion*, 3:281–294, 1972.
- [41] P.H. Geubelle and J. Baylor. Impact-induced delamination of laminated composites: a 2D simulation. *Composites Part B Engineering*, 29(5):589–602, 1998.
- [42] W.A. Gooch, B.H. Chen, M.S. Burkins, R. Palicka, J. Rubin, and R. Ravichandran. Development and ballistic testing of functionally gradient ceramic/metal applique. *Material Science Forum*, 308-311:614–621, 1999.
- [43] A.L. Gurson. Continuum theory of ductile rupture by void nucleation and growth: Part I – Yield criteria and flow rules for porous ductile media. *Journal of Engineering Materials and Technology*, 99:2–15, 1977.
- [44] D.M. Hawken, P. Townsend, and M.F. Webster. The use of dynamic data structures in finite element applications. *International Journal of Numerical Methods in Engineering*, 33(9):1795–1811, 1992.
- [45] J.W. Hutchinson. Singular behavior at the end of tensile crack tip in a hardening material. *Journal of the Mechanics and Physics of Solids*, 16:13–31, 1968.
- [46] E. Iesulauro, A.R. Ingraffea, S. Arwade, and P.A. Wawrzynek. Simulation of grain boundary decohesion and crack initiation in aluminum microstructure models. In W.G. Reuter and R.S. Piascik, editors, *Fatigue and Fracture Mechanics*, volume 33, pages 715–728. American Society for Testing and Materials, West Conshohocken, PA, 2002.
- [47] Z. Jin, G.H. Paulino, and R.H. Dodds Jr. Cohesive fracture modeling of elastic-plastic crack growth in functionally graded materials. *Engineering Fracture Mechanics*, 70:1885–1912, 2003.
- [48] Z.-H. Jin, G.H. Paulino, and R.H. Dodds Jr. Finite element investigation of quasi-static crack growth in functionally graded materials using a novel cohesive zone fracture model. *ASME Journal of Applied Mechanics*, 69:370–379, 2002.
- [49] R. John and S.P. Shah. Mixed-mode fracture of concrete subjected to impact loading. *Journal of Structural Engineering*, 116:585–602, 1990.
- [50] J.F. Kalthoff and S. Winkler. Failure mode transition at high rates of shear loading. In C.Y. Chiem, H.D. Kunze, and L.W. Meyer, editors, *International Conference on Impact Loading and Dynamic Behavior of Materials*, pages 185–195, 1987.

- [51] J.-H. Kim and G.H. Paulino. Isoparametric graded finite elements for nonhomogeneous isotropic and orthotropic materials. *ASME Journal of Applied Mechanics*, 69:502–514, 2002.
- [52] J.-H. Kim and G.H. Paulino. Mixed-mode fracture of orthotropic functionally graded materials using the finite element method and the modified crack closure method. *Engineering Fracture Mechanics*, 14-16:1557–1586, 2002.
- [53] J.-H. Kim and G.H. Paulino. T-stress, mixed-mode stress intensity factors, and crack initiation angles in functionally graded materials: a unified approach using the interaction integral method. *Computer Methods in Applied Mechanics and Engineering*, 192(11-12):1463–1494, 2003.
- [54] J.-H. Kim and G.H. Paulino. Simulation of crack propagation in functionally graded materials under mixed-mode and non-proportional loading. *International Journal for Mechanics and Materials in Design*, 1(3):63–94, 2004.
- [55] P. Klein and H. Gao. Crack nucleation and growth as strain localization in a virtual-bond continuum. *Engineering Fracture Mechanics*, 61:21–48, 1998.
- [56] P.A. Klein, J.W. Foulk, E.P. Chen, S.A. Wimmer, and H. Gao. Physics-based modeling of brittle fracture: Cohesive formulations and the application of mesh-free methods. Technical Report SAND2001-8099, Sandia National Laboratory, 2000.
- [57] P.A. Klein, J.W. Foulk, E.P. Chen, S.A. Wimmer, and H. Gao. Physics-based modeling of brittle fracture: Cohesive formulations and the application of meshfree methods. *Theoretical and Applied Fracture Mechanics*, 37(1-3):99–166, 2001.
- [58] W.G. Knauss and G.U. Losi. Crack propagation in a nonlinearly viscoelastic solid with relevance to adhesive bond failure. *ASME Journal of Applied Mechanics*, 60:793–801, 1993.
- [59] D.V. Kubair, P.H. Geubelle, and Y. Huang. Analysis of a rate-dependent cohesive model for dynamic crack propagation. *Engineering Fracture Mechanics*, 50:685–704, 2003.
- [60] Y. Lee and V. Prakash. Dynamic brittle fracture of high strength structural steels under conditions of plane strain. *International Journal of Solids and Structures*, 36:3293–3337, 1999.
- [61] R. Löhner. Some useful data structures for the generation of unstructured grids. *Communications in Applied Numerical Methods*, 4:123–135, 1998.
- [62] M. Mäntylä. *An Introduction to Solid Modeling*. Computer Science Press, 1988.
- [63] L.F. Martha, P.A. Wawrzynek, and A.R. Ingraffea. Arbitrary crack representation using solid modeling. *Engineering with Computers*, 9:63–82, 1993.

- [64] K. Matous and P.H. Geubelle. Multiscale modelling of particle debonding in reinforced elastomers subjected to finite deformations. *International Journal of Numerical Methods in Engineering*, 65:190–223, 2006.
- [65] D. Maugis and M. Barquins. Fracture mechanics and the adherence of viscoelastic bodies. *Journal of Physics D: Applied Physics*, 11(14):1989–2023, 1978.
- [66] L. Meirovitch. *Analytical Methods in Vibrations*. The Macmillan Company, New York, 1937.
- [67] O. Miller, L.B. Freund, and A. Needleman. Energy dissipation in dynamic fracture of brittle materials. *Modelling and Simulation in Materials Science and Engineering*, 7(10):573–586, 1999.
- [68] Y. Miyamoto, W.A. Kaysser, B.H. Rabin, A. Kawasaki, and R.G. Ford. *Functionally Graded Materials: Design, Processing and Applications*. Kluwer Academic Publishers, Dordrecht, 1999.
- [69] A. Needleman. A continuum model for void nucleation by inclusion debonding. *Journal of Applied Mechanics*, 54:525–531, 1987.
- [70] E. Orowan. Fracture and strength of solids. *Reports on Progress in Physics*, XII:185, 1948.
- [71] M. Ortiz and A. Pandolfi. Finite-deformation irreversible cohesive elements for three-dimensional crack-propagation analysis. *International Journal of Numerical Methods in Engineering*, 44:1267–1282, 1999.
- [72] S.J. Owen and M.S. Shephard. Editorial: special issue on trends in unstructured mesh generation. *International Journal of Numerical Methods in Engineering*, 58:159–160, 2003.
- [73] A. Pandolfi, P.R. Guduru, M. Ortiz, and A.J. Rosakis. Finite element analysis of experiments of dynamic fracture in c300 steel. *International Journal of Solids and Structures*, 37:3733–3760, 2000.
- [74] A. Pandolfi, P. Krysl, and M. Ortiz. Finite element simulation of ring expansion and fragmentation: The capturing of length and time scales through cohesive models of fracture. *International Journal of Fracture*, 95(1-4):279–297, 1999.
- [75] A. Pandolfi and M. Ortiz. Solid modeling aspects of three-dimensional fragmentation. *Engineering with Computers*, 14:287–308, 1998.
- [76] A. Pandolfi and M. Ortiz. An efficient adaptive procedure for three-dimensional fragmentation simulations. *Engineering with Computers*, 18:148–159, 2002.

- [77] K.D. Papoulia, C.H. Sam, and S.A. Vavasis. Time continuity in cohesive finite element modeling. *International Journal of Numerical Methods in Engineering*, 58:679–701, 2003.
- [78] K. Park, G.H. Paulino, and J.R. Roesler. A unified potential-based cohesive model of mixed-mode fracture. *Journal of the Mechanics and Physics of Solids*, 2007, submitted.
- [79] G. H. Paulino. Fracture of functionally graded materials, Editorial. *Engineering Fracture Mechanics*, 69:1519–1520, 2002.
- [80] G.H. Paulino, Z.-H. Jin, and R.H. Dodds Jr. Failure of functionally graded materials. In B. Karihaloo et al., editor, *Encyclopedia of Comprehensive Structural Integrity*, volume 2, pages 607–644. Elsevier, Amsterdam, 2003.
- [81] G.H. Paulino and J.-H. Kim. Poisson’s ratio effect on mixed-mode stress intensity factors and T-stress in functionally graded materials. *International Journal of Computational Engineering Science*, 5(4):833–861, 2004.
- [82] G.H. Paulino and Z. Zhang. Dynamic fracture of functionally graded composites using an intrinsic cohesive zone model. *Material Science Forum*, 492-493:447–452, 2005.
- [83] S. Rafiee, TH. Seelig, and D. Gross. Simulation of dynamic crack curving and branching under biaxial loading by a time domain boundary integral equation method. *International Journal of Fracture*, 120:545–561, 2003.
- [84] K. Ravi-Chandar and W.G. Knauss. An experimental investigation into dynamic fracture - I. Crack initiation and crack arrest. *International Journal of Fracture*, 25:247–262, 1984.
- [85] K. Ravi-Chandar and W.G. Knauss. An experimental investigation into dynamic fracture - II. Microstructural aspects. *International Journal of Fracture*, 26:65–80, 1984.
- [86] K. Ravi-Chandar and W.G. Knauss. An experimental investigation into dynamic fracture - III. On steady-state crack propagation and crack branching. *International Journal of Fracture*, 26:141–154, 1984.
- [87] K. Ravi-Chandar and W.G. Knauss. An experimental investigation into dynamic fracture - IV. On the interaction of stress waves with propagating cracks. *International Journal of Fracture*, 26:189–200, 1984.
- [88] K. Ravi-Chandar and B. Yang. On the role of microcracks in the dynamic fracture of brittle materials. *Journal of the Mechanics and Physics of Solids*, 45:535–563, 1997.

- [89] J.-F. Remacle, B.K. Karamete, and M.S. Shephard. Algorithm oriented mesh database. In *9th International Meshing Roundtable*, pages 349–359. Sandia National Laboratories, October 2000.
- [90] J.-F. Remacle and M.S. Shephard. An algorithm oriented mesh database. *International Journal of Numerical Methods in Engineering*, 58:349–374, 2003.
- [91] J.R. Rice. Mathematical analysis in the mechanics of fracture. In H. Liebowitz, editor, *Fracture, an Advanced Treatise*, volume 2, pages 191–311. Academic Press, New York, 1968.
- [92] J.R. Rice, Y. Ben-Zion, and K.-S. Kim. Three-dimensional perturbation solution for a dynamic planar crack moving unsteadily in a model elastic solid. *Journal of the Mechanics and Physics of Solids*, 42:813–843, 1994.
- [93] G. Ruiz, A. Pandolfi, and M. Ortiz. Three-dimensional cohesive modeling of dynamic mixed-mode fracture. *International Journal of Numerical Methods in Engineering*, 52:97–120, 2001.
- [94] C-H. Sam, K.D. Papoulia, and S.A. Vavasis. Obtaining initially rigid cohesive finite element models that are temporally convergent. *Engineering Fracture Mechanics*, 72:2247–2267, 2005.
- [95] O. Samudrala, Y. Huang, and A.J. Rosakis. Subsonic and intersonic mode II crack propagation with a rate-dependent cohesive zone. *Journal of the Mechanics and Physics of Solids*, 50:1231–1268, 2002.
- [96] E. Sharon and J. Fineberg. Microbranching instability and the dynamic fracture of brittle materials. *Physical Reviews B*, 54:7128–7139, 1996.
- [97] E. Sharon, S.P. Gross, and J. Fineberg. Energy dissipation in dynamic fracture. *Physical Review Letters*, 76:2117–2120, 1995.
- [98] E. Sharon, S.P. Gross, and J. Fineberg. Local crack branching as a mechanism for instability in dynamic fracture. *Physical Review Letters*, 74:5096–5099, 1995.
- [99] S.H. Song, G.H. Paulino, and W.G. Buttlar. A bilinear cohesive zone model tailored for fracture of asphalt concrete considering viscoelastic bulk material. *Engineering Fracture Mechanics*, 73(18):2829–2848, 2006.
- [100] S.H. Song, G.H. Paulino, and W.G. Buttlar. Simulation of crack propagation in asphalt concrete using an intrinsic cohesive zone model. *ASCE Journal of Engineering Mechanics*, 132(11):1215–1223, 2006.
- [101] S. Suresh and A. Mortensen. *Functionally Graded Materials*. The Institute of Materials, IOM Communications Ltd., London., 1998.

- [102] H. Tan, C. Liu, Y. Huang, and P.H. Geubelle. The cohesive law for the particle/matrix interfaces in high explosives. *Journal of the Mechanics and Physics of Solids*, 53:1892–1917, 2005.
- [103] K.H. Tsai and K.S. Kim. Stick-slap in the thin film peel test – I. The 90° peel test. *International Journal of Solids and Structures*, 30(13):1789–1806, 1993.
- [104] V. Tvergaard. Effect of fiber debonding in a whisker-reinforced metal. *Materials Science and Engineering A*, 125:203–213, 1990.
- [105] P.A. Wawrzynek and A.R. Ingraffea. Interactive finite element analysis of fracture processes: an integrated approach. *Theoretical and Applied Fracture Mechanics*, 8:137–150, 1987.
- [106] K. Weiler. *Topological structures for geometric modeling*. PhD thesis, Rensselaer Polytechnic Institute, New York, 1986.
- [107] K. Weiler. The radial edge structure: A topological representation for non-manifold geometric boundary modeling. In M.J. Wozny, H.W. McLauhlin, and J.L. Encarnacao, editors, *Geometric Modeling for CAD Applications*, pages 3–36, Rensselaerville, NY, 1988. IFIP, North Holland.
- [108] X. Xu and A. Needleman. Numerical simulations of fast crack growth in brittle solids. *Journal of the Mechanics and Physics of Solids*, 42(9):1397–1434, 1994.
- [109] X. Xu and A. Needleman. Numerical simulations of dynamic crack growth along an interface. *International Journal of Fracture*, 74:289–324, 1996.
- [110] B. Yang and K. Ravi-Chandar. On the role of the process zone in dynamic fracture. *Journal of the Mechanics and Physics of Solids*, 44(12):1955–1976, 1996.
- [111] E.H. Yoffe. The moving Griffith crack. *Philosophical Magazine*, 42:739–750, 1951.
- [112] C. Yoon and D.H. Allen. Damage dependent constitutive behavior and energy release rate for a cohesive zone in a thermoviscoelastic solid. *International Journal of Fracture*, 96:55–74, 1999.
- [113] P. Zavattieri and H. Espinosa. Grain level model analysis of crack initiation and propagation in brittle materials. *Acta Materialia*, 49:4291–4311, 2001.
- [114] P. Zhang, P.A. Klein, Y. Huang, H. Gao, and P.-D. Wu. Numerical simulation of cohesive fracture by the virtual-internal-bond model. *Computer Modeling in Engineering and Sciences*, 3(2):263–278, 2002.
- [115] Z. Zhang. Cohesive zone modeling of dynamic failure in homogeneous and functionally graded materials. Master’s thesis, University of Illinois at Urbana-Champaign, 2003.

- [116] Z. Zhang and G.H. Paulino. Cohesive zone modeling of dynamic failure in homogeneous and functionally graded materials. *International Journal of Plasticity*, 21:1195–1254, 2005.
- [117] Z. Zhang, G.H. Paulino, and W. Celes. Extrinsic cohesive modeling of dynamic fracture and microbranching instability in brittle materials. *International Journal of Numerical Methods in Engineering*, 72:893–923, 2007.
- [118] F. Zhou, J.-F. Molinari, and T. Shioya. A rate-dependent cohesive model for simulating dynamic crack propagation in brittle materials. *Engineering Fracture Mechanics*, 72:1383–1410, 2005.
- [119] M. Zhou, A.J. Rosakis, and G. Ravichandran. On the growth of shear bands and failure-mode transition in prenotched plates: a comparison of singly and doubly notched specimens. *International Journal of Plasticity*, 14:435–451, 1998.

Curriculum Vitae

Education

- **University of Illinois at Urbana Champaign**

Ph.D. student, 08/2003-present, Structural Engineering

Computational Science and Engineering (CSE) Option Program

Defense passed: **Oct. 30th, 2007** Degree expected: 12/2007

Dissertation: *Extrinsic Cohesive Modeling of Dynamic Fracture and Microbranching Using a Topological Data Structure.*

M.S. degree in Structure Engineering, UIUC, **05/2003**

Thesis: *Cohesive Zone Modeling of Dynamic Failure in Homogeneous and Functionally Graded Materials*

Advisor: Glaucio H. Paulino, Faculty of CEE, MSE, CSE at UIUC

- **Tongji University (China)**

Graduate Student, 09/1996-06/2000

Department of Engineering Mechanics and Technology

Project: *Mechanical Property of Composite Materials*

Advisor: R. J. Zhang, Professor

B.E. degree in Structure Engineering, Tongji University, **12/1995**

Honors and Awards

- ◇ Mavis Memorial Fund Scholarships Award, 2003, UIUC
- ◇ Henry Ford II Scholar Award, 2001, UIUC
- ◇ Computational Science and Engineering fellowship, 2001/2002, UIUC
- ◇ Computational Science and Engineering fellowship, 2000/2001, UIUC
- ◇ Excellence Scholarship, 1996-1997 Academic year, Tongji Univ.
- ◇ Excellent Student Honor, Graduate Student Assessment in Mar. 1998. Tongji Univ.
- ◇ Excellent Student Honor, 1991-1992 Academic year, Tongji Univ.

Peer-reviewed Journal Papers

1. Zhang, Z. and Paulino, G.H. 2005. Cohesive Zone Modeling of Dynamic Failure in Homogeneous and Functionally Graded Materials, *International Journal of Plasticity* **21** (6), 1195-1254.
2. Paulino, G.H. and Zhang, Z. 2005. Dynamic Fracture of Functionally Graded Composites Using an Intrinsic Cohesive Zone Model, *Material Science Forum* **492-493**, 447-452.
3. Zhang, Z. and Paulino, G.H. 2006. Wave Propagation and Dynamic Analysis of Smoothly Graded Heterogeneous Continua Using Graded Finite Elements, *International Journal of Solids and Structures*, **44** (11-12), 3601-3626.
4. Zhang, Z., Paulino, G.H. and Celes, W. 2007. Extrinsic cohesive modeling of dynamic fracture and microbranching instability in brittle materials, *International Journal for Numerical Methods in Engineering*, **72**, 893-923.
5. Paulino, G. H, Celes, W., Espinha, R. and Zhang, Z. 2007. A general topology-based framework for adaptive insertion of cohesive elements in finite element meshes, *Engineering with Computers*, in press (DOI 10.1007/s00366-007-0069-7).
6. Zhang, Z., Paulino, G.H. and Celes, W. 2007. Extrinsic cohesive zone modeling of dynamic mixed-mode fracture using a topological data structure, to be submitted for journal publication.
7. Zhang, Z., Paulino, G.H. Cohesive zone size: static, dynamic and rate effects, to be submitted for journal publication.

Technical Presentations & Abstracts

- Extrinsic Cohesive Zone Modeling of Dynamic Mixed-mode Fracture Using a Topological Data Structure, USNCCM IX, July 24, 2007, San Francisco, California. (presented by Z. Zhang)
- Cohesive Modeling of Dynamic Mixed-mode Crack Propagation in Homogeneous and Functionally Graded Materials, Multiscale and Functionally Graded Materials Conference 2006, October 15-18, 2006, Honolulu, Hawaii. (presented by Z. Zhang)

- Intrinsic Cohesive Zone Modeling of Dynamic Failure in Functionally Graded Materials, US-South America Workshop, Mechanics and Advanced Materials: Research and Education. August 2-6, 2004, Rio de Janeiro, Brazil. (presented by Z. Zhang)
- Cohesive Zone Modeling of Dynamic Fracture Behavior of Functionally Graded Materials, Seventh U.S. National Congress on Computational Mechanics, USNCCM VII, July 30, 2003, Albuquerque, New Mexico. (presented by Z. Zhang)
- Verification and Validation: Cohesive Elements for Dynamic Fracture Analysis in Homogeneous and Functionally Graded Materials, USACM Student Benchmark Competition, USNCCM VII, July 29, 2003, Albuquerque, New Mexico. (presented by Z. Zhang)
- Stress Concentration for Interacting Holes in Functionally Graded Materials, Sixth U.S. National Congress on Computational Mechanics, USNCCM VI, August 1-4, 2001, Dearborn, Michigan. (presented by Z. Zhang)

Conference Papers

- Zhang. Z., Paulino. G. H., Celes, W. 2006. Cohesive Modeling of Dynamic Mixed-mode Crack Propagation in Homogeneous and Functionally Graded Materials, *Multiscale and Functionally Graded Materials Conference 2006 Proceeding* (in press)
- Paulino. G. H., Zhang. Z. 2005. Cohesive Zone Modeling of Propagating Cracks in Homogeneous and Functionally Graded Composites. *5th GRACM International Congress on Computational Mechanics Proceeding*, vol.1, pp. 45-52.

Invited Lectures

- Dynamic Failure and Micro-branching Using Cohesive Zone Modeling, Mar. 27, 2007, Maryland 110, Johns Hopkins University.
- Extrinsic Cohesive Zone Modeling of Dynamic Failure: Crack Propagation and Micro-branching Instability, Jan. 25, 2007, 366 Hollister Hall, Cornell University.

- Cohesive Zone Modeling of Dynamic Failure in Homogeneous and Functionally Graded Materials, *CEE Structural Engineering Seminar Series*, Nov. 11, 2002, 151 Loomis, UIUC.